

University of Wollongong - Research Online

Thesis Collection

Title: Dynamics of conducting polymer actuators

Author: Mehrdad Bahrami-Samani

Year: 2007

Repository DOI:

Copyright Warning

You may print or download ONE copy of this document for the purpose of your own research or study. The University does not authorise you to copy, communicate or otherwise make available electronically to any other person any copyright material contained on this site.

You are reminded of the following: This work is copyright. Apart from any use permitted under the Copyright Act 1968, no part of this work may be reproduced by any process, nor may any other exclusive right be exercised, without the permission of the author. Copyright owners are entitled to take legal action against persons who infringe their copyright. A reproduction of material that is protected by copyright may be a copyright infringement. A court may impose penalties and award damages in relation to offences and infringements relating to copyright material.

Higher penalties may apply, and higher damages may be awarded, for offences and infringements involving the conversion of material into digital or electronic form.

Unless otherwise indicated, the views expressed in this thesis are those of the author and do not necessarily represent the views of the University of Wollongong.

Research Online is the open access repository for the University of Wollongong. For further information contact the UOW Library: research-pubs@uow.edu.au

University of Wollongong Thesis Collections

University of Wollongong Thesis Collection

University of Wollongong

Year 2007

Dynamics of conducting polymer actuators

Mehrdad Bahrami-Samani
University of Wollongong

Bahrami-Samani, Mehrdad, Dynamics of conducting polymer actuators, PhD thesis, School of Mechanical, Materials and Mechatronic Engineering, University of Wollongong, 2007.
<http://ro.uow.edu.au/theses/645>

This paper is posted at Research Online.
<http://ro.uow.edu.au/theses/645>

NOTE

This online version of the thesis may have different page formatting and pagination from the paper copy held in the University of Wollongong Library.

UNIVERSITY OF WOLLONGONG

COPYRIGHT WARNING

You may print or download ONE copy of this document for the purpose of your own research or study. The University does not authorise you to copy, communicate or otherwise make available electronically to any other person any copyright material contained on this site. You are reminded of the following:

Copyright owners are entitled to take legal action against persons who infringe their copyright. A reproduction of material that is protected by copyright may be a copyright infringement. A court may impose penalties and award damages in relation to offences and infringements relating to copyright material. Higher penalties may apply, and higher damages may be awarded, for offences and infringements involving the conversion of material into digital or electronic form.

DYNAMICS OF CONDUCTING POLYMER ACTUATORS

A thesis submitted in fulfilment of the
requirements for the award of the degree

Doctor of Philosophy

From

University of Wollongong



By

Mehrdad Bahrami-Samani, B. Sc., M. Sc. (Mech. Eng.)

School of Mechanical, Materials and Mechatronic Engineering

2007

CERTIFICATION

I, Mehrdad Bahrami-Samani, declare that this thesis, submitted in fulfilment of the requirements for the award of Doctor of Philosophy, in the Faculty of Engineering, University of Wollongong, is wholly my own work unless otherwise referenced or acknowledged. The document has not been submitted for qualifications at any other academic institution.

Mehrdad Bahrami-Samani

July 21, 2007

TABLE OF CONTENTS

CERTIFICATION.....	II
TABLE OF CONTENTS	III
LIST OF FIGURES.....	V
GLOSSARY.....	XI
PUBLICATIONS	XII
ABSTRACT	XIII
ACKNOWLEDGMENTS.....	XV
CHAPTER 1: INTRODUCTION AND LITERATURE REVIEW	1
1.1. MOTIVATIONS AND AIM	1
1.2. CONDUCTING POLYMERS	1
1.3. CONDUCTING POLYMER ACTUATORS	2
1.4. CONDUCTING POLYMER ACTUATORS PERFORMANCE	3
1.5. APPLICATION OF CONDUCTING POLYMER ACTUATORS	6
1.5.1. <i>Bending actuators</i>	6
1.5.2. <i>Linear actuators</i>	7
1.6. MECHANISM OF ACTUATION IN CONDUCTING POLYMERS	9
1.7. CONDUCTING POLYMER ACTUATORS MODELLING	10
1.7.1. <i>Electrochemical Modelling</i>	11
1.7.2. <i>Electromechanical Modelling</i>	15
1.8. AIMS AND SCOPE OF THE THESIS	19
CHAPTER 2: GENERAL EXPERIMENTAL TECHNIQUES.....	22
2.1. INTRODUCTION	22
2.2. POLYPYRROLE HELIX TUBE ACTUATOR PREPARATION.....	22
2.3. ELECTROCHEMICAL BATH AND REFERENCE ELECTRODE	25
2.4. GENERAL EXPERIMENTAL SET UP	26
2.5. PROGRAMMING METHOD	27
CHAPTER 3: PRIMARY MODEL OF PPY HELIX TUBE MICRO ACTUATOR	28
3.1. INTRODUCTION	28
3.2. MATERIALS AND METHODS.....	29
3.3. ACTIVE ELASTIC MODELLING	30
3.4. EXPERIMENTAL RESULTS	30
3.5. MODELLING	36
3.5.1. <i>Modelling principles and approach</i>	36
3.5.2. <i>Electromechanical model</i>	39
3.5.3. <i>Experimental set-up for model validation</i>	41
3.5.4. <i>Comparison of experimental and predicted results</i>	43
3.6. CONCLUSIONS	50
CHAPTER 4: USING VISCOELASTIC MODEL FOR IMPROVEMENT OF PASSIVE PPY HELIX TUBE MICRO ACTUATOR MODELLING.....	52
4.1. INTRODUCTION	52
4.2. MATERIALS AND METHODS.....	52
4.3. PASSIVE VISCOELASTIC MODELLING	53
4.3.1. <i>The stress-strain test case</i>	57
4.3.2. <i>Stress Relaxation Case</i>	59
4.3.3. <i>Creep Case</i>	61
4.3.4. <i>Sinusoidal excitation case</i>	63
4.3.5. <i>Active generated strain term</i>	65
4.4. EXPERIMENTAL RESULTS	68

4.5. 'PASSIVE IMPROVEMENT' MODEL	74
4.6. CONCLUSIONS	83
CHAPTER 5: THE EFFECT OF ELECTRICAL STIMULATION ON THE VISCOELASTIC PARAMETERS.....	85
5.1. INTRODUCTION	85
5.2. EXPERIMENTAL SET UP	87
5.3. METHODOLOGY CONFIRMATION	88
5.4. RESULTS AND DISCUSSIONS	91
5.4.1. <i>Stiffness coefficients results</i>	91
5.4.2. <i>Viscosity coefficients results</i>	102
5.4.3. <i>Time constants results</i>	107
5.5. MODELLING	108
5.6. CONCLUSIONS	116
CHAPTER 6: QUARTZ CRYSTAL MICROBALANCE STUDY OF MASS CHANGES AND MODULUS SHIFT IN ELECTROCHEMICALLY SWITCHED POLYPYRROLE.....	117
6.1. INTRODUCTION	117
6.2. MATERIALS AND METHODS	119
6.2.1. <i>Materials</i>	119
6.2.2. <i>Experimental methodology</i>	119
6.2.3. <i>Numerical methodology</i>	121
6.3. VERIFICATION OF THE METHODOLOGY	123
6.3.1. <i>Verification of polypyrrole film mass per area</i>	124
6.3.2. <i>Confirming calculated film modulus and thickness using standard polymer films</i>	125
6.4. RESULTS AND DISCUSSIONS	127
6.4.1. <i>Electrochemical Switching of PPy in PC electrolyte</i>	127
6.4.2. <i>Electrochemical Switching of PPy in Ionic Liquid (EMI-TFSL) electrolyte</i>	134
6.5. CONCLUSIONS	139
CHAPTER 7: CONCLUSIONS AND RECOMMENDATIONS FOR FUTURE RESEARCH ..	141
7.1. CONCLUSIONS	141
7.2. FUTURE WORK	144
APPENDIX A: LAPLACE TRANSFORM.....	146
APPENDIX B: STATE-SPACE METHOD	149
BIBLIOGRAPHY	151

LIST OF FIGURES

Figure 2.2.1 The electrochemical polymerisation cell used for actuator preparation.....	22
Figure 2.2.2 PPy helix tube.....	23
Figure 2.2.3 cross sectional area. Scale 50 micrometer.....	24
Figure 2.3.1 Electrochemical bath.....	25
Figure 2.3.2 Reference electrode.	26
Figure 2.4.1 Experimental set-up.	27
Figure 3.4.1 Cyclic Voltammetry in different ranges of applied voltages (vs. Ag/AgNO ₃ reference) with 5 mV/s scan rate and 1.528 MPa applied load.	31
Figure 3.4.2 Cyclic Voltammetry in 5 mV/s scan rate and different applied loads (1.5, 2.8 and 3.1 MPa).....	31
Figure 3.4.3 Generated strain result of Cyclic Voltammetry in different range of voltage in 5 mV/s scan rate and 1.528 MPa applied load.....	32
Figure 3.4.4 Generated strain result of Cyclic Voltammetry vs. charge transferred in 5 mV/s scan rate and 1.528 MPa applied load.	34
Figure 3.4.5 Generated strain result of Cyclic Voltammetry vs. charge transferred in different scan rates and 1.528 MPa applied load.	34
Figure 3.4.6 A generalisation of the first derivative of generated strain to charge density transferred based on the Cyclic Voltammetry in 1 mV/s vs. charge transferred density in 1.528 MPa applied load.....	36
Figure 3.5.1 experimental data for 1 mV/s scan rate.	39
Figure 3.5.2 Flow chart showing how electrochemical strain is estimated from measured current.	40
Figure 3.5.3 Experimental results from sinusoidal voltage input over a wide voltage range at different frequencies.....	42
Figure 3.5.4 Stress 0.45 MPa and 1 mHz.....	44
Figure 3.5.5 Stress 0.45 MPa and 5 mHz.....	45

Figure 3.5.6 Stress 0.45 MPa and 10 mHz.....	46
Figure 3.5.7 Stress 3.25 MPa and 1 mHz.....	47
Figure 3.5.8 Stress 3.25 MPa and 5 mHz.....	48
Figure 3.5.9 Stress 3.25 MPa and 10 mHz.....	48
Figure 3.5.10 Stress 5.80 MPa and 5 mHz.....	49
Figure 3.5.11 Stress 5.80 MPa and 10 mHz.	50
Figure 4.3.1 Viscoelastic free body diagram of EAP actuators, containing n blocks in parallel mode.....	54
Figure 4.3.2. Schematic response to Stress-Relaxation test.....	60
Figure 4.3.3. Schematic response to Creep test.....	62
Figure 4.3.4 Schematic diagram of the storage and loss modulus vs. frequency.	65
Figure 4.3.5 Calculation method of electrochemical strain $(k_t = k_r + \sum_{i=1}^n k_i)$	67
Figure 4.4.1 R-Square vs. number of Maxwell blocks in the model.....	69
Figure 4.4.2 Total stiffness and total damping vs. number of Maxwell blocks in the model.....	69
Figure 4.4.3 Total and Relaxed stiffness increase with increasing isometric strain applied during stress-relaxation experiment.....	70
Figure 4.4.4 Maxwell's stiffness of 3 blocks with isometric strain.....	71
Figure 4.4.5. Stress-Strain curves for different lengths of actuators. Inset shows the low strain region in more detail.....	72
Figure 4.4.6 Total damping coefficient changing with isometric strain.....	72
Figure 4.4.7 The time constants of each Maxwell block as a function of isometric step strain input (logarithmic scale).....	73
Figure 4.5.1. the flowchart of the solver program.....	77
Figure 4.5.2 Stress 0.45 MPa and 1 mHz.....	78
Figure 4.5.3 Stress 0.45 MPa and 5 mHz.....	79
Figure 4.5.4 Stress 0.45 MPa and 10 mHz.....	79
Figure 4.5.5 Stress 3.25 MPa and 1 mHz.....	81
Figure 4.5.6 Stress 3.25 MPa and 5 mHz.....	81
Figure 4.5.7 Stress 3.25 MPa and 10 mHz.....	82
Figure 4.5.8 Stress 5.80 MPa and 5 mHz.....	82

Figure 4.5.9 Stress 5.80 MPa and 10 mHz.....	83
Figure 5.1.1 Actuator strain recorded under isotonic conditions at different stress levels in 0.25 M TBA-PF ₆ /PC and ionic liquid EMI-TFSI electrolyte; a current pulse for 30 seconds was applied at 12mA/cm ² . (Xi, 2005).	86
Figure 5.3.1. The rectangular stress waveform and the corresponding strain of DMA experiment.....	90
Figure 5.3.2. Comparison between DMA result and the new method for measuring real modulus.	91
Figure 5.4.1 The real modulus variation, resultant strain and CV diagram at 1mV/s.	92
Figure 5.4.2. The real modulus variation, resultant strain and CV diagram at 2mV/s.	93
Figure 5.4.3 The real modulus variation, resultant strain and CV diagram at 4mV/s.	94
Figure 5.4.4 The real modulus variation, resultant strain and CV diagram at 6mV/s.	94
Figure 5.4.5 The real modulus variation, resultant strain and CV diagram at 8mV/s.	95
Figure 5.4.6 The real modulus variation, resultant strain and CV diagram at 12mV/s.....	95
Figure 5.4.7 The real modulus variation, resultant strain and CV diagram in 20mV/s.....	96
Figure 5.4.8. Modulus variation vs. active strain taken from the data given in Figure 5.4.2 at 2mV/s.....	97
Figure 5.4.9 Modulus variation vs. active strain taken from the data given in Figure 5.4.6 at 12mV/s.....	97
Figure 5.4.10. Modulus variation vs. active strain during oxidation process for different scan rates of cyclic voltammetry.....	98
Figure 5.4.11. The real modulus variation for different frequencies of applied voltage.	99
Figure 5.4.12. Maximum active strain and maximum variation in modulus for different scan rates.....	99

Figure 5.4.13. The real modulus changing over a long time period held at the potentials shown.	100
Figure 5.4.14. Stress-Strain test before actuation by step 1V and two times after actuation.	101
Figure 5.4.15 The total and relaxed stiffness modulus in different applied voltages.	103
Figure 5.4.16 parameters definition using schematic view of the experiment.	105
Figure 5.4.17 The viscosity variation, resultant strain and CV diagram at 1mV/s.	106
Figure 5.4.18 The viscosity variation, resultant strain and CV diagram at different scan rates.	106
Figure 5.4.19 The viscosity variation vs. strain at different scan rates during the oxidation process.	107
Figure 5.4.20 Time constant at 1 mV/s.	108
Figure 5.5.1 Stress 0.450 MPa and 1 mHz.	111
Figure 5.5.2 Stress 0.450 MPa and 5 mHz.	112
Figure 5.5.3 Stress 0.450 MPa and 10 mHz.	112
Figure 5.5.4 Stress 3.250 MPa and 1 mHz.	113
Figure 5.5.5 Stress 3.250 MPa and 5 mHz.	114
Figure 5.5.6 Stress 3.250 MPa and 10 mHz.	114
Figure 5.5.7 Stress 5.8 MPa and 5 mHz.	115
Figure 5.5.8 Stress 5.8 MPa and 10 mHz.	115
Figure 6.1.1. (Top) Bare Crystal oscillates at its natural frequency (F_0). (Bottom) A deposited layer causes a shift in the natural frequency (ΔF) which is proportional to the mass of the layer as determined by Sauerbrey's equation (Sauerbrey, 1959).	117
Figure 6.2.1. Experimental set up of a QCM crystal coated with PPY was stimulated using cyclic voltammetry at different scan rates. The QCM and electrochemical signals were used to determine viscoelastic variables using a mathematical solver.	120
Figure 6.2.2. Experimental Method shows how the QCM device outputs changed during the experiment.	121

Figure 6.2.3. Numerical methodology, in which the measured signals build a complex impedance parameter, which should be equal to the theoretical complex impedance as calculated in the literature (Bandey et al., 1997, Bandey et al., 1999). A program has been designed to solve the equation and find the variables shear modulus (G) and polymer thickness (h_p).....	122
Figure 6.2.4 Dynamic mechanical analysis of a PPy fibre.	123
Figure 6.4.1 The real shear modulus variation and the thickness change are shown vs. voltage beside CV diagram (10mV/s scan rate) and 0.1M TBA-PF ₆ in PC electrolyte.....	128
Figure 6.4.2 The real shear modulus variation and the thickness change are shown vs. voltage beside CV diagram (20mV/s scan rate) and 0.1M TBA-PF ₆ in PC electrolyte.....	128
Figure 6.4.3. The real shear modulus variation and the thickness change are shown vs. voltage beside CV diagram (50mV/s scan rate) using 0.1M TBA-PF ₆ in PC electrolyte.....	129
Figure 6.4.4 Change in shear modulus obtained at different scan rates and 0.1M TBA-PF ₆ in PC electrolyte.....	131
Figure 6.4.5 Change in thickness of PPy at different scan rates in 0.1M TBA-PF ₆ / PC electrolyte.	131
Figure 6.4.6 Cyclic Voltammograms of PPy at different scan rates in 0.1M TBA-PF ₆ / PC electrolyte.	132
Figure 6.4.7 Change in shear modulus obtained at different scan rates and 0.1M TBA-PF ₆ in PC electrolyte vs. charge transferred.....	132
Figure 6.4.8 Change in thickness changing obtained at different scan rates and 0.1M TBA-PF ₆ in PC electrolyte vs. charge transferred.....	133
Figure 6.4.9 Shear Modulus vs. thickness changing of PPy at different scan rates in 0.1M TBA-PF ₆ / PC electrolyte.	133
Figure 6.4.10 The shear modulus variation and thickness change obtained at 20mV/s scan rate in EMI-TSFI Ionic Liquid electrolyte. As expected, the thickness change in IL.....	135

Figure 6.4.11. The shear modulus variation and thickness change obtained at 50mV/s scan rate in EMI-TSFI Ionic Liquid electrolyte. As expected, the thickness change in IL electrolyte is in the inverse direction compared to PC.	135
Figure 6.4.12 The shear modulus variation and thickness change obtained at 100mV/s scan rate in EMI-TSFI Ionic Liquid electrolyte. As expected, the thickness change in IL happened in negative voltage.	136
Figure 6.4.13. Shear modulus change in PPy during switching in EMI-TSFI Ionic Liquid electrolyte obtained at different scan rates.	136
Figure 6.4.14. Thickness variation in PPy during switching at different scan rates in EMI-TSFI Ionic Liquid electrolyte.	137
Figure 6.4.15 Cyclic Voltammograms of PPy at different scan rates in EMI-TFSI electrolyte.	137
Figure 6.4.16 Shear modulus change in PPy during switching in EMI-TSFI Ionic Liquid electrolyte obtained at different scan rates vs. charge transferred.	138
Figure 6.4.17 Thickness variation in PPy during switching at different scan rates in EMI-TSFI Ionic Liquid electrolyte vs. charge transferred.	138
Figure 6.4.18 Shear Modulus shifting vs. thickness changing at different scan rates in EMI-TSFI Ionic Liquid electrolyte.	139

GLOSSARY

σ	Stress
ε	Strain
k_r	Relaxed stiffness coefficient
k_t	Total stiffness coefficient
k_i	Maxwell's i^{th} stiffness coefficient
η_i	Maxwell's i^{th} viscosity coefficient
ε_{ech}	Electrochemical generated strain
ρ	Charge transferred density
q	Charge transferred
ΔF	Frequency change
ΔR	Admittance change
f_0	Resonance frequency of bare crystal
L_u	Inductance of unloaded crystal
ρ_q	Density of the quartz crystal
μ_q	Shear modulus of the quartz crystal
ρ_f	Film density
ρ_l	Liquid density
η_l	Liquid viscosity
h_f	Film thickness
G	Shear modulus of the film

PUBLICATIONS

- **Samani, M.B.**, G.M. Spinks, and C. Cook. "*Mechanical performance of PPy helix tube microactuator*". in Smart Materials III. 2004. Sydney, Australia: SPIE.
- **Samani, M.B.**, Spinks, G. M., Whitten, P. G. and Cook, C. "*Modelling of Polypyrrole Actuators*". in Electroresponsive Polymers and Their Applications. 2005: Mater. Res. Soc. Symp. Proc. 889, Warrendale, PA, 2005.
- Spinks, G., Xi, B., Campbell, T., Whitten, P., Mottaghitalab, V., **Samani, M. B.** and Wallace, G. G. "*In pursuit of high-force/ high-stroke conducting polymer actuators*" (Invited Paper). in Smart Structures and Materials 2005: Electroactive Polymer Actuators and Devices (EAPAD). 2005. San Diego, CA, USA: SPIE.
- **Samani, M.B.**, Whitten, P., Spinks, G. and Cook, C. "*Viscoelastic study of conducting polymers using quartz crystal microbalance*". in Smart Structures and Materials 2006: Electroactive Polymer Actuators and Devices (EAPAD). 2006. San Diego, CA, USA: SPIE.
- Spinks, G.M., Mottaghitalab, V., **Bahrami-Samani, M.**, Whitten, P. G. and Wallace, G. G., "*Carbon-Nanotube-Reinforced Polyaniline Fibers for High-Strength Artificial Muscles*". Advanced Materials, 2006. 18(5): p. 637-640.
- **Samani, M.B.**, Spinks, G. M., Whitten, P. G. and Cook, C. "*Effect of Actuation on Viscoelastic Parameters of Conducting Polymer Actuators*". ready to submit.
- **Samani, M.B.**, Cook, C., Madden, J. D., Spinks, G. M., Whitten, P. G. and "*Quartz Crystal Microbalance Study of Mass Changes and Modulus Shifting in Electrochemically Switched Polypyrrole*". Thin Solid Film, accepted.

ABSTRACT

Considerable research has been carried out to develop actuator technologies such as shape memory alloys, piezoelectric actuators, magnetostrictive actuators, contractile polymers and electrostatic actuators to use in devices such as human-like robots, micro robots and artificial organs for medical applications place of conventional actuators. Though there have been great advances, one or more of high electrical power, low efficiency or low strain limit the application of these new actuator technologies.

Recently, conducting polymers have drawn considerable attention as a new class of advanced functional material for many applications based on the unique properties of electro-activity, conductivity and other physical or chemical properties. The applications being considered include batteries, photovoltaic devices, electro-chromic devices, ion selective membranes, electromagnetic interference shielding, radar absorption, electrical wires, corrosion inhibitors, electrochemical sensors and actuators.

For actuator applications a comprehensive electro-chemo-mechanical model is needed to predict the mechanical output (displacement or force) from the electrical input (current and voltage) to enable control engineers to use these actuators in mechanical systems, new models which describe the dynamic response (actuator output/actuator input) as a function of time and frequency are required. The research in this thesis shows how such models can be derived by exploiting standard control theory analysis tools using Laplace transforms and State-Space techniques. For conducting polymers, such a model needs to include a description of the chemical process occurring between the conducting polymer, dopant and electrolyte. Such a model will enable the application of conducting polymer actuators in automation and robotic applications in which a predictive model is needed to design the control system and also identify the system performance to optimise the actuator characteristics. The aim of the research presented in this thesis is to create a comprehensive predictive model in order to track the output of a typical high-performance conducting polymer actuator: Polypyrrole Helix Tube Fibre Composite Actuator.

The review of literature has revealed that previous models of polypyrrole actuators have been based on the 'strain to charge ratio' parameter, which has been assumed to be constant. In this work, it is shown that the strain to charge ratio is not always constant,

particularly when a wide potential window is used. A master calibration curve approach has been devised to model the mechanical output when the strain to charge ratio is not constant. Secondly, the polypyrrole helix tubes were found to be viscoelastic, so the model was modified to include the viscoelastic (time-dependent) responses. Finally, the model was further modified to allow the viscoelastic parameters to vary with the applied potential. The latter two additions to the model greatly improve its predictive ability when the applied load is changing.

To further investigate the effect of applied potential on the mechanical properties, a measurement method based on Quartz Crystal Microbalance technique has been developed. This method enables the thickness and shear modulus variation of polypyrrole thin films under electrochemical doping and un-doping (oxidation and reduction) to be studied. A complicated 'Modulus Shifting' phenomenon in polypyrrole is revealed by these studies which depend strongly on the electrolyte.

Finally, the results present a full description of the electromechanical characterisation of polypyrrole helix tubes considering the interacting effects of electrochemical and electromechanical parameters. This description may enable further optimization of the design and performance of polypyrrole helix tube actuators.

ACKNOWLEDGMENTS

Most of all, I would like to express my sincere gratitude to my supervisors Professor **Christopher Cook** and Professor **Geoffrey Spinks** for providing both general and technical advice, direction and support and also enthusiastic encouragement throughout my study.

I would like to thank Professor **Gordon Wallace** for providing a great research environment, regularly meetings and conferences in the Intelligent Polymer Research Institute (IPRI) and ARC Centre of Excellence for Electromaterials Science (ACES).

I would like to thank Dr. **Philip Whitten** for his impressive comments and discussions during this work.

I would like to acknowledge A/Professor **John Madden** and his great research group in the University of British Columbia for their technical advices.

I deeply appreciate helpful assistance from staff and students of the Intelligent Polymer Research Institute, especially Dr. Binbin Xi, Dr. Vahid Mottaghitalab and A/Prof. Gursel Alici.

I would like to thank my parents (Simin-Dokht and Mansour) and my beautiful sisters (Niloufar and Yasaman) for their kind and endless supports during my studying.

Last but not least, I would like to thank my lovely wife Maryam Agahi, for her love and never-ending support. I want to thank her for her encouragement when I was desperate or not focused.

CHAPTER 1: INTRODUCTION AND LITERATURE REVIEW

1.1. Motivations and aim

Considerable research has been carried out to develop actuator technologies based on shape memory alloys, piezoelectric actuators, magnetostrictive actuators, contractile polymers and electrostatic actuators. These systems are proposed for use in devices such as human-like robots, micro robots and artificial organs for medical applications or to replace conventional actuators (Hollerbach et al., 1991, Hunter and Lafontaine, 1992). Despite great advances in the performance of actuator materials, there are remaining limitations that restrict their use. Problems such as high electrical power, low efficiency in shape memory alloys and low strain generated, high electrical power in piezoelectric and low strain, high power needed in magnetostrictive actuators and low stress and stiffness in electrostatic actuators have limited the application of these new generation actuator technologies (Hunter and Lafontaine, 1992). Conducting polymer actuators show promise since they require a low voltage input and producing reasonable strain and stress outputs.

The lack of a comprehensive electro-chemo-mechanical model which can predict the mechanical output (displacement or force) from the electrical input (current and voltage) has been limiting the application of conducting polymer actuators in automation and robotic applications. It is particularly important in these areas to have a predictive model to design the control system and also for identification of the system performance to optimise the actuator characteristics. The aim of the research presented in this thesis is to create an inclusive predictive model to track the output of a typical high-performance conducting polymer micro actuator (Polypyrrole Helix Tube) from an engineering point of view for possible use in robotic applications.

In this chapter, a general literature review will be presented on conducting polymers, conducting polymer actuators, conducting polymer actuation mechanism and the existing electrochemical and mechanical models. A clear statement of thesis objectives and scope concludes this chapter.

1.2. Conducting polymers

The Nobel Prize in Chemistry for year 2000 was awarded to Alan J. Heeger, Alan G MacDiarmid, and Hideki Shirakawa for their discovery and development of conducting

polymer materials. Unlike metal, a polymer does not possess free electrons that can move through the lattice in an electric field. These free electrons are considered as charge carriers for electrical conduction in metals. For a polymer to be able to conduct electric current, it must contain overlapping pi-molecular orbitals through a high degree of pi-bond conjugation. Conjugated polymers are insulating materials in their neutral state. When a pi-electron is removed from the polymer backbone, it becomes a radical cation (polaron) that is delocalised over 3-4 monomer units. When a second electron is removed from the polymer, two individual polarons or bipolaron can form. Because the formation of bipolarons is energetically more favourable than the separated polaronic states, bipolarons are spread over the polymer. Polarons and bipolarons are mobile in an electric field and are the charge carriers responsible for electrical conduction in polymer chains (Ding et al., 2003b).

Recently, conducting polymers have drawn considerable attention as a new class of advanced functional materials for many applications based on the unique properties of electro-activity, conductivity and other physical or chemical properties. The applications being considered include batteries (Otero and Cantero, 1999), photovoltaic devices, electro-chromic devices, ion selective membranes, electromagnetic interference shielding, radar absorption, electrical wires, corrosion inhibitors, electrochemical sensors and actuators (Brandrup et al., 1989, Reynolds et al., 1998).

1.3. Conducting polymer actuators

Conducting Polymer (CP) actuators were described initially by Baughman (Baughman et al., 1991, Baughman, 1996). Conducting polymer electrochemical actuators are based on dimensional changes caused by electrochemical doping of conducting polymers such as polypyrrole, polyaniline, polyacetylene, polyalkylthiophene and polyaryvinylenes. Such dimensional changes occur because of the volume needed to accommodate anions, cations or possibly together with intercalating solvent molecules (Baughman, 1996, Otero and Sansinena, 1998). The electrochemical actuators consist of three basic elements: anode, cathode and separating electrolyte similar to both conducting polymer batteries and electro-chromic displays. Either anode or cathode or both can be conducting polymers. These actuators can be categorised as “electrolyte storage” or “electrode storage” actuators. In “electrolyte storage” actuators the dopant salt is stored in the electrolyte during the one extreme of electromechanical cycle (the discharge state for a battery) and in the other extreme of the cycle (the charge state for a battery) the anions

and cations intercalate the anode and cathode. In “electrode storage” actuators, the role of the electrolyte is just to provide ion transport between the anode and cathode (Baughman, 1996). In contrast to electrostatic, piezoelectric and electrostrictive actuators in which the electrically generated strain is proportional to the electric field, the charge transferred between anode and cathode (the integral of current versus time) of the conducting polymer actuators is the essential parameter to determine the electrochemical generated strain (Baughman, 1996).

The history, fabrication methods, electro mechanical characteristics, applications and comparison of all different artificial muscles has been collected and edited by Bar-Cohen (Bar-Cohen, 2001). Bar-Cohen in a comprehensive paper has also reviewed the advances in developing efficient and robust Electro Active Polymer (EAP) materials for practical applications, understanding the behaviour of EAP materials and describing characterization techniques. The processes of synthesizing, fabricating, electrode designing, shaping and handling were also refined to maximize the EAP materials, actuation capability and robustness, as described in this paper (Bar-Cohen, 2002).

1.4. Conducting polymer actuators performance

The essential advantage of conducting polymer actuators compared to piezoelectric or electrostrictive materials is their very low operation voltage that can produce even more than 10% dimensional change and make them suitable for micro applications (Baughman, 1996, Hollerbach et al., 1991, Hunter and Lafontaine, 1992). The mechanical work per volume from one electrochemical cycle is another impressive advantage for properly designed conducting polymer actuators (Baughman, 1996). Since conducting polymers are basically batteries, it is also possible to design an actuator from conducting polymers that operates while it is not connected to an external energy source (Baughman, 1996).

However, there are fundamental limitations that restrict the application of conducting polymer actuators which are a) their electromechanical response dependency on molecular diffusion which can be slow and b) limitation of the electrical response time of the electrode by a high RC time resulting from the double-layer capacitance and the electrolyte resistance effect (Baughman, 1996). The RC time can be reduced by using highly conducting electrolytes, using conducting polymers having negligible resistance, designing short inter-electrode separations and a small effective area of the electromechanical electrode relative to the counter electrode (that can be satisfied by

choosing very thin electromechanical electrodes that have very small effective area) (Baughman, 1996). Since electrochemical doping and de-doping are not completely reversible, the life cycle of conducting polymer actuators is also limited which can be improved by selection of smaller electrochemical stimulation voltage (Baughman, 1996). The low conversion efficiency from electrical to mechanical energy for conducting polymer actuators is also a disadvantage (Baughman, 1996).

The mechanisms behind the basis of electrochemical actuators utilizing inherently conducting polymers (ICPs) were reviewed in (Wallace et al., 2002). The review cited the effects of electrical connection, the auxiliary electrode composition and the supporting electrolyte on the actuator performance. Each was shown to have a dramatic influence and therefore needs to be optimised to maximise actuator efficiency.

Considerable improvement in performance of conducting polymer actuators has occurred over the past decade. Conducting polymers which are electrochemically cycled in ionic liquids (IL) show improved lifetimes without failure (up to 1 million cycles) and fast cycle switching speeds (100 ms) (Lu et al., 2002). The experiments in this publication were carried out under ambient conditions by using environmentally stable, room-temperature ionic liquids (IL) composed of 1-butyl-3-methyl imidazolium (BMI) cations together with anions such as tetrafluoroborate (BF_4) or hexafluorophosphate (PF_6) (Lu et al., 2002). Actuator stability was considerably improved in the BMI ionic liquid compared to the PF_6 electrolyte.

The magnitude of the actuation response has also increased significantly in recent years. The highest linear expansion (12% at a load of 0.5 MPa) that had been reported till 2003 used a centimetre-scale conducting polymer actuator operated in aqueous media and by forming the polymer actuator on a compliant, micro structured gold electrode (Bay et al., 2003). More recently, Hara and co-workers have reported 26% and 40% linear strains during slow electrochemical cycling of polypyrrole and by using novel electrolytes and dopants. A publication by Hara et al. presented a free-standing polypyrrole (PPy) film actuator, prepared electrochemically from an aromatic ester solution of tetra-*n*-butylammonium bis(trifluoromethanesulfonyl) imide (TBA-TFSI), demonstrating 26% electrochemical strain and a peak response rate of 10.8%/s in an H_2O /propylene carbonate (PC) solution of Li-TFSI. The main reason for the achievement of both large and fast electrochemical strain were caused by the fact that the PPy film doped with large

TFSI anions swelled in PC so that TFSI anion can insert and expel to and from the PPy film easily, and that a high ionic conductivity in H₂O/PC solution enabled the TFSI to move quickly (Hara et al., 2005).

In a very recent publication by Kaneto's group a free-standing polypyrrole (PPy) film actuator, prepared electrochemically from a methyl benzoate solution of 1,2-dimethyl-3-propylimidazolium tris(trifluoromethylsulfonyl) methide (DMPIME), exhibited up to 36.7% electrochemical strain in a propylene carbonate (PC) / water solution of lithium bis- (nonafluorobutylsulfonyl) imide, Li(C₄F₉SO₂)₂N (Li-NFSI). It was shown that the maximum electrochemical strain of DMPI Me-doped PPy film depended on the electrolyte used for driving the PPy actuator. for example, when a PC/water mixed solution of lithium bis(trifluoromethylsulfonyl)imide (LiTFSI) was used as the driving electrolyte, the maximum electrochemical strain, measured by cycling between -0.9 and +0.7 V versus Ag/Ag⁺ at 2 mV/s, was 24.2%, smaller than that (30.0%) driven with LiNFSI and when a PC/water suspension of DMPIME was used as the driving electrolyte, the maximum electrochemical strain was 31.9% (Hara et al., 2006).

Improvements in charge transfer efficiency have improved the speed of actuation. In a publication by Ding et al., a polypyrrole helix tube actuator was described based on a thin helical wire embedded in the wall of a hollow PPy tube. This composite system gave strain rates in excess of 10%/s (Ding et al., 2003a). A similar tubular linear actuator of polypyrrole film was fabricated by Kaneto et al. and was shown to give a maximum strain of 7% (Yamato and Kaneto, 2006).

Polypyrrole (PPy) films have also been polymerised onto other metal substrates to improve charge injection. Substrates include platinum (Pt) coated PVDF (polyvinylidene fluoride) membrane and Pt-coated PET (Polyethylene terephthalate) fibre. The metal layers are designed to overcome the inherent electrical resistance of the film/fibre which reduces actuator performance. Both actuators (film and fibre) were laminated with a hydrogel electrolyte and sealed in order to fabricate a solid state actuator (film and fibre). The actuation and mechanical performance of all seven kinds of actuators fabricated: PPy free-standing film, PPy platinised film, PPy platinised laminated film, PPy fibre, PPy platinised fibre, PPy platinised laminated fibre and PPy platinised laminated (with polyester) bundled fibres; were investigated a) with different PPy thickness, b) with different counterions and c) with different cyclic voltammetry scan rates. The results show

that the electrical resistance increases when the film thickness increases and when gel electrolytes are used. It was also observed that the most suitable design to increase the actuation performance of practical actuator devices can be based on a bundled fibre arrangement where the PPy was first coated onto Pt-coated polyester fibres, which produced the highest stress (6.8 MPa) achieved until year 2000 (Hutchison et al., 2000).

A fast contracting encapsulated solid state polypyrrole bi-layer actuator was fabricated by the arrangement of polyethylene (PE)/ Electrode (Au)/ polypyrrole (PPy)/ PMMA (gel electrolyte: 70 wt.% acetonitrile (ACN), 20 wt.% propylene carbonate (PC), 7 wt.% polymethylmethacrylate (PMMA) and 3 wt.% LiClO₄)/ PPy/ Electrode (Au)/ PE. Its mechanical and actuation performance was investigated for different voltage ranges and frequencies. A shaping potential method similar to IR compensation method was proposed to decrease degradation process at longer times while strain rates of 3.2%/s and power to mass ratios of 39 W/kg were achieved in 40 micron thick polypyrrole films (Madden et al., 2000, Madden, 2000).

1.5. Application of conducting polymer actuators

1.5.1. Bending actuators

One of the earliest demonstrations of a conducting polymer actuator was carried out by Elisabeth Smela's group in Sweden with a metal/polymer (polypyrrole) bi-layer actuator. This system was used to produce an electrically controlled micro- "finger" (Smela et al., 1993). The electromechanical performance of the PPy/Au bending actuator was accurately modelled and it was used to lift and precisely position silicon plates. These plates were approximately 40,000 times the actuator weight and the work output to hinge mass ratio was approximately 40mJ/g with a power of 7.5mW/g (Smela et al., 1999). Also a method using Atomic Force Microscopy (AFM) was developed to monitor in-situ volume change and bending angle simultaneously of the bi-layer actuator (Smela and Gadegaard, 1999).

Several interesting bio-medical devices based on the PPy/Au bilayer have been described by Jager et al. Example applications include simple arrays of fingers for positioning or holding small fibres, blood vessels or nerve fibres. The cell clinic is another device consisting of a micro-vial that can be closed by a lid operated by CP actuators. Finally, a micro-robotic arm for manipulation of micrometer sized particles was also fabricated using several independent conducting polymer bending actuators for elbow, wrist and

finger movements. All these applications were limited to operation in a wet environment (Jager et al., 1999b, Jager et al., 1999c, Jager et al., 1999a).

The same configuration using polyaniline film actuator was also fabricated in two forms, backbone-type (polymer/SPE/polymer) (SPE: Solid Polymer Electrolyte) and shell-type (polymer/SPE/insulator/SPE/polymer) by Keichii Kaneto's group. This was proposed to be used in precise chemical valves and bio-medical application (Kaneto et al., 1995). In this research, utilising a solid polymer electrolyte enabled the actuator system to work in air was a breakthrough achievement for conducting polymer actuator application. A similar all-polymer, PPy/SPE/PPy, mechanically stable solid state electromechanical bending triple layer actuator that did not need to be immersed in a liquid electrolyte was demonstrated by Lewis et al. (Lewis et al., 1997b) and its electromechanical performance including force generation, strain rate and strain was maximised by optimising electrochemical parameters like polymer thickness, applied potential limits and dopant ions (Lewis et al., 1997a).

The use of triple layer conducting polymer actuators in an integrated oxygen control system was explored with practical focus on the control of a fruit storage atmosphere at 5% oxygen by Andrews et al. (Andrews et al., 2004). The actuator consisted of a PPy/SPE/PPy tri-layer with additional thin metal layers to improve electrical connection to the PPy layers.

1.5.2. Linear actuators

In continuation of Lewis' research on all-polymer solid state electrochemical actuators, a CP actuator consisting of a laminated structure with two PPy layers separated by a water-base hydro-gel ion source/sink, capable of developing axial forces along its own length was demonstrated by Lewis et al. (Lewis et al., 1999). The actuator was mechanically stable, can operate in air and both PPy layers can contribute to actuation since the two layers used different dopant ions so that both layers expanded or contracted at the same time. In previous tri-layer bending actuators, one layer expands while the other contracts so that a bending motion results (Lewis et al., 1999). In separate research, a similar arrangement was demonstrated using a metal electrode instead of PPy for the outer electrode by Madden et al. (Madden et al., 1999, Madden, 2000).

In a publication by De Rossi et al. an unconventional design factor was considered for electromechanical devices, i.e., "wearability". Sensors and actuators endowed with this

property have been implemented and tested. A sensing glove which also contains conducting polymer (PPy and PANi) actuating fibres has been realized and its potential use in virtual reality and rehabilitation engineering outlined. Other devices endowed with similar features have been constructed in their laboratory in Italy: a sensing sock, a sensing full fabric car seat cover and a sensing dancer body (De Rossi et al., 1999).

In another application, conducting polymer (PPy) encapsulated actuators doped by hexafluorophosphate (PF_6) were used to create actively shaped hydrodynamic foils to allow control over camber, much like the ailerons of an airplane wing. Camber enables control the system to have variable thrust in propellers and screws, increased manoeuvrability, and improved stealth. The design and fabrication of the active foils were presented, the forces were measured and operation was demonstrated both in still air and water (Madden et al., 2003). A scaled prototype was constructed using polypyrrole actuators within the blade itself to vary camber. The limited blade volume enabled an application that is not feasible by using direct drive electric motors (Madden et al., 2004a). Madden et al. also presented the examples of potential undersea applications of electro-active actuators including dielectric elastomers, ferroelectric polymers, liquid crystal elastomers, thermal and ferroelectric shape memory alloys, ionic polymer/metal composites, conducting polymers and carbon nanotubes; and examined them in order to assist those involved in device design and in actuator research to evaluate the current status and the developing potential of these artificial muscle technologies. Relative merits and challenges associated with the artificial muscle technologies were described in two case studies and a summary table which was also added to EAP web-hub, provides a quick guide to all technologies that were discussed (Madden et al., 2004b).

Recently, a conducting polymer actuator and conducting polymer strain gauge were used for the first time to build a reflex or position feedback loop that rejects position disturbances (Madden, 2003). The successful operation of the conducting polymer based reflex loop has been an important step towards building an all polymer reflex loop that is directly integrated into a bulk material. Such a reflex loop is able to be used to control position and force or to dynamically change the material characteristics such as stiffness and viscosity (Madden, 2003). The research on using conducting polymers as a simultaneously sensor and actuator has also been pursued by Otero et al. A microscopic electro-chemo-mechanical device with tactile sensitivity and capable of pushing an

obstacle while sensing the required effort (simultaneously sensor and actuator) was produced and fabricated (Otero and Cortés, 2003).

Since there is a great need to develop a computer screen based on Braille technology that allows blind people to access computer-based information to the same extent as sighted people, and also the lack of a “graphical user interface” for the blind severely restricts employment, educational and recreational opportunities, the development progress made to fabricate a prototype multi-dot Braille cell using conducting polymer actuators was reviewed by Spinks et al. (Spinks et al., 2003a). This research developed the helix tube PPy linear actuator that is subject of the current thesis. In another application, the design of polypyrrole helix tube fibre actuators for use in a glove to open and close the human hand (for assisting those with paralysis or hand injuries) was described in which the key requirements were the simultaneous generation of 16 mm of contractile movement and 2.9 N of force. A fabric strain gauge with polymer actuators was chosen as a convenient way for providing feedback control to the actuating element (Spinks et al., 2003b, Spinks et al., 2003c).

The conducting polymers capabilities for future applications have been reviewed in bio-mimetic applications including conducting polymer muscles, strain gauges, transistors, and super-capacitors by Madden et al. (Madden et al., 2001b) and in bio-medical applications including steerable catheter, cell clinic, micro-valve for controlling urine flow and Braille display screen by Smela et al. (Smela, 2003).

1.6. Mechanism of actuation in conducting polymers

Conductive polymers, such as polypyrrole, undergo complicated mechanical responses when subjected to applied electrical potentials. The molecular mechanisms of such responses in PPy with specific reference to the role of the counterion and electrolyte cation have been investigated by Wallace et al (Gandhi et al., 1995). The results of a) stress relaxation at constant applied zero potential on PPy/PVS film immersed in NaPVS, in NaNO_3 and $\text{Mg}(\text{NO}_3)_2$ electrolyte and b) electromechanical behaviour with cyclic potential waveforms from -0.8 V to +0.4 V vs. Ag/AgCl on PPy/pTS and PPy/PVS both in NaPVS, in NaNO_3 and $\text{Mg}(\text{NO}_3)_2$ electrolyte, have been presented. It has been found that a four-stage oxidation/reduction process occurs in the general case: (1) oxidation by cation ejection; (2) oxidation by anion incorporation; (3) reduction by anion ejection; and (4) reduction by cation incorporation (Gandhi et al., 1995). When immobile counterions

and/or electrolyte anions were used, steps 2 and 3 were suppressed and also, when divalent cations were used steps 1 and 4 produced minor volume changes only (Gandhi et al., 1995).

The volume change of a conducting polymer during redox switching can be divided into a part stemming from osmotic expansion and an intrinsic part from the changes in bond length and conformation in the polymer backbone. A model for osmotic expansion that is due to changes in the number of free particles (ions and solvent) in the polymer, has been used to explain the observed (by EQCM) change of expansion of PPy(DBS) with electrolyte concentration (Bay et al., 2001b, Bay et al., 2001a). The contribution to actuation by osmosis was found to be larger when the electrolyte concentration was lower.

1.7. Conducting polymer actuators modelling

The simplest approach to model the electromechanical performance of the conducting polymer actuator is to consider a simple elastic mechanical model super-imposed with the electrochemically generated movement that is assumed to be directly proportional to the charge density, as shown in Equation 1.7.1. The research attempting to model conducting polymer actuators have involved modification and improvement of this model. A set of experiments was performed by Madden et al. to describe the actuation of PPy film. In addition, stress-strain tests were performed at constant applied potential to determine polypyrrole stiffness and the admittance transfer function of polypyrrole and the associated electrolyte was also measured over the potential range in which polypyrrole is highly conductive. The admittance model was used to predict the electrochemical charge from the input voltage or current. The admittance was described by treating the polymer as a volumetric capacitance whose charging rate is limited by electrolyte resistance and diffusion within polypyrrole. The relationship between strain and charge was also investigated by carrying out a constant current experiment and showing that strain is directly proportional to charge via the strain to charge density ratio (α) at loads of up to 4 MPa. Beyond 4 MPa the strain to charge ratio was time dependent. The admittance models, stress/strain relation and strain to charge relationship were combined to form a model of polypyrrole electromechanical response (Madden, 2000, Madden et al., 2001a).

$$\varepsilon(t) = \frac{\sigma(t)}{E} + \alpha \cdot \rho$$

Equation 1.7.1

In the equation above, ϵ , σ , E , α and ρ are strain, stress, Young's modulus, strain to charge ratio and charge density parameters, respectively. This model works successfully to describe the behaviour of conducting polymer film actuator under low applied load and narrow range of stimulus voltage or pulse current experiments (Madden, 2000, Madden et al., 2001a).

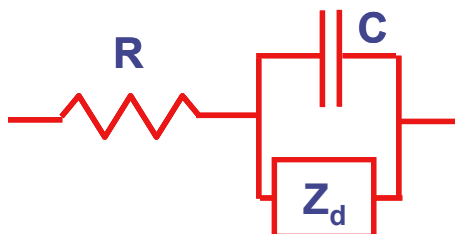
In another paper by Madden et al., the relationship between strain and charge as a function of time and load in polypyrrole film was explored (Madden et al., 2002). A reasonable first approximation was that strain is directly proportional to the density of charge transferred to these actuators. That is, the strain to charge ratio was assumed constant. The relationship between strain and charge, however, exhibited some load and time dependences, which became important when the actuator was operated under stresses between 2 MPa and 34 MPa. It was also shown that the strain to charge ratio exhibits time dependence, dropping by 30 to 45% from its starting value under pulse current stimulus condition. The drop in strain to charge ratio was consistent with frequency response results, which show an electrochemical creep or relaxation in the strain to charge ratio (Madden et al., 2002).

Madden et al. in a subsequent paper investigated the importance of fundamental actuation mechanisms and the fundamental material properties of conducting polymer muscles such as ionic diffusion rate, electrochemical operating window, strain to charge ratio, ratio of charge carried by positive versus negative ions and salt draining; their effect on performance was discussed and reviewed but these effects were not incorporated into a model (Madden et al., 2004c).

1.7.1. Electrochemical Modelling

The electrical impedance behaviour of the conducting polymer actuators working in the electrolyte against a counter electrode is modelled as a resistive-capacitive-diffusive equivalent system as shown below (Madden, 2000). In this system, R is the resistive element (incorporating the electrolyte and polymer resistance) and C is the double-layer capacitance. Also, Z_d which is called Warburg's element, consists of a function of the diffusion coefficient D (Madden, 2000). In this model, the resistive current occurs when an initial voltage is applied, and then increasing voltage causes the ions to concentrate around the polymer and form the double-layer capacitor. By continuing the actuation process or increasing the applied a voltage, some ions start to behave as a dopant and

diffuse to the polymer backbone which produces the actuation displacement (Madden, 2000). This simple and fundamental method which was used by researchers to model the electrochemical behaviour of the polymer or to predict the current signal from the input applied voltage signal will be reviewed in this section.



An AC impedance method was applied to the reduced (nonconductive) form of the polypyrrole conducting polymer thin film to determine apparent diffusion coefficients associated with the oxidation of polypyrrole in three different DC applied voltage (-0.333, -0.350 and -0.361 V vs. SCE) by Penner et al. (Penner and Martin, 1988). A mathematical formulation was created to interpret the impedance data by using apparent diffusion coefficients using finite and semi finite transmission line methods. The apparent diffusion coefficients obtained were similar in magnitude to coefficients obtained by a related current-pulse method (Penner et al., 1988, Penner et al., 1989) and the theoretical models based on a transmission line equivalent circuit. Diffusion coefficients obtained from finite diffusion data were approximately a factor of 3.4 times larger than coefficients obtained from semi infinite diffusion data (Penner and Martin, 1988). Although the range of applied voltage used to oxidise the polymer was low, the results showed a dramatic change in electrochemical impedance and apparent diffusion coefficient when the DC applied voltage was changed (Penner and Martin, 1988, Penner et al., 1988, Penner et al., 1989).

In research done by Tanguy et al., the results obtained by the impedance spectroscopy method on three different conducting polymers: polypyrrole, polyaniline and poly (3methylthiophene) were reported. Their electrochemical behaviour could be explained by two doping mechanisms: a) ionic doping associated with a double layer formation described with an ionic relaxation model and b) a diffusive Faraday doping mechanism (Tanguy et al., 1989). Further development using the Nernst equation to calculate the capacitive and Faradic currents was used to predict the CV diagram (Tanguy, 1991). The result was a complicated electrochemical model containing parameters that have to be calculated from cyclic voltametry data and the relation between capacitive and diffusive charges is needed (Tanguy, 1991). The model also does not consider the dramatic changes

in electrochemical parameters during oxidation and reduction processes shown by Penner (Penner and Martin, 1988, Penner et al., 1988, Penner et al., 1989).

A series of articles published by West et al. studied a) the nature of the interaction between dopant ions and a polypyrrole host matrix (West et al., 1992); b) the influence of the current density during electro-polymerization on the properties of polypyrrole in LiClO_4 and propylene carbonate with current density varied between 0.0064 mA/cm^2 and 3.84 mA/cm^2 (West et al., 1993b, Dyreklev et al., 1996); and c) the kinetics of insertion of perchlorate ions into polypyrrole (PPy) in LiClO_4 /propylene carbonate (PC) by electrochemical impedance spectroscopy. A proposed simple transmission line model for the coupled diffusive transport of ions and electrons/holes in these films showed that the values of the diffusion coefficients were slightly dependent on potential and film thickness, but not on the current density used during synthesis (West et al., 1993a, Skaarup et al., 2000, Vidanapathirana et al., 2002, Skaarup et al., 2003, Careem et al., 2004, Careem et al., 2006).

In a publication by Pickup et al., ionic conductivities determined from impedance measurements on polypyrrole and a polypyrrole + polystyrene sulphonate composite films were used to distinguish between several morphological models of these materials. Both materials showed ionic conductivities that depend strongly on potential and electrolyte concentration and was strongly affected by changing the counterion. Addition of a co-ion, however, had little influence (Ren and Pickup, 1995).

Impedance spectra of pyrrole-based and thiophen-based polymers of different thickness and at different values of injected charge have been obtained by Ferloni et al. The films were potentiostatically charged for 600 s before the measurement and AC amplitude of 5 mV was used in cells with either liquid electrolytes or solid polymer electrolytes. The electrochemical parameters including resistance, double-layer capacitance and diffusive element (Warburg's element) were evaluated and the deviation from the ideal behaviour discussed (Ferloni et al., 1996).

A bilayer conducting polymer artificial muscle actuator using PPy doped by LiClO_4 in acetonitrile was developed by Otero et al. and its electrochemical performance was modelled under the conformation relaxation method by fitting to a simple function of the current signal (Otero and Sansinena, 1995). The mentioned model was further developed as a more inclusive function of applied voltage in a narrow voltage range of -0.2 V and

+0.3 V vs. SCE (Otero et al., 1995, Otero et al., 1996c) and experimentally validated (Otero et al., 1996a, Otero et al., 1996b, Grande and Otero, 1999, Grande et al., 1998). The degradation process of PPy conducting polymer that is caused by high applied oxidation voltage was also studied by Otero et al. and it was simulated by the electrochemically conformational relaxation model introduced above (Otero and Boyano, 2006).

A new technique for direct measurement and visualization of ion transport in electrochromic materials has been presented by Wang et al. The ion transport was analysed using diffusion, drift and Nernst-Planck equations and incorporated with Maxwell's equation to give a physics-based model of electrochemical reactions. Initial experimental and modelling results were obtained by applying the method to dodecylbenzene-sulfonate-doped Polypyrrole (PPy-(DBS)) (Wang et al., 2004). It was shown that there are different rate-limiting processes at different potentials. Migration plays a critical role in ion transport, and a simple model can account for much of the behaviour. Experimental work included quantification of the coefficients in the equations as well as studies of the oxidation process and correlations between ion transport and volume change (Wang et al., 2004).

In research by Otero et al., the ion transport across a free-standing polypyrrole (PPy) film was investigated by measuring the ionic conductivity of the film working as a membrane in a special cell. The cell design included two electrochemical cells using a 4-electrode configuration (2 reference electrodes were used) separated by the PPy membrane. The diffusion coefficient of ions across the film was estimated by this method and was compared with those diffusion coefficients calculated by the chronoamperometric method for a particular electrolyte concentration and temperature (Otero et al., 1996c, Otero and Grande, 1996, Otero et al., 1996a, Otero et al., 1996b, Grande et al., 1998). It was also shown that the membrane ionic conductivity depends on the oxidation degree of the film, which points to the control of membrane selectivity by the oxidation depth. This research presents the possible applications of conducting polymer films as smart ion exchange membranes. It was also shown that for a certain electrolyte concentration, the diffusion coefficient across the film is one order of magnitude lower than those obtained by oxidative processes of the free-standing polypyrrole film and the diffusion coefficient of such oxidative processes is also one order of magnitude higher than that reported in

other research on thinner PPy films supported on a metallic electrode (Ariza and Otero, 2005).

The aim of the electrochemical model for conducting polymers is to predict one electrical signal (voltage/current) from the other signal (current/voltage) during the oxidation/reduction processes and caused by the electrochemical charge transferred. Madden et al. presented a model to explain the charge transfer process happening during stimulation of a PPy film. The model included moving phase fronts on charging from the reduced, insulating state; residual charge in the polymer after complete reduction; and, the sharp anodic peak and flattened cathodic peak observed in cyclic voltammetry. The electrochemistry of this process was modelled as an RC transmission line, typical of a distributed capacitor network, with the addition that the oxidation state dependence of the polymer's electronic conductivity was explicitly included. The transient charges and currents during potentiostatic steps and linear sweeps were simulated and solved using the finite differences method (FDM) in the time domain, and compared with experiment (Warren and Madden, 2006a). The model was able to reproduce the shape of conducting polymer cyclic voltammetry without relying on the Nernst equation. It has been mentioned that the transmission line model can be modified to simulate other experimental geometries (Warren and Madden, 2006a).

In parallel research by Madden et al., the electronic, structural and chemical properties of polypyrrole doped with the hexafluorophosphate (PF_6) ion were investigated as a function of oxidation state. It was shown that the properties are highly correlated since the electronic conductivity of the film changed by two orders of magnitude through the transition potential. X-ray diffraction and macroscopic actuation measurements revealed a structural change in the polymer that suggested a loss of pi-stacking in the polymer crystals, and a re-ordering of the dopant ions in the matrix. Finally, the equilibrium charge on the polymer with oxidation state was consistent with a constant DC capacitance and the AC impedance spectrum showed increased constant phase element behaviour in the reduced state (Warren and Madden, 2006b).

1.7.2. Electromechanical Modelling

The first investigation on coupled electro-chemo-mechanical phenomena in polypyrrole (PPy) free-standing films was done by De Rossi et al. (Chiarelli et al., 1995). An experimental set-up containing an isotonic transducer and servo controller was used to

monitor length and maintain the isotonic condition (constant force). Quantitative measurements of isotonic length and relaxed elastic modulus changes were performed on PPy samples during a) immersion in the electrolyte until stabilization occurred under free-swelling condition; b) cyclic voltammetry at three different scan rates 10, 1 and 0.1 mV/s, and in -1 to +1 V vs. SCE; and c) square-wave current experiment with four current pulses and each for 1000 seconds. The published results show a) increasing length and decreasing elastic modulus during immersion in electrolyte; b) cyclic change in the relaxed elastic modulus during the first cycle of cyclic voltammetry that shows similarity between current (or charge) signal and modulus; and c) a good quasi-linear proportionality between the charge transferred and resultant displacement. The link between dimensional and mechanical changes in the samples and doping salt (sodiumbenzenesulfonate, $\text{Na}^+ \text{BS}^-$, in acetonitrile) exchange kinetics were investigated and possible interpretations were proposed (Chiarelli et al., 1995).

A continuum mechanics model based on the theory of elasticity of porous materials (Biot, 1941, Biot, 1955, Biot, 1956) was proposed to describe the passive mechanical behaviour of a generic porous conducting polymer saturated by a fluid (Della Santa et al., 1996, Della Santa et al., 1997c, Mazzoldi et al., 2000). This model was solved for a stress-relaxation test and applied in the specific case of a BS^- doped polypyrrole porous matrix saturated by an electrolytic solution $\text{Na}^+ \text{BS}^-$ in acetonitrile. The goodness of fit between experimental data and theoretical data confirmed the validity of the model (Della Santa et al., 1996, Della Santa et al., 1997c, Mazzoldi et al., 2000). The model was built up using the fundamental equilibrium equation of continuum solid body under porous pressure with Darcy's law for mass transfer caused by ion diffusion. Therefore, the model was able to predict the viscoelastic behaviour of the polymer under load including creep and stress-relaxation. The relationship between the charge transferred and electrochemical generated strain was not discussed in this model and the diffusion rate of ions was considered as the actuation parameters. The mechanical parameters including Young's modulus were considered constant during the process of ion diffusion (Della Santa et al., 1996, Della Santa et al., 1997c, Mazzoldi et al., 2000).

A performance analysis of a conducting polymer polypyrrole (PPy) film doped by benzenesulfonate (BS^-) linear actuator was reported by De Rossi et al. (Della Santa et al., 1997a, Della Santa et al., 1997b). Electro-chemo-mechanical characterizations of the active displacement at different loading conditions using a) a cyclic voltammetry at 1

mV/s between ± 1 V and b) a current square wave between 0.02 and 0.1 Hz were performed. The actuating properties of the material were investigated and quantified in terms of both isotonic displacement and isometric developed force. A lumped parameter model describing the parallel arrangement of two Maxwell elements and an electrochemical strain generator was developed. The electrochemically induced strain was taken as proportional to the exchanged charge and was inserted in series with the viscoelastic body component. The viscoelastic parameters were determined by curve fitting to the experimental stress-relaxation test but the dynamic performance of the model was not tested by comparing the simulation program output and experimental data (Della Santa et al., 1997a, Della Santa et al., 1997b, Mazzoldi et al., 1998, De Rossi et al., 1999, Mazzoldi et al., 2000).

The first research on the effect of different applied voltage on the mechanical characteristics, like breaking stress, Young's modulus and extension percentage at break, of tosylate-doped polypyrrole film in different electrolytes (NaNO_3 , $\text{Mg}(\text{NO}_3)_2$, KCl, NaCl, LiCl, MgCl_2 and H_2O) was done by Murray et al. using stress-strain test with 1 mm/min rate and electrical stimulation simultaneously (Murray et al., 1998). A transition from a ductile to brittle behaviour was observed resulting from reduction and oxidation of the polymer. The electrochemical potential at which the transition occurred was found to depend upon the electrolyte used, with NaNO_3 and NaCl undergoing reduction at higher potentials than occurred with $\text{Mg}(\text{NO}_3)_2$ and MgCl_2 . The ductile--brittle transition observed was found to be due to the formation of ionic cross-linking during oxidation, and their removal during reduction (Murray et al., 1998).

The performance of PPy conducting polymer actuator (the electrochemical strain generated) when subjected to external loads was investigated and it was shown that increasing external loads applied to polypyrrole causes a linear decrease in the electrochemical generated strain response. Analysis of the effects of the applied load on the actuator strain showed that the rate of strain decrease with increasing load depended upon the difference in the Young's modulus of the polymer in the doped and un-doped states. Also, a simple analytical model showed good agreement with the experimental data (Spinks et al., 2002). It was also presented in another publication that operation of polypyrrole actuators in ionic liquids produces much smaller changes in elastic modulus than is observed in propylene carbonate electrolytes. The measurement was carried out using different stimulation methods such as cyclic voltammetry and constant current. The

smaller modulus shift results in a more stable isotonic strain with increasing applied stress and a greater work-per-cycle in ionic liquids (Spinks et al., 2004).

In addition to investigations of shown the strain response with increasing applied force in isotonic condition, the force generated by a polypyrrole (PPy) actuator operating under isometric conditions was demonstrated to decrease as the preload force applied to the actuator increases. It was also shown that the model based on modulus shifting described above can describe the force output (Spinks et al., 2005).

Additionally, the energy output (work) generated by polypyrrole film and helix tube actuators fabricated with the configuration described by Ding et al. (Ding et al., 2003a) was determined from the actuator strain operating against a constant force. The work per cycle depended upon the applied electrical stimulation and on the actuator geometry. Flat films were found to be inferior to hollow tubes, which, in turn, were inferior to similar tubes containing a helical platinum wire in the tube wall. A maximum work capacity of $83\text{kJ}/\text{m}^3$ was determined for the helix tubes, which was the highest reported work capacity of polypyrrole actuators (Spinks et al., 2003d).

In continuation of the above research, work-per-cycle calculations were demonstrated for two modes of actuation behaviour: a) working against a dead weight (isotonic actuation) and b) working against a restoring spring. Importantly, the influence of the electrical stimulus on the elastic modulus of the actuator material, was included in the analysis and its significant influence on the work-per-cycle amount shown (Spinks and Truong, 2005).

In recent published research, bi-layer actuators of gold and polypyrrole doped with dodecylbenzenesulfonate, PPy (DBS), were micro-fabricated and connected to rigid plates. The curvature of the bi-layers was examined as a function of PPy and gold layer thicknesses to enable a determination of the actuation strain and Young's modulus of the PPy (DBS). A model was developed, which included strain and modulus variations along the direction of film thickness and were fitted to the experimental data. The model can enable the bi-layer micro-actuators to be designed to achieve a specified radius of curvature (Christophersen et al., 2006).

In a very recent publication by Otero et al., the Young's modulus of free-standing polypyrrole films, doped with ClO_4^- , was determined in both dry and wet states, under different applied external load and also in different applied stimulus voltage. The

mechanical results obtained in this publication show that the Young's modulus of polypyrrole films, doped with ClO_4^- , is almost constant in the dry state under different external loads, but in the wet state, the Young's modulus depends on the force applied to the film, increasing almost linearly with increasing external applied load. The modulus was lower than the value obtained in its dry state. The Young's modulus increased with the oxidation state of the polymer till achieving a plateau at the fully oxidized state of the polymer. Additionally, a linear relationship was observed between electrochemical charge transferred and electrochemical generated film strain (Otero et al., 2006).

In separate published research by Madden, the change in the mechanical characteristics under different external loads was reported. The cycle life and creep response in polypyrrole film actuators operated in propylene carbonate under stresses of up to 60 MPa were presented, showing a non-linear and history dependent response at high loads. Polypyrrole films passively cycled at peak-to-peak amplitude of 8 MPa under an average load of 10 MPa for one million cycles showed no apparent fatigue, suggesting that loading is not limiting cycle life. Films cycled by applying square wave potentials showed a drop in active strain. The reduction in strain amplitude correlated with a decrease in charge transferred, suggesting degradation of the polymer is the cause of the loss in strain amplitude (Madden et al., 2006).

1.8. Aims and scope of the thesis

The aim of the research presented in this thesis is to create a comprehensive predictive model in order to track the output of a typical high-performance conducting polymer actuator: the Polypyrrole Helix Tube Fibre Composite Actuator which provides high linear actuation strain (up to 5% axial reversible strain), usable strains ($>1\%$) to at least 8 MPa and strain rate up to $13\% \text{ s}^{-1}$ (Ding et al., 2003a). This model is needed to predict the mechanical output (displacement or force) from the electrical input (current and voltage) involving a chemical process between the conducting polymer, dopant and electrolyte to enable control engineers to use these actuators in mechanical systems, new models which describe the dynamic response (actuator output/actuator input) as a function of time and frequency are required. The research in this thesis shows how such models can be derived by exploiting standard control theory analysis tools using Laplace transforms and State-Space techniques. Such a model will enable the application of conducting polymer actuators in automation and robotic applications in which a predictive model is needed to design the control system, and also to identify the system performance and to optimise

the actuator characteristics. Finally, the results present a full description of the electromechanical characterisation considering the cross-effects of electrochemical and electromechanical parameters. It is hoped that this description will enable the design of actuators with higher performance.

As reviewed in Section 1.7, considerable research has already been conducted into the modelling of CP actuator performance. The common feature in these prior models is the direct coupling of the mechanical output (i.e. strain) to the electrochemical charge transferred to the polymer. Several different approaches have been devised to couple the charge transferred to the input voltage. This thesis will build on these prior models and attempt to include the variable viscoelastic behaviour of PPy under electrochemical stimulation. It is known that PPy is a viscoelastic material (Mazzoldi et al., 2000) and it is also known that mechanical parameters such as Young's modulus change with doping level (Spinks et al., 2002). These complex behaviours have not previously been modelled. Another unique aspect of the thesis is the application of prior models to the helix tube actuator design. Previous research has concentrated on PPy free standing films and this thesis will investigate the validity of the prior models to the helix tube design.

In Chapter 2, the general experimental set up and instrument configuration will be described in brief. Since, the experimental set up of the research carried out in each chapter is different, the specific experiment methodology will be provided at the beginning of each chapter.

In Chapter 3, the electrochemical response of the PPy helix tube actuator will be investigated under different external loads, cyclic voltammetry scan rates and different stimulation voltage ranges. The results obtained are modelled using a 'primary model' to predict the strain response of the actuator under different stimulation condition and under the different loads. The primary model assumes constant mechanical properties in the polymer and explores the applicability of the linear charge-strain relationship in helix tube actuators. A set of experiments will be carried out to validate the performance of the model by applying the same input as the experiment input and then comparing the response of the model with the experiment response.

The model will be modified by investigating the effect of external load in Chapter 4. In particular, the viscoelastic behaviour of the actuator material will be studied to improve the model to predict the time dependency of the actuator response to the external loads.

The viscoelastic parameters are assumed to be constant for all oxidation states in this “passive improvement” model. The performance of the “passive improvement” model will be examined with the same method of the previous chapter.

In Chapter 5, a method which has been developed in this research to measure the viscoelastic parameters of the actuator during the electrochemical stimulation will be introduced and the accuracy of this measurement method will be validated. The measurement method will be applied to monitor the viscoelastic parameters during cyclic voltammetry actuation with different conditions and under different external loads. The results will be used to improve the model performance. As in previous chapters, the new “active and passive improvement” model performance will be examined under the same conditions.

In Chapter 6, the modulus shift of a PPy thin film will be investigated during oxidation/reduction process using Quartz Crystal Microbalance (QCM) method. The ordinary output signal of the QCM will be correlated with the shear modulus and thickness of the film using a numerical program developed in this research. This detailed study of the modulus shift highlights the importance of this parameter in actuator modelling.

Finally, Chapter 7 concludes the results presented in this research and suggests possible future work

CHAPTER 2: GENERAL EXPERIMENTAL TECHNIQUES

2.1. Introduction

The experimental techniques used in this thesis are briefly described in this chapter, including the techniques for polymer actuator preparation, characterisation and actuation tests. The general procedures are described below; details of specific procedures will be given in the experimental part of each corresponding chapter.

2.2. Polypyrrole helix tube actuator preparation

There were two types of electrochemical cells employed, one for electrochemical polymerisation and one for actuation testing. Although used for different purposes, the cells have similar constructions that usually consist of a working electrode, an auxiliary electrode and a reference electrode. For electrochemical polymerisation, a two-electrode cell was used, as shown in Figure 2.2.1.

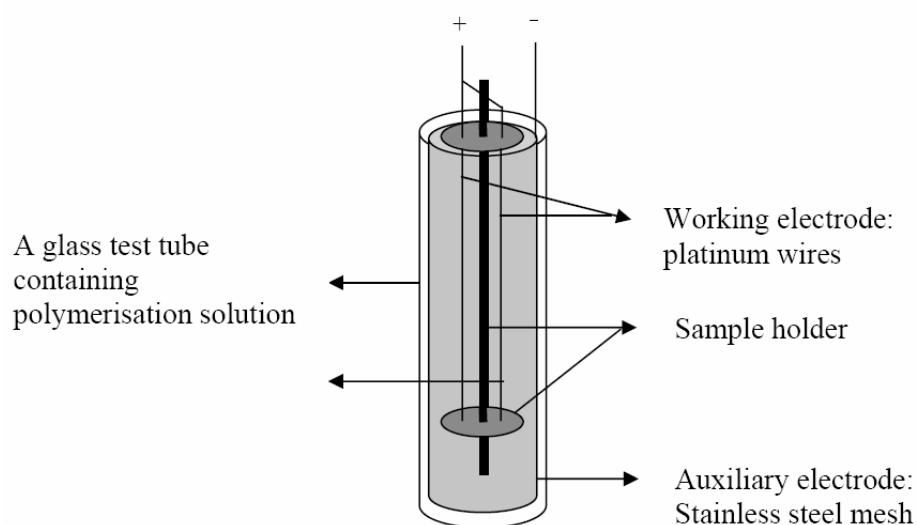


Figure 2.2.1 The electrochemical polymerisation cell used for actuator preparation.

The working electrode material was of critical consideration because it has a marked effect on the polymer microstructure, which in turn influences the mechanical properties of the polymer (Ding et al., 2003a). For example, strong, dense and flexible coatings can be

obtained on platinum electrodes, whereas brittle, rough and stiff films are usually deposited on aluminium electrodes. The working electrode requires a geometry that is suitable for producing polymer in the desirable size and shape. In this thesis, the working electrode was a 250 μm platinum wire with a 50 μm platinum wire wound around it as a helix. The polymer was deposited on the platinum wire working electrode.

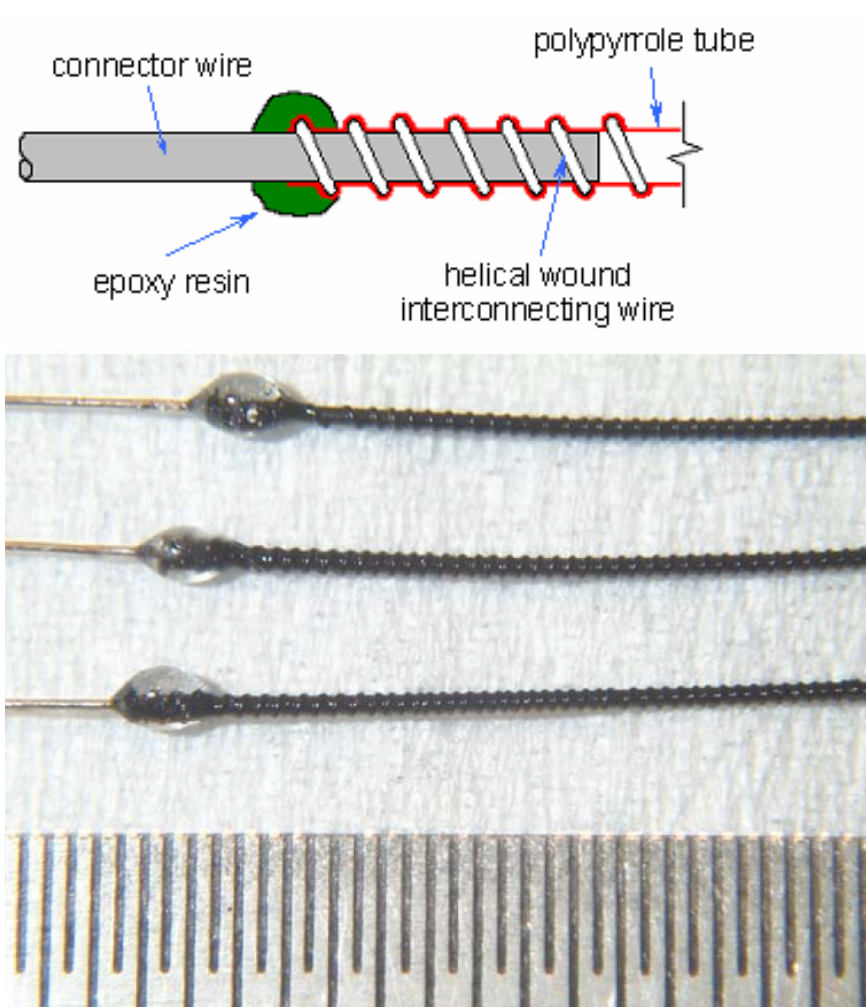


Figure 2.2.2 PPy helix tube.

The auxiliary electrode material should be inserted and capable of maintaining rapid cathodic reactions to keep the desired polymerisation rate at the working electrode surface. It should have a large surface area to allow the passage of current, ideally 10-100 times larger than the working electrode. The most common auxiliary electrodes are

stainless steel, platinum or carbon. In this thesis, the auxiliary electrode in the polymerisation cell was a piece of stainless steel mesh.

According to the control used for electrical signals, electrochemical polymerisation approaches can be divided into different types, namely galvanostatic, potentiostatic and potentiodynamic polymerisation. Galvanostatic polymerisation is a widely used technique and was employed to prepare polypyrrole in this thesis.

The polymerisation temperature is another factor that affects polymer properties. The conductivity of polymers decreases with increasing temperature; however at temperatures that are too low, no coherent polymer films can be obtained (Ding et al., 2003a). In this thesis, polypyrrole actuators were electro-polymerised at -28°C to -25°C .

The platinum wire used as the working electrode was pulled out after the polymerisation process and two platinum wires with the same size inserted in both sides of the helix tube in order to connect the actuator to the electrical power during the actuation. Epoxy resin was used as the clamping material, as shown in the Figure 2.2.2.

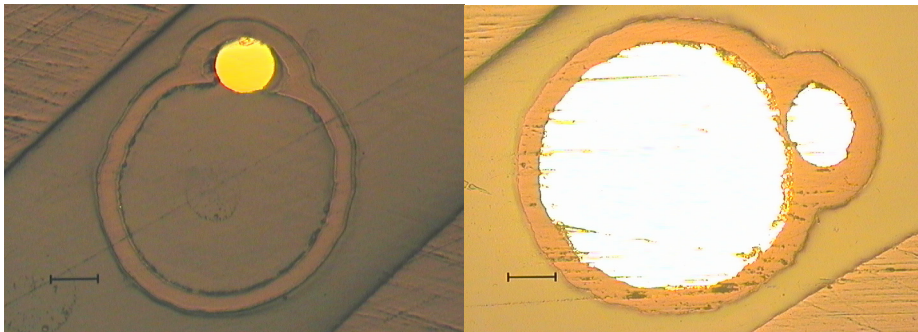


Figure 2.2.3 cross sectional area. Scale 50 micrometer.

Polymerisation was carried out for 16 hours with a 0.15 mA/cm^2 current density. An optical microscope was used to show that the average thickness was $24.1 \text{ }\mu\text{m}$ and the average cross sectional area $26.53 \times 10^{-9} \text{ m}^2$. The cross sectional area of the generated actuator is shown in Figure 2.2.3.

2.3. Electrochemical bath and reference electrode

For actuation testing, the electrochemical cell was a three-electrode system using a reference electrode. The working electrode was the polymer actuator and the auxiliary electrode was a piece of stainless steel mesh as shown in Figure 2.3.1.

A Dual Mode Lever Arm System (Aurora Scientific Inc) was used for the actuation tests. The sample extension/contraction was measured by the arm on which the sample was attached. The device is able to work in both mechanical modes: isotonic (control force, measure displacement) and isometric (control displacement, measure force). Two system models, 300B and 305B were used with a maximum force output of 500 mN and 5000 mN, respectively.

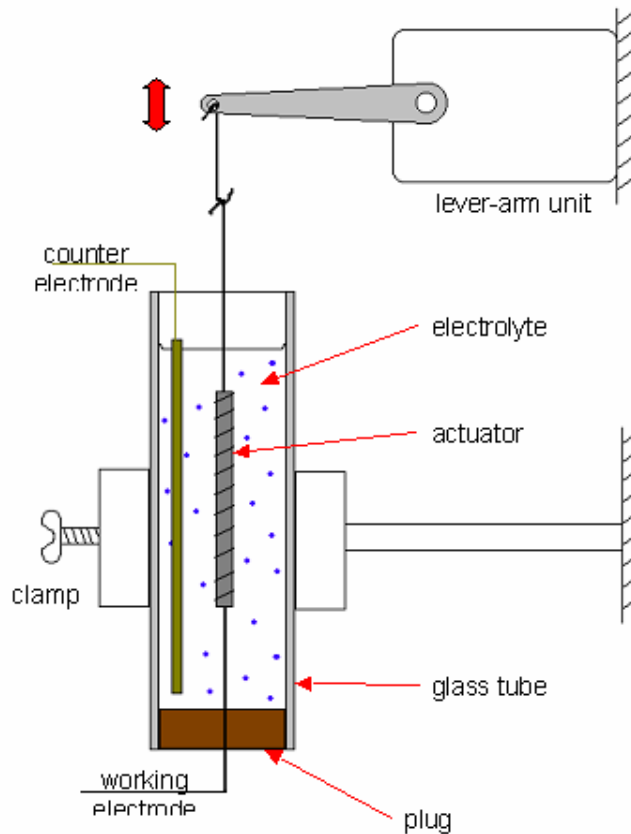


Figure 2.3.1 Electrochemical bath.

The reference electrode was Ag wire in 0.01M AgNO₃ and 0.1M TBA.PF₆ in Acetonitrile (ACN) using 0.1M TBA.PF₆ in PC as a salt bridge. Figure 2.3.2 displays their arrangement.

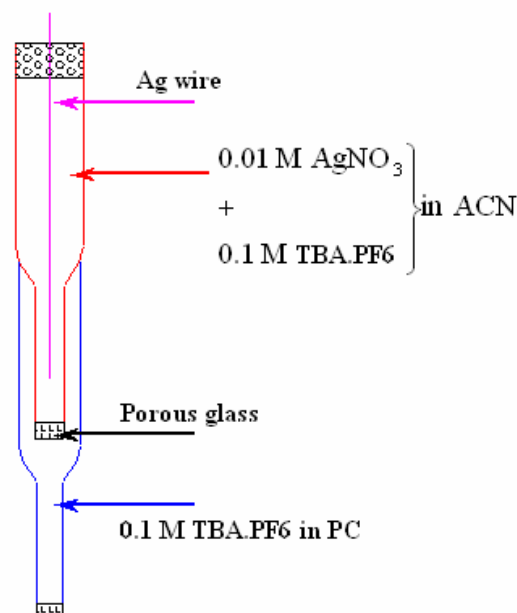


Figure 2.3.2 Reference electrode.

2.4. General experimental set up

All the experimental data was processed and recorded by MacLab/4e AD instruments and computer. Isometric and isotonic conditions were applied using a force/length controller (Aurora Scientific, Dual Mode Model300B). This unit has four analogue input channels that were used to record the voltage and current generated by the potentiostat, and the force and position of the actuator, which was measured by the lever-arm system. The input signals are then digitised and can be sampled at very high rates (up to 200,000Hz). The unit can also filter the signals if necessary before passing them on to the computer. The resulting data is recorded on a personal computer using a software package known as Chart. Chart provides various options for processing and presenting the data; for example it allows the user to change the scaling or the sampling rate of the signal. The experimental set up is shown in Figure 2.4.1.

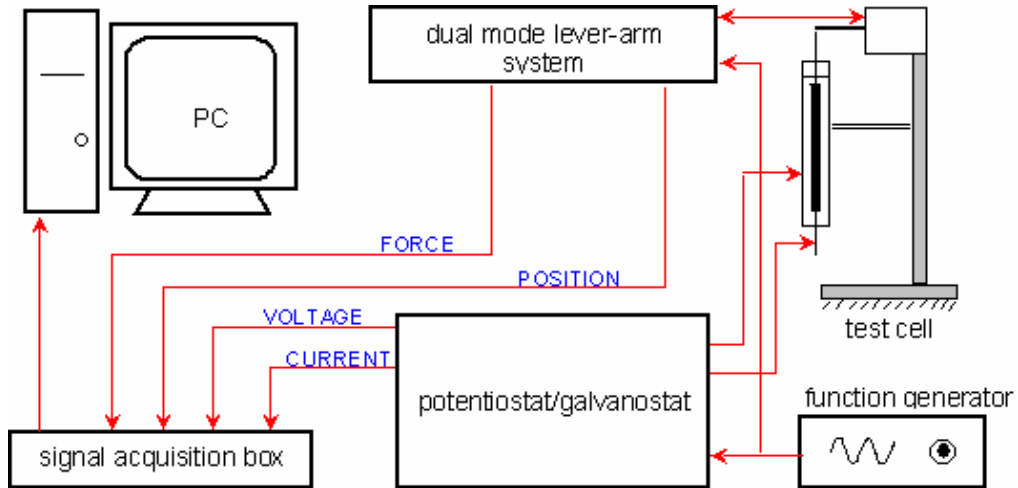
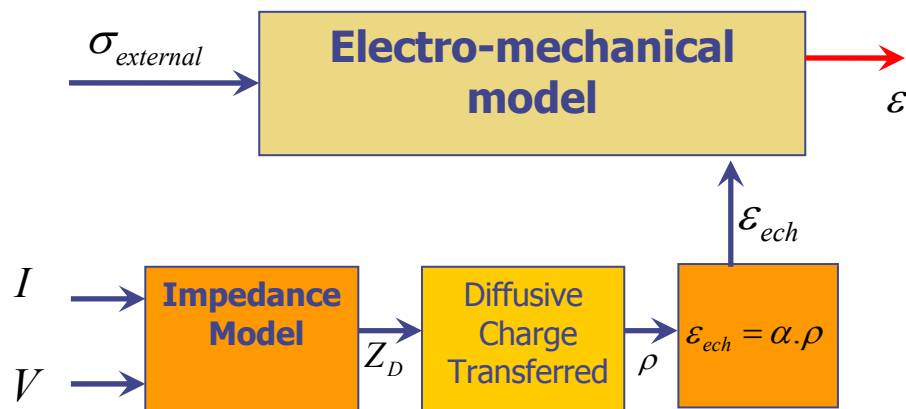


Figure 2.4.1 Experimental set-up.

2.5. Programming method

The electro- mechanical model that is the result of the present research is developed using the s-function in MATLAB software to simulate and validate the output results by comparing with the experimental results (as shown in the chart below). The reason for using an s-function is that the model is built up in Laplace space because of the viscoelastic components of the model.



The s-function tool is a useful technique to solve and simulate nonlinear complicated dynamic systems which cannot be solved using simple linear transfer functions in Laplace space.

CHAPTER 3: PRIMARY MODEL OF PPY HELIX TUBE MICRO ACTUATOR

3.1. Introduction

Recent advances in micro robotics have generated a growing demand for micro actuators. Conventional motors and drive trains have limited performance in micro dimension applications. Therefore, interest in using direct drive actuators like shape memory alloys, piezoelectric polymers and polyelectrolyte gel is increasing. The slow response of shape memory alloys, high voltage and low power density of piezoelectric polymers and low elastic modulus and yield strength of gel polymers have limited their micro applications (Baughman, 1996). Alternatively, electro active polymers (EAP) have a good muscle-like behaviour (Hunter and Lafontaine, 1992, Baughman, 1996) and recent research has shown prototype applications using different forms of conducting polymer actuators (Smela, 2003).

Consequently, much work has been carried out on modelling of EAP actuators, both in structural mode and actuation performance. Initially, the mechanical properties of EAP film actuators were investigated using continuum mechanics methods (Della Santa et al., 1996, Della Santa et al., 1997c, Mazzoldi et al., 2000) based on the theory of elasticity of porous materials (Biot, 1941, Biot, 1955, Biot, 1956). Later, the lumped parameters method which utilized Maxwell's linear viscoelastic blocks, was employed to model passive behaviour (Della Santa et al., 1997a, Mazzoldi et al., 2000) assuming the active electrochemical generated strain was proportional to the charge transferred to the actuator (Madden et al., 2001a, Mazzoldi et al., 2000, Madden, 2000).

As discussed in Chapter 1, it has been recently shown that Polypyrrole actuators formed into a hollow tube containing a helically wound platinum wire in the tube wall, show superior performance to conventional flat films. These "PPy helix tube" actuators show higher actuation strains and strain rates than conventional PPy films (Ding et al., 2003a).

In this chapter, a 'primary model' is introduced to predict the response of PPy helix tube micro actuator to the input voltage. In order to determine the 'primary model', the displacement response of the actuator to different input voltages with various conditions including range, frequency and pattern, is considered. The fabrication methodology of the actuator and experimental methodology are explained in section 3.2; then the active

electrochemical model is described in section 3.3. The predictive performance of the active model is tested against mechanical test data in section 3.5.

3.2. Materials and Methods

Propylene carbonate (PC) (Aldrich) and tetrabutylammonium hexafluorophosphate (TBA-PF₆, obtained from Sigma) both of AR grade were used. Pyrrole monomer from Merck was distilled and stored under -18°C before use. Platinum (Pt) wires in 250 and 50 μm diameters were from Goodfellow. The constant current required for polymerization was measured using an EG and G Princeton Applied Research Model 363 potentiostat / galvanostat. All the experimental data was processed and recorded by MacLab/4e AD instruments and computer. PPy fibre was grown galvanostatically for 16 hours with a 0.15 [mA/cm^2] current density. Polymerization solution was PC containing 0.06M Pyrrole and 0.05M TBA-PF₆. The polymerization temperature was controlled around -25 to -28°C . A two-electrode configuration was used; the working electrode was 250 μm Pt wire tightly wound by 50 μm Pt wire as helix and the auxiliary electrode was a stainless steel mesh. After growth, the 250 μm Pt wire was pulled out leaving a hollow PPy fibre containing the thinner Pt wire embedded as a helix in the tube wall. Two pieces of 250 μm Pt wire were inserted to each end of the PPy helix tube to enable electrical connection and mechanical clamping and then sealed by hot-melt polystyrene. PPy helix tubes were stored wet in PC containing 0.25M TBA-PF₆ before testing. Further fabrication information is given in (Ding et al., 2003a).

Isometric and isotonic conditions were applied using a force/length controller (Aurora Scientific, Dual Mode Model300B). The reference electrode was Ag wire in 0.01 M AgNO₃ and 0.1M TBA-PF₆ in Acetonitrile (ACN) using 0.1 M TBA-PF₆ in PC as a salt bridge. This is equivalent to +0.30 V vs. aqueous Saturated Calomel Electrode (aq. SCE) (Meites, 1963).

The experiments have been carried out using cyclic-voltammetry in different voltage ranges with respect to the reference electrode and also with different scan rates. The generated strain at a constant stress of 1.5 MPa has been recorded using the force/length controller (Aurora Scientific, Dual Mode Model300B) in order to measure strain to charge ratio.

3.3. Active elastic modelling

Several researchers (Mazzoldi et al., 2000, Della Santa et al., 1997b, Della Santa et al., 1997a, Chiarelli et al., 1995, Madden, 2000, Madden et al., 2001a) have shown that electrochemical generated strain can be assumed proportional to transferred charge density to the polymer surface described as in Equation 3.3.1.

$$\begin{aligned}\varepsilon(t) &= \frac{\sigma(t)}{E} + \varepsilon_{ech}(t) \\ \varepsilon_{ech}(t) &= \alpha \cdot \rho(t)\end{aligned}\tag{Equation 3.3.1}$$

In previous models, the mechanical part has been considered elastic and also the strain to charge ratio (α) and elastic modulus (E) assumed constant. The strain to charge ratio in hexafluorophosphate-doped polypyrrole is shown to exhibit time dependence (Madden et al., 2002). The studies presented here have been conducted at frequencies up to 0.010 Hz. Above this frequency the strain generated would be less than 0.3% and so too small to be useful. The time dependence of α can be neglected for frequencies less than 0.005 Hz.

3.4. Experimental results

Firstly, a cyclic voltammetry (CV) test was carried out on a PPy helix tube with 9mm length over different voltage ranges to optimise the range of stimulating voltage vs. reference electrode Ag/AgNO₃ as shown in Figure 3.4.1. The CV results shows that the oxidation and reduction peak shifts depending upon the voltage range used from the range of -1.0→+0.2 V to the range -1.0→+0.6 V and then the oxidation peak stabilises at the voltage of approximately +0.25 V for a wider voltage range.

Figure 3.4.2, which is the result of an experiment carried out to study the effect of load on the electrochemical properties of PPy helix tube, shows there is negligible effect of load. So the charge transferred can be considered independent of the loading for a given polymer and cell configuration.

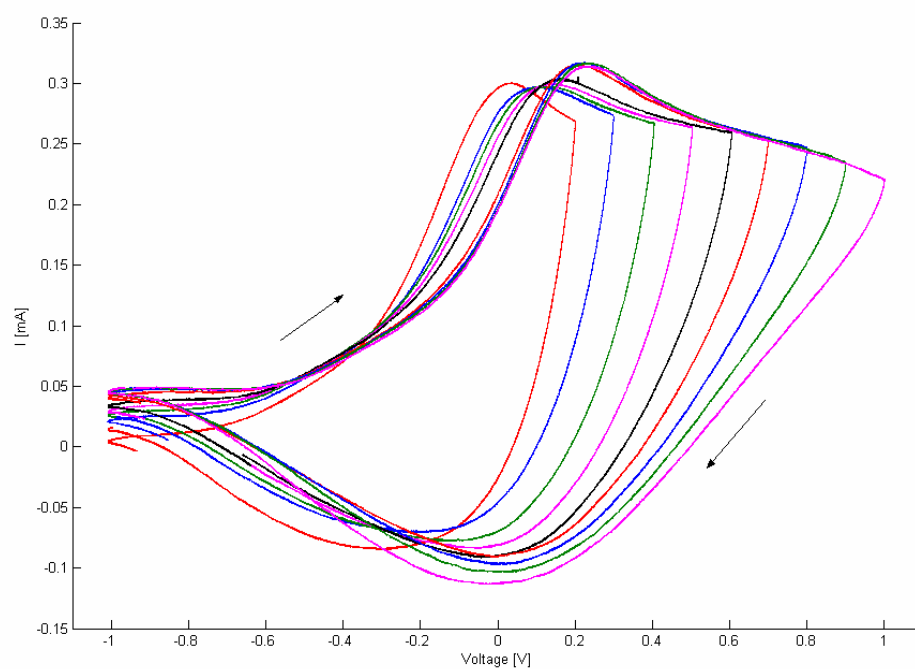


Figure 3.4.1 Cyclic Voltammetry in different ranges of applied voltages (vs. Ag/AgNO₃ reference) with 5 mV/s scan rate and 1.528 MPa applied load.

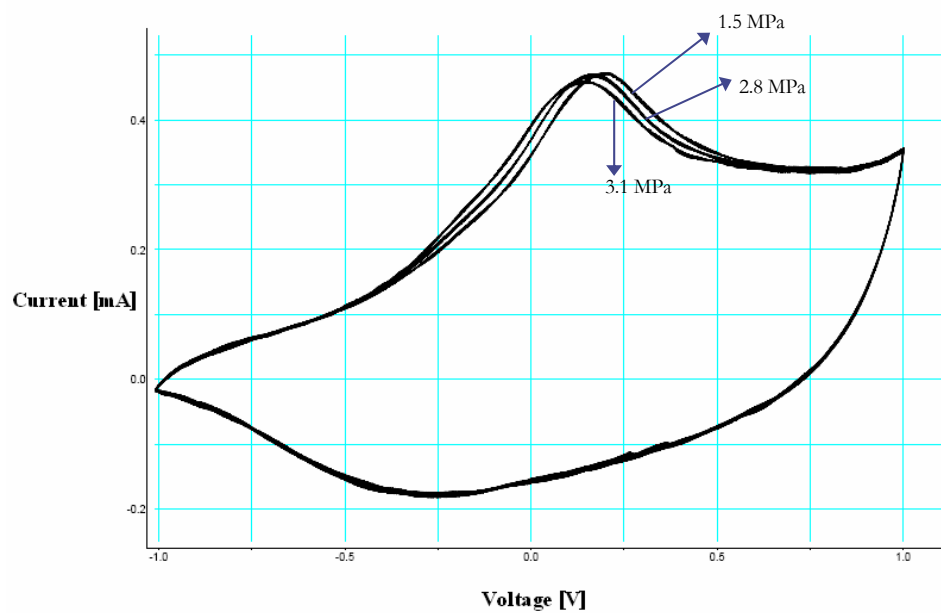


Figure 3.4.2 Cyclic Voltammetry in 5 mV/s scan rate and different applied loads (1.5, 2.8 and 3.1 MPa).

The strain generated by the actuator is shown in Figure 3.4.3 during cyclic voltammetry against reference electrode Ag/AgNO₃. As shown in this figure, the shapes of the strain graphs are similar for different stimulating voltage ranges. Starting the scan at -1 V, there is almost no strain recorded until ~0 V after which the PPy expands continuously as the voltage is increased to the maximum. During the reverse scan, the strain continues to increase at first before reaching a maximum and decreasing steadily. Below -0.5 V the strain is again constant. A wider range of voltage caused bigger peak strains. Hysteresis effects were amplified dramatically when higher anodic voltages were used. The shapes of the strain curves are also similar, but the creep strain is shown by the offset in the starting and finishing strains, and becomes significant when voltages >0.6 V were used.

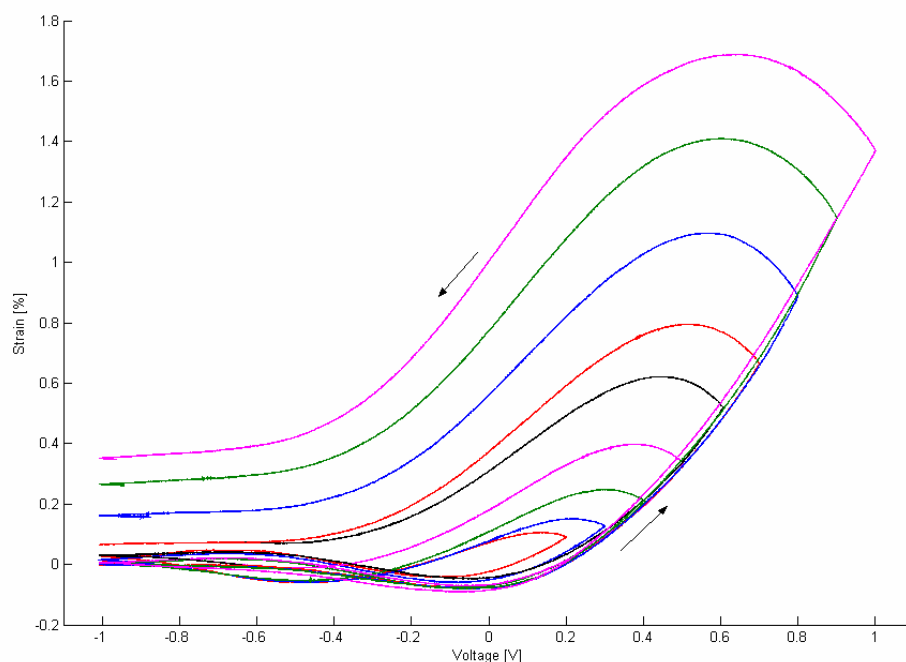


Figure 3.4.3 Generated strain result of Cyclic Voltammetry in different range of voltage in 5 mV/s scan rate and 1.528 MPa applied load.

The electrochemical strain has been plotted vs. charge transferred to the polymer, which is calculated directly from integrating the current signal starting at -1 V going up to the maximum voltage and then back to -1 V, and shown in Figure 3.4.4 and Figure 3.4.5. In Figure 3.4.4, the electrochemical strain generated is increasing roughly parabolically with

increasing charge transferred during oxidation and is decreasing roughly linearly with decreasing charge transferred during reduction. More complicated strain-charge behaviour occurs during the initial part of the anodic scan. Because of the small strains involved, this part of the strain-charge relationship will not be considered in the model. Figure 3.4.4 shows that the trend of electrochemical strain generated vs. the charge transferred is mostly independent of the voltage range. During oxidation the generated electrochemical strain increases parabolically and changes only slightly when higher anodic voltages are used. The shapes of the reduction curves are also similar. The hysteresis seen for voltages greater than 0.6 V appears to be largely related to the non-recoverable creep occurring under these conditions. It should be noted that the hysteresis in strain-charge curves are very much smaller than the corresponding strain-voltage curves. The CVs in Figure 3.4.1 show that anodic (oxidative) currents continue to flow to the helix tube actuator for some time after the potential scan direction has been reversed. The strain peaks in Figure 3.4.3 correspond approximately to the voltage at which the current becomes zero during the decreasing voltage scan (Figure 3.4.1). Thus, the electrochemically generated strains are proportional to the electrochemical charge transferred to the actuator, with the exception of a non-recoverable creep component.

Figure 3.4.5 shows the effect of the stimulation voltage scan rate on the trend of electrochemical strain generated vs. the charge transferred for a voltage range of -1 V to +1 V. The shape of the strain-charge curve is seen to be very sensitive to the scan rate and at least four separate effects can be observed at slower scan rates:

- A larger strain amplitude results.
- A higher charge transfer occurs.
- A more significant non-recoverable creep occurs.
- Evidence of cation exchange is present (shown by the decreasing strain during the initial part of the increasing voltage sweep and increasing strain during the last part of the decreasing voltage scan).

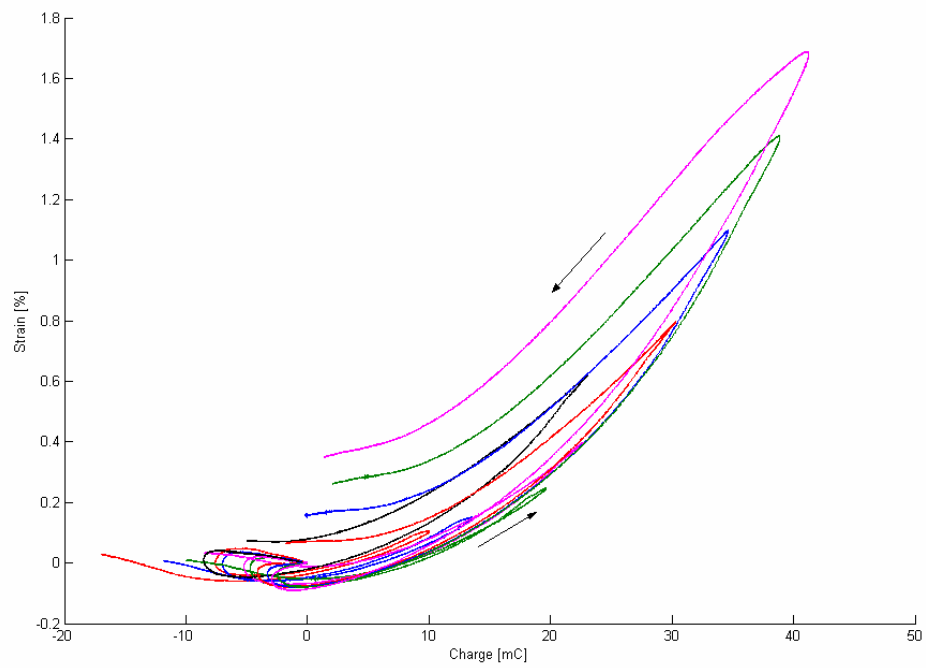


Figure 3.4.4 Generated strain result of Cyclic Voltammetry vs. charge transferred in 5 mV/s scan rate and 1.528 MPa applied load.

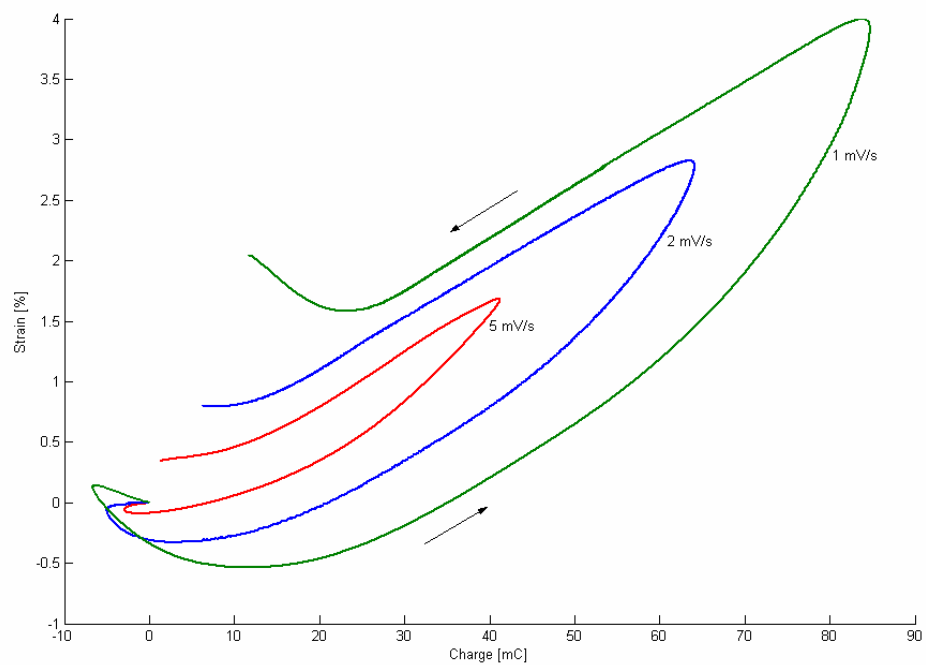


Figure 3.4.5 Generated strain result of Cyclic Voltammetry vs. charge transferred in different scan rates and 1.528 MPa applied load.

The larger strain amplitudes at slow scan speeds may be due to more oxidation and reduction occurring, which is supported by the higher charge transferred. However, it is also possible that the higher charge is associated with parasitic electrochemical reactions. The higher strains may also result from solvent osmosis effects, which are thought to be slow and, therefore, more apparent at slow scan rates. Similarly, the cation contribution to the actuation may be related to kinetic effects related to ion diffusion rates. The effect of scan rate on creep is not known, although the results suggest that the longer the polymer is exposed to higher voltages, the higher is the creep.

Figure 3.4.6 shows the strain to charge derivative vs. the charge transferred density with the polymer initially in the fully reduced state. The data from the slowest voltage scan rate (1 mV/s) was used to generate this curve. As shown, there is a resistive current and charge transferred without causing strain from 0 to near 0.4 C/m³. The absence of strain in this region may reflect competing anion plus cation movement that produce no net strain. Alternatively, the charge consumed at these voltages may not be associated with polymer redox activity and therefore does not contribute to strain generation. From 0.4 C/m³ to 1 C/m³, the amount of strain produced per unit of charge transferred increases linearly and may reflect a shift toward more anion incorporation and less cation expulsion as the charge transferred increases. Between 1.0 C/m³ and 1.6 C/m³ the strain to charge ratio is constant and equal to $150 \times 10^{-12} \text{ m}^3/\text{C}$ which is similar to the value reported in the literature (Madden et al., 2002, Madden, 2000). After 1.6 C/m³, the strain derivative again increases probably due to osmotic and/or creep processes.

A simpler relationship exists during reduction of the polymer from the fully oxidised state. The strain to charge ratio is constant until the net charge transferred decreases to $\sim 1.0 \text{ C/m}^3$. When the charge is further reduced, the strain to charge ratio decreases to zero (below 0.4 C/m³)

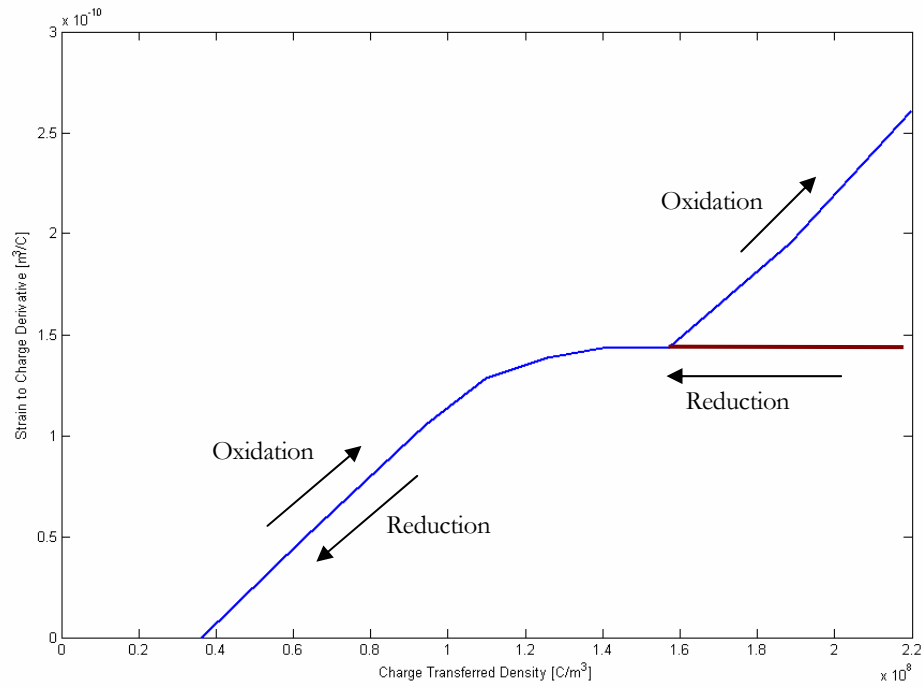
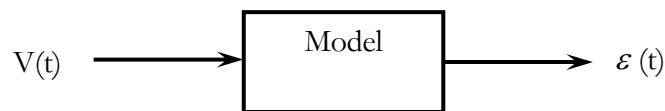


Figure 3.4.6 A generalisation of the first derivative of generated strain to charge density transferred based on the Cyclic Voltammetry in 1 mV/s vs. charge transferred density in 1.528 MPa applied load.

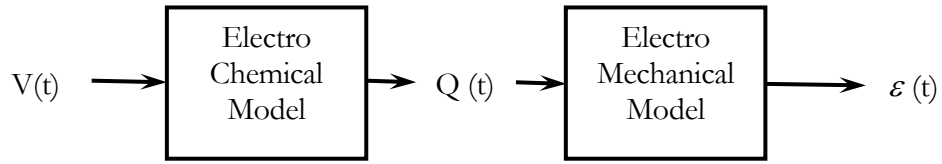
3.5. Modelling

3.5.1. Modelling principles and approach

The aim of the model presented in this section is to be able to predict the strain output over time given a defined voltage input.



As recognised in previous studies, the strain output is more directly linked to the charge transferred to the polymer. The first modelling step, therefore, is to predict the charge (or current) for a given voltage (Electrochemical Impedance model) and the second step is to calculate strain from the charge passed (Electromechanical model).



Several electrochemical impedance models have been proposed previously (Penner and Martin, 1988, Penner et al., 1988, Penner et al., 1989, Tanguy et al., 1989, Tanguy, 1991, Ren and Pickup, 1995, Ferloni et al., 1996, Madden, 2000) which are based on impedance spectroscopy in a small range of stimulation voltage. These assume that the electrical behaviour is almost linear. These models cannot be applied to predict the nonlinear current signal of PPy from fully reduced state to fully-oxidised state. The Electrochemical Impedance Spectroscopy of PPy for different DC voltages has been carried out by Madden et al. who showed that the measured impedance over a small range of voltage cannot be applied to the whole range of oxidation and reduction. That is, the PPy impedance varies for different DC voltage inputs (Warren and Madden, 2006b).

A very recent publication by Madden et al. shows the first attempt to predict the CV diagram or current behaviour of PPy using a variable resistance transmission line method. The method avoids the need to solve the complicated Nernst equation. This method has been developed for a rectangular thin PPy film and successfully predicts the electrochemical behaviour of the film but has not been able to predict the parasitic charge that is seen at high voltages or predict the current (or charge) signal in the fully-oxidised state accurately (Warren and Madden, 2006a). The variable resistance transmission line model is not directly applicable to the PPy helix tube actuator which can be more complicated because of a) the geometrical complication and b) the strong parasitic effect which cannot be neglected in these actuators. Since the focus of this research is to develop the electromechanical model and validate it as accurately as possible the adaptation of the transmission line model to PPy helix tubes was considered beyond the scope of the present thesis. Instead, the actual measured current signal has been used in order to cancel the effect of inaccuracies in the current signal in the electrochemical model, especially in high voltage ranges.

Previously reported electromechanical models have taken the strain to charge ratio ($\alpha = \Delta\epsilon/\Delta Q$) as a constant and then simply predicted strain from $\epsilon_{ech}(t) = \alpha Q(t)$. The strain to charge ratio is defined as the ratio of strain changes to changes in the charge transferred in a complete cycle, such models have been quite successful when applied to actuation produced by a small voltage input. Since a dynamic model as a continuous function of time is required in this thesis, it is necessary to consider the strain: charge parameter more generally in the time-domain as $\alpha = d\epsilon/dQ$. The results shown in Section 3.3 have shown that α is not constant when a wide voltage input range is used. In fact α varies with the transferred charge in a complicated manner as shown in Figure 3.4.6. By defining $\alpha = d\epsilon/dQ$ it is still possible to determine the actuation strain at a given charge input, and that approach is used in the following modelling sections.

In this section the modelling of the full oxidation and reduction of the polymer is considered. The actuation strains are much larger when the polymer is switched between its fully reduced and fully oxidised states. Therefore, it is important to be able to model the strain response from a wide voltage input. The experimental data collected at a slow scan rate (1 mV/s) and over a wide potential range (-1 V to +1 V, vs. Ag/AgNO₃) at an applied load of 1.528 MPa has been used to develop a model. These experimental data are shown in Figure 3.5.1. Separate experiments have been performed using different voltage inputs to provide data that will be used to assess the validity of the simulated outputs from the model. The experimental data for these simulations are given in Figure 3.5.3 and the experimental conditions are described in the Section 3.5.3.

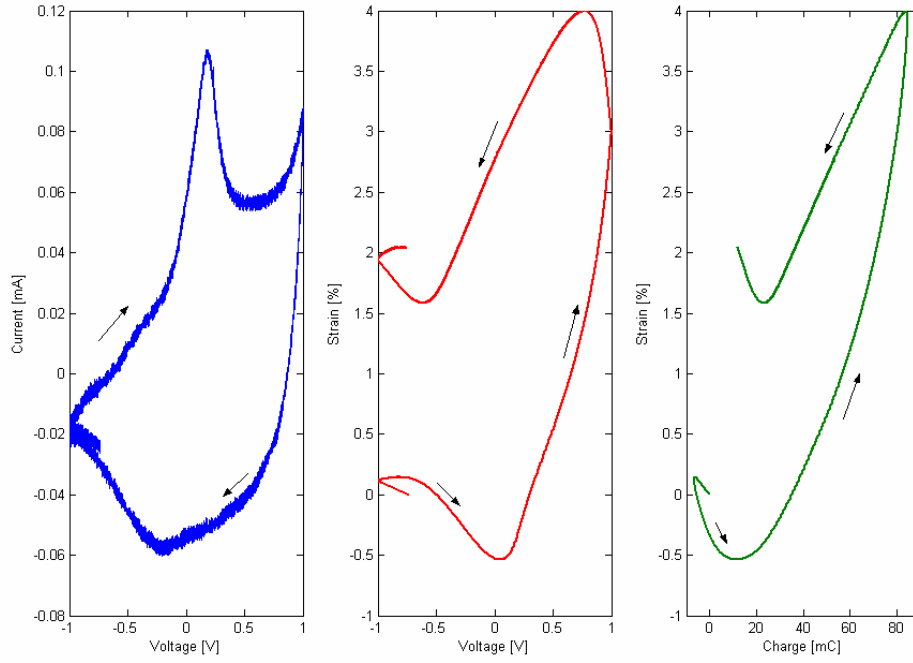


Figure 3.5.1 experimental data for 1 mV/s scan rate.

3.5.2. Electromechanical model

In previous models the strain to charge ratio (α) had been considered a constant for a particular polymer/dopant/electrolyte system. From the experimentally determined α , the electrochemically-induced strain (ε_{ech}) has been calculated using Equation 3.5.1. Since the testing conditions used a constant applied stress (σ), and it is assumed that the modulus (E) is constant, the passive strain (σ/E) is constant and can be ignored. The situation where the modulus is not considered constant is discussed in Chapter 4:

$$\varepsilon(t) = \frac{\sigma(t)}{E} + \varepsilon_{ech}(t)$$

Equation 3.5.1

$$\varepsilon_{ech}(t) = \alpha \left[\frac{\%}{mC} \right] \cdot q(t)[mC]$$

$$\alpha \left[\frac{\%}{mC} \right] = \alpha_v \left[\frac{m^3}{C} \right] \cdot \frac{[C]}{10^3 [mC]} \cdot \frac{100 [\%]}{L_i A [m^3]} \quad \text{Equation 3.5.2}$$

$$q = \int i dt$$

$$q [mC] = Q \left[\frac{C}{m^3} \right] \cdot L_i A [m^3] \cdot \frac{10^3 [mC]}{[C]}$$

$$L_i = 52 [mm]$$

$$A = 2.6535 \times 10^{-2} [mm^2]$$

The model used to generate a predicted strain output is shown in Figure 3.5.2 . Firstly, the measured current (at time t) is converted to the total charge transferred to the polymer by integration (Equation 3.5.2). This charge is then normalised by dividing by the sample volume:

$$Q (C / m^3) = \frac{q (mC)}{L_i A (m^3)} \quad \text{Equation 3.5.3}$$

This charge transferred is then used to identify the appropriate strain to charge density ratio (α_v) from Figure 3.4.6. After conversion to the strain to charge ratio (α) using Equation 3.5.2, the strain is then determined from Equation 3.5.1. The process is illustrated in Figure 3.5.2.

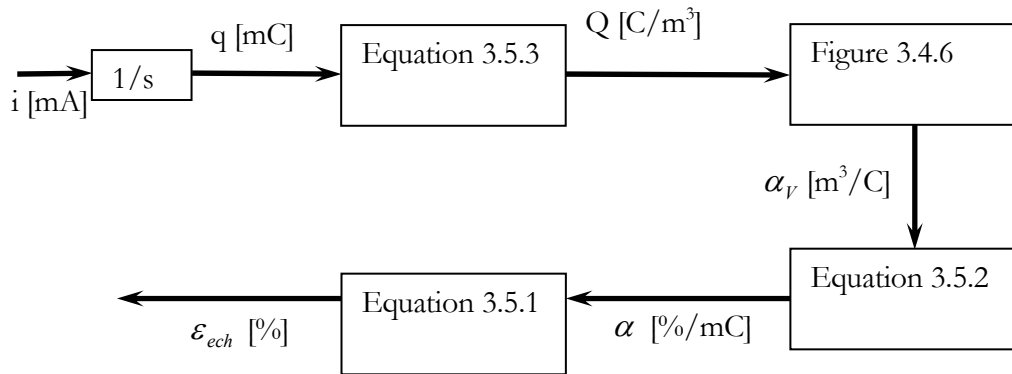


Figure 3.5.2 Flow chart showing how electrochemical strain is estimated from measured current.

This process is repeated for each increment in time so that the strain output over time can be estimated. The predicted results for the simulation experiments are given in Section 3.5.4.

3.5.3. Experimental set-up for model validation

The actuator used for the results presented in this section had 58 mm length and was stimulated by applying a sinusoidal voltage ($-0.75\text{ V} \rightarrow +0.55\text{ V}$ vs. Ag/AgNO₃ reference electrode as shown in Figure 3.5.3) with different frequencies (1, 5 and 10 mHz) and under different external loads (450 kPa, 3.25 MPa and 5.80 MPa). Figure 3.5.3 shows the input and output signals in Chart software format vs. experimental time. The reason for choosing a sinusoidal signal for stimulation voltage is to use a different kind of experimental data to validate the model that was derived from the cyclic voltametric data. After applying the external load, the sinusoidal voltage signal at a particular frequency was applied to the polymer using a function generator connected to a potentiostat and then the applied frequency increased after a few full cycles. Then, the applied external load was increased and the procedure repeated. The voltage, current, displacement and load signals were recorded throughout the experiment.

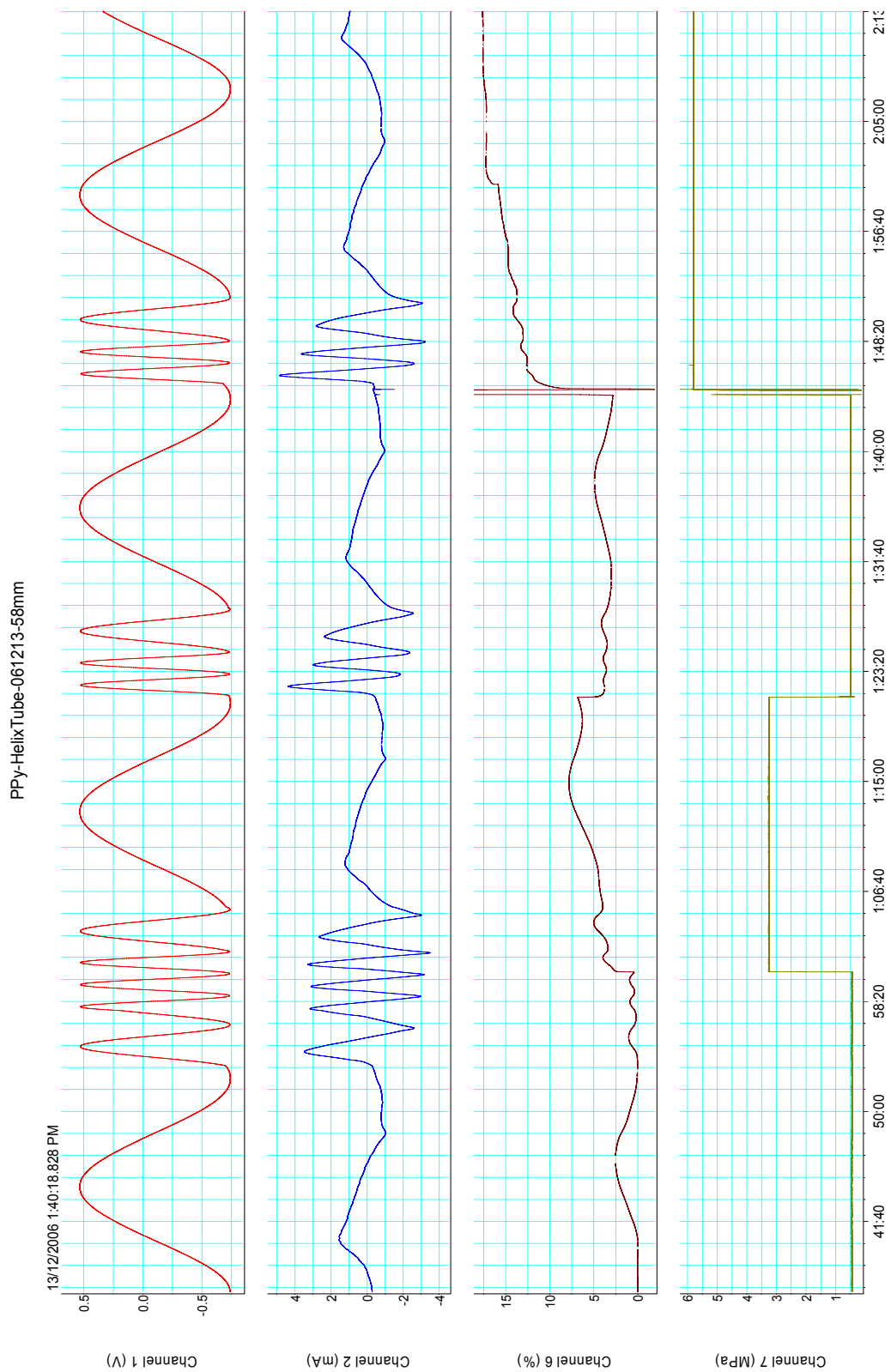


Figure 3.5.3 Experimental results from sinusoidal voltage input over a wide voltage range at different frequencies.

The simulation part of the modelling was carried out using an s-function written in MATLAB for each model. The aim of the simulation was to try to predict the mechanical behaviour of the actuator during the electrochemical stimulation. The applied voltage was changed from -0.75 V to +0.55 V vs. Ag/AgNO₃ and then returned to -0.75 V to complete one full cycle. The measured current during this cycle was used to determine the strain output, as described in the previous section.

The simulation results using the approach described in Section 3.5.2 are also compared with a constant strain-charge ratio model. The ‘primary’ model considers the strain-charge ratio as a function of the charge transferred as shown in Figure 3.4.6. In contrast, the constant strain to charge ratio model assumes a constant value of “ $1.46 \times 10^{-10} \text{ m}^3/\text{C}$ ” across the entire charge range.

3.5.4. Comparison of experimental and predicted results

The experimental and calculated results are presented in Figure 3.5.4 to Figure 3.5.6 with 450 kPa applied stress and different electrical stimulation frequencies from 1 mHz to 10 mHz. Similar results are given in Figure 3.5.7 to Figure 3.5.11 for an applied stress of 3.25 MPa and 5.80 MPa.

The experimental data obtained over this very wide potential range and at different frequencies and stresses are similar to those reported in Section 3.4 from CV tests. In most cases, two strain peaks were observed during oxidation of the initially reduced polymer. The first small expansion and contraction during the initial part of the first voltage cycle is most likely to be caused by cation incorporation (due to final reduction) and expulsion (due to initial oxidation). The main actuation, however, occurs in the second half of the voltage cycle with oxidation producing an expansion (due to anion incorporation) and subsequent reduction causing shrinkage (anion expulsion). For low frequency cycling there is also a creep component to the strain that is non-recoverable. The effect of higher frequency cycling is to reduce the strain amplitudes such that the first expansion/contraction peak and creep become negligible. An increasing applied stress also tends to decrease the magnitude of the strain response.

A first comparison of simulated strain output and experimentally measured strain is given in Figure 3.5.4 for slow (1 mHz) cycling at a low stress (450 kPa). The elastic mechanical model with elastic modulus equal to 110 MPa has been applied in both simulations: the Primary model and the constant strain to charge ratio model. The results produced by the

‘primary’ model, in which the strain to charge relationship is taken from Figure 3.4.6, gives a reasonably good simulation of the measured strain response. The generally good agreement demonstrates that this modelling approach is valid.

The primary model is able to predict the experimental strain shape successfully using the “master curve” for strain to charge ratio. Thus, there is no strain predicted during the initial part of the cycle since $\alpha = 0$ below 0.4 C/m^3 . This prediction is in close agreement with experimental results. The constant strain to charge ratio model cannot predict this complex behaviour. The first point and the final point of the experimental strain have also been predicted accurately by the primary model.

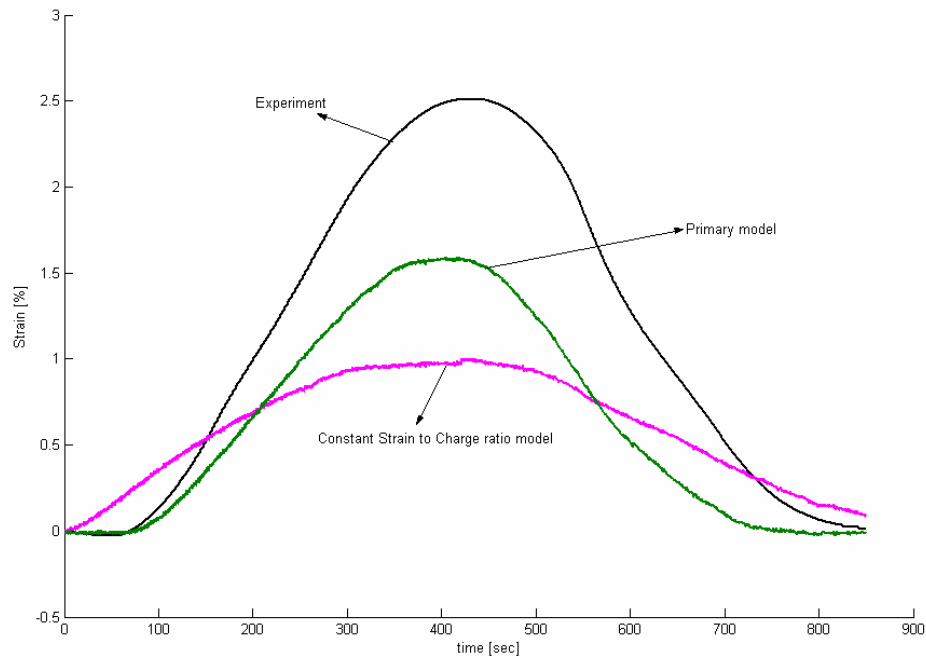


Figure 3.5.4 Stress 0.45 MPa and 1 mHz.

As shown in Figure 3.5.5, the same performance is shown by the primary model to predict the experimental strain shape. The applied frequency was 5 mHz during this peak so the peak strain was decreased from 2.5 % at the slow frequency (Figure 3.5.4) to 0.8 %, which is in agreement with the results shown in the literature.

The same performance is shown in Figure 3.5.6 with 10 mHz; here the peak of the experimental strain has been more successfully predicted compared to the lower frequency results (1 and 5 mHz).

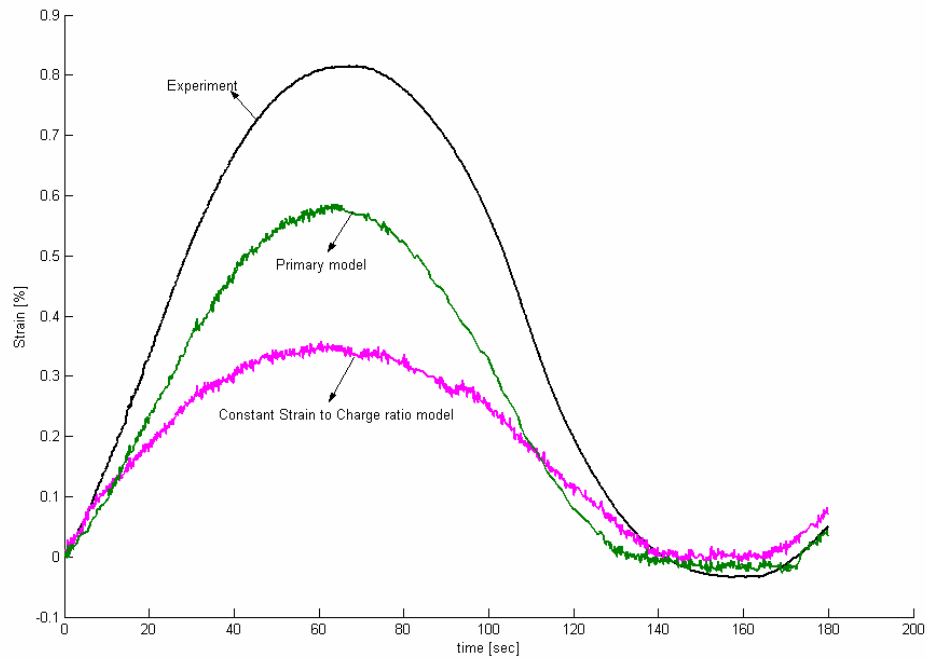


Figure 3.5.5 Stress 0.45 MPa and 5 mHz.

Reviewing the results presented in Figure 3.5.4 to Figure 3.5.6, it is shown that despite the major improvement of the primary model, the predicted results still do not closely match the experimental strain results. The experimentally observed peak strain was always higher than the value predicted using the primary model. The predictions were generally better when higher stimulation frequencies were used.

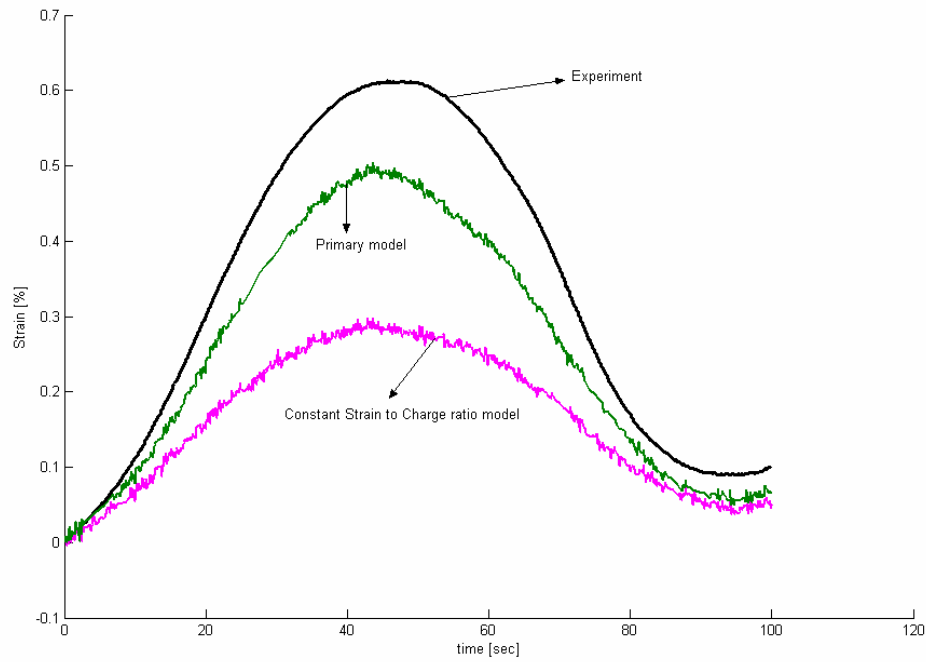


Figure 3.5.6 Stress 0.45 MPa and 10 mHz.

The results shown in Figure 3.5.7 have been taken at 3.25 MPa and 1 mHz. Firstly, it is important to mention that creep behaviour results in $\sim 2\%$ irrecoverable strain in 600 seconds after the load was increased. This load-induced creep is super-imposed on the ‘normal’ actuation processes. The creep response means that the elastic mechanical model needs to be modified to be able to track the creep that results when the applied external load is changed.

By comparing Figure 3.5.7 and Figure 3.5.4, the peak strain predicted by the primary model in 1 mHz at two different loads, 450 kPa and 3.25 MPa are almost the same and equal to 1.5 %. Since it has been shown in Figure 3.4.2 that the applied load does not have a major effect on the electrochemical parameters, it is reasonable to have the same peak strain predicted by the primary model at different stresses. More accurate prediction of actuation strain under different loading conditions requires the introduction of a viscoelastic component. This aspect of the model is considered in the following chapters.

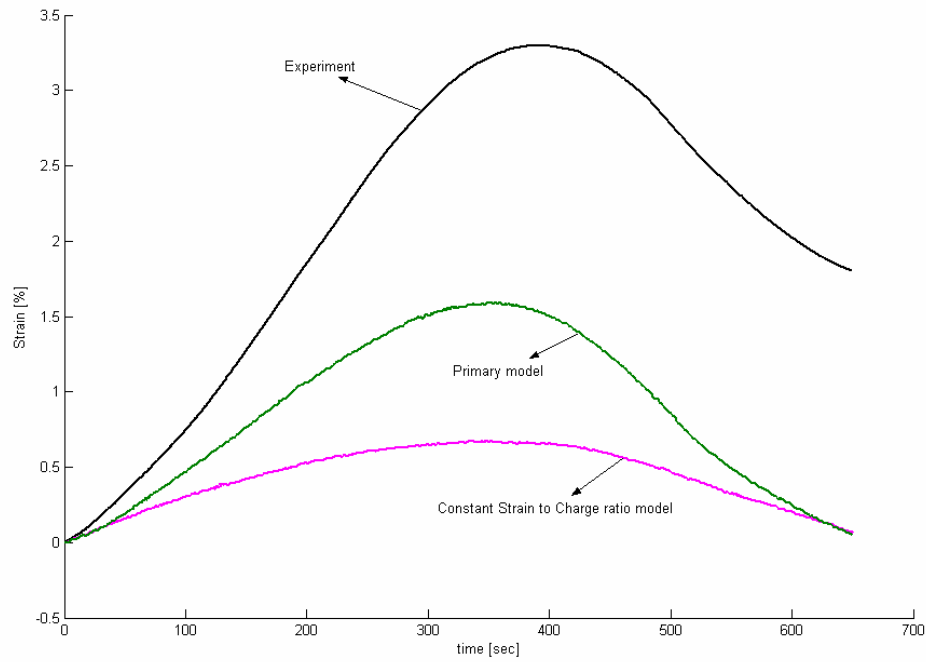


Figure 3.5.7 Stress 3.25 MPa and 1 mHz.

The same creep behaviour is observed in the results presented in Figure 3.5.8 and Figure 3.5.9, for cycles at higher frequencies. The extent of creep that was observed is approximately constant for each cycle, indicating that the viscoelastic relaxation time of the PPy is very much longer than the voltage cycle times imposed. These results highlight the importance of accurately predicting the viscoelastic response as it will dominate the strain output when load changes (which is a common situation with practical applications for actuators).

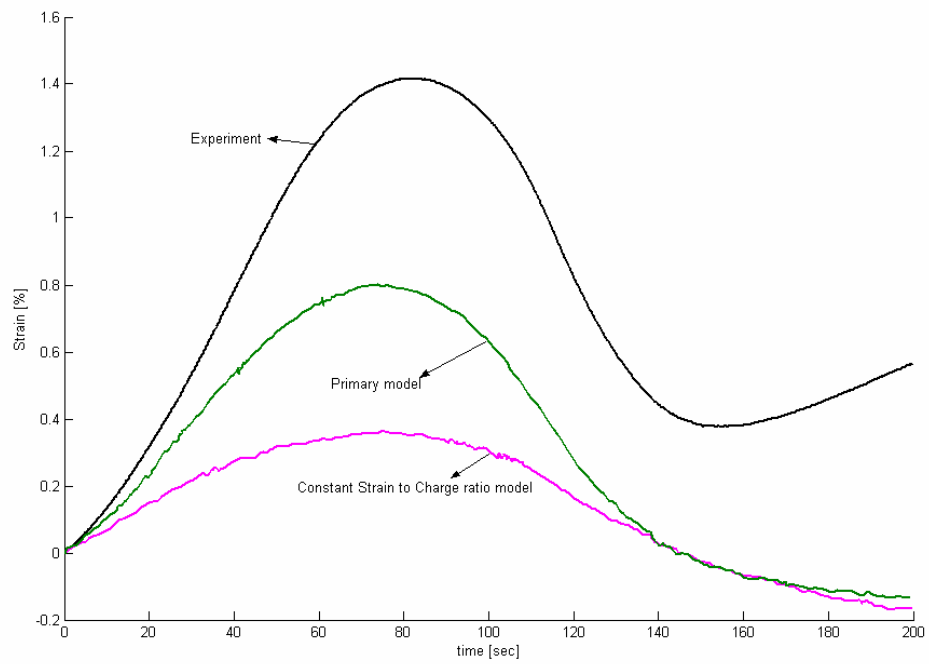


Figure 3.5.8 Stress 3.25 MPa and 5 mHz.

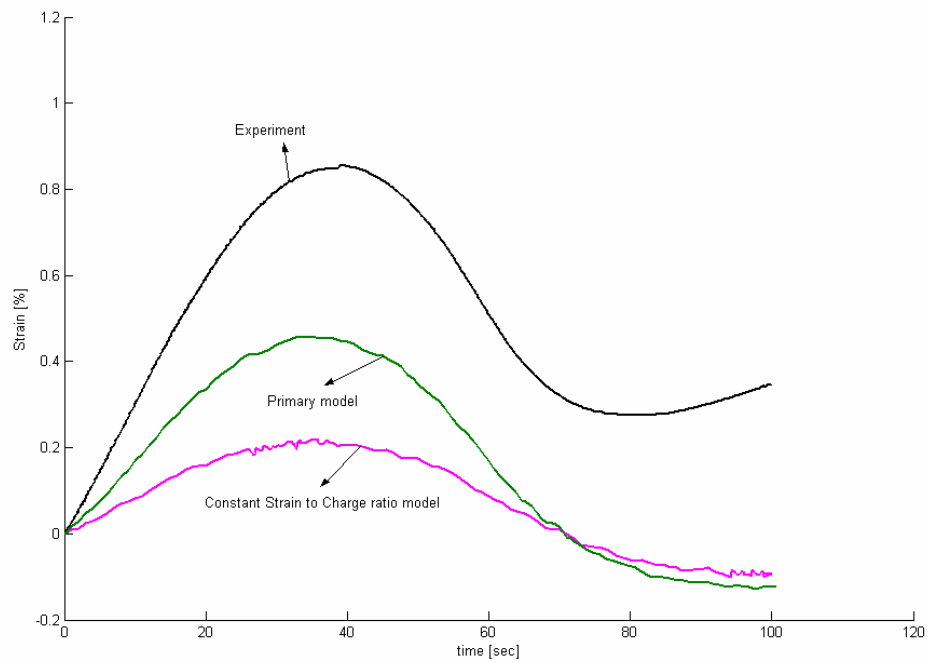


Figure 3.5.9 Stress 3.25 MPa and 10 mHz.

Finally, a higher external stress of 5.80 MPa has been applied to investigate the performance of the primary model with the results shown in Figure 3.5.10 and Figure 3.5.11. The creep response is nearly double that observed at 3.25 MPa and was nearly 80% of the peak generated. The maximum strain was also lower at this high stress which confirms the published results by Spinks et al. (Spinks et al., 2005, Spinks and Truong, 2005, Spinks et al., 2003d). The effect of load on the actuation strain has been attributed in these previous studies to a change in elastic modulus that occurs during voltage cycling of the PPy. This effect is considered in chapter 5.

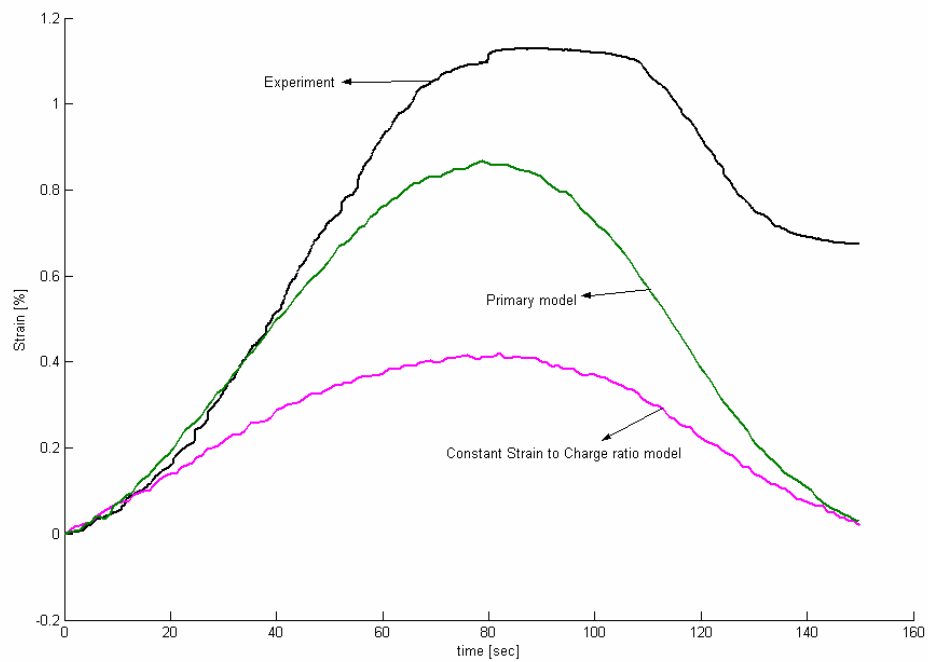


Figure 3.5.10 Stress 5.80 MPa and 5 mHz.

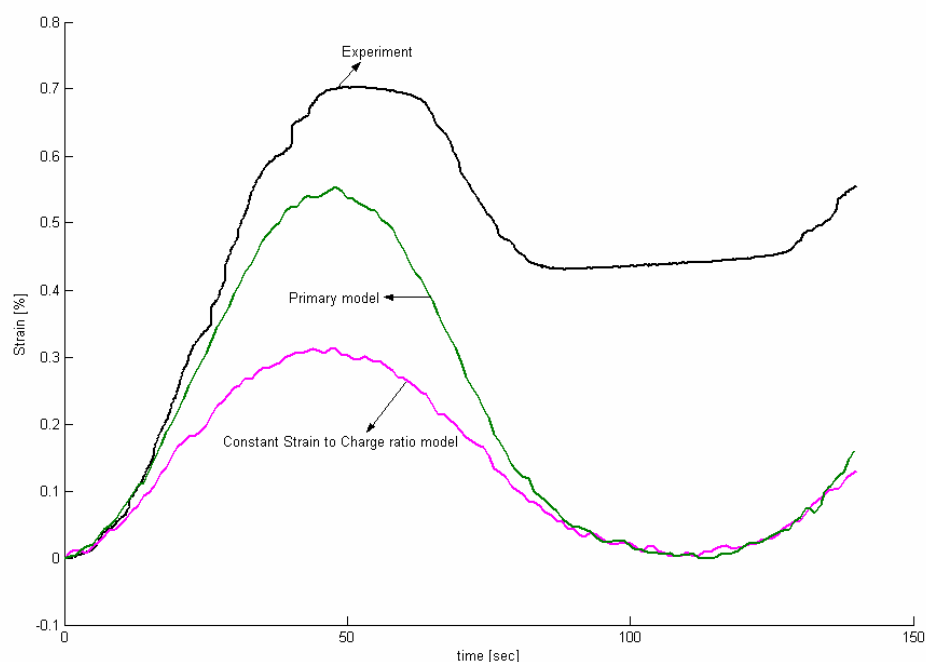


Figure 3.5.11 Stress 5.80 MPa and 10 mHz.

3.6. Conclusions

The active electrochemical properties of a PPy helix tube actuator have been considered in this chapter. Cyclic voltammetry over different ranges of voltage was used to optimise the stimulation voltage range to maximise the strain generated. The strain generated as a function of charge transferred was also studied for different stimulating voltage ranges and scan rates. This study shows that the voltage ranges and stimulation scan rate have negligible effect on strain to charge ratio in the practical range of stimulation of PPy helix tube.

The trend of the strain generated vs. the charge transferred was also modelled as parabolic during oxidation and linear in reduction. The relation of this trend and the strain to charge ratio reported in the literature was specified. It has also been shown that applied load has negligible effect on the cyclic voltammetric result of PPy helix tube which means the electrical charge transferred is independent of mechanical loading.

A 'primary model' was proposed based on the 'master curve' for the strain to charge ratio and compared with the constant strain to charge ratio model. These models were

investigated by setting up a simulation program to predict the experimental strains resulting from sinusoidal voltages applied with different frequencies and under different load conditions. The results showed that the primary model better simulated the strain output during wide voltage cycling compared with the constant strain to charge ratio model.

Also, the primary model was seen to fail when the external load was changed. Additional elements need to be included in the model to account for viscoelastic effects and changes in the modulus. These modifications are considered in the following chapters.

CHAPTER 4: USING VISCOELASTIC MODEL FOR IMPROVEMENT OF PASSIVE PPy HELIX TUBE MICRO ACTUATOR MODELLING

4.1. Introduction

In the previous chapter, a ‘primary model’ was introduced to predict the PPy actuator response to the voltage stimulation under different external loads. Although the performance of the model under the low load condition was satisfactory, improvements at higher external loads are needed. Much work has been carried out on modelling of EAP actuators in structural mode especially the effects of load and its time-dependency. Initially, the mechanical properties of EAP film actuators were investigated using continuum mechanics methods (Della Santa et al., 1996, Della Santa et al., 1997c, Mazzoldi et al., 2000) based on the theory of elasticity of porous materials (Biot, 1941, Biot, 1955, Biot, 1956). Later, the lumped parameters method which utilized Maxwell’s linear viscoelastic blocks, was employed to model passive behaviour (Della Santa et al., 1997a, Mazzoldi et al., 2000).

In this chapter, the viscoelastic mechanical model is used to enhance the performance of the ‘primary model’ which was developed in Chapter 3 using a fully elastic mechanical model. It is shown that this ‘passive improvement’ model predicts the response of PPy helix tube actuators under the external load better than the ‘primary model’ developed in previous chapter. The fabrication methodology of the actuator and experimental methodology are explained in section 4.2; then a lumped-parameter viscoelastic model is presented in section 4.4. The predictive performance of the passive model is tested against mechanical test data in section 4.5.

4.2. Materials and Methods

The sample preparation, experimental set up and reference electrode configuration is as described in Chapter 2 and Section 3.2. Isometric and isotonic conditions were applied using a force/length controller (Aurora Scientific, Dual Mode Model300B). Stress-Relaxation tests were arranged in seven different isometric step strains up to 0.73 % strain to produce 3.2 MPa total stresses and 2.2 MPa relaxed stress. Recent research illustrates that the actuation performance decreases with increasing external load on a PPy helix tube fibre actuator. Also the strain generated by applied voltage reduces to 0.5 percent of free

standing actuation strain with 3.8 MPa external stress and apparently there is no actuation after 4 MPa (Spinks et al., 2002, Spinks et al., 2004). Hence, the range of isometric step input strain used in these experiments was up to 0.8 percent corresponding to 3.2 MPa. The length of the fibre was 59 mm and the voltage was adjusted to zero relative to the reference electrode, which was Ag wire in 0.01 M AgNO_3 and 0.1M TBA- PF_6 in acetonitrile (ACN) using 0.1 M TBA- PF_6 in PC as a salt bridge. This is equivalent to +0.30 V vs. aqueous Saturated Calomel Electrode (aq. SCE) (Meites, 1963). Finally, the stress-strain curves were generated with different lengths of actuator also using the force/length controller and operated at constant displacement rate of 4.6 mm/s.

4.3. Passive viscoelastic modelling

The stress in elastic mechanical systems is proportional to the strain and in viscous materials proportional to the rate of strain. Some materials like polymers exhibit both elastic and viscous behaviour simultaneously. There are two methods to simulate their behaviour: Kelvin's and Maxwell's model (Ebewele, c2000). The Kelvin model contains a spring and dashpot in parallel and Maxwell's model has these elements in series. Each approach has a good performance in different tests. Maxwell's approach can model the stress-relaxation test and Kelvin's has good performance in estimating the creep test. It is possible to have a combination of both methods in one model, containing two springs and one dashpot, a spring in series with the dashpot and the other in parallel to both of them, which is known as the Standard Linear Solid model.

The viscoelastic model has been solved for simple and standard cases such as stress relaxation (step stress input) and creep (step strain input) tests in text books of viscoelastic theory (Ebewele, c2000). However, the aim of the viscoelastic modelling carried out in this thesis is to provide a comprehensive model which is able to simulate the dynamic behaviour of the actuators as a continuous function of time so that they can be incorporated into engineering control systems. For this purpose the Ordinary Differential Equation (ODE) describing the viscoelastic model has to be solved. A widely used technique for examining and solving ODE's uses Laplace Transform theory, and the main benefits and results of this theory are described in Appendix A.

In this chapter many standard results from Laplace transform theory will be used in deriving the equations. The Laplace transforms used for derivatives, step and ramp inputs

etc are listed in Appendix A., where the ‘initial and final value theorems’ which allow straightforward solutions for dynamic systems are also described.

The polymer system can be considered as a configuration of many finite elements and each element can be modelled in Kelvin’s or Maxwell’s mode. The result is simply many Kelvin’s models in series or many Maxwell’s in parallel. The EAP actuator is assumed as a configuration of n Standard Linear Solid models, with the active strain generation term considered as a box in this circuit (Della Santa et al., 1997a, Mazzoldi et al., 2000). This configuration and all the model parameters are shown in Figure 4.3.1.

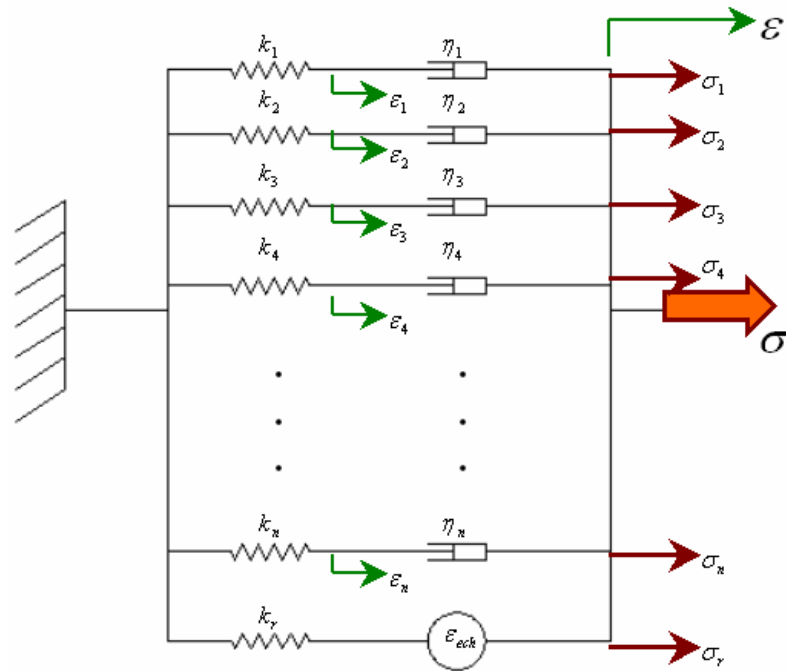


Figure 4.3.1 Viscoelastic free body diagram of EAP actuators, containing n blocks in parallel mode.

In Figure 4.3.1, k_i and η_i ($i=1$ to n) are the stiffness and viscosity coefficient (damping ratio) of the spring and dashpot in each branch respectively which form the time constants. Also k_r is the stiffness of the main branch and is also called the relaxed stiffness coefficient. The overall stress and strain applied to the polymer are σ and ϵ which are distributed amongst all the branches and classified using the index i .

De Rossi et al (Della Santa et al., 1997a, Mazzoldi et al., 2000) have shown that it is appropriate to include the electrochemical generated strain ε_{ech} in series with k_r to model conducting polymer actuators.

Equation 4.3.1 satisfies the equilibrium condition where the applied stress at any given time t is shared between the different spring-dashpot branches:

$$\left(\sum_{i=1}^n \sigma_i(t) \right) + \sigma_r(t) = \sigma(t) \quad \text{Equation 4.3.1}$$

Where $\sigma_r(t)$ is the stress applied to the main branch, as shown in Figure 4.3.1.

Equation 4.3.2 and Equation 4.3.3 show the viscoelastic formulation where the stress generates a strain in each branch (ε_i) that is proportional to the stiffness (k_i) and a viscous deformation that depends on the viscosity coefficient (η_i) and strain rates at time t ($\dot{\varepsilon}_i(t)$).

$$\sigma_i(t) = k_i \cdot \varepsilon_i(t) \quad \text{Equation 4.3.2} \quad (a)$$

$$\sigma_i(t) = \eta_i \cdot (\dot{\varepsilon}(t) - \dot{\varepsilon}_i(t)) \quad \text{Equation 4.3.2} \quad (b)$$

$$\sigma_r(t) = k_r \cdot \varepsilon_r(t) \quad \text{Equation 4.3.3}$$

Since polypyrrole is a cross-linked material, there is no viscous (dashpot) element in the main branch of the free body diagram shown in Figure 4.3.1. Equation 4.3.3 gives the stress-strain relationship in this main branch, where k_r is the relaxed stiffness of the polypyrrole/Pt helix composite.

The effect of the strain generation due to electrochemical processes is shown in Equation 4.3.4. The approach used here to add the electrochemical strain generator ($\varepsilon_{ech}(t)$) in series with the main branch spring element has been previously verified by De Rossi (Della Santa et al., 1997b, Della Santa et al., 1997c, Mazzoldi et al., 2000).

$$\varepsilon_{ech}(t) = \varepsilon(t) - \varepsilon_r(t)$$

Equation 4.3.4

Equation 4.3.5 is the Laplace transform of Equation 4.3.2 (b), which contains the initial conditions of both strains and strain rates. The Laplace Transform is needed to solve the viscoelastic ODE of the actuator, because modelling the response of the system to any external excitation (strain or stress) is the aim of the current research. Although the response of this linear system to standard and simple step excitation (creep and stress-relaxation) is available in viscoelastic textbooks, the aim of the present research is to develop a comprehensive model which can simulate the actuator response to any desired input. The strain as a function of the Laplace parameter ('s') for each branches is then:

$$\varepsilon_i(s) = \frac{s\eta_i \cdot \varepsilon(s) - \eta_i \cdot \varepsilon(0) + \eta_i \cdot \dot{\varepsilon}_i(0)}{k_i + s\eta_i}$$

Equation 4.3.5

This expression is derived using Transforms 1 and 2 given in Table A- 1 (Appendix A).

By substituting Equation 4.3.5 in Equation 4.3.2a, the following Equation 4.3.6 is obtained.

$$\sigma_i(s) = \frac{s\eta_i \cdot k_i \cdot \varepsilon(s) - \eta_i \cdot k_i \cdot \varepsilon(0) + \eta_i \cdot k_i \cdot \dot{\varepsilon}_i(0)}{k_i + s\eta_i}$$

Equation 4.3.6

Equation 4.3.7 is the Laplace transform of Equation 4.3.4 substituted into Equation 4.3.3.

$$\sigma_r(s) = k_r \cdot (\varepsilon(s) - \varepsilon_{ech}(s))$$

Equation 4.3.7

Using Transform 1 from Table A- 1.

Equation 4.3.8 is the governing equation of the viscoelastic system, which is calculated by substitution of Equation 4.3.6 and Equation 4.3.7 in Equation 4.3.1.

$$\left(\sum_{i=1}^n \frac{s.\eta_i.k_i.\varepsilon(s) - \eta_i.k_i.\varepsilon(0) + \eta_i.k_i.\varepsilon_i(0)}{k_i + s.\eta_i} \right) + k_r.(\varepsilon(s) - \varepsilon_{ech}(s)) = \sigma(s) \quad \text{Equation 4.3.8}$$

This equation contains $(2n+1)$ parameters that can be determined for a specified material by applying some standard tests, which are described in the next section. This analysis has considered the viscoelastic behaviour of the PPy/Pt helix composite at a single, fixed electrochemical potential. Thus, the ‘passive’ viscoelastic behaviour of the actuator is modelled in the following section. The ‘active’ viscoelastic behaviour is considered in Chapter 5, where the changing potential may alter the viscoelastic parameters. To model the passive viscoelastic behaviour, the following constraints are applied in Equation 4.3.9 where the electrochemically generated strain is always zero (potential does not change) and the strains in all spring-dashpot branches are zero at time zero:

$$\varepsilon_{ech}(t) = 0 \quad \& \quad \varepsilon(0) = \varepsilon_i(0) \quad \text{Equation 4.3.9}$$

4.3.1. The stress-strain test case

The essential parameter of the stress-strain curve, Young’s modulus, is predictable by the model given in Equation 4.3.8. Assuming the stress-strain experiment involves the input strain as a ramp function given by Equation 4.3.10 in which ε_{ramp} is the slope of the ramp ($\varepsilon(t) = \varepsilon_{ramp}.t$) and converted to Laplace space using transform 8 in Table A- 1. Substituting this expression in Equation 4.3.8 gives the value of stress by Equation 4.3.11.

$$\varepsilon(s) = \frac{\varepsilon_{ramp}}{s^2} \quad \text{Equation 4.3.10}$$

$$\sum_{i=1}^n \frac{s.\eta_i.k_i.\mathcal{E}(s)}{k_i + s.\eta_i} + k_r.\mathcal{E}(s) = \sigma(s) \quad \text{Equation 4.3.11}$$

$$\sum_{i=1}^n \frac{\eta_i.k_i.\mathcal{E}_{ramp}}{s.(k_i + s.\eta_i)} + \frac{k_r.\mathcal{E}_{ramp}}{s^2} = \sigma(s)$$

$$\sigma(t) = \left(\sum_{i=1}^n 2.\eta_i.e^{-\frac{k_i}{2\eta_i}.t}.\sinh\left(\frac{k_i}{2\eta_i}.t\right) + k_r.t \right) \mathcal{E}_{ramp} \quad \text{Equation 4.3.12}$$

The inverse Laplace transformation then gives the stress as a function of time, as shown in Equation 4.3.12. The Young's modulus after time t is defined in Equation 4.3.13,

$$\text{Young's Modulus : } E = \frac{\sigma(t)}{\mathcal{E}(t)} \quad \text{Equation 4.3.13}$$

Consequently, the value of Young's modulus is computed in Equation 4.3.14.

$$E = \frac{\sum_{i=1}^n 2.\eta_i.e^{-\frac{k_i}{2\eta_i}.t}.\sinh\left(\frac{k_i}{2\eta_i}.t\right)}{t} + k_r \quad \text{Equation 4.3.14}$$

This equation shows that the Young's modulus is equal to the relaxed stiffness coefficient plus a positive value, which decreases with increasing t (time) over the stress-strain experiment's duration. The modulus approaches the relaxed stiffness coefficient as t approaches infinity which is expected since PPy is a cross-linked polymer and does not 'flow' even after a long time. The duration of the stress-strain experiment has a significant role in determining the value of the modulus. Predictions from Equation 4.3.14 are given in Figure 4.3.4.

4.3.2. Stress Relaxation Case

In this case, a step isometric strain is the system input and the stress response is defined as the output. Equation 4.3.15 is the input strain signal in Laplace space in which ε_{step} is the step amplitude, as explained in transform 7 given in Table A- 1 (Appendix A).

$$\varepsilon(s) = \frac{\varepsilon_{step}}{s} \quad \text{Equation 4.3.15}$$

The value of response stress is shown in Equation 4.3.16 by substitution of Equation 4.3.15 and Equation 4.3.9 into Equation 4.3.8.

$$\sigma(s) = \left(\sum_{i=1}^n \frac{\varepsilon_{step} \cdot k_i}{s + \frac{k_i}{\eta_i}} \right) + \frac{\varepsilon_{step} \cdot k_r}{s} \quad \text{Equation 4.3.16}$$

The value of stress is computed from the inverse Laplace transforms in Equation 4.3.17 using transform 1 and 2 from Table A- 1 (Appendix A).

$$\sigma(t) = \varepsilon_{step} \cdot \left(\left(\sum_{i=1}^n k_i \cdot e^{-\frac{k_i}{\eta_i} t} \right) + k_r \right) \quad \text{Equation 4.3.17}$$

The initial and final values of the response stress are calculated by using the Final Value and Initial Value Theorem, (see Appendix A), giving Equation 4.3.18 and Equation 4.3.19.

$$\lim_{t \rightarrow \infty} (\sigma(t)) = \lim_{s \rightarrow 0} (s \cdot \sigma(s)) = \quad \text{Equation 4.3.18}$$

$$\lim_{s \rightarrow 0} \left(\left(\sum_{i=1}^n \frac{s \cdot \varepsilon_{step} \cdot k_i}{s + \frac{k_i}{\eta_i}} \right) + \varepsilon_{step} \cdot k_r \right) = \varepsilon_{step} \cdot k_r$$

$$\lim_{t \rightarrow 0}(\sigma(t)) = \lim_{s \rightarrow \infty}(s \cdot \sigma(s)) = \text{Equation 4.3.19}$$

$$\lim_{s \rightarrow \infty} \left(\left(\sum_{i=1}^n \frac{s \cdot \varepsilon_{step} \cdot k_i}{s + \frac{k_i}{\eta_i}} \right) + \varepsilon_{step} \cdot k_r \right) = \varepsilon_{step} \cdot \left(\left(\sum_{i=1}^n k_i \right) + k_r \right)$$

Figure 4.3.2 is the schematic diagram of this function for a system with one Maxwell block. The stress relaxes from the initial value, determined by the sum of all the spring elements (Equation 4.3.19), to a constant value determined by k_r (Equation 4.3.18).

Figure 4.3.2 is derived using the Laplace transformation method described above to solve the ODE of Equation 4.3.16. The exponential decay in stress at constant strain as shown in this figure exhibits the same shape as that given in textbook descriptions of stress relaxation in a Maxwell element.

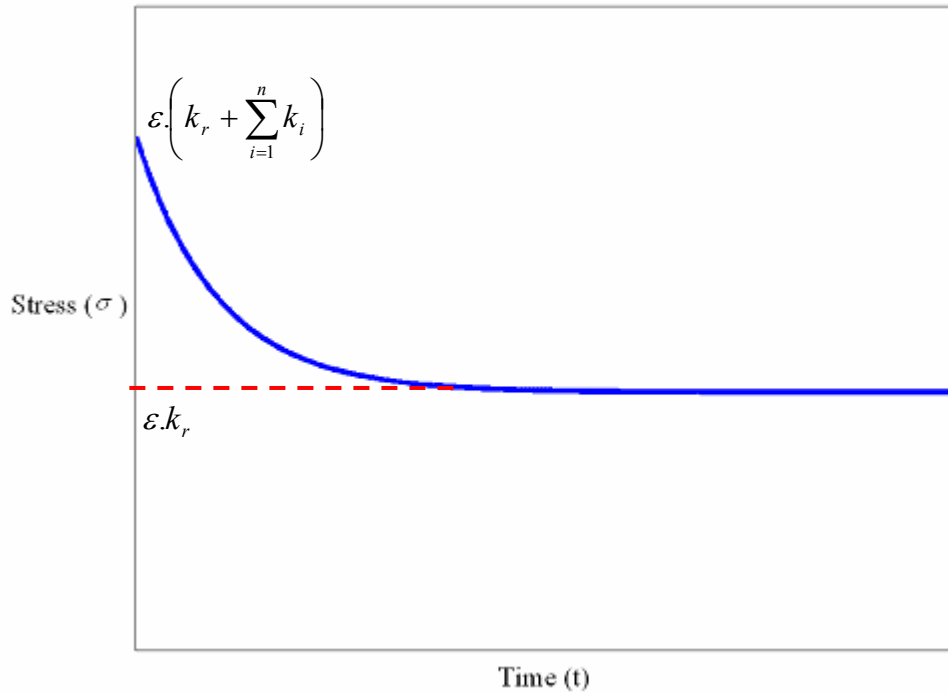


Figure 4.3.2. Schematic response to Stress-Relaxation test.

4.3.3. Creep Case

In a creep test, the isotonic step stress with step amplitude of σ_{step} is assumed as the input signal as shown in Equation 4.3.20 which again uses the Laplace space to describe the unit stress step (transform 7 in Table A- 1).

$$\sigma(s) = \frac{\sigma_{step}}{s} \quad \text{Equation 4.3.20}$$

Equation 4.3.21 is the result of substitution of Equation 4.3.20 and Equation 4.3.9 in Equation 4.3.8.

$$\left(\sum_{i=1}^n \frac{s \eta_i k_i \mathcal{E}(s)}{k_i + s \eta_i} \right) + k_r \mathcal{E}(s) = \frac{\sigma_{step}}{s} \quad \text{Equation 4.3.21}$$

Re-arranging Equation 4.3.21 then gives the expression for strain in Laplace transform (Equation 4.3.22):

$$\mathcal{E}(s) = \frac{\sigma_{step}}{s \cdot \left(\sum_{i=1}^n \frac{s \eta_i k_i}{k_i + s \eta_i} + k_r \right)} \quad \text{Equation 4.3.22}$$

If the number n is set to 1, the inverse Laplace transform using transforms 1 and 2 (Table A- 1) is given by Equation 4.3.23.

$$n = 1 \Rightarrow \quad \text{Equation 4.3.23}$$

$$\mathcal{E}(t) = \sigma_{step} \cdot \left(\frac{1}{k_r} - \frac{k_1}{k_r \cdot (k_r + k_1)} \cdot e^{\left(-\frac{k_r k_1}{\eta_1 (k_r + k_1)} t \right)} \right)$$

Equation 4.3.24 and Equation 4.3.25 show the final and initial values, respectively.

$$\left. \begin{array}{l} n=1 \\ t=0 \end{array} \right\} \Rightarrow \varepsilon(t) = \sigma_{step} \cdot \left(\frac{1}{k_r} - \frac{k_1}{k_r \cdot (k_r + k_1)} \right) = \sigma_{step} \cdot \left(\frac{k_r + k_1 - k_1}{k_r \cdot (k_r + k_1)} \right) = \sigma_{step} \cdot \left(\frac{1}{k_r + k_1} \right) \quad \text{Equation 4.3.24}$$

$$\left. \begin{array}{l} n=1 \\ t=\infty \end{array} \right\} \Rightarrow \varepsilon(t) = \sigma_{step} \cdot \left(\frac{1}{k_r} \right) \quad \text{Equation 4.3.25}$$

Therefore, the response for the system containing one Maxwell block is as shown in Figure 4.3.3. The strain increases from an initial value of Equation 4.3.24 to a constant value, again determined by k_r (Equation 4.3.25).

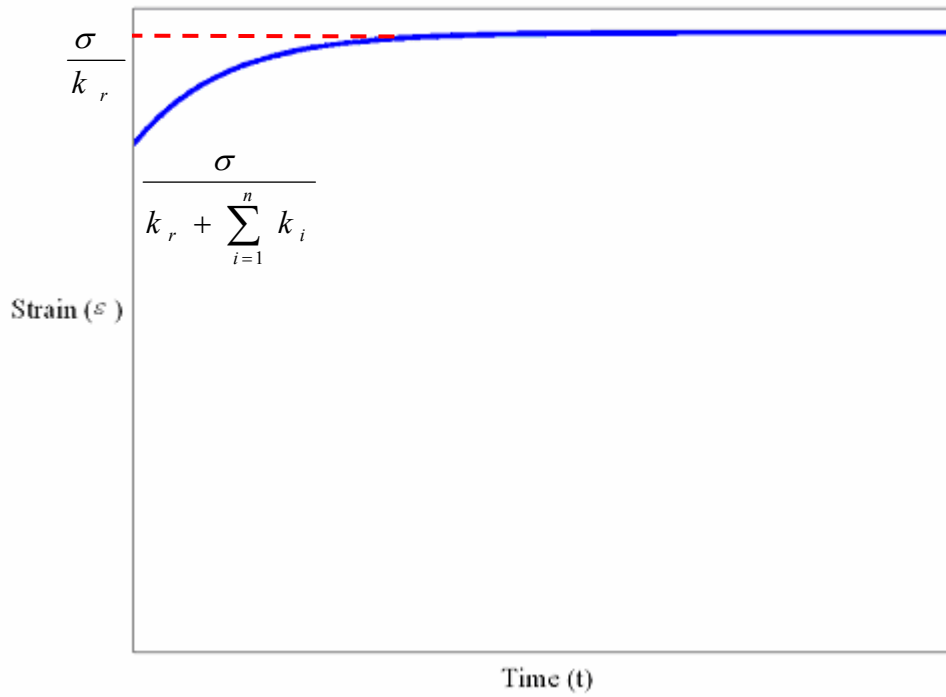


Figure 4.3.3. Schematic response to Creep test.

The values in Equation 4.3.26 and Equation 4.3.27 are the final and initial values of the strain response to isotonic stress input for systems involving n Maxwell elements.

$$\lim_{t \rightarrow \infty} (\varepsilon(t)) = \lim_{s \rightarrow 0} (s \cdot \varepsilon(s)) = \text{Equation 4.3.26}$$

$$\lim_{s \rightarrow 0} \left(\frac{\sigma_{step}}{\left(\sum_{i=1}^n \frac{s \cdot \eta_i \cdot k_i}{k_i + s \cdot \eta_i} \right) + k_r} \right) = \frac{\sigma_{step}}{k_r}$$

$$\lim_{t \rightarrow 0} (\varepsilon(t)) = \lim_{s \rightarrow \infty} (s \cdot \varepsilon(s)) = \text{Equation 4.3.27}$$

$$\lim_{s \rightarrow \infty} \left(\frac{\sigma_{step}}{\left(\sum_{i=1}^n \frac{s \cdot \eta_i \cdot k_i}{k_i + s \cdot \eta_i} \right) + k_r} \right) =$$

$$\lim_{s \rightarrow \infty} \left(\frac{\sigma_{step}}{\left(\sum_{i=1}^n \frac{\eta_i \cdot k_i}{\frac{k_i}{s} + \eta_i} \right) + k_r} \right) = \frac{\sigma_{step}}{\left(\sum_{i=1}^n k_i \right) + k_r}$$

Equation 4.3.23, Equation 4.3.24, Equation 4.3.26 and Equation 4.3.27 demonstrate that both the stress-relaxation test and the creep test enable the evaluation of the relaxed stiffness coefficient (k_r) from the steady state test conditions and the total stiffness coefficient ($k_t = k_1 + k_2 + \dots + k_n + k_r$) at the initial point of the experiment.

4.3.4. Sinusoidal excitation case

A practical method of studying the viscoelastic properties is to apply an isometric swift sinusoidal strain signal as an input and then to measure the transfer function of the system with strain as input and stress as output. The transfer function would be the complex modulus of the polymer containing a real part (storage modulus, E') and an imaginary part (loss modulus, E''). In Equation 4.3.28, the modulus has been calculated using Equation 4.3.8 and Equation 4.3.9.

$$E(s) = \frac{\sigma(s)}{\varepsilon(s)} = \left(\sum_{i=1}^n \frac{s \eta_i k_i}{k_i + s \eta_i} \right) + k_r \quad \text{Equation 4.3.28}$$

For a steady state sinusoidal input Equation 4.3.28 the response is easily derived by replacing 's' by ' $j\omega$ ' which is a fundamental result of the Laplace transform theory as explained in Appendix A:

$$E(j\omega) = \left(\sum_{i=1}^n \frac{j\omega \eta_i k_i}{k_i + j\omega \eta_i} \right) + k_r \quad \text{Equation 4.3.29}$$

which leads to the familiar result:

$$E = E' + jE'' \quad \text{Equation 4.3.30}$$

The storage and loss modulus is calculated in Equation 4.3.31 as a function of the viscoelastic parameters of the material, stiffness and viscosity coefficients. Obviously they are dependent on the excitation frequency and curve fitting to storage and loss modulus results can lead to estimation of principal viscoelastic parameters, stiffness and viscosity coefficients.

$$E'(\omega) = \left(\sum_{i=1}^n \frac{(\omega \eta_i)^2 k_i}{k_i^2 + (\omega \eta_i)^2} \right) + k_r \quad \text{Equation 4.3.31}$$

$$E''(\omega) = \sum_{i=1}^n \frac{\omega \eta_i k_i^2}{k_i^2 + (\omega \eta_i)^2}$$

In Equation 4.3.32 and Equation 4.3.33, it is shown that the initial and final values of storage modulus are equal to relaxed and total stiffness coefficients, respectively.

$$E'(\omega \rightarrow 0) = k_r \quad \text{Equation 4.3.32}$$

$$E''(\omega \rightarrow 0) = 0$$

$$E'(\omega \rightarrow \infty) = \left(\sum_{i=1}^n k_i \right) + k_r \quad \text{Equation 4.3.33}$$

$$E''(\omega \rightarrow \infty) = 0$$

In the case of using one viscoelastic block, the maximum value of the loss modulus will be as follows,

$$\max\{E''\}_{\omega=\frac{k_1}{\eta_1}} = \frac{k_1}{2} \quad \text{Equation 4.3.34}$$

$$E'_{\omega=\frac{k_1}{\eta_1}} = k_r + \frac{k_1}{2}$$

The schematic diagrams of the loss and storage modulus are shown in Figure 4.3.4.

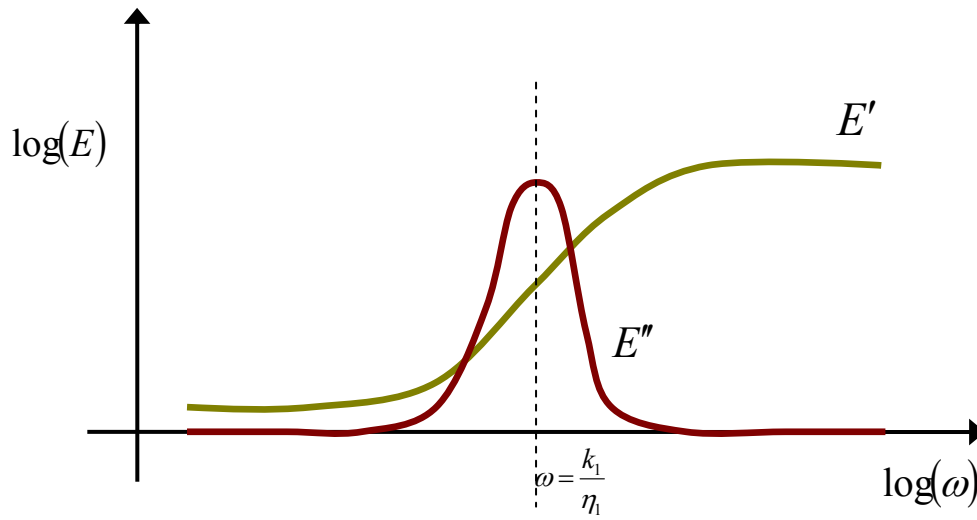


Figure 4.3.4 Schematic diagram of the storage and loss modulus vs. frequency.

The above derivations establish the general equation describing the viscoelastic response of a system described by Figure 4.3.1. The general equation has been solved for common test conditions (stress-relaxation, creep and sinusoidal excitation) using Laplace transformations. The same techniques can be used to solve for practically any input condition. In the following sections, the derived equations will be used to model the actuation response of PPy/Pt helix tube actuators.

4.3.5. Active generated strain term

Several researchers (Mazzoldi et al., 2000, Della Santa et al., 1997b, Della Santa et al., 1997a, Chiarelli et al., 1995, Madden, 2000, Madden et al., 2001a) have shown that

electrochemical generated strain can be assumed proportional to the density of charge transferred to the polymer surface described as in Equation 4.3.35.

$$\varepsilon_{ech}(t) = \alpha \cdot \rho(t) \quad \text{Equation 4.3.35}$$

As mentioned above, De Rossi et al have shown that it is appropriate to include the electrochemical generated strain ε_{ech} in series with k_r to model conducting polymer actuators (Della Santa et al., 1997a, Mazzoldi et al., 2000).

To determine the strain to charge ratio in PPy helix tube actuator it is necessary to unambiguously separate the ε_{ech} component from the overall strain. To calculate this strain from experimental data, Equation 4.3.8 has been used as shown in Equation 4.3.36.

$$\sum \frac{s \cdot \eta_i \cdot k_i \cdot \varepsilon(s)}{k_i + s \cdot \eta_i} + k_r \cdot (\varepsilon(s) - \varepsilon_{ech}(s)) = \sigma(s) \quad \text{Equation 4.3.36}$$

Now the ε_{ech} term is not zero, but the viscoelastic parameters are assumed to be those obtained at a constant electrochemical potential. The above equation has been re-arranged to find the electrochemical strain generated as shown in Equation 4.3.37 and Equation 4.3.38.

$$k_r \cdot \varepsilon_{ech}(s) = \varepsilon(s) \cdot \left(\sum \frac{s \cdot \eta_i \cdot k_i}{k_i + s \cdot \eta_i} + k_r \right) - \sigma(s) \quad \text{Equation 4.3.37}$$

$$\varepsilon_{ech}(s) = \varepsilon(s) \cdot \left(\sum \frac{k_i}{k_r} \cdot \frac{s \tau_i}{1 + s \tau_i} \right) + \varepsilon(s) - \frac{\sigma(s)}{k_r} \quad \text{Equation 4.3.38}$$

$$\tau_i = \frac{\eta_i}{k_i}$$

Considering Equation 4.3.38, the term $\varepsilon(s) - \sigma(s)/k_r$ is the total strain minus the strain caused by the applied stress after the system has achieved the fully relaxed state. When a constant stress is applied, the experimental procedure is as shown in Figure 4.3.5. Since the frequency of stimulation during typical CV experiments is low (about 0.01 Hz) the term $s\tau_i/(1+s\tau_i)$ approaches zero, which allows the total strain to be simplified to $(\varepsilon(s) - \sigma(s)/k_r)$ during stimulation and this simplification allows the electrochemical strain to be calculated as:

$$\varepsilon_{ech} \cong \varepsilon - \sigma/k_r$$

Equation 4.3.39

Obviously, if the stimulation frequency had been higher then a complicated calculation would be needed to measure the exact electrochemical strain generated (ε_{ech}). Equation 4.3.38 and Equation 4.3.39 show that the experimental method used to measure “Active Electrochemical Strain” is reasonable and accurate. These equations prove that the “Active Electrochemical Strain” can be measured from the creep base-line precisely when the creep response after initial application of the external stress has relaxed.

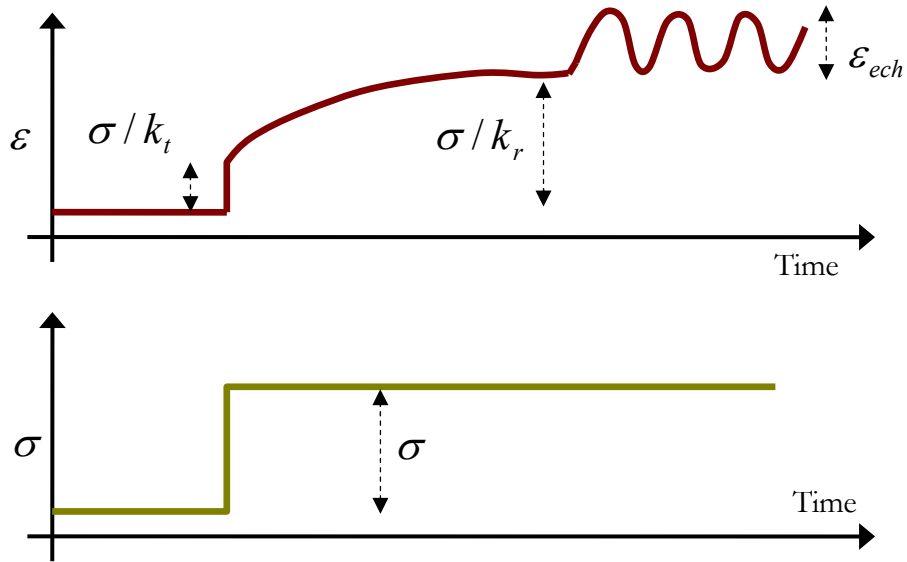


Figure 4.3.5 Calculation method of electrochemical strain

$$(k_t = k_r + \sum_{i=1}^n k_i).$$

The above theoretical treatment shows that a viscoelastic material will show a strain response for some time after the external load has been applied. For viscoelastic actuators, it is important to be able to model the stress-induced response over time, since this strain may be occurring at the same time as the voltage-induced actuation. The viscoelastic behaviour of PPy helix tube actuators has not previously been studied. It is, therefore, not known how important the viscoelastic response of the PPy helix tube is to the overall strain occurring during typical actuator experiments. The aim of this chapter is to measure the viscoelastic behaviour of the PPy helix tube and include the viscoelastic response in the predictive model (primary model) introduced in chapter 3. The new model is called the ‘passive improvement’ model.

4.4. Experimental results

Seven stress-relaxation tests were performed with different isometric strain inputs. As described in the experimental section, the strain inputs covered the range known to be important for actuation testing. Also, the polymer was tested in electrolyte (0.1 M TBA-PF₆ in PC) and held at 0 V (vs. Ag/AgNO₃ ref.). The viscoelastic behaviour of the helix tube under these conditions was assumed to hold for all voltages. The situation where the mechanical properties change with the applied voltage is considered in chapter 5. The viscoelastic model, which was described in Equation 4.3.8, was utilized to explain the viscoelastic behaviour of a PPy helix tube actuator. Experiments were carried out to characterise the viscoelastic parameters of the actuator in wet and at constant potential ($\varepsilon_{ech}(t) = 0$). The curve fitting technique applied to calculate the parameters used Trust-Region methods for Nonlinear Minimizing in the MATLAB[®] curve fitting toolbox; further information describing this method is referred to in references (Moré and Sorensen, 1983, Draper and Smith, 1998). The results of this section are used to build the viscoelastic model which will be used for simulation purpose in Section 4.5.

Initially, it was thought important to find the minimum number of Maxwell’s blocks to generate a good result with low computation time. Therefore, a set of data was fitted with different values of n , from 1 to 5. Figure 4.4.1 and Figure 4.4.2 show the Regression Factor, total stiffness and total damping coefficient vs. the number n . These graphs show that $n=3$ is the optimal value for the number of Maxwell’s blocks in the specified model. Very little change in the key parameters was achieved by using $n>3$, but the computation time increased markedly.

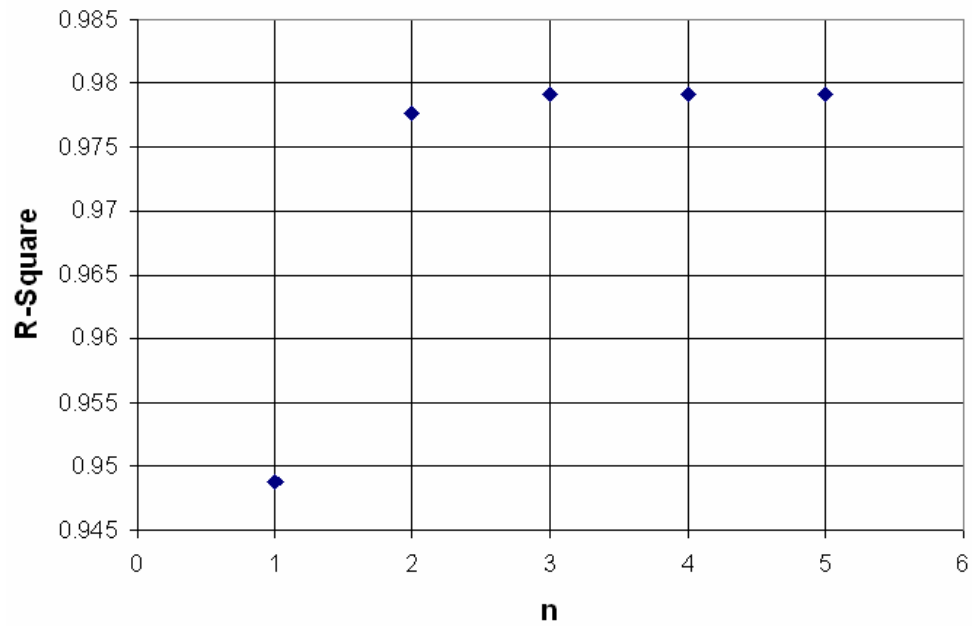


Figure 4.4.1 R-Square vs. number of Maxwell blocks in the model.

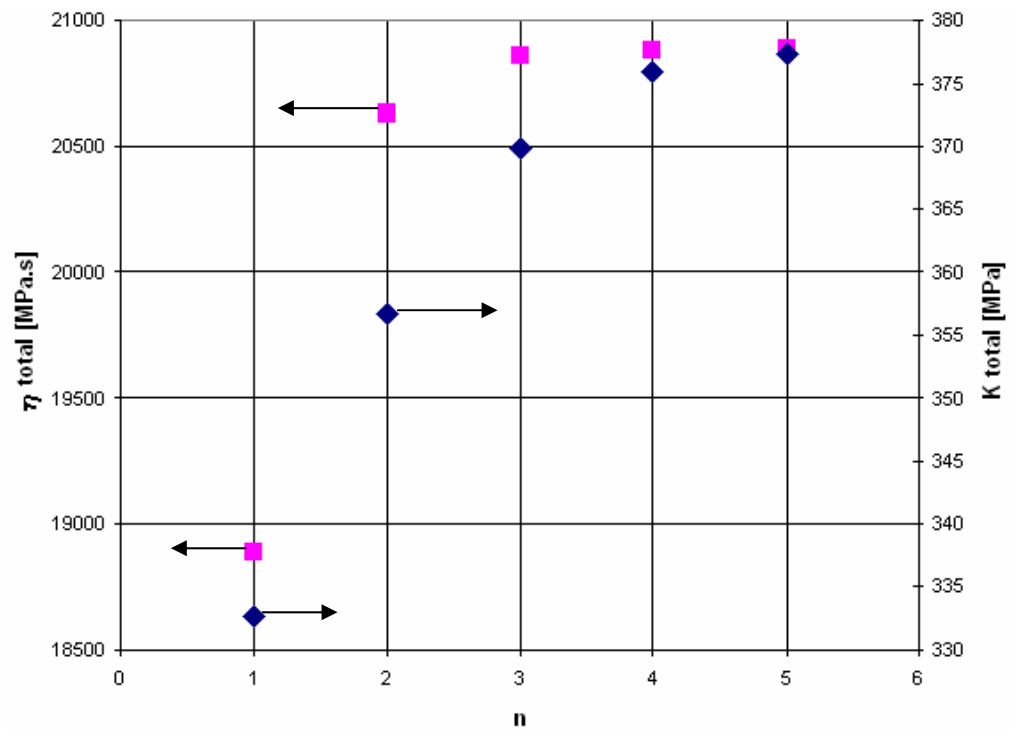


Figure 4.4.2 Total stiffness and total damping vs. number of Maxwell blocks in the model.

Next, the viscoelastic parameters of stiffness and damping coefficient were determined from stress relaxation tests at different input strain levels. For linear viscoelastic materials, these parameters are independent of the applied stress. However, as shown in Figure 4.4.3 total stiffness coefficient increases with increasing strain. This increase appeared linear with high regression factor (0.9782) in the strain range used in actuator tests (<1% initial strain). The residual stiffness (k_r) shows a similar trend with increasing input strain. The stiffness coefficients of the individual Maxwell elements are not strongly affected by the strain applied.

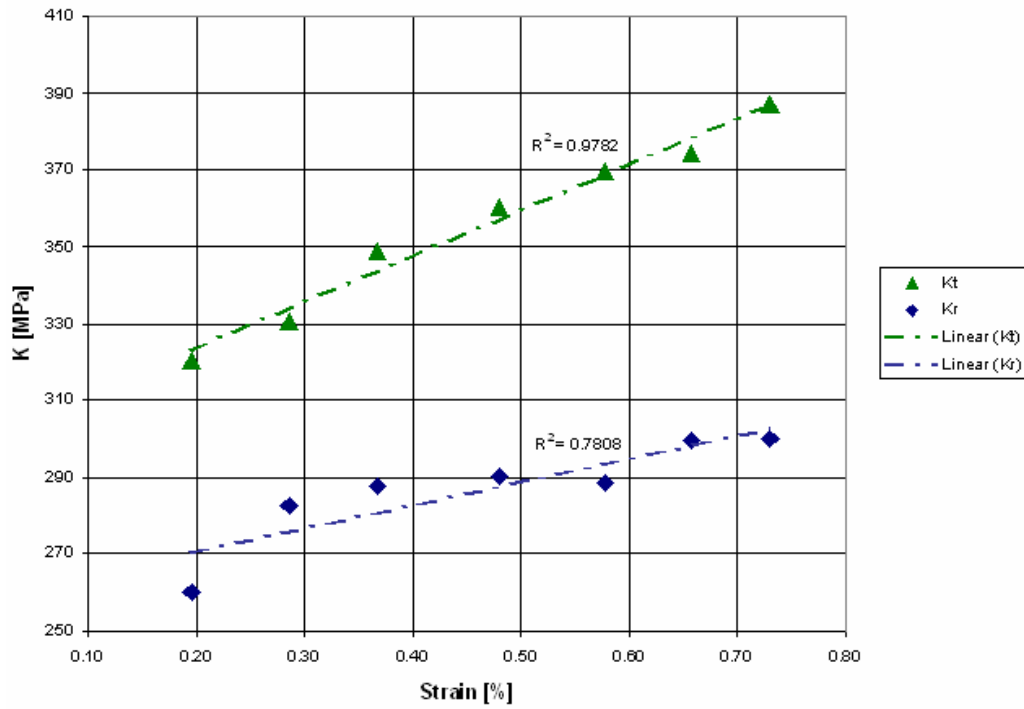


Figure 4.4.3 Total and Relaxed stiffness increase with increasing isometric strain applied during stress-relaxation experiment.

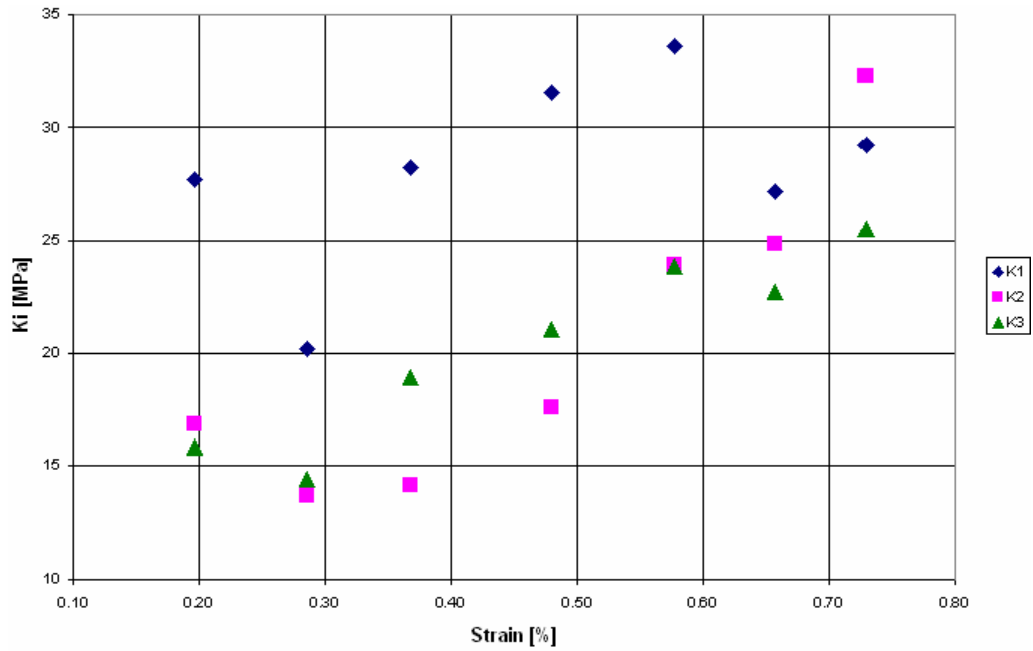


Figure 4.4.4 Maxwell's stiffness of 3 blocks with isometric strain.

The fitted parameters show that the PPy helix tube actuators become stiffer at higher input strains. The reason for this seemingly anomalous behaviour can be determined from the non-linear stress/strain curve for these materials (Figure 4.4.5). These curves are parabolic to strains of 1-2% due to the fact that these high aspect ratio fibres are not perfectly straight at zero strain. Thus, relatively large strains occur at small stresses due to the bending and straightening of the helix tube fibres. This non-linear stress-strain region extended to higher strains when longer fibres were used. As stated above, these actuators are used at initial strains of <1%. Thus, the modelling of the actuators must take this into account. Fortunately, the change in stiffness with strain is approximately linear, so the stiffness at any strain can be determined readily from the data given in Figure 4.4.3 and Figure 4.4.4.

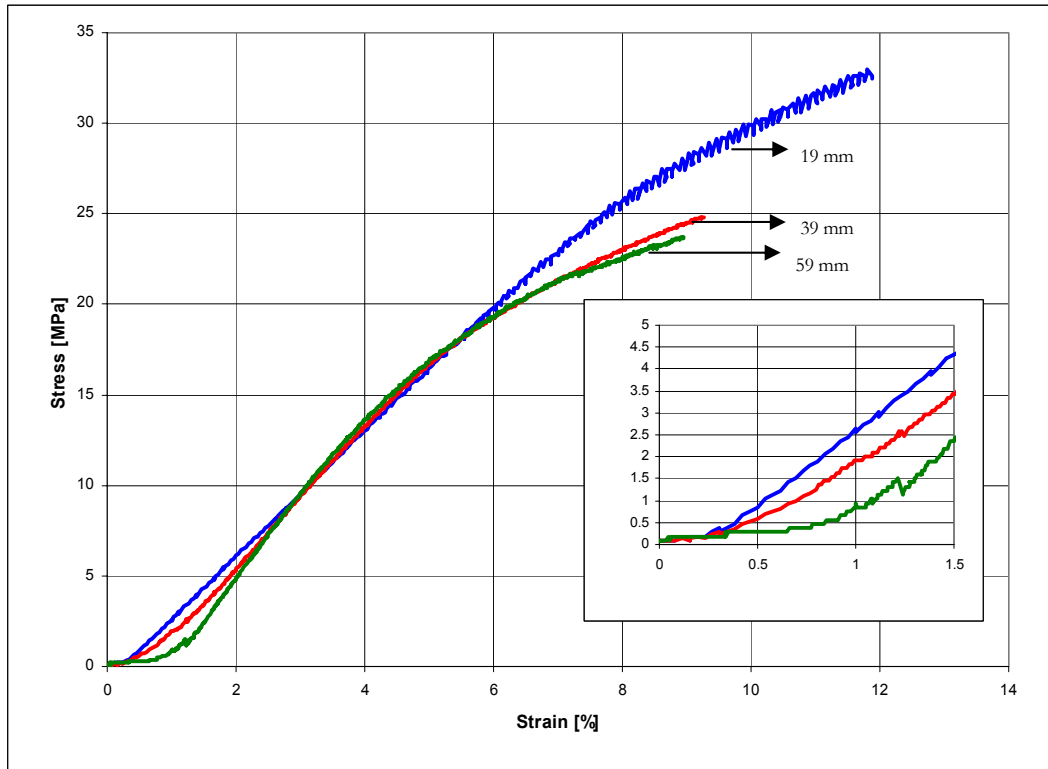


Figure 4.4.5. Stress-Strain curves for different lengths of actuators. Inset shows the low strain region in more detail.

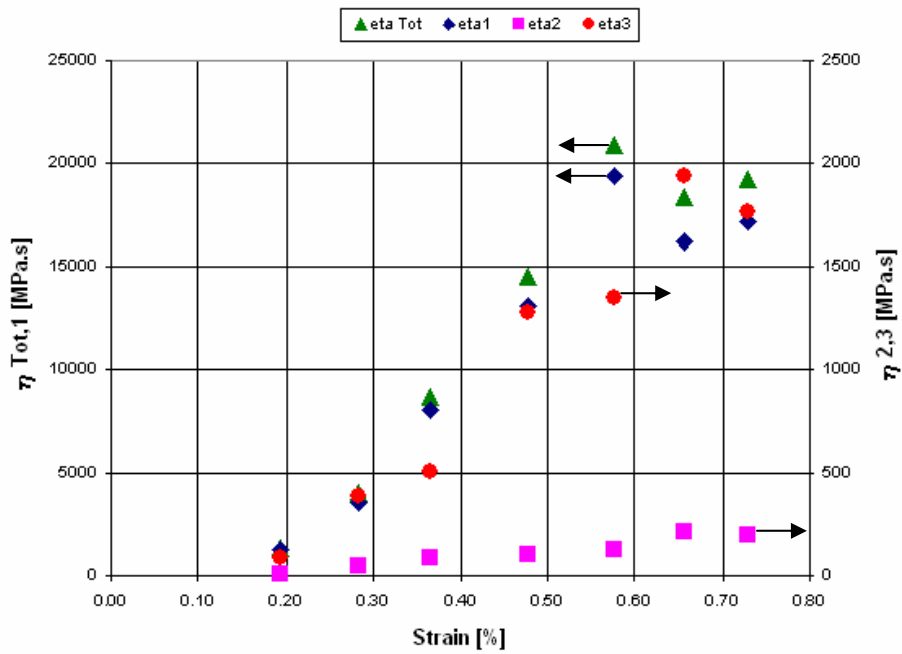


Figure 4.4.6 Total damping coefficient changing with isometric strain.

The damping coefficients are similarly affected by the magnitude of the input strain, as shown in Figure 4.4.6. Up to a strain of $\sim 0.6\%$ the damping coefficient increases and then remains approximately constant. The first Maxwell branch dominates the total damping, with smaller contributions from the third and second branches; note that different scales are used in Figure 4.4.6 for η_{tot}, η_1 and η_2, η_3 . The straightening of the helix tube fibre at small strains is likely to be the cause of the increasing damping coefficient at higher strains. In linear viscoelastic materials these coefficient are independent of strain. Fortunately in the present case, the damping coefficients change in an approximately linear fashion with strain. The linear relationship means that the coefficients can be readily calculated from the data given in Figure 4.4.6.

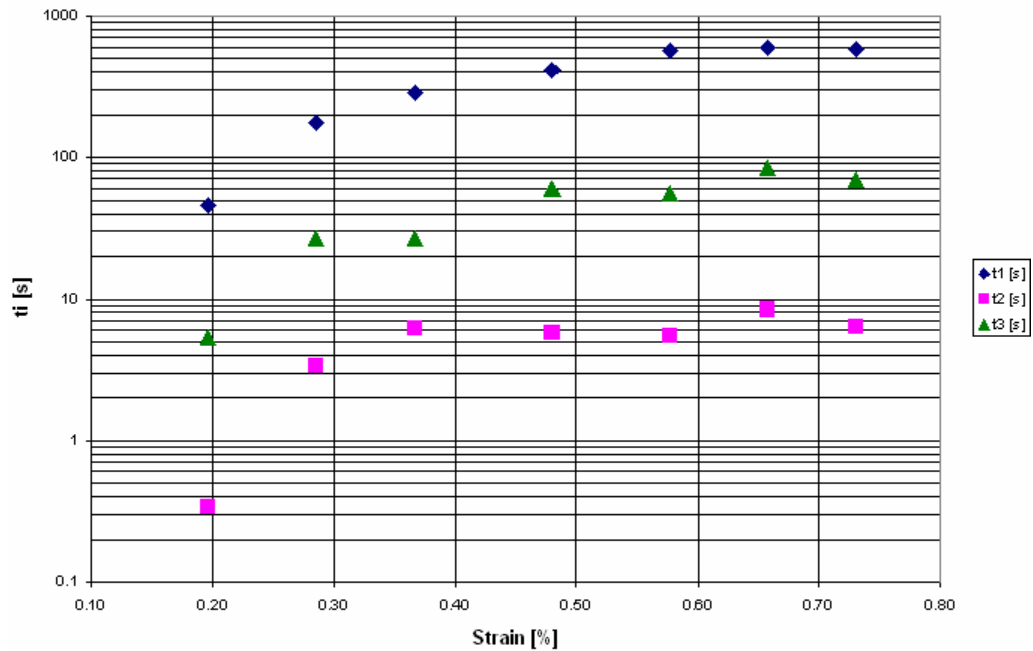


Figure 4.4.7 The time constants of each Maxwell block as a function of isometric step strain input (logarithmic scale).

Additionally, it would be useful to investigate the variation of the time constant parameters, which were computed using Equation 4.4.1.

$$\tau_i = \frac{\eta_i}{k_i}$$

Equation 4.4.1

The time constants depend on the applied strain since both the η and k terms are strain dependent. The relaxation times are rather long indicating that creep should not affect the helix tube actuators at fast switching speeds (e.g. >1 Hz). However creep will be important for slower processes, including DC control.

Table 4.4-1 The time constants of each Maxwell's block as a function of isometric step strain input.

Strain [%]	t1 [s]	t2 [s]	t3 [s]
0.20	45.65139	0.340462	5.300567
0.29	175.7065	3.402768	26.9508
0.37	286.9195	6.193503	26.85322
0.48	414.6882	5.835227	60.46512
0.58	576.6141	5.388471	56.62752
0.66	595.1417	8.473006	85.49383
0.73	588.2353	6.277485	69.28207

It is shown in Table 4.4-1 that the time constant parameters increase linearly up to a limit. The time constants are dominated by the change in damping coefficient with input strain.

4.5. ‘Passive Improvement’ Model

The modelling process has been carried out by setting up the model in state-space as shown in Equation 4.5.1, in which “x” is the state vector and “u” the input vector. The state space model provides a convenient and compact way to analyse systems with multiple inputs and outputs. The reason for transforming the second order Ordinary Differential Equation (ODE) of the electro-chemo-viscoelastic model of the actuator to a State Space representation is to reduce the order of the ODE to a set of first order ODE’s. State Space is routinely used in the analysis of high order systems and enables the simulation and solution of the differential equations in the time-domain using standard simulation programs and methods in numerical analysis such as Runge-Kutta, Adams-Bashforth-Moulton and Gear’s method. Further information about State-Space modelling is provided in Appendix B. The complexity of the analysis means that only one Maxwell block is used to model the PPy-Pt helix composite in the following section.

$$\begin{aligned}\dot{x}_{1 \times 1} &= A_{1 \times 1}x_{1 \times 1} + B_{1 \times 4}u_{4 \times 1} \\ y_{1 \times 1} &= x_{1 \times 1}\end{aligned}\tag{Equation 4.5.1}$$

As shown in Equation 4.5.2, the input vector contains four input parameters which are current (and integrated current) and external load signal (and derivative of external load).

$$x_{1 \times 1} = [\varepsilon] \quad \& \quad u_{4 \times 1} = \begin{bmatrix} \int idt \\ i \\ \sigma \\ \dot{\sigma} \end{bmatrix} \quad \text{Equation 4.5.2}$$

The parameters of Equation 4.5.1 have been calculated in Equation 4.5.3 using Equation 4.3.8 using just one Maxwell block in parallel with the main branch.

$$\begin{cases} \frac{s.\eta_1.k_1.\varepsilon(s)}{k_1 + s.\eta_1} + k_r.(\varepsilon(s) - \varepsilon_{ech}(s)) = \sigma(s) \\ \varepsilon_{ech}(t) = \alpha \int idt \end{cases}$$

$$\therefore s.\eta_1.k_1.\varepsilon(s) + k_r.(\varepsilon(s) - \varepsilon_{ech}(s))(k_1 + s.\eta_1) = \sigma(s).(k_1 + s.\eta_1)$$

$$\begin{aligned} \therefore \eta_1.k_1.\dot{\varepsilon}(t) + k_r.(\varepsilon(t) - \varepsilon_{ech}(t)).k_1 + k_r.(\dot{\varepsilon}(t) - \dot{\varepsilon}_{ech}(t)).\eta_1 \\ = \sigma(t).k_1 + \dot{\sigma}(t).\eta_1 \end{aligned}$$

$$\therefore \eta_1(k_1 + k_r)\dot{\varepsilon}(t) = -k_1k_r\varepsilon(t) + k_1k_r\varepsilon_{ech}(t) + \eta_1k_r\dot{\varepsilon}_{ech}(t) + \sigma(t).k_1 + \dot{\sigma}(t).\eta_1$$

$$\begin{aligned} \therefore \dot{\varepsilon}(t) = \frac{-k_1k_r}{\eta_1(k_1 + k_r)}\varepsilon(t) + \frac{k_1k_r}{\eta_1(k_1 + k_r)}\varepsilon_{ech}(t) + \frac{\eta_1k_r}{\eta_1(k_1 + k_r)}\dot{\varepsilon}_{ech}(t) + \\ \sigma(t).\frac{k_1}{\eta_1(k_1 + k_r)} + \dot{\sigma}(t).\frac{\eta_1}{\eta_1(k_1 + k_r)} \end{aligned}$$

$$A_{1 \times 1} = \left[\frac{-k_1k_r}{\eta_1(k_1 + k_r)} \right]$$

$$B_{1 \times 4} = \frac{1}{\eta_1(k_1 + k_r)} \cdot \begin{bmatrix} k_1k_r\alpha & \eta_1k_r\alpha & k_1 & \eta_1 \end{bmatrix}$$

$$\text{Equation 4.5.3}$$

As shown in Chapter 3, the strain to charge ratio (α) may be considered as a function of charge as shown in Figure 3.4.6 which is a characteristic of PPy/Pt helix tube. The dimensions of α and q must be changed from the dimensions used in Figure 3.4.6 to use in the modelling process in this section.

$$\begin{aligned}\alpha \left[\frac{\%}{mC} \right] &= \alpha \left[\frac{m^3}{C} \right] \cdot \frac{[C]}{10^3[mC]} \cdot \frac{100[\%]}{L_i A [m^3]} \\ q &= \int i dt \\ q[mC] &= Q \left[\frac{C}{m^3} \right] \cdot L_i A [m^3] \cdot \frac{10^3[mC]}{[C]} \\ L_i &= 58[mm] \\ A &= 2.6535 \times 10^{-2} [mm^2]\end{aligned}\tag{Equation 4.5.4}$$

In the previous section it was shown that the stiffness and viscosity parameters depend highly on the applied stress. The effect of external stress on the mechanical parameters is considered using a modulus to stress coefficient (β_k) and dummy parameters $k_{total,0}$ and $k_{total,0,0}$ in Equation 4.5.5.

$$\begin{aligned}k_{total,0} &= k_{total,0,0} + \beta_k \cdot \sigma \\ k_{total} &= k_{total,0}\end{aligned}\tag{Equation 4.5.5}$$

As shown in Figure 3.5.3, the pre-simulation data was used to estimate the parameters in Equation 4.5.6 and are measured for a particular actuator by conducting small stress-strain tests during cyclic voltammetry.

$$\begin{aligned}\beta_k &= 0.06786 \left[\frac{1}{\%} \right] \\ k_{total,0,0} &= 1.07 \left[\frac{MPa}{\%} \right] = 107[MPa]\end{aligned}\tag{Equation 4.5.6}$$

As explain later (in Section 5.4.2), the viscoelastic parameters can be assumed as a fraction of total stiffness coefficient, as shown in Equation 4.5.7

$$\begin{aligned}k_r &= \kappa \cdot k_{total} \\ k_1 &= (1 - \kappa) \cdot k_{total}\end{aligned}\tag{Equation 4.5.7}$$

In the viscoelastic model presented in this chapter the viscosity parameter is calculated from the time constant which also depends on the external load.

$$\eta_1 = \tau_1 \cdot k_1$$

$$\tau_1 = \tau_{1,0} + \beta_\tau \cdot \sigma$$

Equation 4.5.8

$$\begin{cases} \tau_{1,0} = 37.15 [\text{sec}] \\ \beta_\tau = 31.56 \left[\frac{\text{sec}}{\text{MPa}} \right] \end{cases}$$

The actuator used in this section had 58 mm length and was stimulated by applying sinusoidal voltages (-0.75 V \rightarrow +0.55 V) with different frequencies under different external loads 450 kPa, 3.25 MPa and 5.80 MPa. A summary of the calculation method is given in Figure 4.5.1.

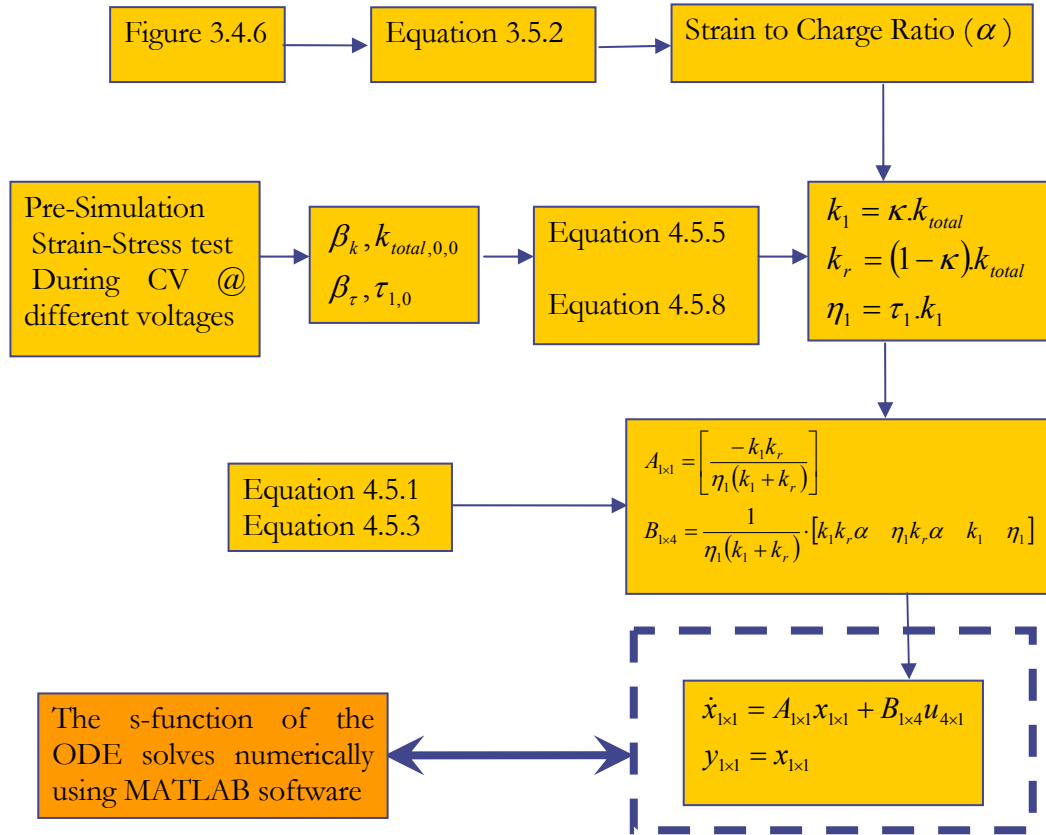


Figure 4.5.1. the flowchart of the solver program.

A comparison of the model predictions and experimental results is considered first for the low load case (450 kPa). As expected and shown in Figure 4.5.2 to Figure 4.5.4, the passive improvement result should not vary from the primary model output, because the external load was small and also the actuator experiment was started a long time after applying this load. The low load used here is found to be the minimum necessary to keep the actuator connected to the load measurement cell. Therefore, the influence of this load is incorporated into the strain to charge ratio master curve. Consequently, it is not surprising that the viscoelastic model behaves like the previous elastic model and no improvement is observed.

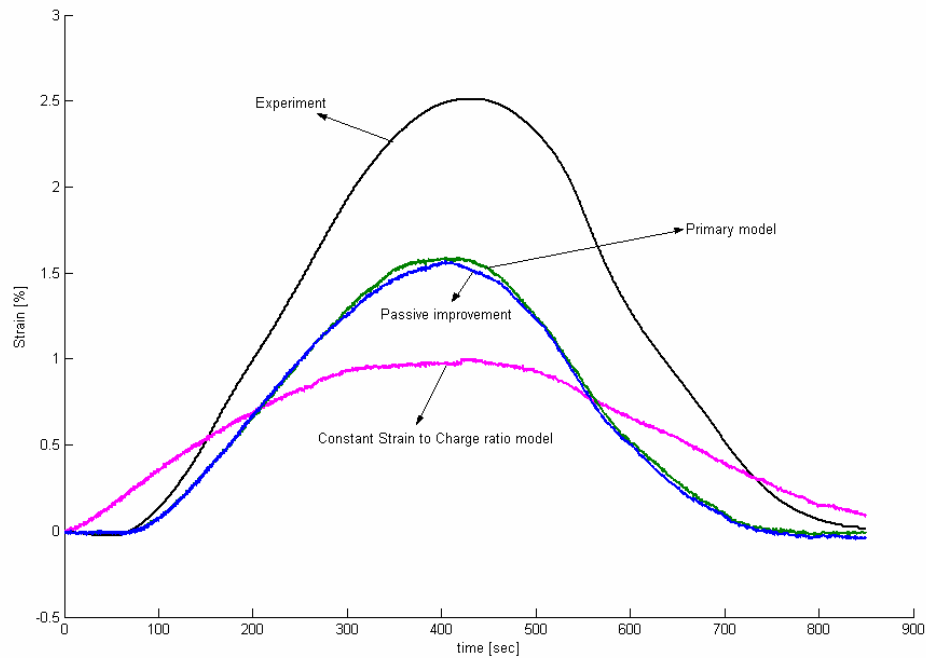


Figure 4.5.2 Stress 0.45 MPa and 1 mHz.

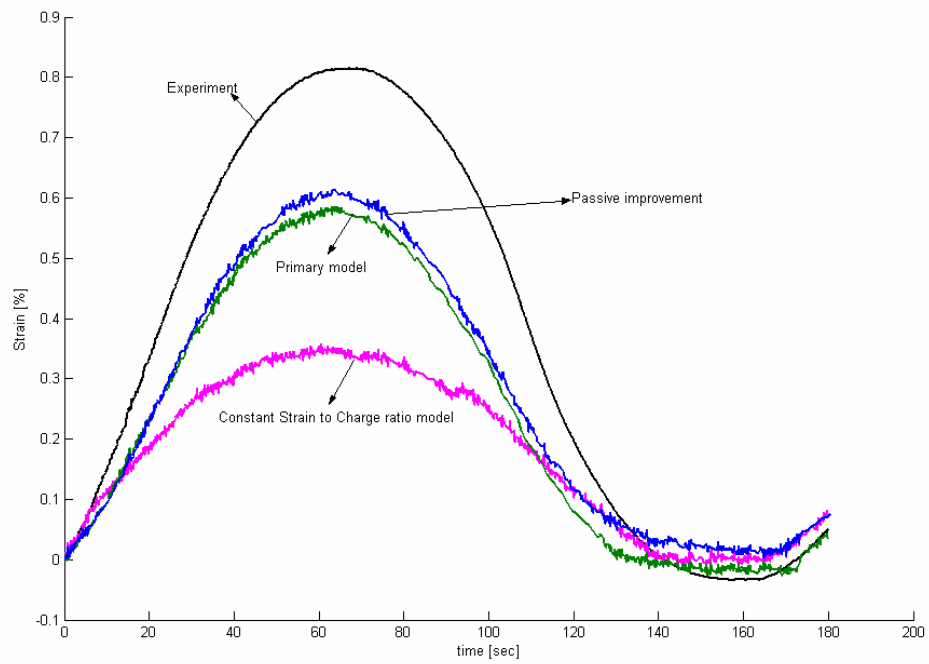


Figure 4.5.3 Stress 0.45 MPa and 5 mHz.

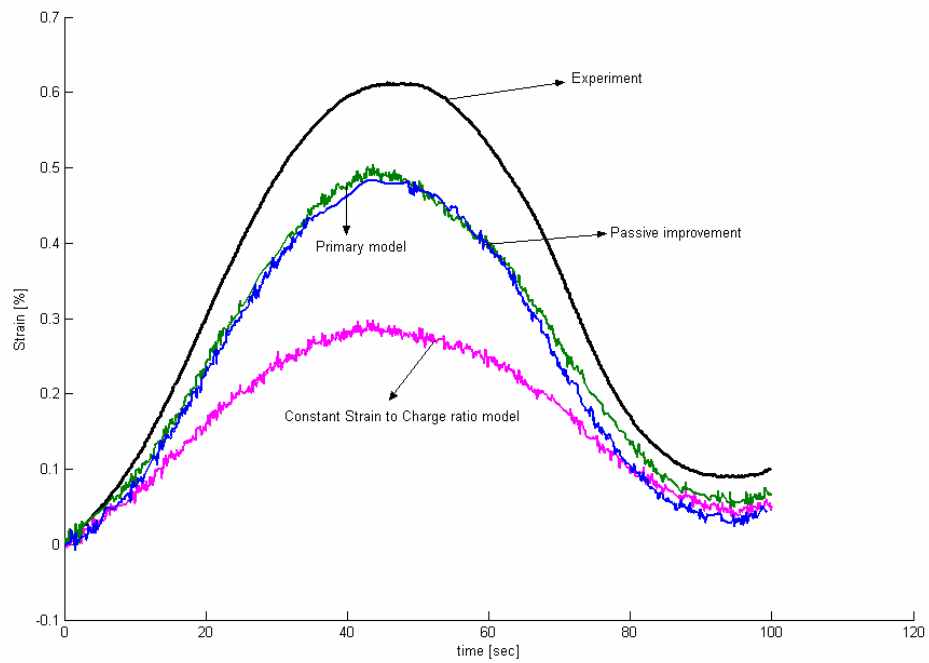


Figure 4.5.4 Stress 0.45 MPa and 10 mHz.

The situation is quite different, however, when higher loads were applied. As shown in the Figure 4.5.5 to Figure 4.5.7, the ‘passive improvement’ viscoelastic mechanical model was better able to predict the experimental results than the simple elastic model.

In all the experimental studies at higher loads, a non-recoverable strain was observed after the completion of the voltage cycle. This creep is due to the slow viscoelastic response of the polymer due to the increase in load. Incorporating the ‘passive improvement’ to the predictive model includes the stress-induced viscoelastic strain. A very close agreement between the ‘passive improvement’ model and the experimental results is seen in some cases (eg. Figure 4.5.5) and the general creep phenomenon is shown in all cases.

Some subtle effects were noted in the experimental data that were not well predicted by the ‘passive improvement’ model. At higher frequencies, for example, the strain first decreases after the maximum before showing a pronounced increase. The ‘passive improvement’ model generally shows a steady decrease after the maximum. This flaw in the model is noted particularly in Figure 4.5.6 and Figure 4.5.7 where the final strain is predicted to be higher than the experimental strain. These differences in predicted and actual strain may reflect the fact that the viscoelastic parameters change when the voltage is changed (recall that it has been assumed in the passive improvement model that the viscoelastic parameters measured at 0 V hold). In addition, the passive improvement model generally under-estimates the magnitude of the strain peak.

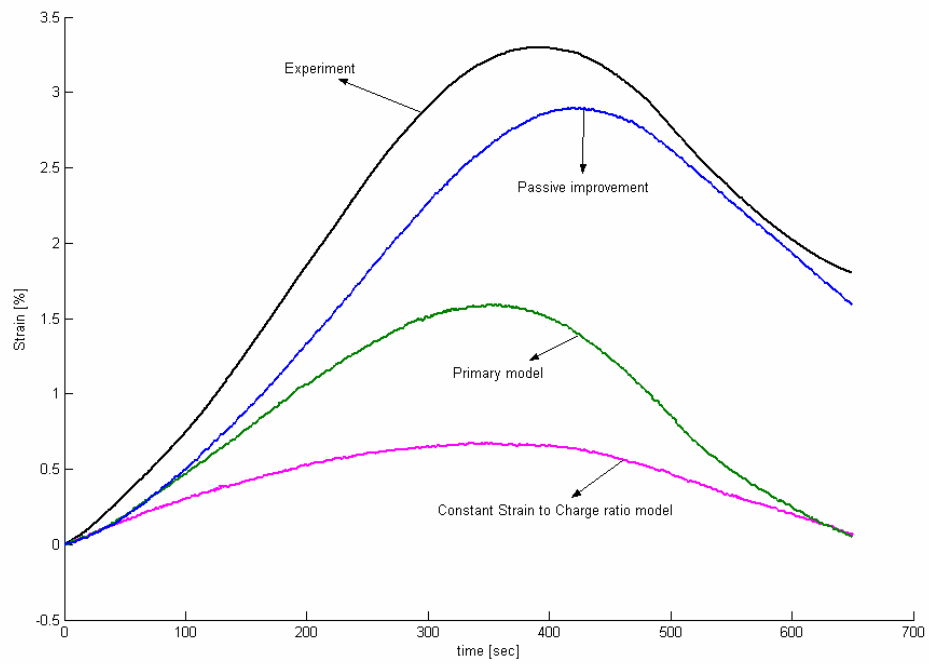


Figure 4.5.5 Stress 3.25 MPa and 1 mHz.

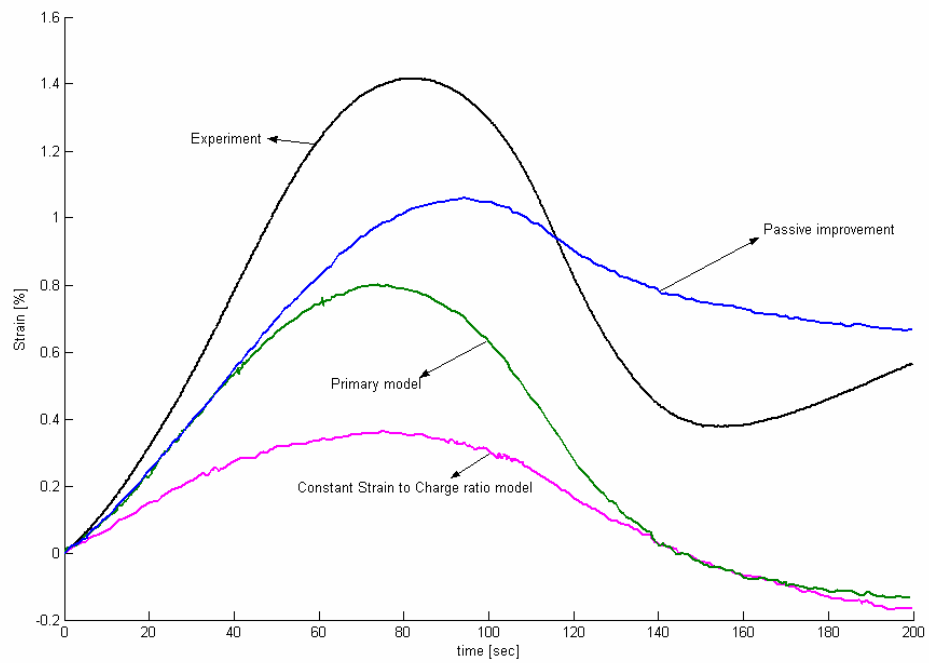


Figure 4.5.6 Stress 3.25 MPa and 5 mHz.

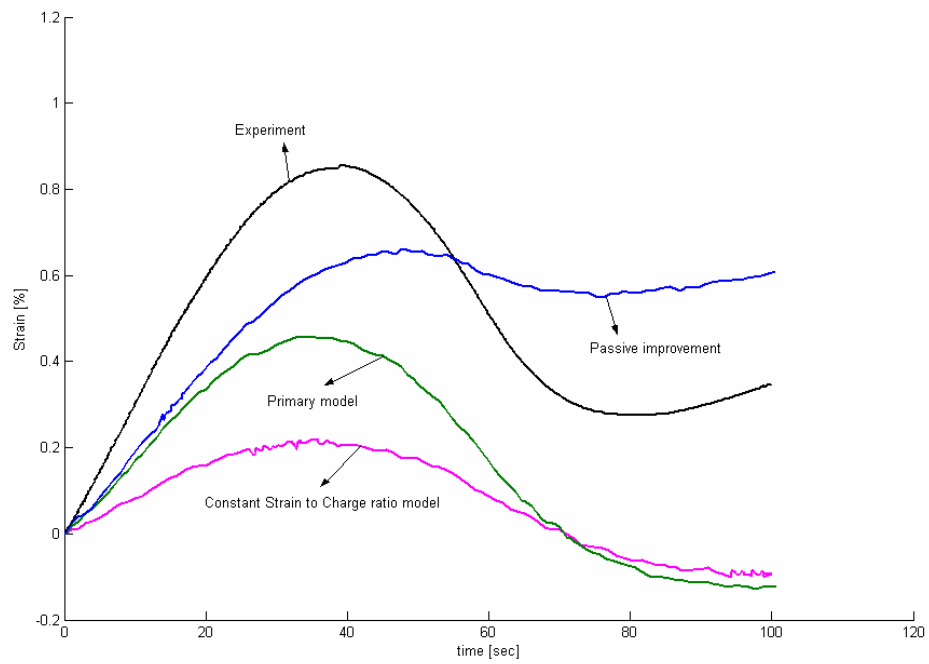


Figure 4.5.7 Stress 3.25 MPa and 10 mHz.

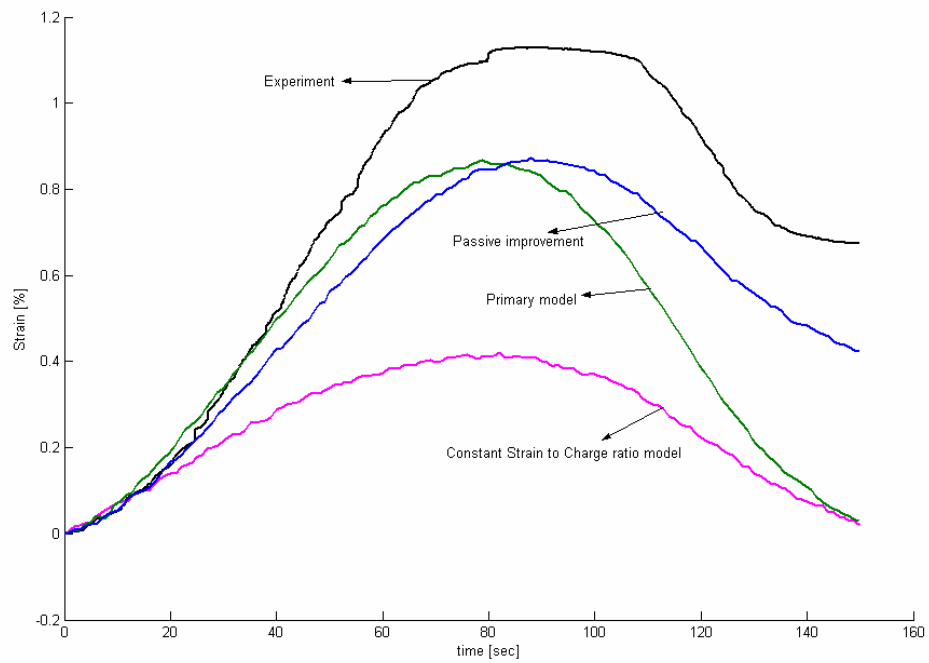


Figure 4.5.8 Stress 5.80 MPa and 5 mHz.

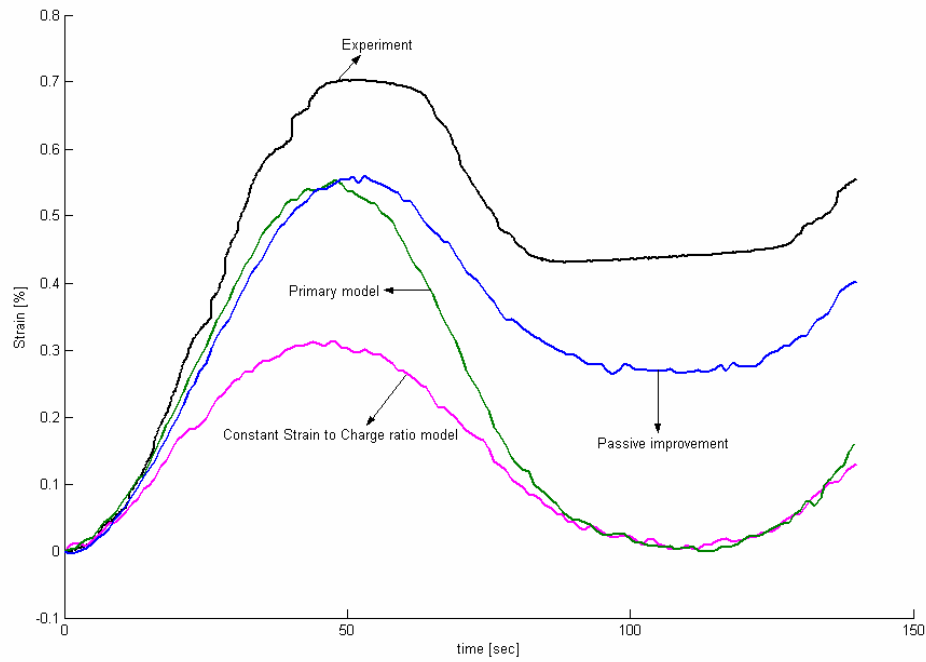


Figure 4.5.9 Stress 5.80 MPa and 10 mHz.

4.6. Conclusions

The Lumped Parameters technique (Della Santa et al., 1997a, Della Santa et al., 1997b, Mazzoldi et al., 2000) was applied to a PPy helix tube actuator and utilized to describe the viscoelastic behaviour. The results demonstrate that the linear viscoelastic models cannot estimate the mechanical behaviour of PPy fibre, although they are successful on EAP films (Mazzoldi et al., 2000, Della Santa et al., 1997a, Della Santa et al., 1997b, Della Santa et al., 1996, Della Santa et al., 1997c). It was found that at the stresses/strains typically encountered in actuator testing, the PPy helix tube fibres were not fully straight and, hence, showed non-linear stress-strain curves. A wet stress relaxation test at 0 V was carried out and a mathematical model fitted to the data to give values of stiffness and damping coefficients calculated under different test conditions. It was shown that three viscoelastic branches ($n=3$) plus one main spring in parallel adequately describes the mechanical properties of PPy helix tube actuator in specified isometric strain since the values of R-square, total stiffness and total damping coefficients are not significantly changed by increasing the number of viscoelastic branches.

Both stiffness and damping coefficients varied for different applied isometric strains, but the graphs illustrate that the variations were almost linear. This means that the stress-strain diagram is parabolic in the actuation strain area, giving an S-shaped curve over the entire strain range. This behaviour makes the dynamic explanation of the fibre actuators very complicated, because the phenomenon of active strain generation of EAP fibres is modelled as a configuration of many springs and dashpots which do not behave like linear elements. Hence, all elements of the system would be altered during displacement under the effect of electrical stimulation. Thus the system proposed here moves through different isometric strain conditions during the process of actuation and consequently the characteristic of system elements varies during the stimulation. However, this variation is predictable linearly and these linear methods can be generalized for PPy fibre actuators.

Finally, the new model was validated by applying the sinusoidal voltage signal with different frequencies under different external loads. A simulation program was designed to predict the output strain and compare it to the experimental strain output. The passive improvement model greatly improved the primary model performance by predicting the general creep phenomenon due to an increase in the applied stress. However, the passive improvement model did not predict some subtle variations in the experimental data and also under-estimated the peak strains. Further modification to the predictive model is discussed in Chapter 5 where the effect of applied voltage on the viscoelastic parameters is considered.

CHAPTER 5: THE EFFECT OF ELECTRICAL STIMULATION ON THE VISCOELASTIC PARAMETERS

5.1. Introduction

Prior to any physical application of a conducting polymer (CP) actuator, the actuator strain has to be predicted in a reliable manner. The first models to predict the strain of CP actuators divided the strain into an active electro-chemical part and a passive viscoelastic part, where the parts are superimposed to model the behaviour of the actuator. The actuation strain was considered proportional to the amount of charge transferred and independent of the force induced strain (Penner et al., 1988, Penner and Martin, 1988, Penner et al., 1989). These initial models were developed by employing the viscoelastic lumped parameter method to describe the passive viscoelastic behaviour of CP actuators (Della Santa et al., 1997a, Mazzoldi et al., 2000), where performance was verified both experimentally and using the complicated continuum mechanics method (Della Santa et al., 1996, Della Santa et al., 1997c, Mazzoldi et al., 2000) based on Biot's poroelastic theory (Biot, 1941, Biot, 1955).

Recently, it was observed that the elastic modulus, and hence the force induced strain is a function of the oxidation state of the CP (Spinks et al., 2003d, Spinks et al., 2002, Chiarelli et al., 1995, Della Santa et al., 1997b). The research was performed on PPy film actuators with a static method of calculating the Young's modulus showing that the modulus was a function of the voltage applied to the polymer. The change in modulus produced a strain when the actuator was loaded (Spinks et al., 2004). In this chapter the elastic modulus measured in situ as a function of different input functions of the electric potential is studied. It is shown that the elastic modulus is not a simple function of the electric potential, but is also dependent on the history of previous electric potentials.

The standard technique for measuring the modulus in situ is to apply a sinusoidal stress or strain and observe the corresponding strain or stress, respectively. Experimentally, this approach becomes difficult when the resultant oscillating stress or strain is of comparable magnitude to that due to external stimuli. Employing a rectangular stress signal is a much simpler approach to measuring the elastic modulus. Consequently, in this thesis a rectangular stress signal is used for the analysis of elastic modulus prior to using the approach on polypyrrole actuators.

The change in modulus has been linked to the effect of load on the electrochemical strain generated. Experiments on PPy have been previously conducted using pulsed currents under isotonic conditions at different stress levels in 0.25 M TBA-PF₆/PC and ionic liquid EMI-TFSI electrolyte; a current pulse for 30 seconds was applied at 12mA/cm² as shown in Figure 5.1.1. Further explanations are given in reference (Xi, 2005). The results demonstrate that the electrochemical strain generated decreases with increasing load. This effect in IL electrolyte is not as dramatic as in PC electrolyte.

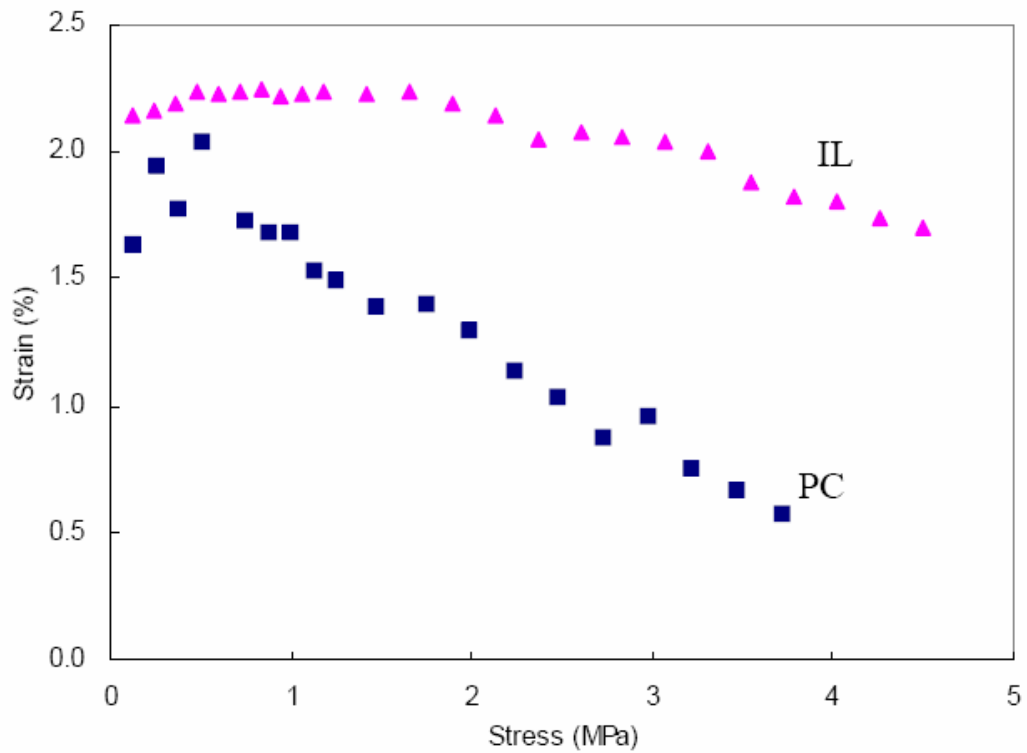


Figure 5.1.1 Actuator strain recorded under isotonic conditions at different stress levels in 0.25 M TBA-PF₆/PC and ionic liquid EMI-TFSI electrolyte; a current pulse for 30 seconds was applied at 12mA/cm². (Xi, 2005).

There are two theories to explain the effect of load on the actuation. The first theory by Madden (Madden et al., 2002) and Della Santa (Della Santa et al., 1997b) is that this effect is caused by decreasing the strain to charge ratio with increasing load. But the second theory by Spinks (Spinks and Truong, 2005) considers that the effect is caused by Young's modulus change in the polymer during the actuation process. In Equation 5.1.1, the subtraction of the final value of strain from the initial value includes a term containing the

modulus shift. If the modulus increases after oxidation ($E_f > E_o$) then the net expansion strain will decrease with increasing load. Static measurement of modulus has confirmed this prediction.

$$\begin{aligned}\varepsilon_o &= \frac{\sigma}{E_o} \Rightarrow \varepsilon_f = \frac{\sigma}{E_f} + \alpha\rho \\ \Delta\varepsilon &= \varepsilon_f - \varepsilon_o = \sigma \left(\frac{1}{E_f} - \frac{1}{E_o} \right) + \alpha\rho\end{aligned}\tag{Equation 5.1.1}$$

Equation 4.3.39 mathematically proves that the experimental method to measure “Active Electrochemical Strain” used to provide the results in Figure 5.1.1 and also the first part of Equation 5.1.1 is reasonable and accurate.

The second theory explains not only the effect of loading on actuation strain but also the loading effect on the work per cycle parameter. The Young’s modulus was reported to be increasing during the oxidation process in PPy film in TBA-PF₆ (Spinks et al., 2002, Spinks et al., 2003d) and PPy helix tube in EMI-TFSI (Spinks et al., 2004) but decreasing in PPy/pTS (Wallace et al., 2002), PPy doped by BS⁻ (Della Santa et al., 1997b), PPy doped with tetraphenylborate anion and BS⁻ (Chiarelli et al., 1995), Polyaniline film in HNO₃ (Xi, 2005), Polyaniline fibre HNO₃ (Xi, 2005), Polyaniline and CNT composite with 1.25% and 2.50% in HNO₃ (Xi, 2005).

The ‘primary model’ was introduced in Chapter 3 to track the experimental data, then in Chapter 4, the “passive improvement’ model considered a viscoelastic model with constant viscoelastic coefficients to predict the creep behaviour of the polymer. In this chapter, study of the effect of the electrical stimulation on the viscoelastic coefficients will be presented and these influences will be included in anew ‘Active and Passive improvement’ model.

5.2. Experimental set up

A TA Instruments-Q800 dynamic mechanical analyser (DMA) was used to measure the elastic modulus of polyethylene terephthalate (PET) with dimensions 19.66 × 7.98 × 0.10 mm during a temperature ramp. This experiment was performed to determine the accuracy of measuring modulus using a load-step procedure. Two different stress inputs

were applied during the temperature ramp. The first stress input consisted of the standard sinusoidal wave at a frequency of 1 Hz, and a heating rate of 0.08 °C/s. The second stress input consisted of a pulse waveform by applying the stress input of 3 MPa with 6 seconds duration every 180 second at a heating rate of 0.03 °C/s.

The sample preparation, experimental set up and reference electrode configuration is as described in Section 3.2.

5.3. Methodology confirmation

When measuring the dynamic properties of a material, the standard approach involves applying an oscillating strain or stress to the sample, and recording the corresponding oscillating stress or strain. For the case of an oscillating stress:

$$\sigma = \sigma_p + \sigma_0(\sin \omega t) \quad \text{Equation 5.3.1}$$

Where, σ is the total stress, σ_p is the preload stress, σ_0 is the amplitude of stress oscillation, t is the time and ω is the angular frequency.

The observed response would be:

$$\varepsilon = \varepsilon_p + \varepsilon_0(\sin \omega t + \delta) \quad \text{Equation 5.3.2}$$

Where, ε is the total strain, ε_p is the preload strain, ε_0 is the amplitude of the strain oscillation, and δ is the phase angle by which the strain lags behind the stress. The strain can be represented by an in phase component and an out of phase component. The in-phase component is known as the real modulus, whilst the out of phase component is known as the imaginary, or loss modulus. Using such an approach the real modulus, $\tan \delta$ and imaginary modulus can be calculated; these are functions of frequency and should be curve-fitted in order to find the viscoelastic constants in the Standard Linear Model described in section 4.3. Commercial instruments that use such an approach are known as DMA's (short for dynamic mechanical analysis). The parameters measured from

such a test are dependent on the frequency, with typical test frequencies being of the order of 1 Hz.

The standard approach is intended to measure the real and loss modulus whilst the sample is undergoing change due to an external stimulus. A temperature ramp is the most common external stimuli. A major challenge of the standard technique is to isolate the strain due to the oscillating stress from that due to external stimuli. There are several numerical, digital or electronic approaches to isolating the two signals (for example a moving average, a Fourier transform or a lock in amplifier). All of these approaches become difficult when the rate of change of strain resulting from the external stimuli becomes comparable to that of the oscillating stress input. A simple technique to avoid this situation is to increase the frequency of the oscillating stress. At high frequencies, the sinusoidal oscillation approaches a similar rate to that of a rectangular stress signal. Performing data analysis on a rectangular stress signal is simpler than that of a sinusoidal signal, as the real component is easily extracted.

In this case, a high frequency rectangular stress is applied to the material like a creep test and the initial strain response is used for measuring the real modulus at high frequency, which is equal to the total stiffness coefficients shown in Figure 4.3.3 and Equation 4.3.33. The pulse stress not only reduces the effect of actuation strain as the equipment applies a step input within a period of time close to the sampling time, but also gives the opportunity to measure the viscosity (dash-pot) coefficient as well as the stiffness coefficients of the Standard Linear Model which are independent of applied frequency.

A comparison of the sinusoidal and rectangular stress input signals was performed using a commercial DMA instrument. The method was confirmed by comparing results with that from a sinusoidal stress input. Thus, a sample material, polyethylene terephthalate (PET), was tested with both methods in thermo-elastic conditions. Figure 5.3.1 shows the rectangular stress waveform and the corresponding strain waveform for one cycle.

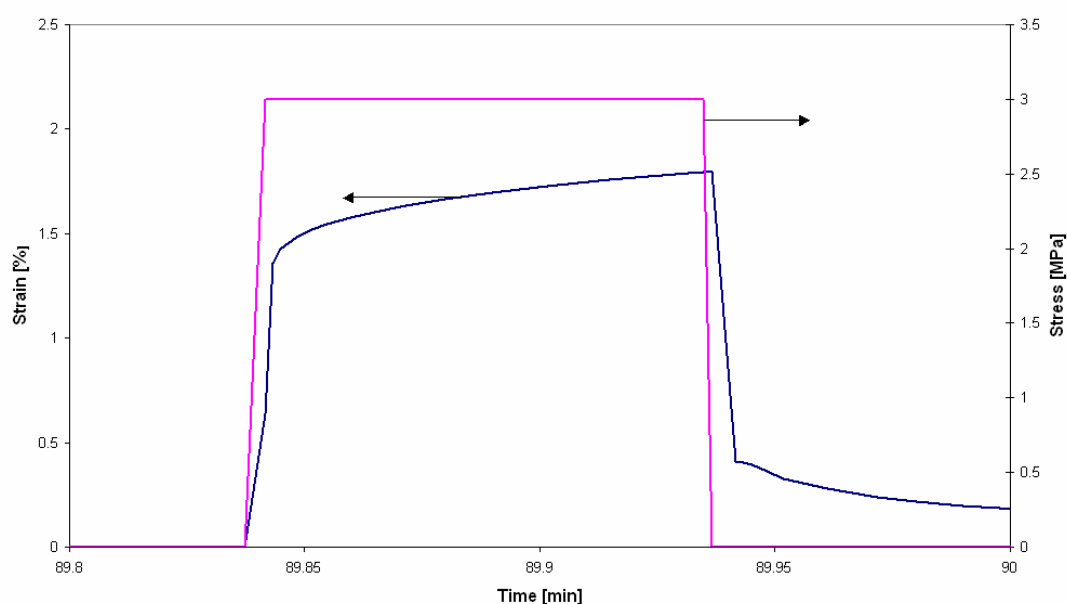


Figure 5.3.1. The rectangular stress waveform and the corresponding strain of DMA experiment.

The real modulus measured from a sinusoidal waveform was quantitatively and qualitatively similar to that measured by the rectangular waveform (Figure 5.3.2). At low temperatures the rectangular waveform provides a slightly higher modulus; this is due to the effective higher frequency. At higher temperatures, during the large drop in modulus at approximately 100°C, the real modulus from the rectangular waveform is lower than that of the sinusoidal waveform. The reason for the small difference is the different temperature ramp times i.e. 23 and 95 minutes in DMA and the new method respectively. Despite these small differences, the test results show that the stress pulse test is suitable for determining the real modulus during dynamic conditions. This method has been applied to electrochemical stimulation of PPy, as described in the following section.

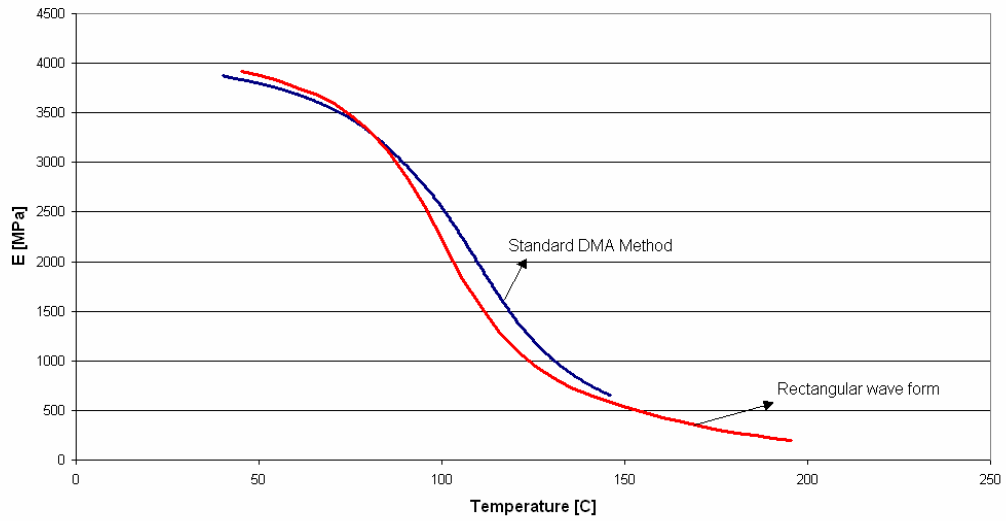


Figure 5.3.2. Comparison between DMA result and the new method for measuring real modulus.

5.4. Results and discussions

5.4.1. Stiffness coefficients results

The rectangular stress input was applied to the actuator with 1.47MPa initial value, 0.3MPa amplitude and 0.5Hz frequency. Simultaneously, cyclic voltammetry was carried out with 1, 2, 4, 6, 8, 12 and 20 mV/s scan rate. The results illustrate the large effect of actuation voltage on the real modulus, which is nearly 20 percent. Figure 5.4.1 to Figure 5.4.7 show the modulus variation beside the CV diagram and active strain in 1, 2, 4, 6, 8, 12 and 20 mV/s stimulation rate. The plot of strain also shows the value of passive strain relative to active strain. The modulus plot was smoothed using the moving average method (Moré and Sorensen, 1983). It is clear that the trend of modulus changing is in the same direction with CV, which verifies that changes in the doping levels affect the mechanical properties of CP actuators and this effect is reversible.

In Figure 5.4.1 to Figure 5.4.7, the current signal remains constant at almost zero and the strain signal is almost constant as well, while the voltage is increasing from -1V to -0.5V. From -0.5V to -0.2V, the current signal increases linearly i.e. the material behaves resistively showing that the voltage is producing a Faradic charge transfer (polymer oxidation). The strain signal decreases showing the shrinkage of the polymer caused by

the expulsion of cations and PC electrolyte molecules. During this process, the real modulus signal is increasing which is caused by the shrinkage of the polymer and the charging of the polymer causing a stiffening of the chains.

From -0.2V to +0.1V, the current changes from a resistive nature to a capacitive diffusive nature as ion diffusion limits the polymer oxidation reaction. The strain and modulus are affected by this process but after a time delay. The capacitive diffusive behaviour occurs from +0.1V to +1V; the current signal is constantly positive caused by concentration of PF_6^- or diffusion of PF_6^- to the polymer backbone after saturation and oxidation of the polymer. This process causes a dramatic increase in strain signal due to the incorporation of PF_6^- anions and PC solvent. Decrease in the modulus signal is observed in this region due to the volume expansion of the polymer.

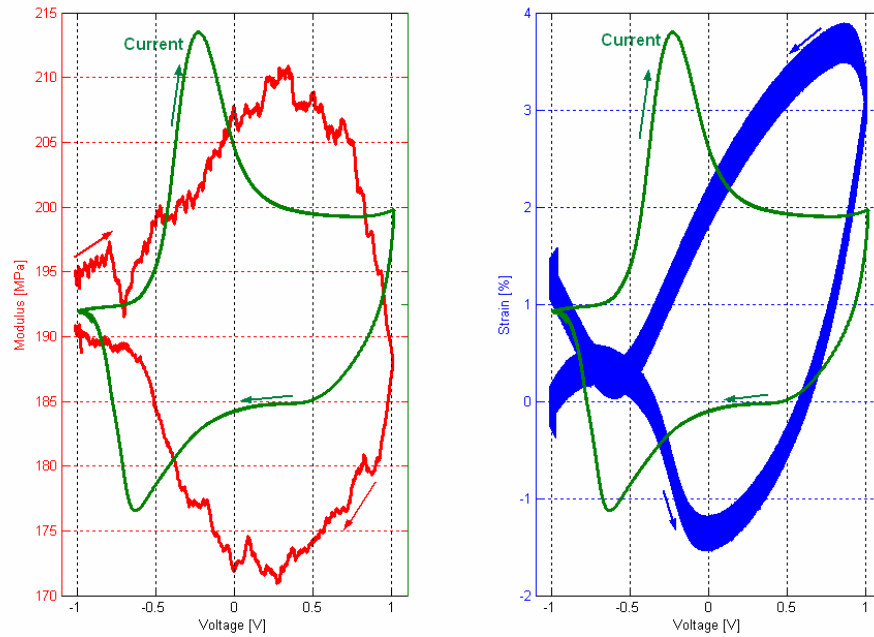


Figure 5.4.1 The real modulus variation, resultant strain and CV diagram at 1mV/s.

In the return from +1V, the switching from the charging process of the capacitor to the discharge process occurs from +1V to +0.5V. This discharging is reflected in the strain and modulus signal after a time delay with strain decreasing due to the expulsion of anions and solvent from the polymer.

From +0.5V to -0.1V, the current is constantly negative which means that the polymer is discharging and PF_6^- ions are exiting the polymer backbone. So the strain is decreasing and the modulus value starts to increase due to the volume shrinkage.

A negative peak current occurs between -0.1V and 1V due to reduction of the polymer. This reduction first causes a reduction in strain due to expulsion of PF_6^- and PC, but then an expansion results. This expansion is due to the incorporation of TBA^+ cations which balance the charge of remaining PF_6^- anions in the polymer. The modulus tends to increase over this voltage range, as it is dominated by the initial volume shrinkage.

At higher voltage scan speeds, the same basic processes were observed. In scanning from -1V to +1V and back, the modulus first increases, then decreases and then increases again to close to the initial volume. The strain relationship becomes simpler at higher scan rates with the cation expulsion/incorporation becoming absent.

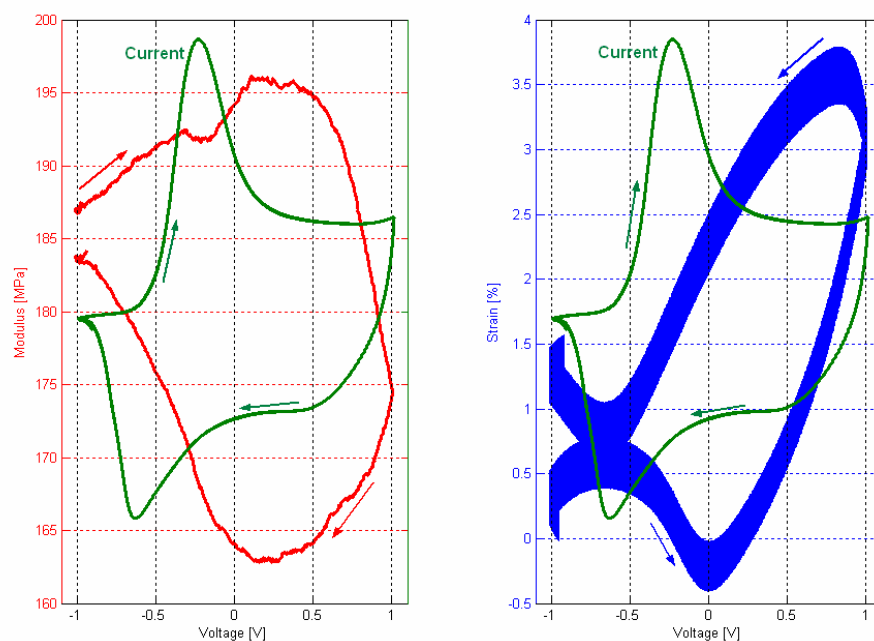


Figure 5.4.2. The real modulus variation, resultant strain and CV diagram at 2mV/s.

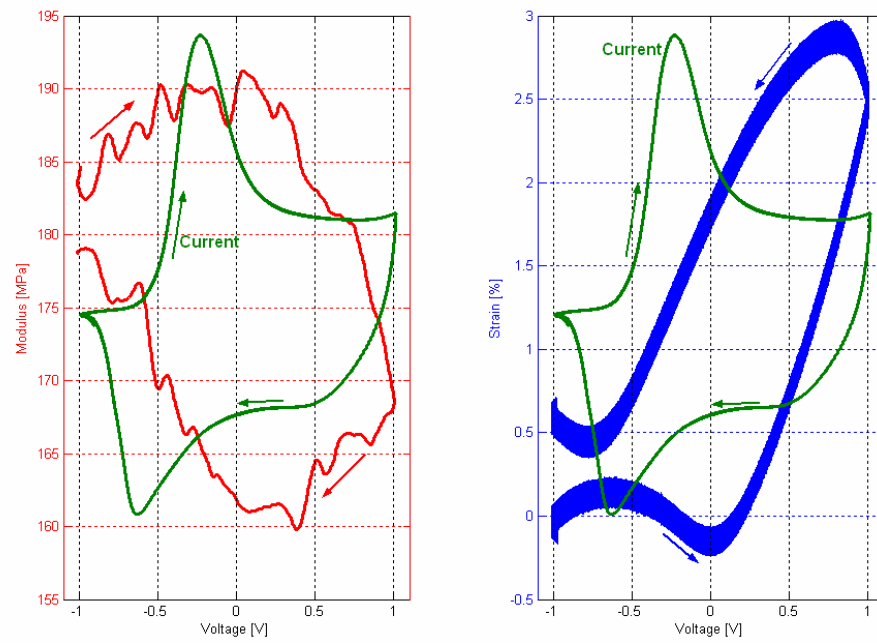


Figure 5.4.3 The real modulus variation, resultant strain and CV diagram at 4mV/s.

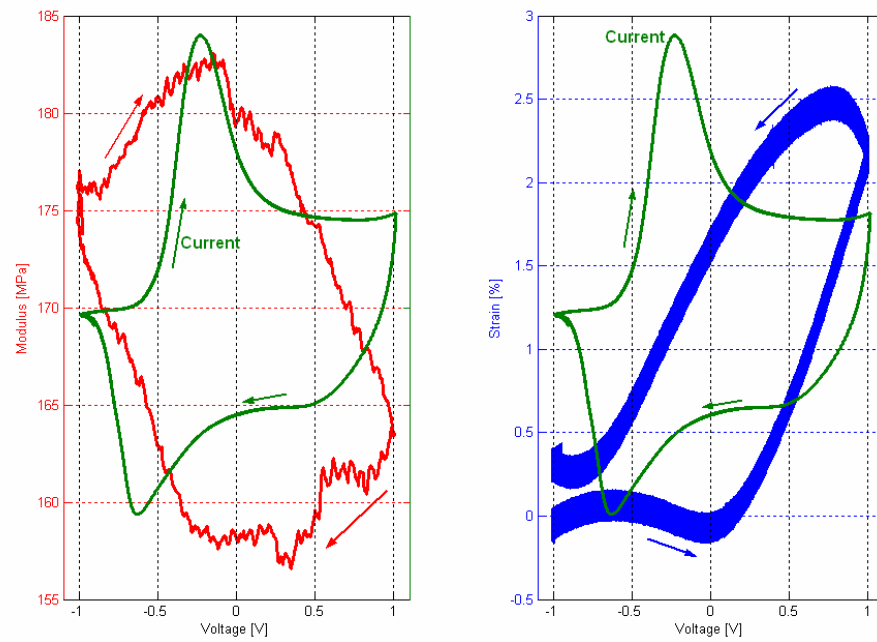


Figure 5.4.4 The real modulus variation, resultant strain and CV diagram at 6mV/s.

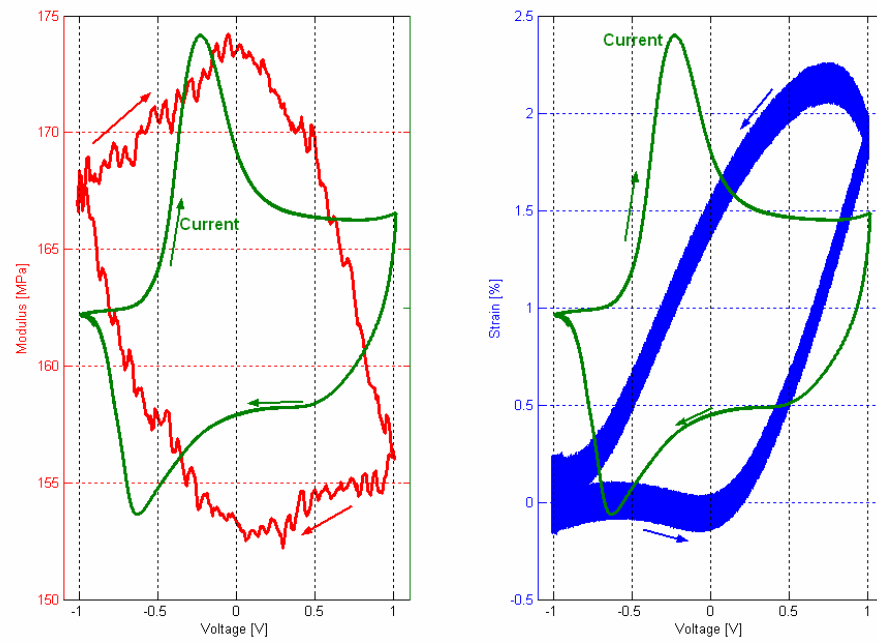


Figure 5.4.5 The real modulus variation, resultant strain and CV diagram at 8mV/s.

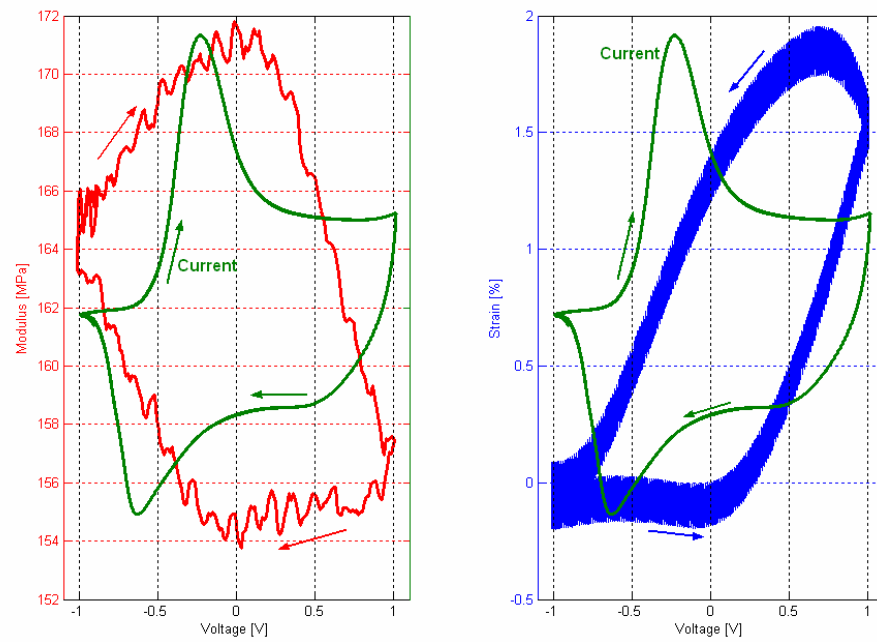


Figure 5.4.6 The real modulus variation, resultant strain and CV diagram at 12mV/s.

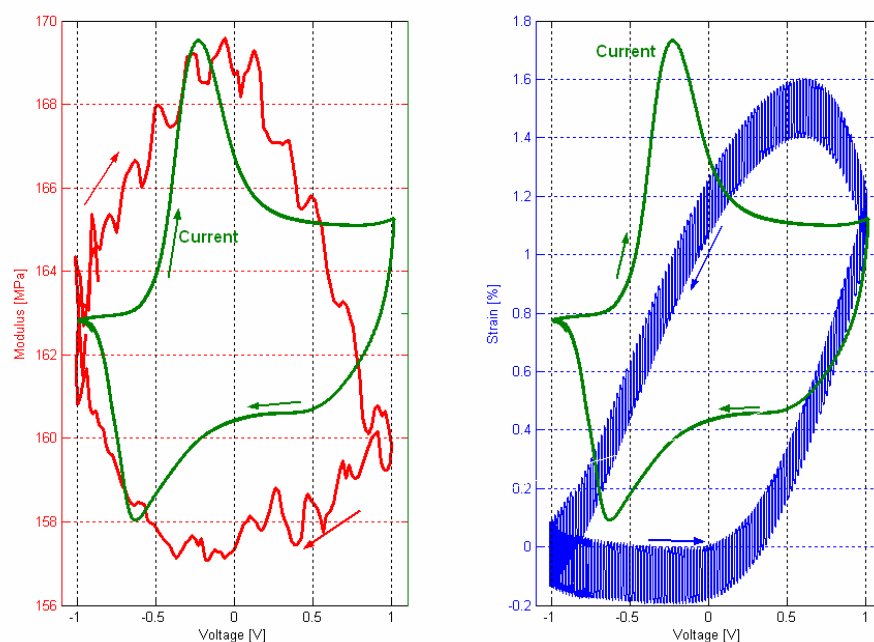


Figure 5.4.7 The real modulus variation, resultant strain and CV diagram in 20mV/s.

Figure 5.4.8 shows the modulus variation vs. strain generated taken at slow scan speeds, in which three special regions are described. In regions A and B, mixed cation/anion movements produce complex strain behaviour. A much simpler modulus – strain relationship was found at higher scan speeds, since actuation only involves anion movement. The modulus value decreases linearly during normal actuation while oxidising and increases linearly while contracting in the reduction process. The point is the slope of the linear decrease during oxidation is the same as for the increase during reduction; this slope is shown during the oxidation process at different scan rates in Figure 5.4.10. It is clear that the linear slopes are almost the same at different scan rates. In region C, where the peak strain occurs, a modulus shift causes an offset to the linear curve during reduction.

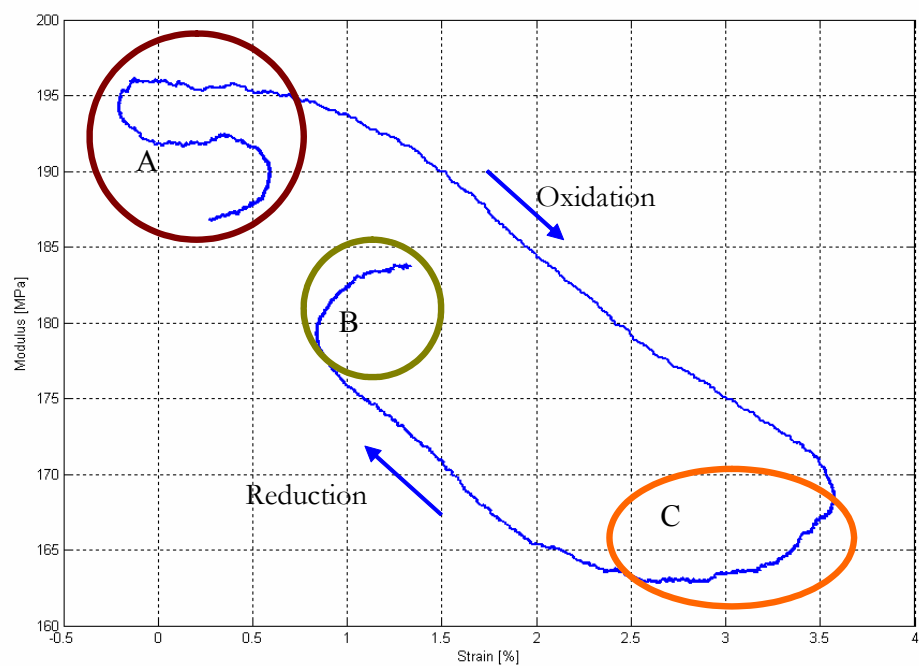


Figure 5.4.8. Modulus variation vs. active strain taken from the data given in Figure 5.4.2 at 2mV/s.

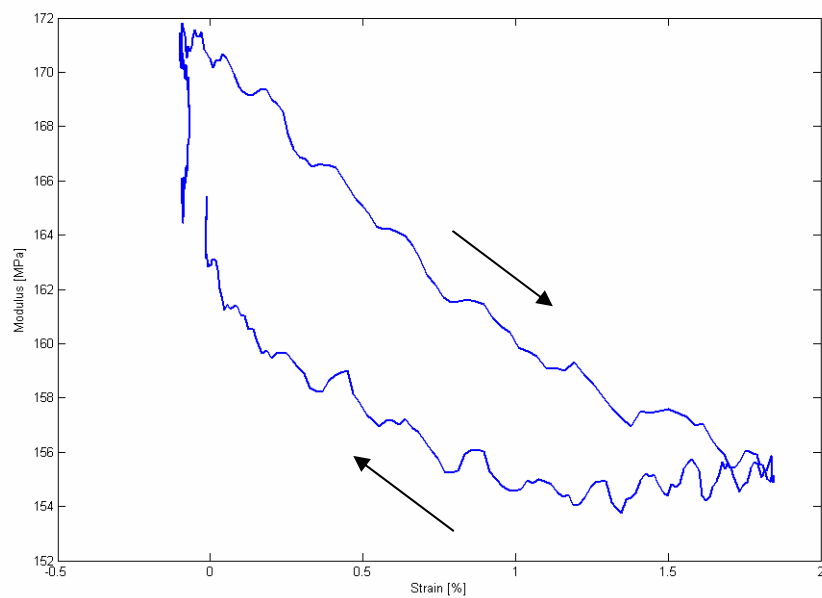


Figure 5.4.9 Modulus variation vs. active strain taken from the data given in Figure 5.4.6 at 12mV/s.

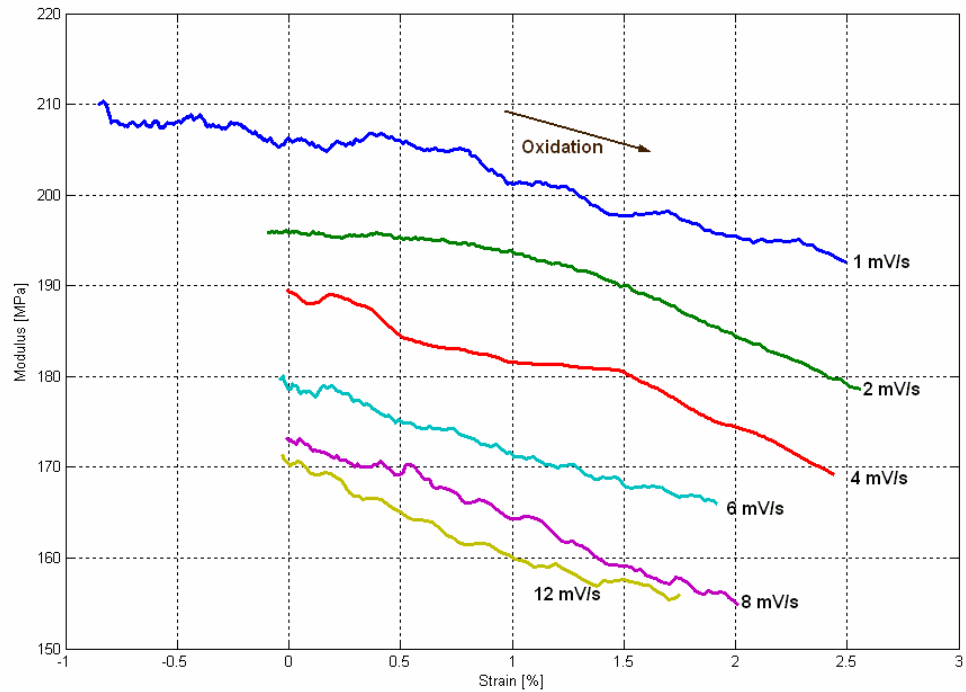


Figure 5.4.10. Modulus variation vs. active strain during oxidation process for different scan rates of cyclic voltammetry.

Figure 5.4.11 shows that increasing the frequency of applied voltage produces a smaller change in real modulus; its logarithmic trend is also shown in Figure 5.4.12. At higher frequencies, the actuation strain is also smaller due to less time being available for osmotic processes. Since there is a smaller volume change at higher frequencies, the modulus is also less affected.

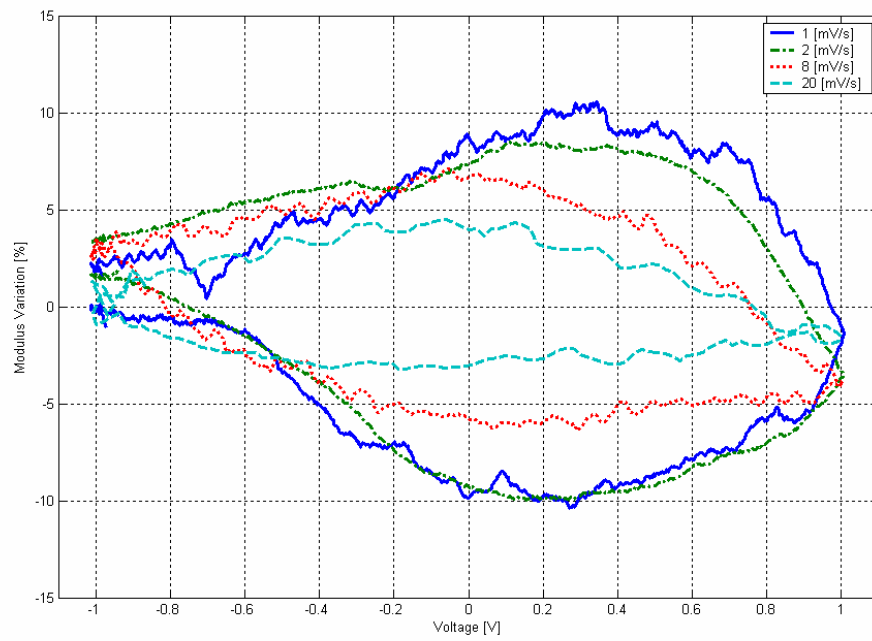


Figure 5.4.11. The real modulus variation for different frequencies of applied voltage.

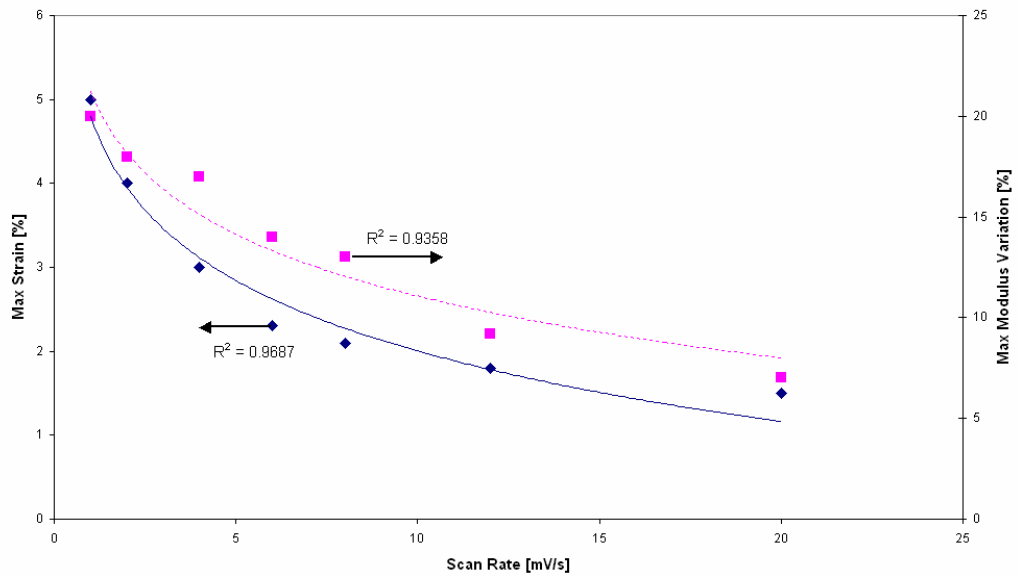


Figure 5.4.12. Maximum active strain and maximum variation in modulus for different scan rates.

Figure 5.4.13 shows the long time effect on actuation strain and on real modulus. Step voltages of +1 V, -1 V, +0.5 V, -0.5 V, +0.7 V and -0.7 V were applied to the actuator for a long time period. The results show that variation in the value of modulus and strain occurs over very long time periods, due to the slow diffusion of solvent.

Over long times the modulus is relatively constant at all potentials except at 0.7 V vs. SCE (-1 V in vs. NO_3^- . The time constant for change is about 10 minutes.). However there is a drift in the zero volts vs. AgNO_3 potential. What is seen is that the modulus tends to increase from zero V vs. NO_3^- when the potential is switched such that it goes to a voltage of less than about 0.5 V vs. NO_3^- , and goes down for high voltages. The drop in change in modulus is likely to be caused by a gradual irreversible degradation of the film. It appears from the numbers that the modulus at negative potentials is 127 MPa and at positive potentials is 120 MPa. However there is a change in modulus of about 30 MPa.

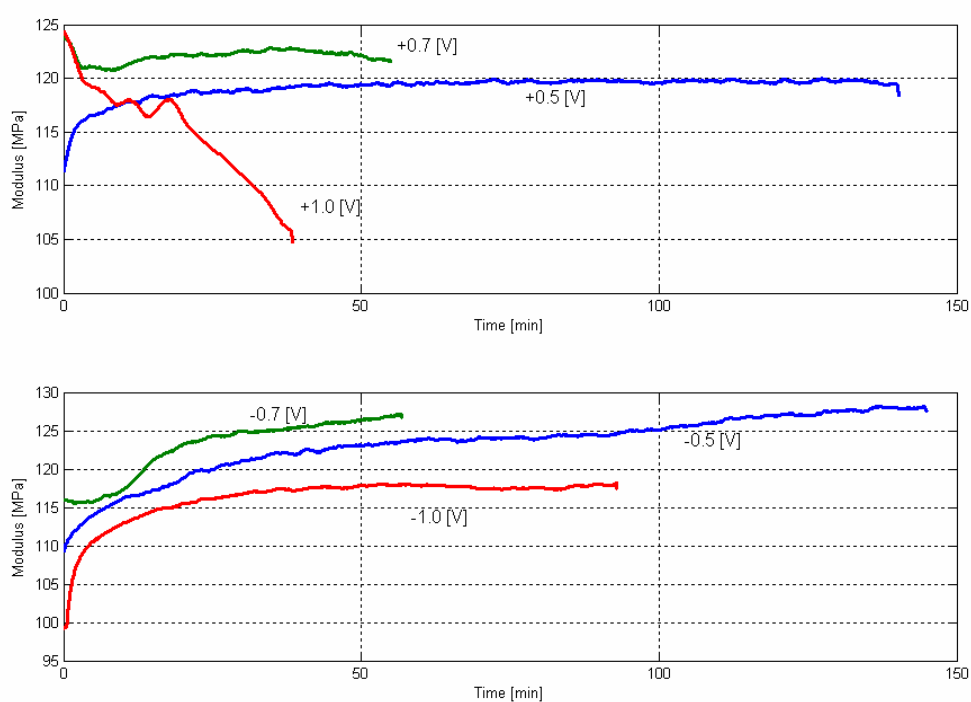


Figure 5.4.13. The real modulus changing over a long time period held at the potentials shown.

Stress-strain tests were carried out with previous methods (Spinks et al., 2002, Wallace et al., 2002, Murray et al., 1998) to confirm the results presented by Figure 5.4.13. For this

purpose, a stress ramp 6MPa/min (equivalent to 1.2mm/min) was applied to the helix tube. The stress-strain curves in Figure 5.4.14 show that the modulus values decrease after application of +1V.

It should be noted that the modulus trends reported in this thesis differ from literature reports for similar systems. In particular, Spinks et al. reported that the modulus of PPy films increased during oxidation (Spinks et al., 2002). It is possible that the different results reported in this thesis result from the helix tube geometry used. For example, it is known that electro-polymerised PPy films are anisotropic with higher modulus in the plane of the film compared with the thickness direction (Smela et al., 1999). This anisotropy is likely to be related to the molecular structure where PPy chains lay flat on the electrode and the thickness direction consists of PPy layers separated by dopant. It is not clear whether the helix tube template produces a different molecular structure compared with a flat electrode. The investigation of the PPy helix tube molecular structure and the origin of the modulus changes were considered beyond the scope of this thesis.

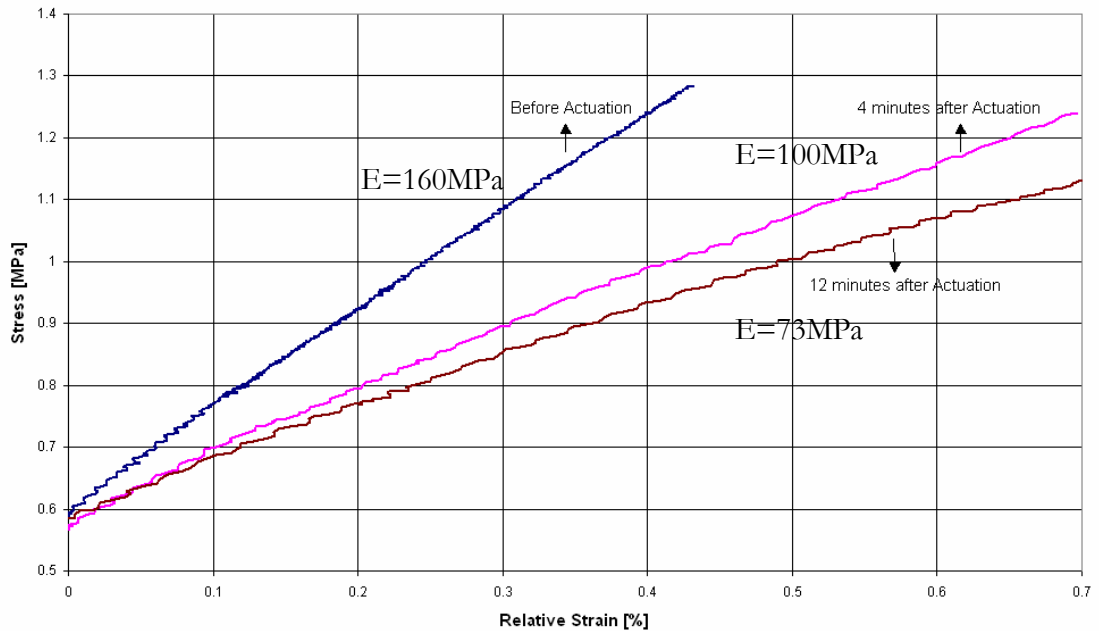


Figure 5.4.14. Stress-Strain test before actuation by step 1V and two times after actuation.

5.4.2. Viscosity coefficients results

The next step in studying the effect of actuation on the viscoelastic properties was to determine the viscosity coefficient by analysing the time-dependent strain response. A stress pulse gives an initial strain of $\varepsilon(0^+)$ and the strain continues to increase with time $\varepsilon(t)$ for viscoelastic materials. With reference to Equation 4.3.23 and Equation 4.3.24, the viscoelastic strain can be calculated from:

$$\Delta\varepsilon(t) = \varepsilon(t) - \varepsilon(0^+) = \sigma_{step} \left(\frac{1}{k_r} - \frac{k_1}{k_r \cdot (k_1 + k_r)} e^{-\frac{k_1 \cdot k_r}{(k_1 + k_r) \eta_1} t} - \frac{1}{k_1 + k_r} \right) = \sigma_{step} \cdot \frac{k_1}{k_r \cdot (k_1 + k_r)} \left(1 - e^{-\frac{k_1 \cdot k_r}{(k_1 + k_r) \eta_1} t} \right)$$

Equation 5.4.1

The modulus results described in the previous section can be used to calculate the initial stiffness $k_t = k_1 + k_r$. The final strain (long time) can be used to determine k_r and so k_1 can be determined. However, as shown in Figure 5.4.15 which obtained by performing the simple stress-relaxation test to the actuators with different length and under different applied strain amplitude, there is an empirical relationship between k_r and k_t that simplified the analysis. For all voltages, the ratio k_r/k_t ($\kappa = \frac{k_r}{k_r + k_1} = \frac{k_r}{k_t} = 80\%$) ($k_t = k_r + k_1$) was found to be approximately 0.8. The measured value of k_t from a simple creep test described in Chapter 4 was used to estimate k_r using this ratio and then k_1 determined.

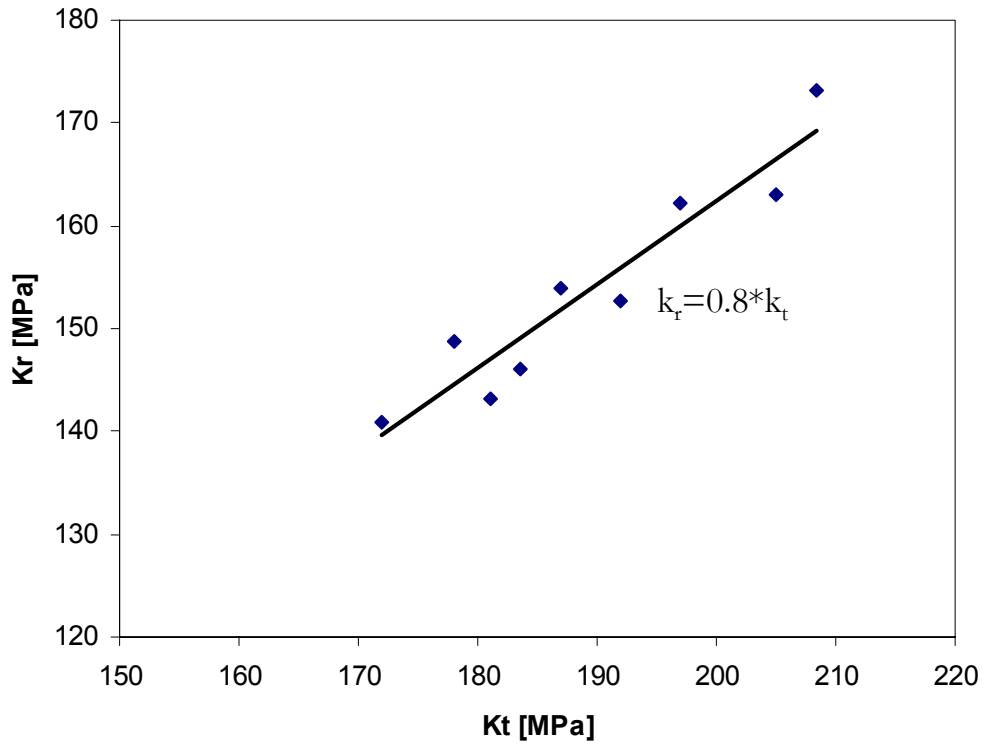


Figure 5.4.15 The total and relaxed stiffness modulus in different applied voltages.

Equation 5.4.1 can be further simplified using Equation 5.4.2 and Equation 5.4.3

considering $\kappa = \frac{k_r}{k_r + k_1} = \frac{k_r}{k_t} = 80\%$,

$$\frac{k_1}{k_r \cdot (k_1 + k_r)} = \frac{(1 - \kappa)k_t}{\kappa \cdot k_t^2} = \frac{0.25}{k_t} \quad \text{Equation 5.4.2}$$

$$\frac{k_1 \cdot k_r}{k_1 + k_r} = \frac{(1 - \kappa)\kappa \cdot k_t^2}{k_t} = 0.16k_t \quad \text{Equation 5.4.3}$$

The simplified form is shown in Equation 5.4.4,

$$\Delta \varepsilon(t) = \varepsilon(t) - \varepsilon(0^+) = \sigma_{step} \cdot \frac{0.25}{k_t} \left(1 - e^{-\frac{0.16k_t}{\eta_1} t} \right) \quad \text{Equation 5.4.4}$$

Equation 5.4.4 was obtained by replacing Equation 5.4.2 and Equation 5.4.3 in Equation 5.4.1. The experimental data points were fitted to this equation to determine the viscosity value as shown in Equation 5.4.5.

$$\eta_1 = - \frac{0.16(t.k_t)}{\text{Ln} \left(1 - \frac{\Delta \varepsilon(t).k_t}{\sigma_{step}.0.25} \right)} \quad \text{Equation 5.4.5}$$

Figure 5.4.16 clarifies the definition of the parameters used in Equation 5.4.4 in a schematic view of the experiment. The total stiffness coefficient used in this calculation was obtained from the results reported in the previous section and depends on the voltage applied, as explained. to specify the $\Delta \varepsilon$ parameter resulting from the step stress change (the ‘passive strain’), the total strain must be separated into ‘active’ and ‘passive’ parts. The active strain is due to the changing voltage and is superimposed on the active strain resulting from the change in stress. Since the voltage scan rate was slow compared with the step stress frequency, the active strain could easily be subtracted from the total strain using simple curve fitting procedure. The subtraction resulted in the results shown schematically in Figure 5.4.16, where the passive strain/time relationship is graphically illustrated. Using this method, the viscosity parameter (η_1) was determined as a function of time (and, therefore, voltage) using Equation 5.4.5. The strain signal which is varying with applied voltage needed to be subtracted from the ‘Active Electrochemical Strain’ and the active and passive parts are needed to be separated.

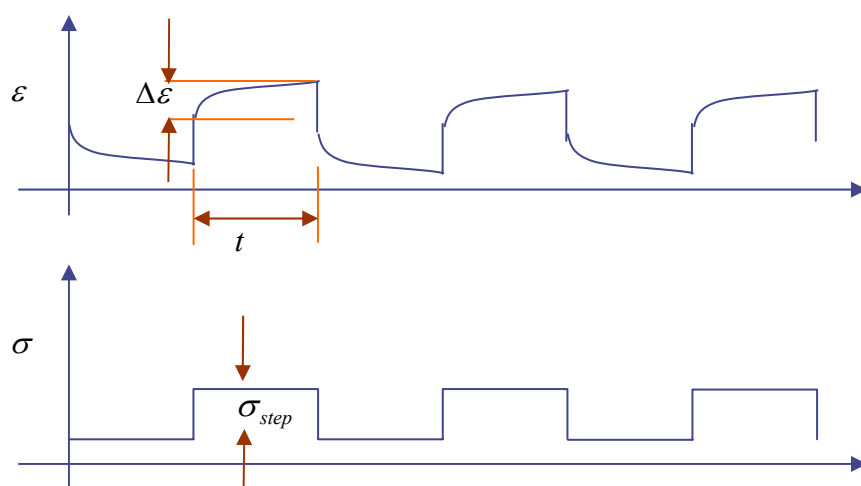


Figure 5.4.16 parameters definition using schematic view of the experiment.

Figure 5.4.17 shows the calculated viscosity parameter plotted against applied voltage for the 1mV/s scan rate. The viscosity changes in magnitude a significant amount (50-95 MPa.s) during the oxidation reduction of the PPy. The shape of the viscosity-voltage curve is qualitatively similar to the modulus-voltage curves. The major change in viscosity occurs during oxidation, with the viscosity first increasing and then decreasing. The increase in viscosity is probably related to increased inter-chain interaction that slows down or reduces the amount of strain. The subsequent decrease in viscosity may be due to the large volume swelling that occurs at high voltages. Similar shapes of curves were obtained at higher scan rates, but the magnitude of the viscosity change decreased when the voltage was scanned more quickly.

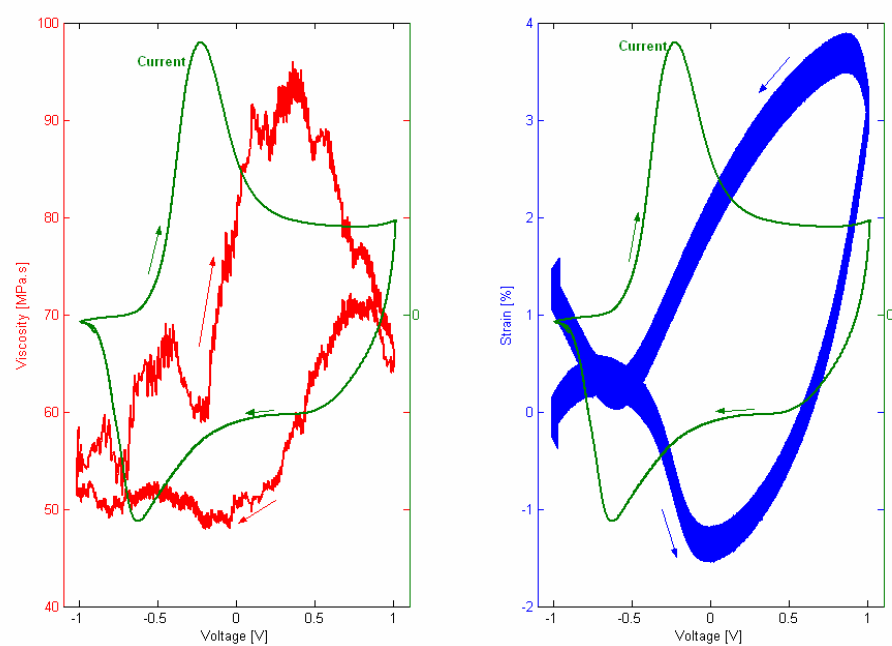


Figure 5.4.17 The viscosity variation, resultant strain and CV diagram at 1mV/s.

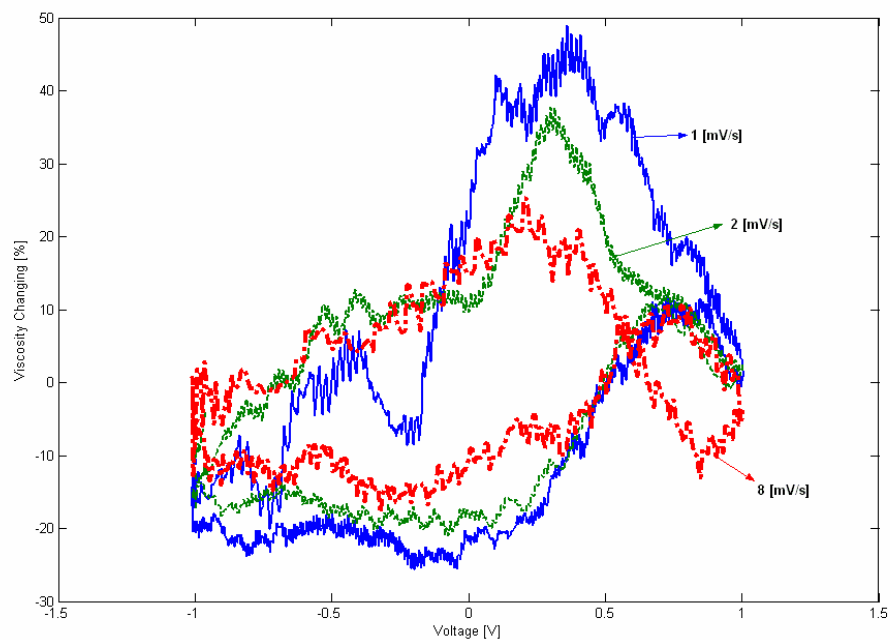


Figure 5.4.18 The viscosity variation, resultant strain and CV diagram at different scan rates.

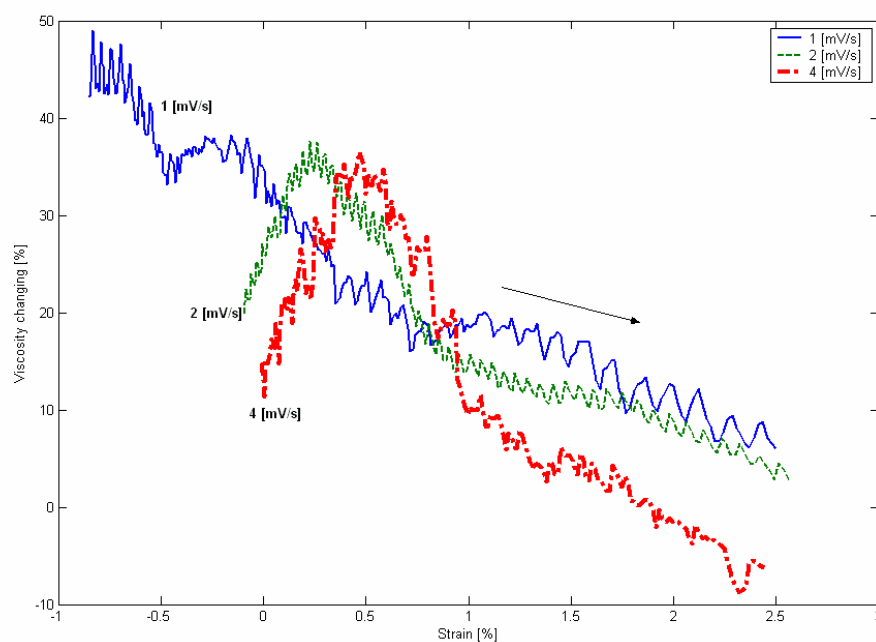


Figure 5.4.19 The viscosity variation vs. strain at different scan rates during the oxidation process.

5.4.3. Time constants results

Finally, the time constants have been calculated using the stiffness coefficient and the viscosity coefficient data. The values of time constants obtained were about 2 seconds and varied by ~ 0.5 second depending on the redox state of the polymer. This range of values agrees with the time constant reported in the previous chapter. Figure 5.4.20 shows the calculated time-constant values for different applied voltages

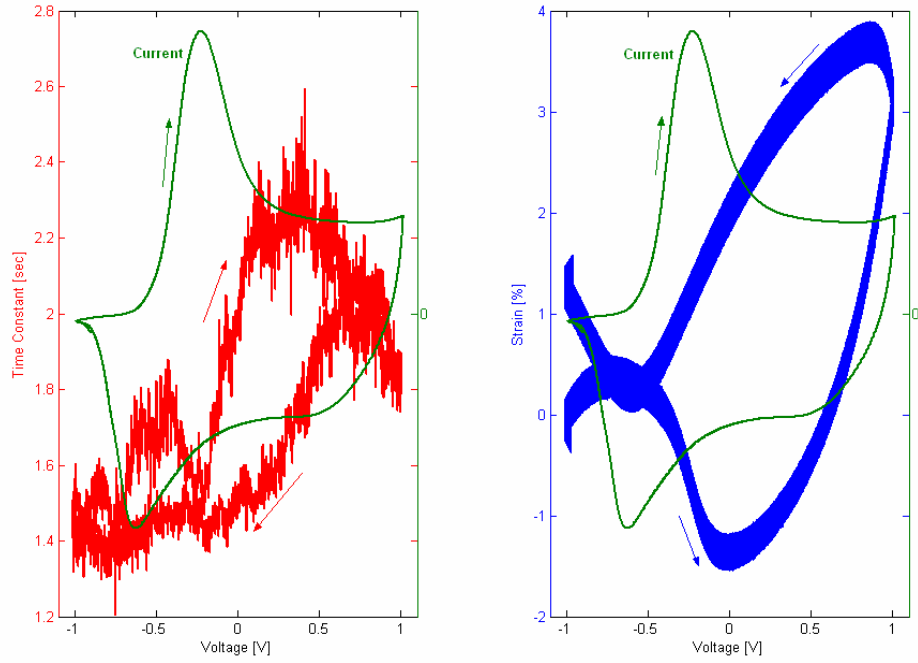


Figure 5.4.20 Time constant at 1 mV/s.

5.5. Modelling

As in Section 4.5 the modelling process has been carried out here by setting up the model in state-space as shown in Equation 5.5.1, in which ‘x’ is the state vector and ‘u’ the input vector. As in Section 4.5 the advantage of this approach is that the order reduction provided by State Space analysis enables the simulation and solving of the differential equations in the time-domain using standard simulation programs and methods in numerical analysis such as Runge-Kutta, Adams-Bashforth-Moulton and Gear’s method. Further information about State-Space is provided in Appendix B.

$$\begin{aligned}\dot{x}_{1 \times 1} &= A_{1 \times 1}x_{1 \times 1} + B_{1 \times 4}u_{4 \times 1} \\ y_{1 \times 1} &= x_{1 \times 1}\end{aligned}\tag{Equation 5.5.1}$$

As shown in Equation 5.5.2, the input vector contains four input parameters which are current (and integrated current) and external load signal (and derivation of external load).

$$x_{1 \times 1} = [\varepsilon] \quad \& \quad u_{4 \times 1} = \begin{bmatrix} \int idt \\ i \\ \sigma \\ \dot{\sigma} \end{bmatrix} \quad \text{Equation 5.5.2}$$

$$\begin{aligned} \varepsilon(s) = & \sigma(s) \left(\frac{k_1 + s.\eta_1}{k_1 k_r + s.\eta_1.(k_1 + k_r)} \right) \\ & + k_r . \varepsilon_{ech}(s) \left(\frac{k_1 + s.\eta_1}{k_1 k_r + s.\eta_1.(k_1 + k_r)} \right) \end{aligned} \quad \text{Equation 5.5.3}$$

The parameters of Equation 5.5.1 have been calculated in Equation 5.5.4 using Equation 4.3.8 .

$$\begin{aligned} A_{1 \times 1} &= \left[\frac{-k_1 k_r}{\eta_1 (k_1 + k_r)} \right] \\ B_{1 \times 4} &= \frac{1}{\eta_1 (k_1 + k_r)} \cdot \begin{bmatrix} k_1 k_r \alpha & \eta_1 k_r \alpha & k_1 & \eta_1 \end{bmatrix} \end{aligned} \quad \text{Equation 5.5.4}$$

Regarding Chapter 3, the strain to charge ratio (α) had been considered as a function of charge as shown in Figure 3.4.6 which is a characteristic of the PPy conducting polymer. The dimensions of α and q need to be changed from the dimensions used in Figure 3.4.6 to use in the modelling process in this section.

$$\begin{aligned} \alpha \left[\frac{\%}{mC} \right] &= \alpha \left[\frac{m^3}{C} \right] \cdot \frac{[C]}{10^3 [mC]} \cdot \frac{100 [\%]}{L_i A [m^3]} \\ q &= \int idt \\ q [mC] &= q \left[\frac{C}{m^3} \right] \cdot L_i A [m^3] \cdot \frac{10^3 [mC]}{[C]} \\ L_i &= 58 [mm] \\ A &= 2.6535 \times 10^{-2} [mm^2] \end{aligned} \quad \text{Equation 5.5.5}$$

Considering the results presented in Chapter 4 and Chapter 5, the effect of external load and electrical charging on the mechanical parameters must be considered in a model for actuation.

$$\begin{aligned} k_{total,0} &= k_{total,0,0} + \beta_k \cdot \sigma \\ k_{total} &= k_{total,0} - \alpha_k \cdot \left(\alpha \cdot \int idt \right) \end{aligned} \quad \text{Equation 5.5.6}$$

The parameters in Equation 5.5.6 are defined in Equation 5.5.7 for the actuator used in this experiment.

$$\begin{aligned} \beta_k &= 0.06786 \left[\frac{1}{\%} \right] \\ k_{total,0,0} &= 1.07 \left[\frac{MPa}{\%} \right] = 107 [MPa] \\ \alpha_k &= 0.25 \left[\frac{MPa}{\% \cdot \%} \right] \end{aligned} \quad \text{Equation 5.5.7}$$

As shown in Section 5.4.2, the viscoelastic parameters can be assumed as a fraction of total stiffness coefficient, as given in Equation 5.5.8

$$\begin{aligned} k_r &= \kappa \cdot k_{total} \\ k_1 &= (1 - \kappa) \cdot k_{total} \end{aligned} \quad \text{Equation 5.5.8}$$

Regarding Chapter 3, the viscosity parameter is calculated from a time constant affected by an external load.

$$\begin{aligned} \eta_1 &= \tau_1 \cdot k_1 \\ \tau_1 &= \tau_{1,0} + \beta_\tau \cdot \sigma \end{aligned} \quad \text{Equation 5.5.9}$$

Model simulation given below now used values of k_1 and η_1 that are functions of the applied voltage. In contrast, the method simulations presented in Chapter 4 assumed that k_1 and η_1 were independent of voltage. The actuator used in this section had 58 mm length and was stimulated by applying a sinusoidal voltage (-0.75 V \rightarrow +0.55 V) with different frequencies (1, 5 and 10 mHz) under different external (450 kPa, 3.25 MPa and 5.80 MPa).

As shown in Figure 5.5.1 and Figure 5.5.3, the active and passive improvement has improved the performance of the primary model to track the experimental results. The main improvement was in predicting the peak value of the experimental strain. For one case (Figure 5.5.3), it was observed that the simulated results completely tracked the experimental results and so validated the model described in this research.

The ‘active and passive’ improvement model gives higher peak strains as the model incorporates the measured changes in modulus and viscosity. The peak strain occurs during the early part of the cathodic voltage scan ($+1V \rightarrow -1V$) when the modulus is close to its smallest value and the viscosity parameter is roughly in the middle of its range. Naturally, the decrease in modulus contributes to the expansion strain. A decrease in viscosity would increase the time-dependent strain, particularly at high applied stresses.

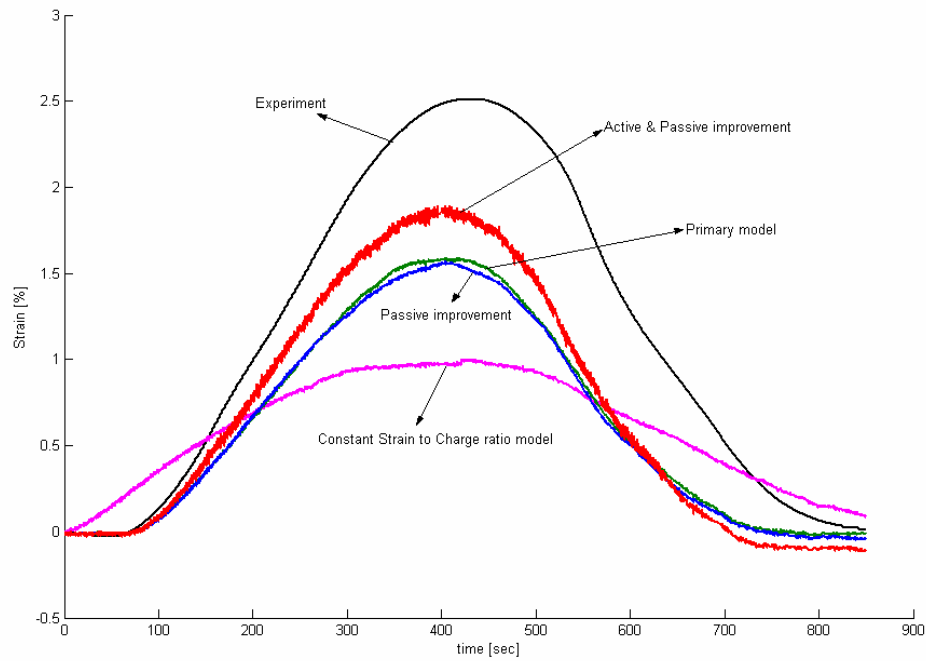


Figure 5.5.1 Stress 0.450 MPa and 1 mHz.

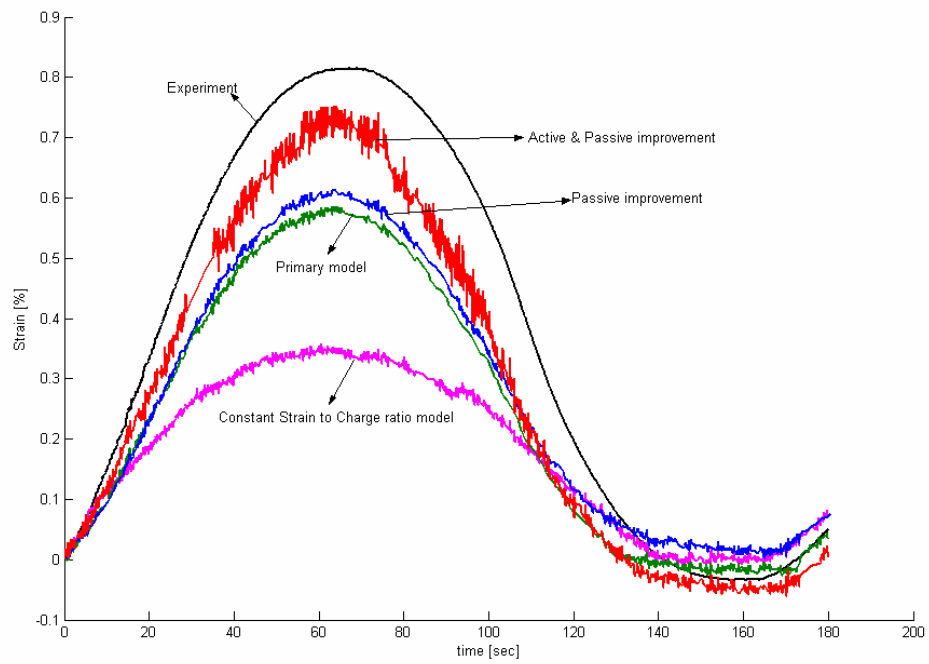


Figure 5.5.2 Stress 0.450 MPa and 5 mHz.

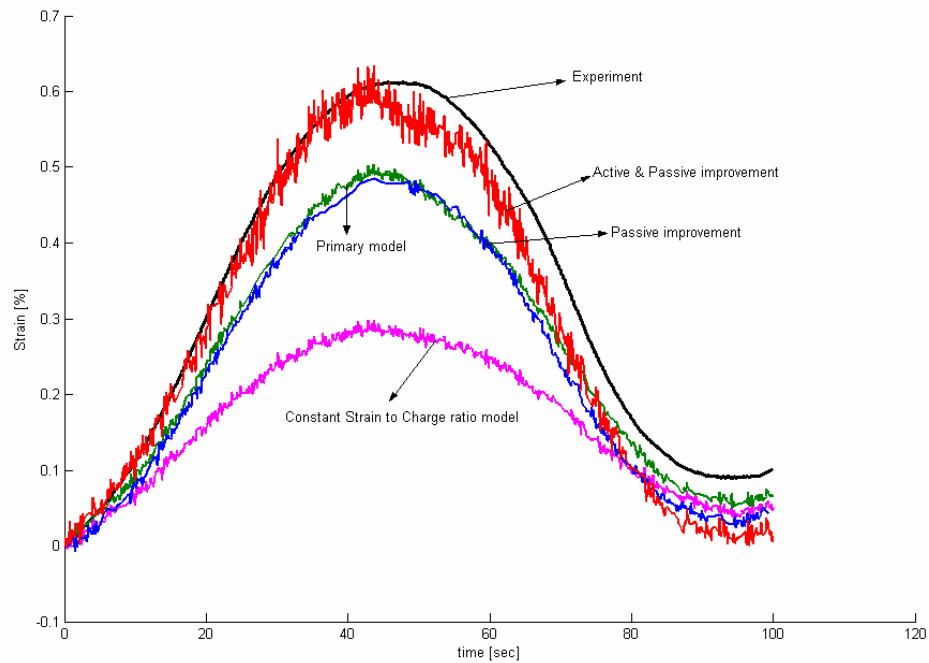


Figure 5.5.3 Stress 0.450 MPa and 10 mHz.

Figure 5.5.4 to Figure 5.5.6 show the results in which a high external load has been applied to the polymer and large creep behaviour observed. The ‘active and passive improvement’ predicts a larger strain than the ‘passive improvement’ model at all times. This higher strain can be related to the lower modulus and viscosity parameters that are included in the ‘active and passive improvement’. At low stimulation frequencies, the active and passive improvement model quite closely tracks the experimental data. At higher stimulation frequencies, the experimental data is more complicated and is only approximately tracked by the predicted results.

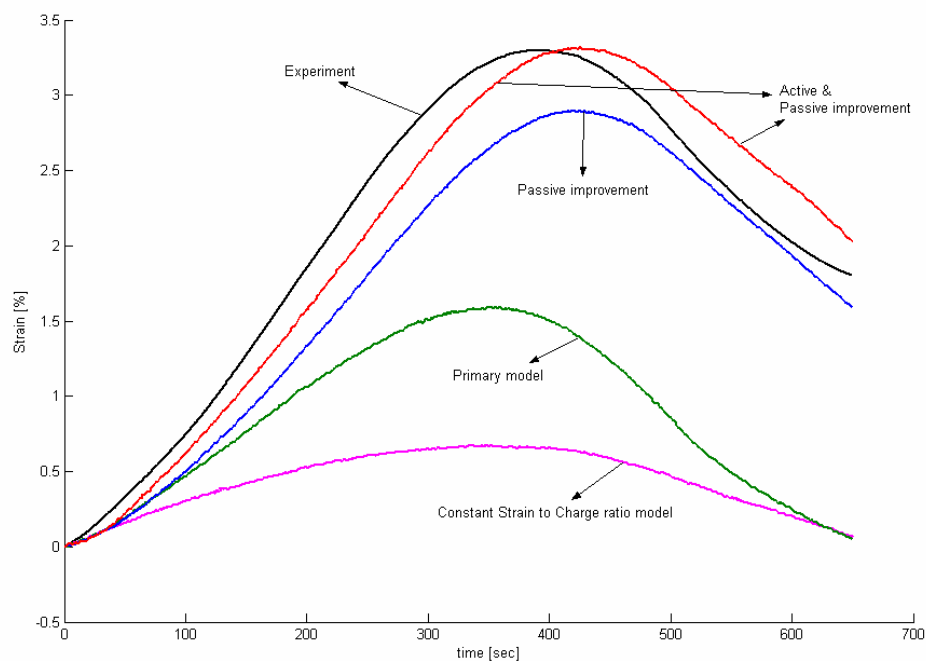


Figure 5.5.4 Stress 3.250 MPa and 1 mHz.

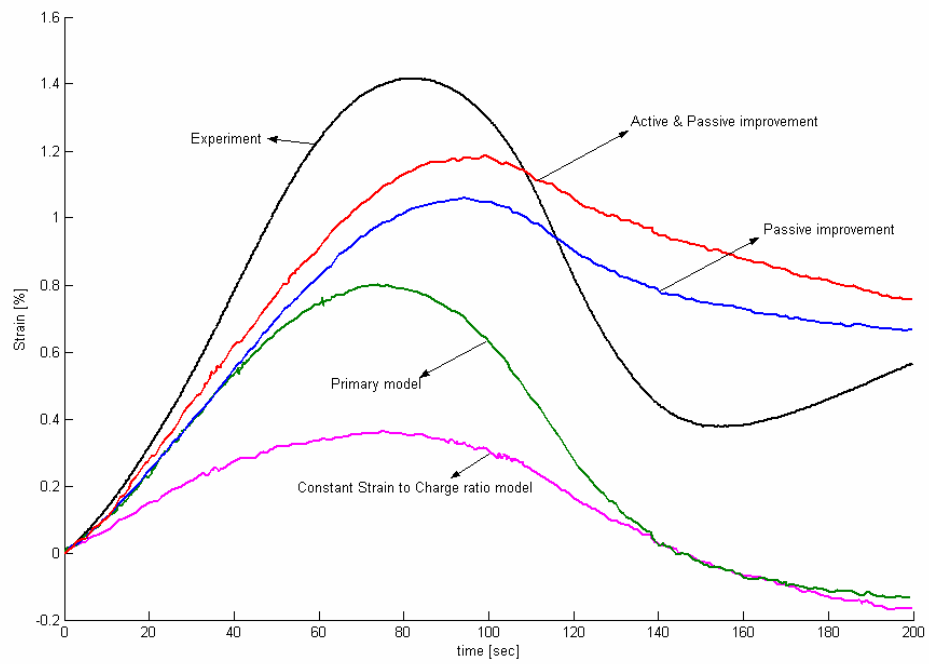


Figure 5.5.5 Stress 3.250 MPa and 5 mHz.

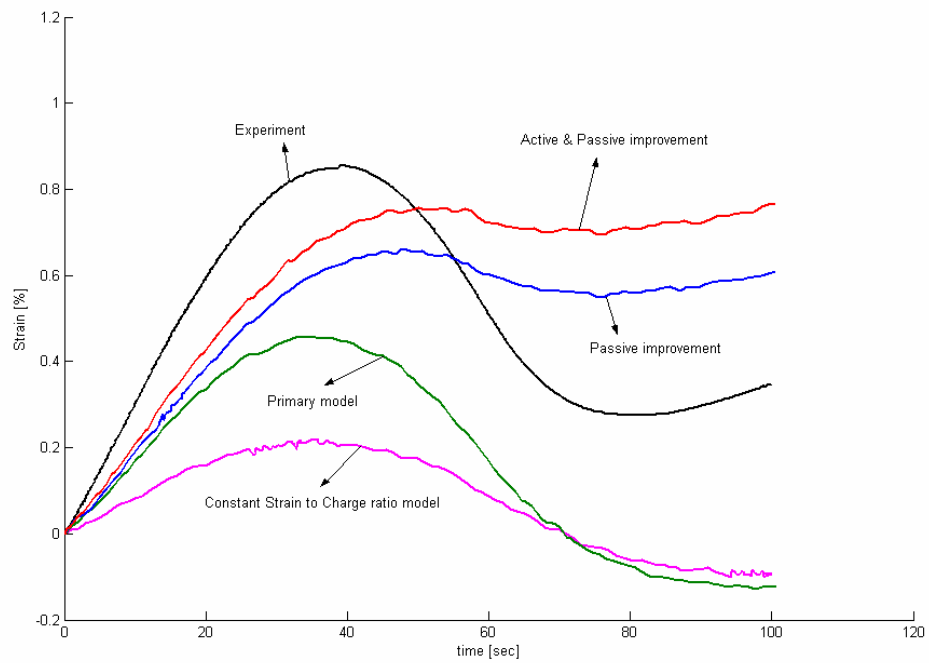


Figure 5.5.6 Stress 3.250 MPa and 10 mHz.

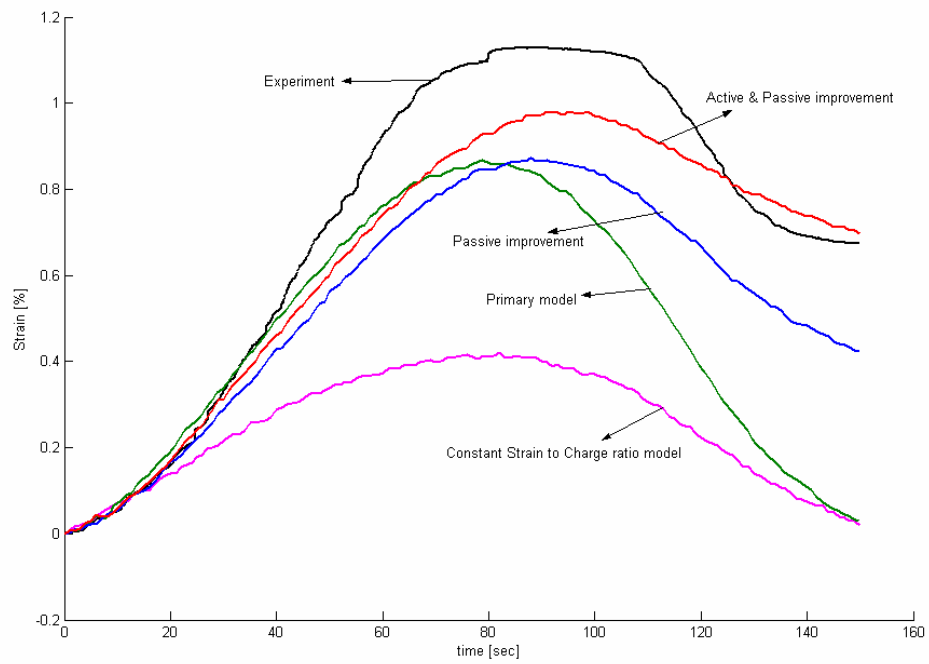


Figure 5.5.7 Stress 5.8 MPa and 5 mHz.

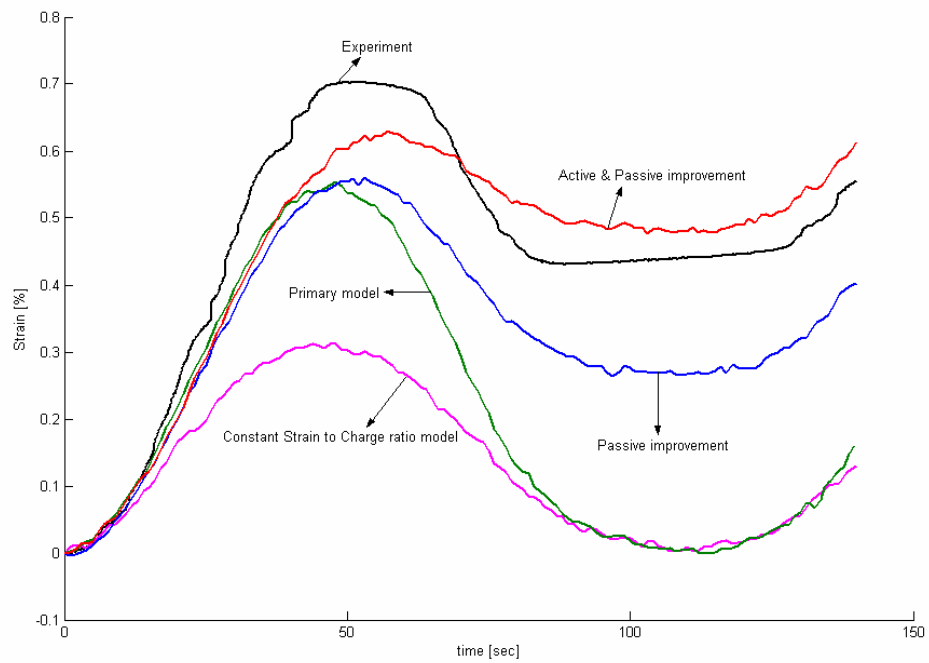


Figure 5.5.8 Stress 5.8 MPa and 10 mHz.

The results of experiments and stimulation at the highest applied stress are given in Figure 5.5.7 and Figure 5.5.8 for two different stimulation frequencies. The ‘active and passive improvement’ model again predicts a higher strain at all times. The agreement between this model and the experimental data is much improved. The overall shape and magnitude of the strain vs. time curve is more closely predicted by the model.

5.6. Conclusions

In the research presented in this chapter, the mechanical properties of the PPy helix tube have been determined at different applied voltages. These mechanical properties have then been used to calculate the strain response under load and added to the electrochemical strain to give the ‘active and passive improvement’ model. A high frequency square wave isotonic stress was employed to compute the total stiffness coefficient, viscosity coefficient and the first viscoelastic time constant values and the accuracy of the results has been confirmed by comparison with the Dynamic Mechanical Analyser instrument.

Results demonstrate that there is a directly proportional relationship between doping level variation and the total stiffness coefficient, viscosity coefficient and the first viscoelastic time constant of the actuator. The modulus changes in a complex manner with doping level, reflecting the effect of volume changes and inter-chain interaction. Similarly, the viscosity term also changes in a complex manner with doping.

The phenomena can be modelled using the fact that the viscoelastic elements coefficients decrease almost linearly during oxidation while the actuator is expanding and increase almost linearly during reduction while the actuator is contracting.

Finally, experimental data from sinusoidal stimulation have been simulated using the ‘active and passive improvement’ model. This model is significantly more accurate compared with the ‘passive improvement’ model. In many cases, the experimental data was closely tracked by the predicted results of the ‘active and passive improvement’ model. It can be concluded that the changes in mechanical properties of the polymer make significant contributions to the strain response when an external load is applied.

CHAPTER 6: QUARTZ CRYSTAL MICROBALANCE STUDY OF MASS CHANGES AND MODULUS SHIFT IN ELECTROCHEMICALLY SWITCHED POLYPYRROLE

6.1. Introduction

The frequency response shift of a quartz crystal resonator caused by deposition of a thin layer has created methods which have been broadly used to study film properties (Bandey et al., 1999). Devices including a thin AT-cut quartz crystal plate stimulated harmonically by an electronic driver have been fabricated to sense the deposited layer mass and such devices are known as quartz crystal microbalances (QCM). The conventional application of QCM devices is to detect nano-scale mass changes on the working surface as shown in Figure 6.1.1.

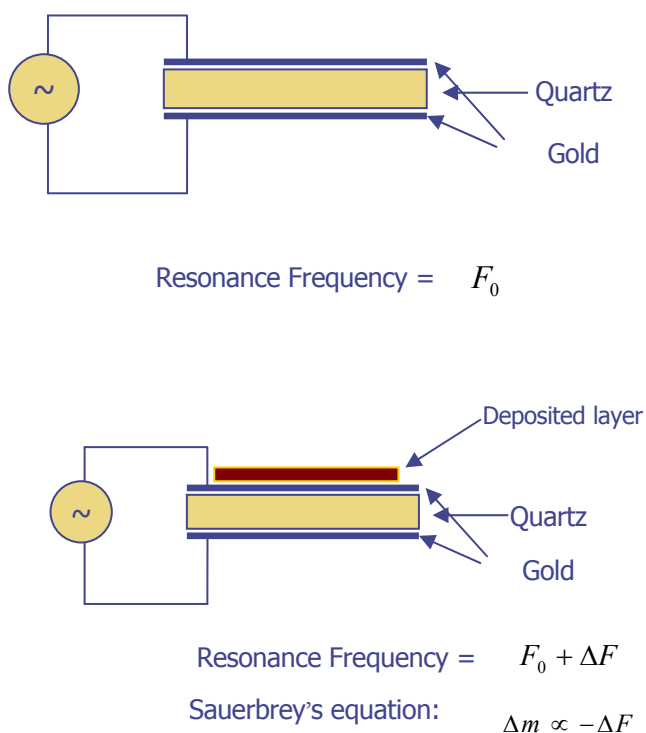


Figure 6.1.1. (Top) Bare Crystal oscillates at its natural frequency (F_0). (Bottom) A deposited layer causes a shift in the natural frequency (ΔF) which is proportional to the mass of the layer as determined by Sauerbrey's equation (Sauerbrey, 1959).

The analysis of a rigid thin deposited layer at the gas/solid interface is described by the well-known Sauerbrey's equation. This equation states that the mass change of the layer is proportional to the shift in resonance frequency (Sauerbrey, 1959). More recently, researchers have been attempting to understand the influences of non rigid films and liquid/solid interfaces on the resonator response. The behaviour of the QCM in a liquid environment was quantitatively formulated by Kanazawa and Gordon (Kanazawa and Gordon, 1985). However, the surface layer properties of the deposited film have been known to influence the QCM response for fully elastic and fully viscous cases since 1985 (Kanazawa and Gordon, 1985). In recent years, the aim of QCM modelling research has been to formulate the surface properties of viscoelastic layers since it has been observed frequently that the viscoelasticity of the deposited layer on the crystal surface causes a deviation from Sauerbrey's equation (Bandey et al., 1997).

Electrochemical QCM has proved useful for studying the behaviour of conducting polymer films. For example, a QCM operated using the impedance spectroscopy approach was used to observe the viscoelastic changes during deposition of polybithiophene (PBT) conducting polymer by Hillman and co-workers (Gidley et al., 1991). They did not relate the output signals of the QCM to the shear modulus and thickness of the film. Equivalent circuit models, such as the Butterworth van Dyke (BVD) or transmission line models, have been used to interpret QCM outputs ΔR (the change in admittance of the Electrical equivalent model of the QCM system) and ΔF the PBT film mechanical characteristics in interface with the solution (Bandey et al., 1997). More generally, the mechanical impedance of finite and infinite multi layers of elastic, viscous and viscoelastic materials have been summarised and formulated by Bandey *et al.* (Bandey et al., 1999). This work has shown that the QCM provides an opportunity to detect the viscoelastic properties of the deposited layer. This technique has been developed and applied to study different physical phenomena of polythiophene (Cooper et al., 2004, Lagier et al., 2005, Hillman et al., 2005, Theisen et al., 2004, Hillman, 2003, Hillman et al., 2002, Hillman et al., 2001, Martin et al., 2000, Brown et al., 2000). Similarly, the QCM has been used to determine the viscoelastic parameters of a deposited film during thermo mechanical analysis of polymers, (Lucklum and Hauptmann, 1997, Behling et al., 1998, Behling et al., 1999, Lucklum and Hauptmann, 2000a, Lucklum and Hauptmann, 2000b, Lucklum et al., 2000, Lucklum et al., 2001, Lucklum and Hauptmann, 2001).

The aim of the present chapter is to determine how the shear modulus and polymer thickness changed during cyclic voltammetry of polypyrrole in two different electrolytes: tetrabutyl ammonium hexafluorophosphate (TBA-PF₆) in propylene carbonate (PC) and an ionic liquid (IL), 1-ethyl, 3-methyl imidazolium trifluoromethane sulfonimide (EMI-TFSI) (Randriamahazaka et al., 2005a, Randriamahazaka et al., 2005b, Matsumoto et al., 2003). In the following, firstly the materials (section 6.2.1) and experimental set up (section 6.2.2) are described then the mathematical methodology (section 6.2.3) is explained and verified (section 6.3) and finally results are presented and discussed for both electrolytes PC (section 6.4.1) and IL (section 6.4.2).

6.2. Materials and Methods

6.2.1. Materials

Propylene carbonate (PC) (Aldrich) and tetrabutylammonium hexafluorophosphate (TBA-PF₆) (obtained from Sigma) both of AR grade were used. Pyrrole monomer from Merck was distilled and stored under nitrogen at -18°C before use. The constant current required for polymerisation was supplied using an EG & G Princeton Applied Research Model 363 potentiostat / galvanostat. Polypyrrole (PPy) films were grown galvanostatically with a 0.15 mA/cm^2 current density. The polymerisation solution was PC containing 0.06 M Pyrrole and 0.05 M TBA-PF₆. The polymerization temperature was controlled to around 0°C because the operational temperature of the QCM device is 0°C to 40°C . The reference electrode was Ag wire in 0.01 M AgNO₃ and 0.1M TBA-PF₆ in acetonitrile (ACN) using 0.1 M TBA-PF₆ in PC as a salt bridge which is equal to $+0.30\text{ V}$ vs. aqueous Saturated Calomel Electrode (aq. SCE) (Meites, 1963). All the experimental data was processed and recorded by MacLab/4e AD instruments and computer.

The QCM was a Stanford Research Systems QCM200 with an electrochemical bath with liquid electrolyte and equipped with a Capacitance Cancellation system. The physical parameters of the device are as follows, $C_1 = 33\text{ fF}$, $L_1 = 30\text{ mH}$ and the crystal area is 1.37 cm^2 for electrical calculation and 0.4 cm^2 for viscoelastic measurement.

6.2.2. Experimental methodology

The experimental set up is shown in Figure 6.2.1, illustrating the QCM electrode on which a PPy layer has been deposited, and subsequently stimulated by cyclic voltammetry. The output signals of QCM are the change in resonance frequency in Hz and the admittance variation parameter in Ohms.

The methodology of the experiment is explained in Figure 6.2.2, showing the signal divided into four regions. In the first region, the bare crystal is in air, the resonance frequency signal is 5 MHz and the frequency variation signal Δf is zero. In the next region, the crystal has been placed in the liquid environment, so that ΔR and Δf can be related to the viscosity and density of the electrolyte. This part of the experiment confirmed that the QCM is a very precise instrument for detecting the density and viscosity of both Maxwell's and Newton's liquids. Polymerisation has been carried out in the third step for 10 minutes; the frequency signal is varying while the admittance signal remains constant. The constant admittance signal guarantees that the deposited layer fits Sauerbrey's equation criteria so that the layer thickness using the frequency signal can be calculated. By comparing AFM thickness measurement and QCM output, polymer density has been calculated. Finally, the electrolyte was exchanged and actuation of the PPy was studied using cyclic voltammetry (CV).

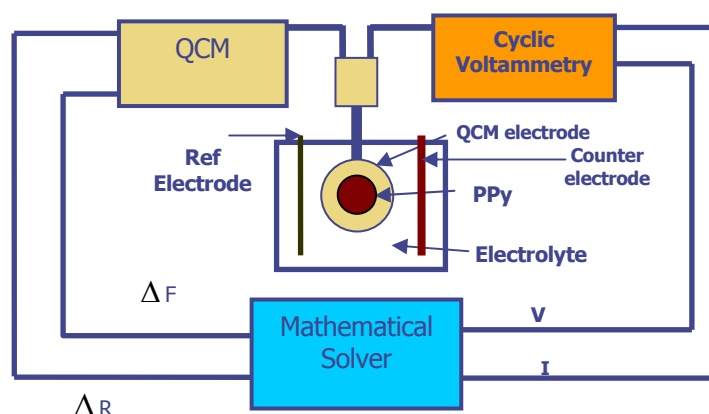


Figure 6.2.1. Experimental set up of a QCM crystal coated with PPy was stimulated using cyclic voltammetry at different scan rates. The QCM and electrochemical signals were used to determine viscoelastic variables using a mathematical solver.

At this point, both a change in frequency and admittance were detected during potential cycling. As explained in the next section, these outputs were related to changes in the polymer thickness and shear modulus, respectively.

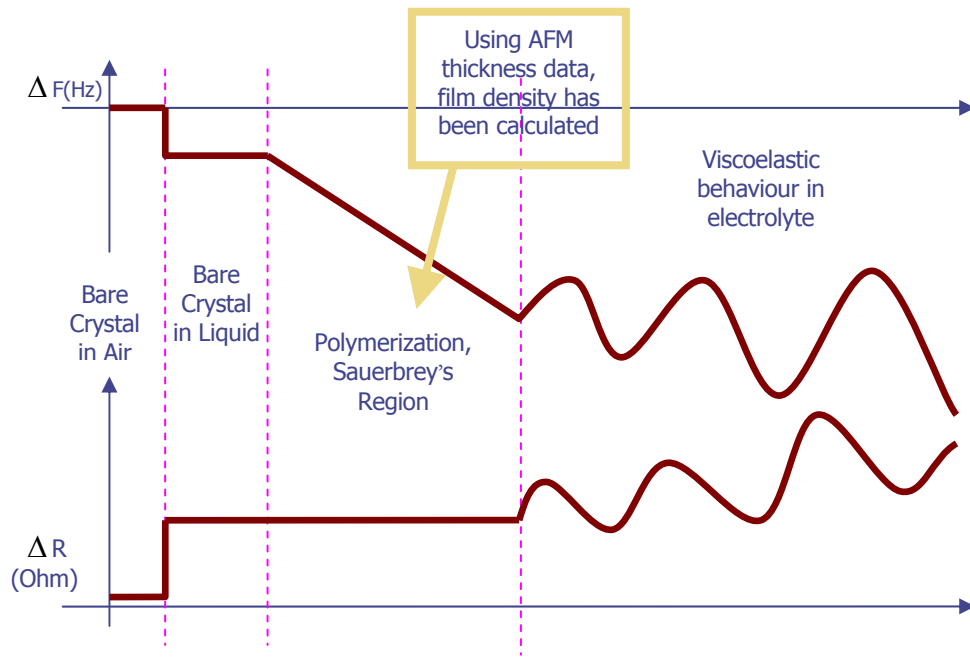


Figure 6.2.2. Experimental Method shows how the QCM device outputs changed during the experiment.

6.2.3. Numerical methodology

The next step after the experiment was the interpretation of the QCM output signals to produce the desired mechanical data. As shown in Figure 6.2.3, the output signals form complex (containing both real and imaginary parts) parameters which should be equalised with the mechanical impedance. This analysis is derived from a mathematical model of a viscoelastic layer deposited on an oscillating surface (Bandey et al., 1997, Bandey et al., 1999).

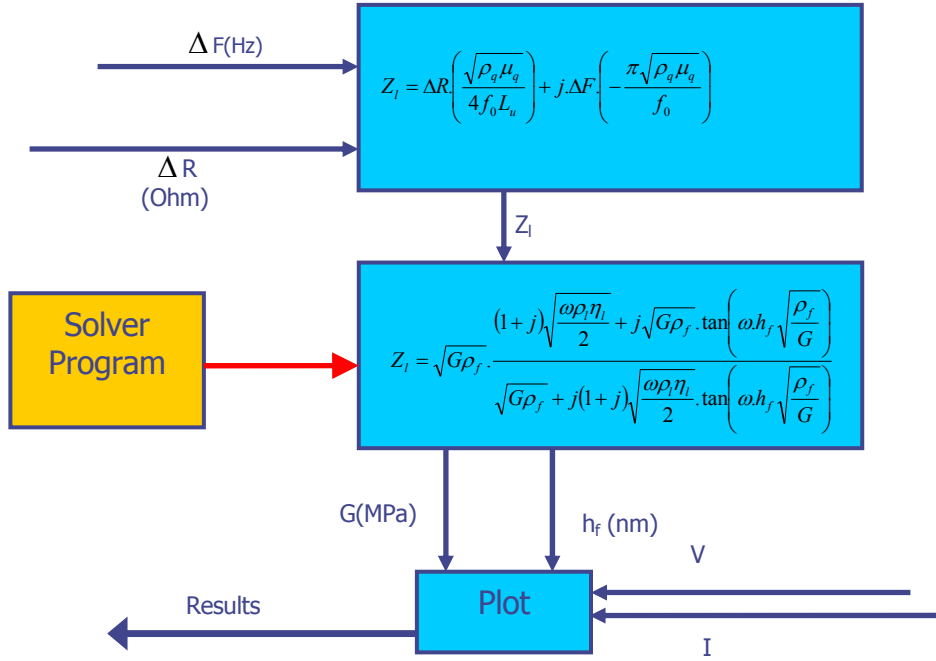


Figure 6.2.3. Numerical methodology, in which the measured signals build a complex impedance parameter, which should be equal to the theoretical complex impedance as calculated in the literature (Bandey et al., 1997, Bandey et al., 1999). A program has been designed to solve the equation and find the variables shear modulus (G) and polymer thickness (h_f).

The unknown parameters in this calculation are the real part of the shear modulus of the polymer and its thickness. The imaginary part of the shear modulus is set to zero based on dynamic mechanical analysis which was done on a PPy fibre and is shown in Figure 6.2.4. This analysis confirms that the phase angle of PPy tends to zero above 10 Hz so that the imaginary part of the modulus is close to zero at the 5 MHz QCM frequency.

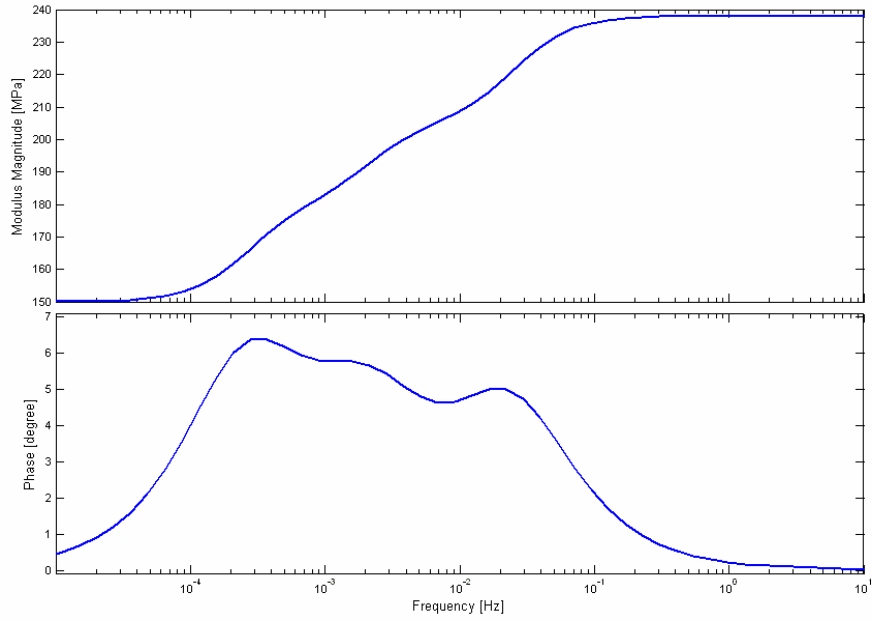


Figure 6.2.4 Dynamic mechanical analysis of a PPy fibre.

A solver program has been designed to solve the real and imaginary parts of this equation as a simultaneous system of equations in MATLAB[®] software. In the equations shown in Figure 6.2.3, $\rho_q = 2.648 (gr.cm^{-3})$ and $\mu_q = 2.947 \times 10^4 (MPa)$ are the density and shear modulus of the quartz crystal, respectively as specified in the data sheet. Additionally, f_0 is the initial frequency of QCM (5 MHz) and $L_u = 47.4 (mH)$ is the inductance of unloaded crystal.

Moreover, $\rho_f = 1.0956 (gr.cm^{-3})$, ρ_l and η_l are the film density, electrolyte density and electrolyte viscosity in Bandy's impedance equation, respectively. The liquid density and viscosity are respectively $1.2706 (gr.cm^{-3})$ and $2.58 (cP)$ for propylene carbonate electrolyte and $1.3906 (gr.cm^{-3})$ and $19.34 (cP)$ for EMI-TFSI Ionic Liquid, as determined from manufacturer data sheets and viscosity measurements.

6.3. Verification of the methodology

The method verification has been carried out on both sections, a) electro-polymerisation which provides us polymer density and b) numerical methodology which analyses the two output signals of the QCM device to calculate the two physical parameters: polymer thickness and shear modulus.

6.3.1. Verification of polypyrrole film mass per area

The deposited polypyrrole film mass per area has been determined by two independent methods to verify the QCM results. The film mass per area has first been calculated using the charge transferred during electro-polymerisation. Secondly, the film mass per area has been calculated by Sauerbrey's equation, as explained in Figure 6.2.2 (polymerisation section). Then mass per area from both methods can be used to calculate film density by measuring the film thickness by AFM and dividing the mass per area by thickness.

The polymerisation has been carried out galvanostatically at 0.15 mA.cm^{-2} current density. Since the area of the quartz crystal is 1.37 cm^2 , the current was 0.2055 mA . The charge transferred was 0.185 C over the 15 minutes of electro-polymerisation time. The next step is to determine the mass of PPy deposited from the known electrochemical reactions occurring. The electrons consumed per monomer of pyrrole is 2.3 (Madden, 2000), so the number of monomers is equal to transferred charge divided by total charge extracted from a monomer during polymerization, which is equal to the charge of a single electron ($1.602 \times 10^{-19} \text{ C}$) multiplied by the number of electrons per monomer (2.3). The number of monomers of pyrrole (N_{py}) is estimated to be 5.0×10^{17} as shown in Equation 6.3.1.

$$N_{py}(\text{monomer}) = \frac{0.185(\text{C})}{1.602 \times 10^{-19} \left(\frac{\text{C}}{\text{electron}} \right)} \cdot \frac{1}{2.3 \left(\frac{\text{electron}}{\text{monomer}} \right)} \quad \text{Equation 6.3.1}$$

The molecular weight of a monomer of Pyrrole and PF_6 is 0.067 and 0.145 kg/mol respectively (Madden, 2000). The mass of deposited PPy (M_{ppv}) is equal to the number of Pyrrole monomers multiplied by the molecular weight of Pyrrole monomer (minus two protons) divided by Avogadro's constant ($6.023 \times 10^{23} \text{ mol}^{-1}$), which is equal to $5.585 \times 10^{-8} \text{ kg}$ as shown in Equation 6.3.2.

$$M_{ppv}(\text{gr}) = N_{py}(\text{monomer}) m_{py} \left(\frac{\text{gr}}{\text{mol.monomer}} \right) \cdot \frac{1}{\text{Avg} \left(\frac{1}{\text{mol}} \right)} = 5.02 \times 10^{17}(\text{monomer}) \times 0.067 \left(\frac{\text{gr}}{\text{mol.monomer}} \right) \cdot \frac{1}{\text{Avg} \left(\frac{1}{\text{mol}} \right)} \quad \text{Equation 6.3.2}$$

The same calculation procedure can be replicated for the mass of dopant (M_{dopant}) as follows: the number of dopants is equal to (Electrons per monomers – 2) multiplied by

the number of monomers of pyrrole (N_{Py}). In total, the mass of PPy polymer and dopant is estimated to be 9.211×10^{-8} kg using Equation 6.3.3.

$$M_{dopant}(gr) = \left(N_{\frac{electron}{monomer}} - 2 \right) N_{Py} (monomer) m_{PF_6} \left(\frac{gr}{mol.monomer} \right) \cdot \frac{1}{Avg \left(\frac{1}{mol} \right)} =$$

$$0.3 \times 5.02 \times 10^{17} (monomer) \times 0.145 \left(\frac{gr}{mol.monomer} \right) \cdot \frac{1}{Avg \left(\frac{1}{mol} \right)}$$

Equation 6.3.3

In addition to the polymer, the deposited layer also contains considerable solvent. The mass of the polymer is approximately 60 percent of the total mass of the deposited film including the mass of diffused solvent (Madden, 2000), so that the total mass of doped PPy including solvent is estimated as 9.211×10^{-8} kg / 0.6 = 1.535×10^{-7} kg. The PPy mass per area is obtained by dividing total mass of PPy 1.535×10^{-7} kg by the area of the layer 1.37 cm^2 and is equal to 1.1×10^{-4} gr/cm².

In order to calculate the mass per area experimentally, PPy has been deposited on three different quartz crystals and the mass per area of the film was measured by the QCM using Sauerbrey's equation. The frequency change (Δf) for the same crystal mentioned in this section was 4604.375Hz which is equal to 8.14×10^{-5} gr/cm² mass per area.

Finally, the polymer density has been estimated in both cases by dividing mass per area values by the film thickness which was measured by AFM and is equal to 742.5nm for the sample used for QCM experiment, and 970 nm for the first sample crystal used in the calculation. The polymer density is equal to 1.0956gr/cm³ from experiment and 1.155gr/cm³ from calculation. The error of 5.1% shows the good agreement between charge analysis estimation and QCM experiment.

6.3.2. Confirming calculated film modulus and thickness using standard polymer films

Two well characterised polymers were used to verify the QCM measurements and analysis method for determining film thickness and shear modulus. The two polymers chosen had very different moduli: polystyrene (PS) from Polysciences Inc. (density 1050kg/m³, Young's modulus 3.6GPa and Poisson's ratio 0.33 (Brandrup et al., 1989)) and Styrene-Isobutylene-Styrene (SIBS) from Boston Scientific (density 950kg/m³ with Young's

modulus 99.7MPa and Poisson's ratio 0.33 (Kwee et al., 2005)). Each polymer was dissolved separately in toluene from Sigma Aldrich at 3wt% and 10wt%, respectively. Next, a layer of PS on one crystal and SIBS on another was spin-coated onto both quartz crystals and Si wafers from Compant Technology Ltd. These were first cleaned in a UV cleaner for 40 minutes, at a speed of 1300 RPM for 1 minute, and annealed at 110°C in vacuum for 2 hours.

The film thickness of PS and SIBS on the Si wafers was measured using an Ellipsometer from Rudolph Research/AutoEL and it has been assumed that the film thickness is the same on the Si wafer as on the quartz crystal, since both substrates were coated identically. The measured thickness of the PS layer was 314.9nm and of the SIBS layer was 704.7nm.

Since the shear modulus can be calculated from Young's modulus and Poisson's ratio in an isotropic material using the following equation, $G = \frac{E}{2(1+\nu)}$, the shear modulus for PS and SIBS are 1.35 GPa and 37.48 MPa, respectively.

Table 6.3-1 QCM results on PS and SIBS samples.

Material	Output signal	Before annealing	After annealing
SIBS	$\Delta f(Hz)$	-3767	-3762
	$\Delta R(\Omega)$	-11.98	-10.24
PS	$\Delta f(Hz)$	-1849	-1790
	$\Delta R(\Omega)$	-1.62	-0.21

The QCM raw results and analysed data on PS and SIBS coated crystal before annealing and after annealing are presented in Table 6.3-1 and Table 6.3-2. The calculated values of both thickness and modulus agree very well with the independently measured thicknesses and the known moduli. The errors are well within the experimental accuracies of the instruments and procedures. These results confirm that QCM is able to accurately

determine the shear moduli of polymers having moduli covering the range from rubbery to glassy behaviour.

Table 6.3-2 The results for PS and SIBS properties.

Material	Shear modulus			Thickness		
	QCM	References	error	QCM	Ellipsometer	error
PS	1.34 GPa	1.35GPa	0.96%	301 nm	294.4	2.30%
SIBS	36.6 MPa	37.48MPa	2.37%	697 nm	704.7	1.12%

6.4. Results and Discussions

6.4.1. Electrochemical Switching of PPy in PC electrolyte

Figure 6.4.1, Figure 6.4.2 and Figure 6.4.3 show the shear modulus and thickness variation of PPy in PC electrolyte taken at 10, 20 and 50 mV/s scan rate from -1V to +1V (vs. Ag/Ag⁺ reference). Both patterns are reversible with a small hysteresis. Starting from -1V, expansion of the PPy film begins when an oxidation current occurs at approximately -0.5V. The oxidation of the PPy induces anions and solvent to enter the film causing swelling. The film continues to expand, however, after the oxidation peak has been reached, perhaps as a result of continuing electro-migration as recently described by Smela (Wang et al., 2004). Swelling also continues for a short time during the reverse scan due to kinetic delays and then the film contracts as a result of the reverse electro-migration and reduction of the polymer film causing the ejection of the counter ions and solvent. A small net increase in film thickness occurs after the complete oxidation / reduction cycle.

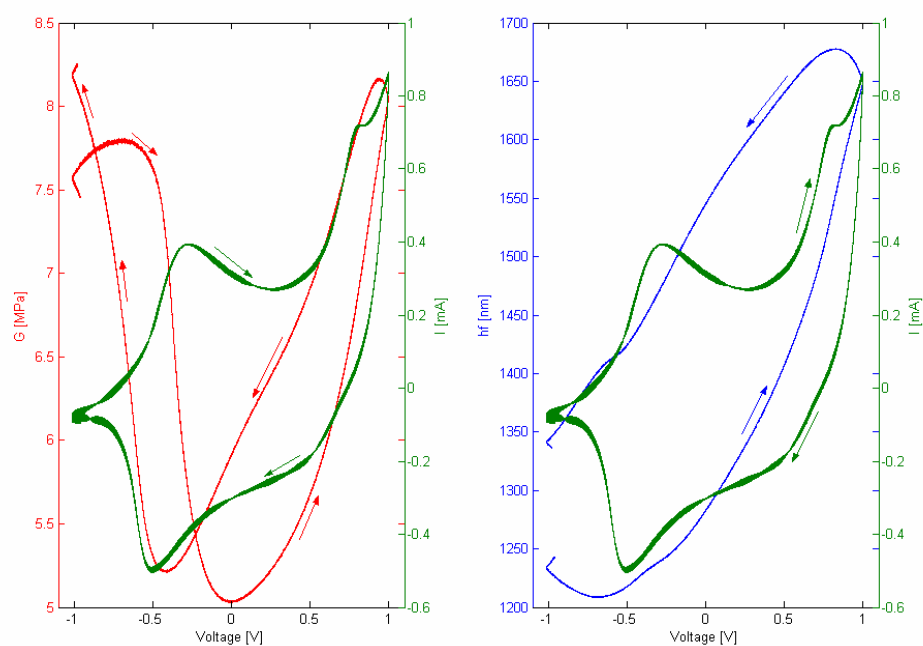


Figure 6.4.1 The real shear modulus variation and the thickness change are shown vs. voltage beside CV diagram (10mV/s scan rate) and 0.1M TBA-PF6 in PC electrolyte.

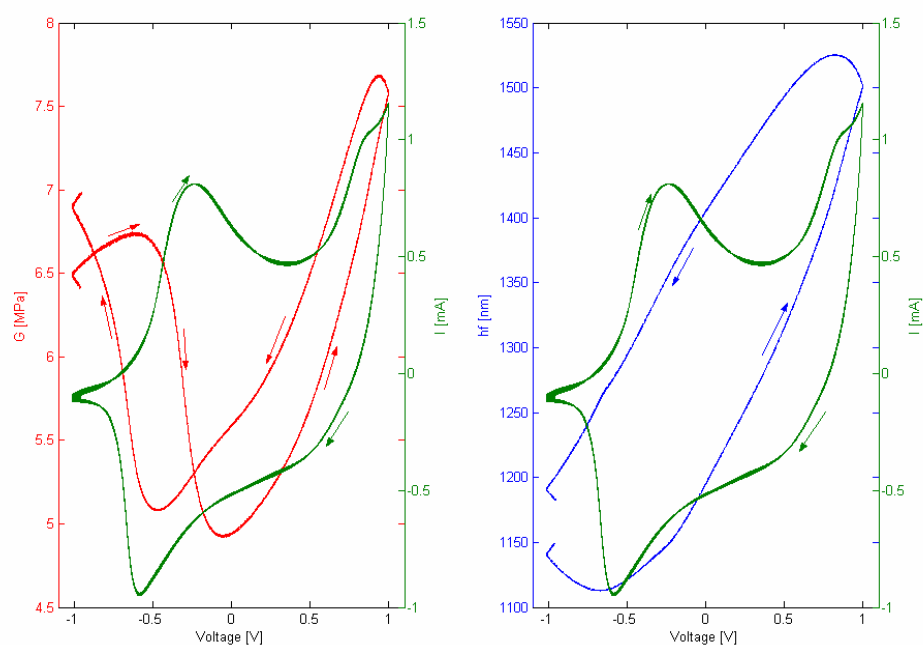


Figure 6.4.2 The real shear modulus variation and the thickness change are shown vs. voltage beside CV diagram (20mV/s scan rate) and 0.1M TBA-PF6 in PC electrolyte.

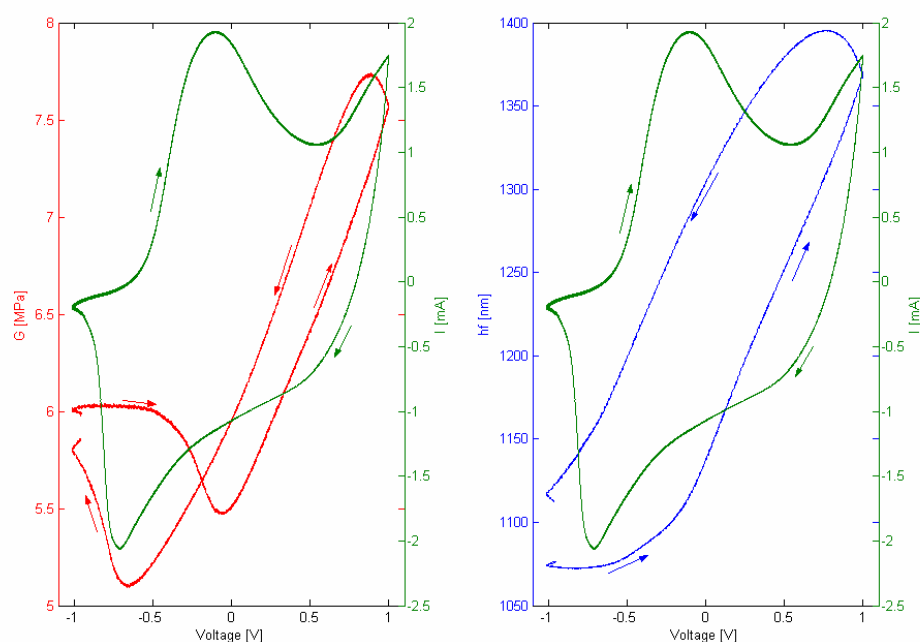


Figure 6.4.3. The real shear modulus variation and the thickness change are shown vs. voltage beside CV diagram (50mV/s scan rate) using 0.1M TBA-PF₆ in PC electrolyte.

In addition to the change in thickness, the QCM results show that the shear modulus also changes significantly during electrochemical cycling, as has also been observed in previous studies (Spinks et al., 2002, Della Santa et al., 1997a). The shear modulus changes between 5 and 8MPa, corresponding to elastic moduli of ~ 13 to ~ 21 MPa. These values are lower than measured in other studies on bulk films and fibres although the preparation conditions such as electro-polymerisation temperature and film thicknesses differ which may reflect a different structure formed in the different studies.

The change in the modulus value during CV cycling is approximately 25% but seems to involve two processes. From the fully reduced state, the modulus first decreases and then increases as the polymer is further oxidised. The initial decrease in modulus coincides with the start of polymer oxidation as shown by the increase in anodic current and increase in film thickness. It is possible that this swelling reduces the concentration of elastically-active network chains, therefore reducing the modulus. However, the charging of the chains would also stiffen the molecules therefore increasing the modulus. A third effect relates to the structural changes in PPy noted in X-ray diffraction studies (Warren

and Madden, 2006b). Here a distinct change in microstructure occurred at -0.2 V (vs. SCE or +0.1 V vs. Ag/AgNO₃) which coincides with a change in modulus noted in the present study. All three effects occur simultaneously and contribute to the complex changes in modulus observed. Further studies outside the scope of this thesis are required to identify and quantify all the processes occurring.

Similar experiments were repeated at slower scan rates and the results are summarised in Figure 6.4.4 and Figure 6.4.5. Only a very slight increase from 21% to 24% in the thickness change was observed as the scan rate decreased (Figure 6.4.5). The calculated change in thickness is of the order of 30%, which is similar to that reported previously for thickness direction actuation in PPy (Smela and Gadegaard, 1999). It appears, therefore, that nearly complete oxidation and reduction occurs at all scan speeds. The charge passed during the anodic scan was 67.5, 54.6 and 44.2mC for scan speeds 10, 20 and 50mV/s respectively. Figure 6.4.4 shows that a larger change in modulus was observed at lower scan rates. Both the initial decrease in modulus that occurs during the anodic scan that coincides with the onset of oxidation, and the subsequent increase in modulus show larger changes in value when the scan occurs more slowly. The reasons for these changes are not yet fully understood. Figure 6.4.6 shows CV diagram in different scan rates. Figure 6.4.7 to Figure 6.4.9 show the shear modulus variation vs. thickness and charge transferred parameters.

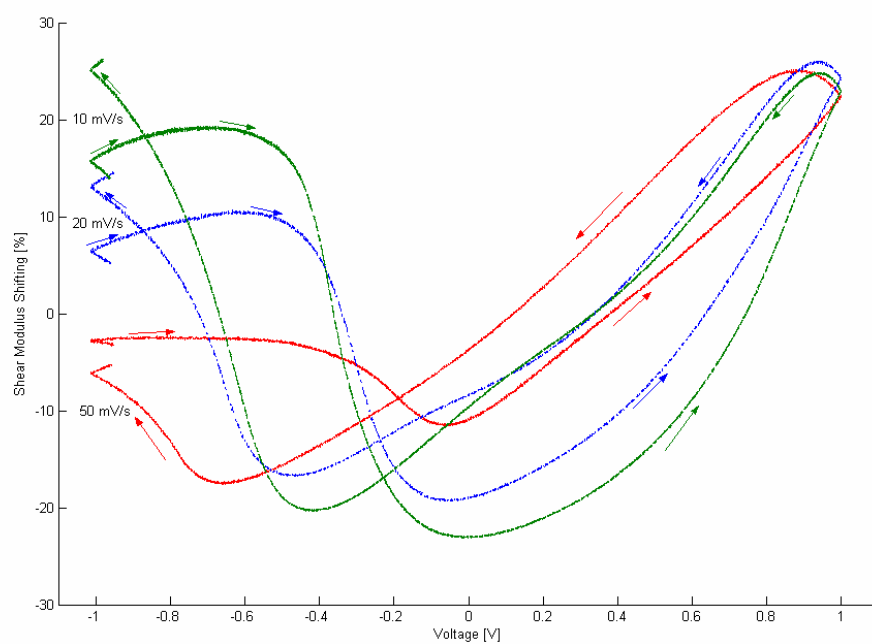


Figure 6.4.4 Change in shear modulus obtained at different scan rates and 0.1M TBA-PF6 in PC electrolyte.

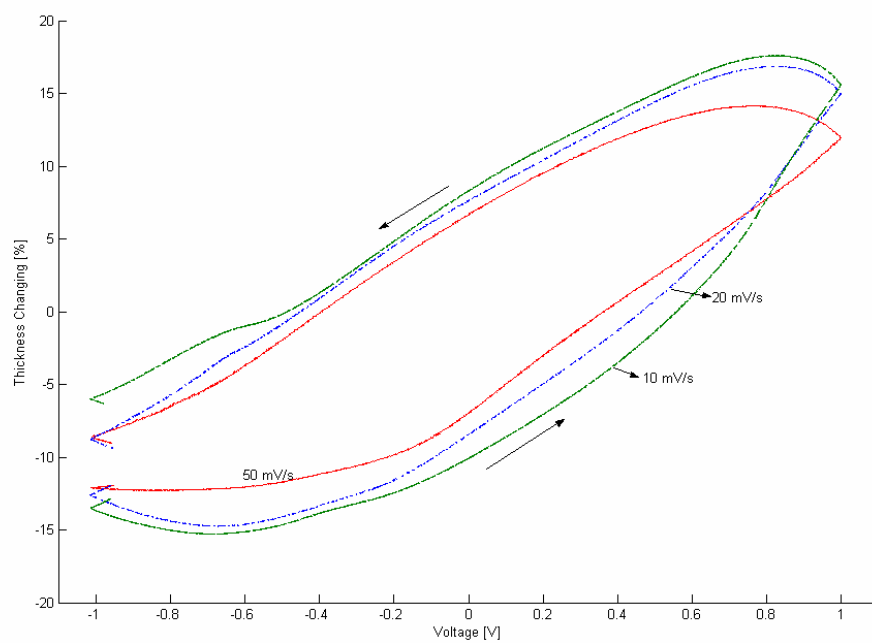


Figure 6.4.5 Change in thickness of PPy at different scan rates in 0.1M TBA-PF6 / PC electrolyte.

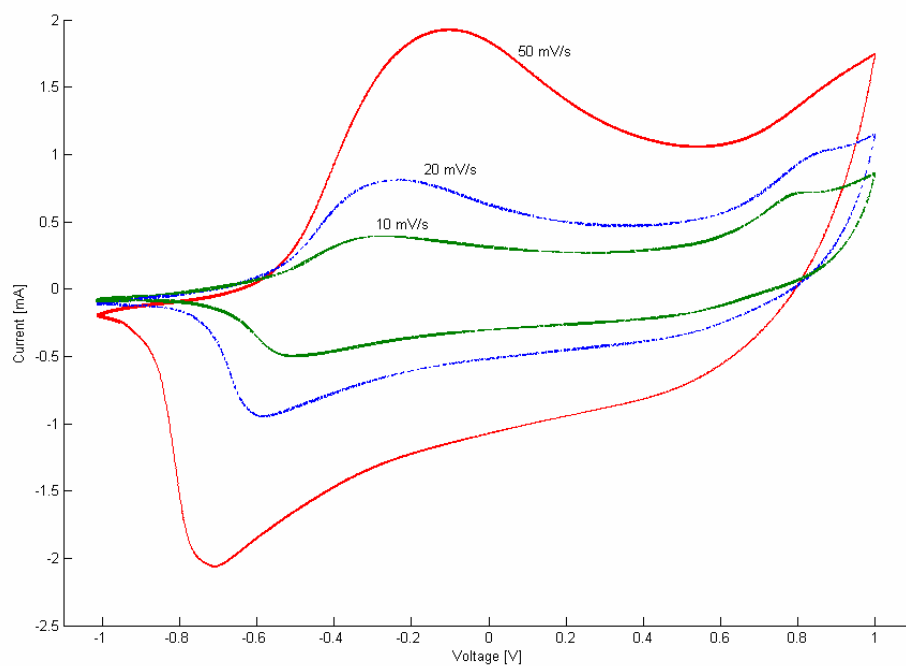


Figure 6.4.6 Cyclic Voltammograms of PPy at different scan rates in 0.1M TBA-PF6 / PC electrolyte.

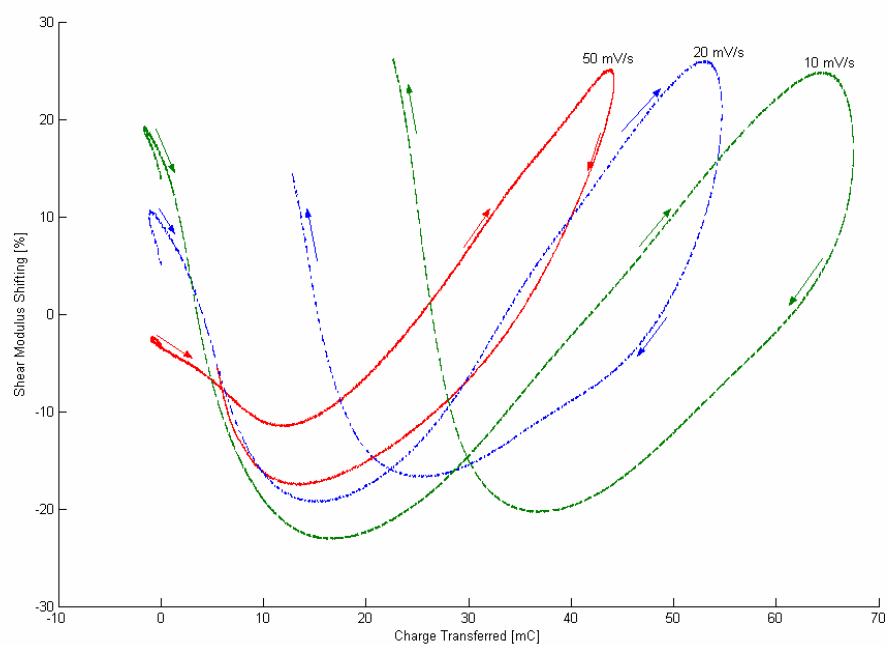


Figure 6.4.7 Change in shear modulus obtained at different scan rates and 0.1M TBA-PF6 in PC electrolyte vs. charge transferred.

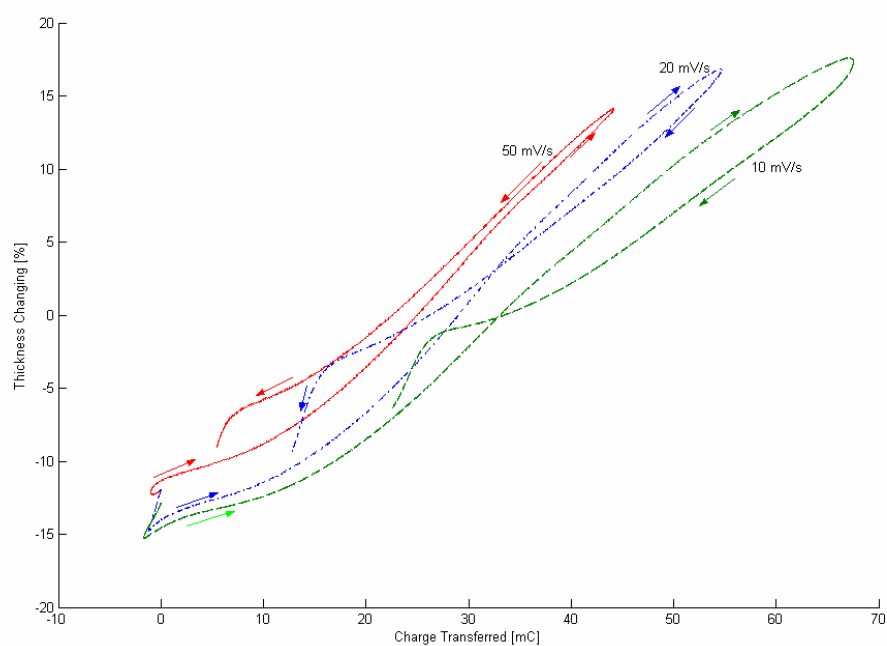


Figure 6.4.8 Change in thickness changing obtained at different scan rates and 0.1M TBA-PF6 in PC electrolyte vs. charge transferred.

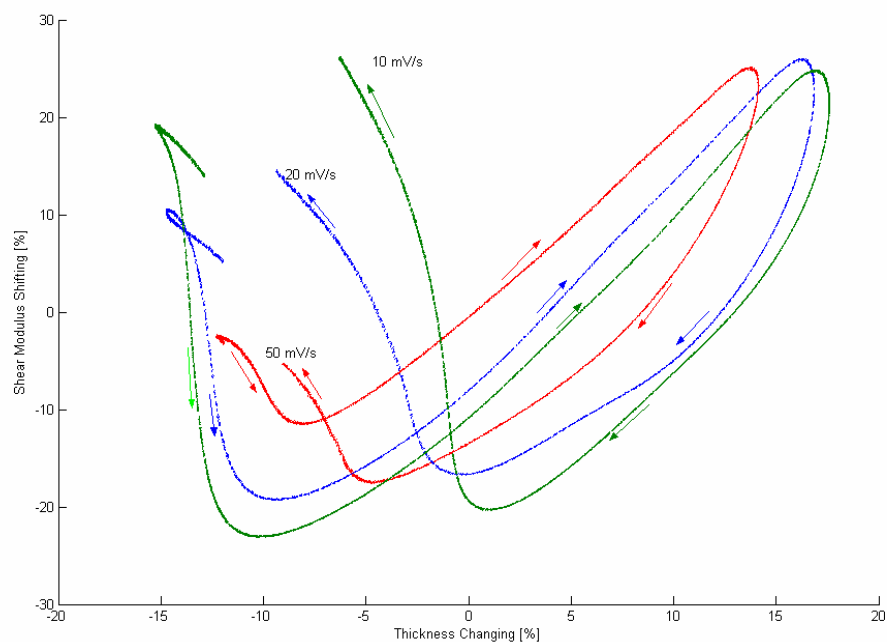


Figure 6.4.9 Shear Modulus vs. thickness changing of PPy at different scan rates in 0.1M TBA-PF6 / PC electrolyte.

6.4.2. Electrochemical Switching of PPy in Ionic Liquid (EMI-TFSI) electrolyte

Figure 6.4.10, Figure 6.4.11 and Figure 6.4.12 show the results of thickness, modulus and current obtained during electrochemical switching of PPy in ionic liquid electrolyte. Using this kind of electrolyte can eliminate the effects of solvent molecules diffusion into and out of the polymer. As expected, the maximum thickness change in the ionic liquid is about half of that obtained from PC electrolyte (almost 16%) and the swelling occurs in the reverse direction. It has been shown previously that cation movement dominates the actuation of PPy in EMI-TFSI (Randriamahazaka et al., 2005a, Matsumoto et al., 2003). As in the PC electrolyte, the change in scan rate had only a small effect on the change in thickness.

The CVs in both electrolytes were similar with oxidation peaks at $\sim 0.1\text{V}$ and reduction peaks occurring near -0.5V (vs. Ag/AgNO_3 reference electrode). The amount of charge passed during the oxidation process in IL is 25.4mC and compares with PC electrolyte of 44.2mC .

The modulus also changes significantly in the ionic liquid electrolyte. The absolute values of the shear moduli in ionic liquid are higher than measured in PC, which is perhaps due to the absence of swelling solvent in the ionic liquid. As shown in Figure 6.4.11, the change in modulus during the anodic sweep from -1V again shows an initial decrease in modulus followed by a larger increase. This behaviour is similar to that observed in the PC electrolyte. At the slower scan speed (Figure 6.4.13), the initial decrease in modulus is very small and the modulus shift is dominated by the increase that occurs above -0.3V . The shear modulus changed by as much as 45% at a scan rate of 20mV/s but this change was reduced to less than 20% when the scan rate increased to 100mV/s . Interestingly, the increase in modulus observed in both electrolytes at anodic potentials is not directly related to changes in volume. At these potentials, the volume is low in the ionic liquid but is high in the PC electrolyte. Further analysis is needed to fully elucidate the mechanisms for the modulus shift (Figure 6.4.14 to Figure 6.4.18).

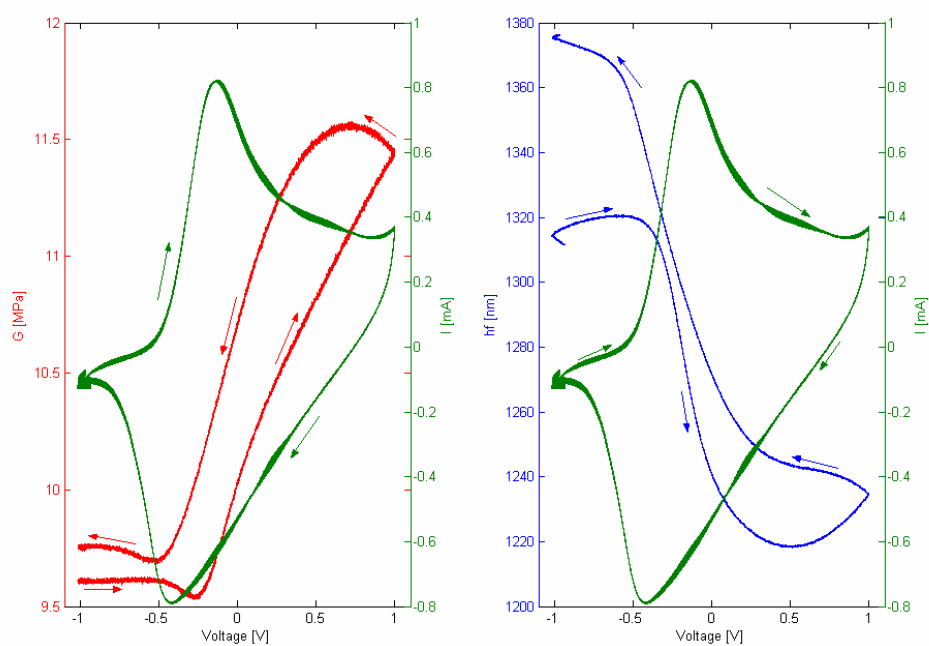


Figure 6.4.10 The shear modulus variation and thickness change obtained at 20mV/s scan rate in EMI-TSFI Ionic Liquid electrolyte. As expected, the thickness change in IL

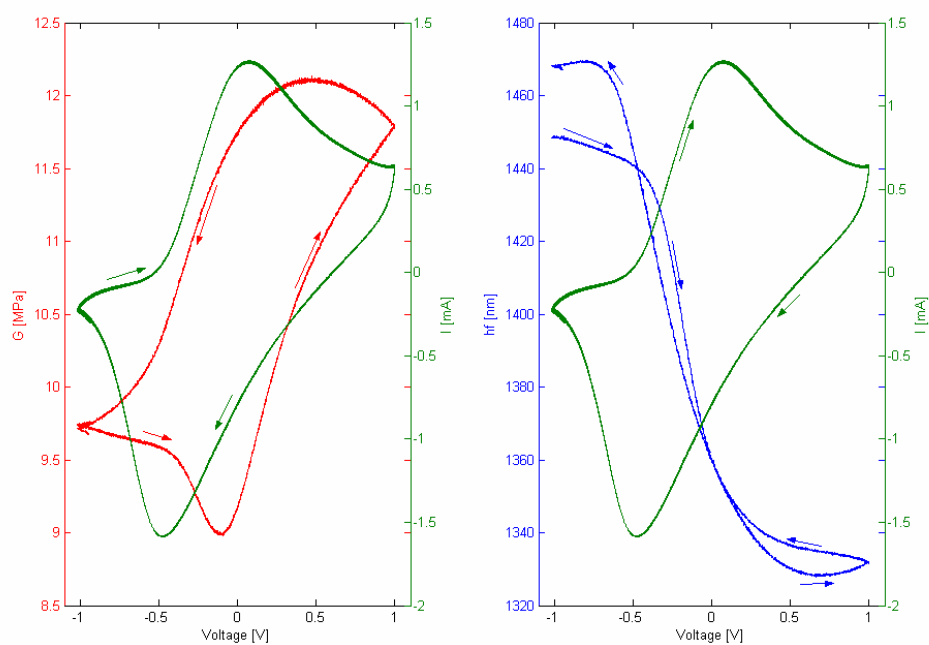


Figure 6.4.11. The shear modulus variation and thickness change obtained at 50mV/s scan rate in EMI-TSFI Ionic Liquid electrolyte. As expected, the thickness change in IL electrolyte is in the inverse direction compared to PC.

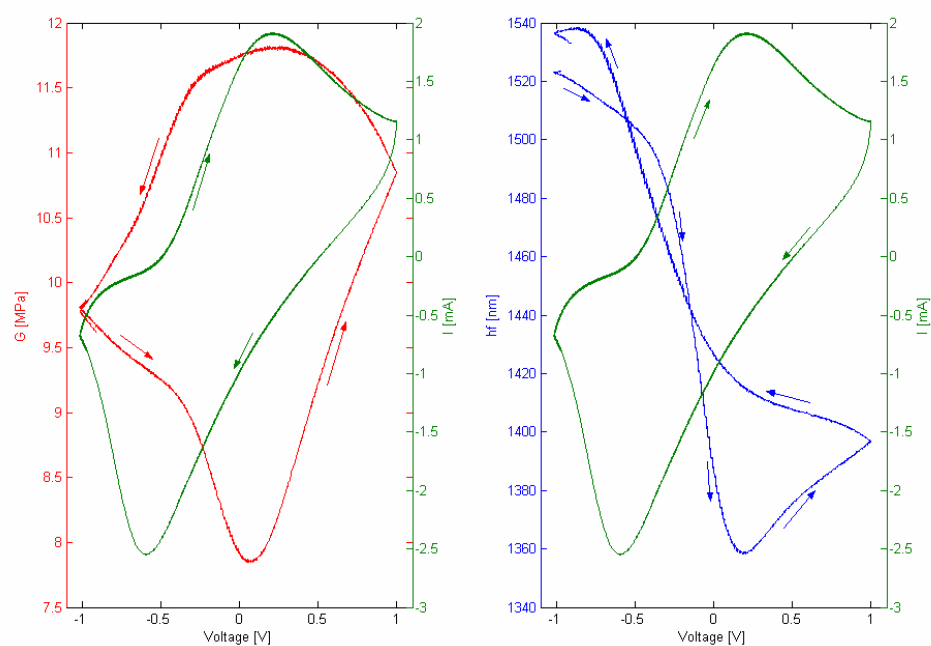


Figure 6.4.12 The shear modulus variation and thickness change obtained at 100mV/s scan rate in EMI-TSFI Ionic Liquid electrolyte. As expected, the thickness change in IL happened in negative voltage.

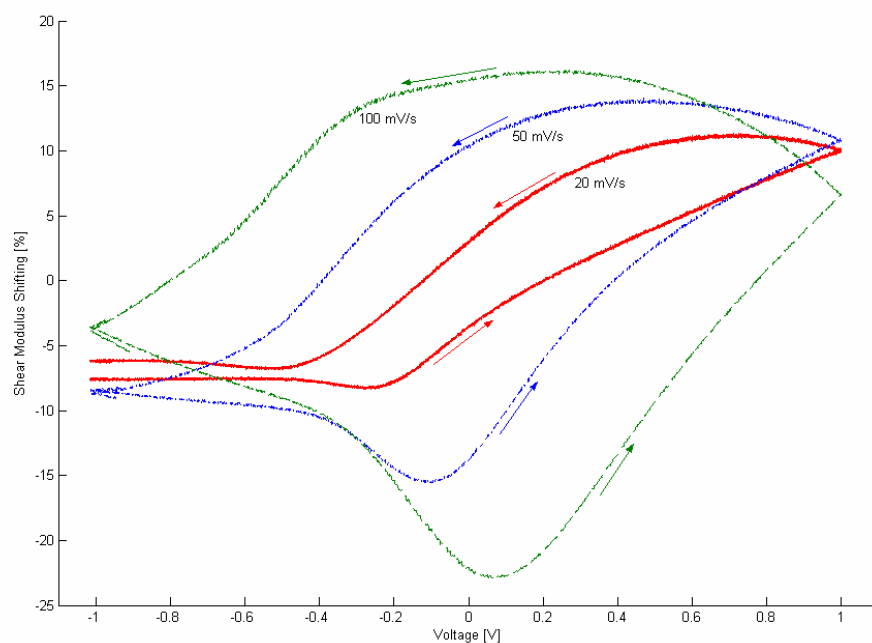


Figure 6.4.13. Shear modulus change in PPy during switching in EMI-TSFI Ionic Liquid electrolyte obtained at different scan rates

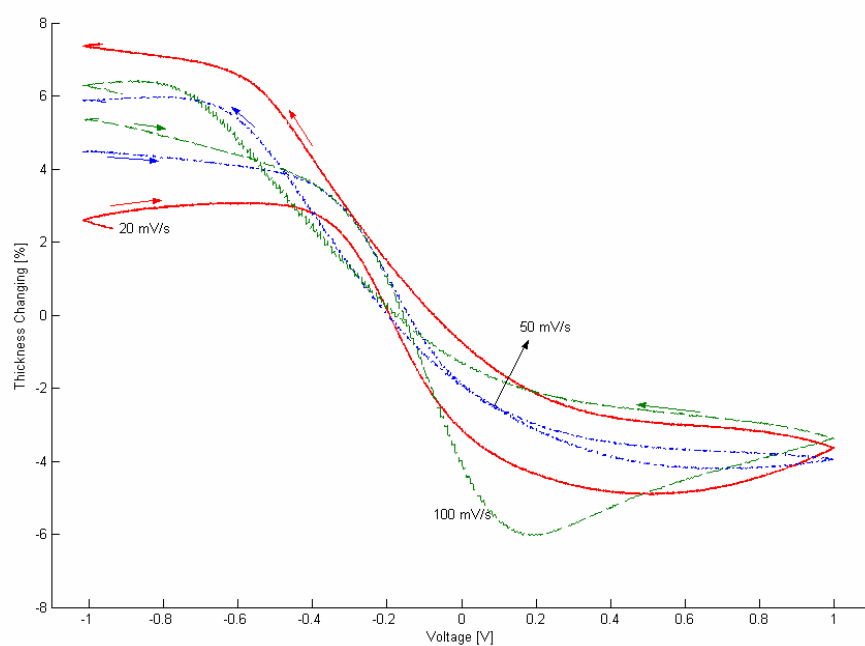


Figure 6.4.14. Thickness variation in PPy during switching at different scan rates in EMI-TSFI Ionic Liquid electrolyte

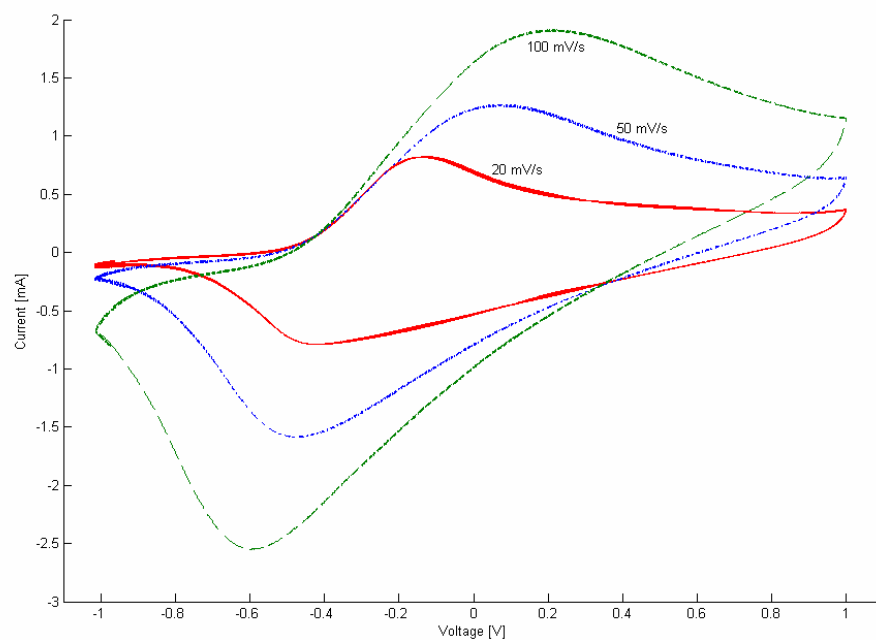


Figure 6.4.15 Cyclic Voltammograms of PPy at different scan rates in EMI-TFSI electrolyte.

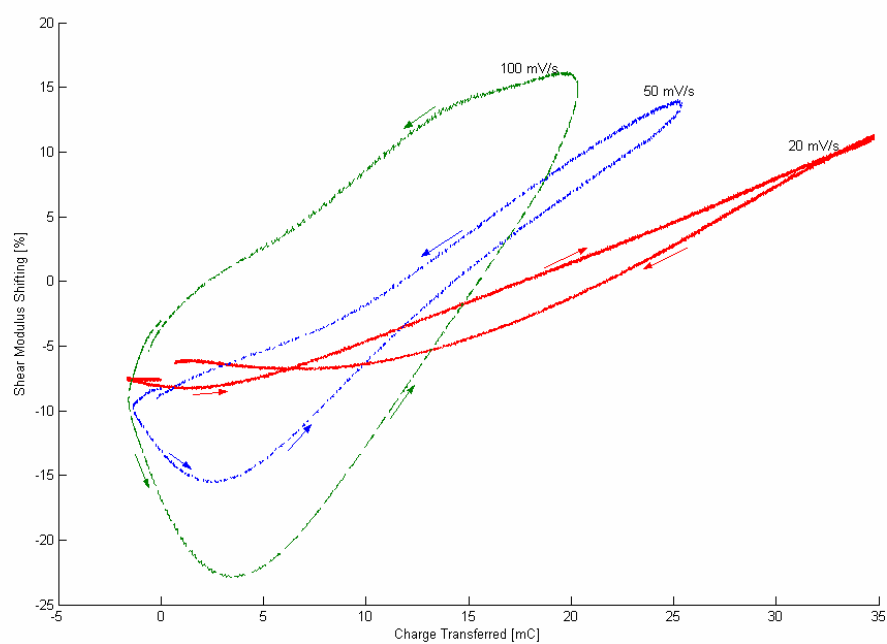


Figure 6.4.16 Shear modulus change in PPy during switching in EMI-TSFI Ionic Liquid electrolyte obtained at different scan rates vs. charge transferred.

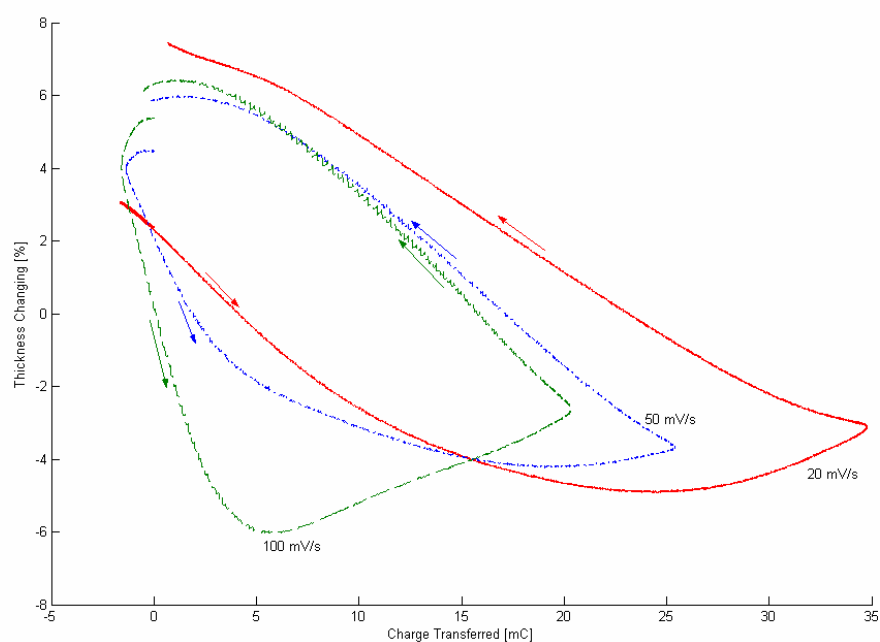


Figure 6.4.17 Thickness variation in PPy during switching at different scan rates in EMI-TSFI Ionic Liquid electrolyte vs. charge transferred.

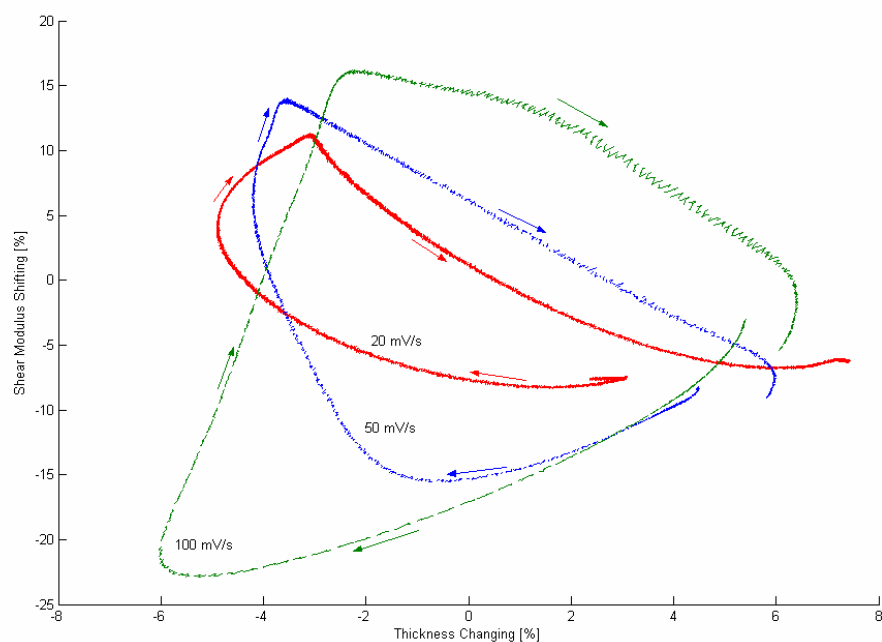


Figure 6.4.18 Shear Modulus shifting vs. thickness changing at different scan rates in EMI-TSFI Ionic Liquid electrolyte.

6.5. Conclusions

New techniques have been developed which show that the QCM can be used to develop a better understanding of the real-time dynamic behaviour of polymer actuators. This study has focused on the development of new techniques using a QCM to measure the effect of electrochemical stimulation on real shear modulus of PPy during electrochemical cycling in both IL and PC electrolytes. Software was developed using numerical optimisation methods for solving complicated simultaneous equations to interpret two signals from the QCM system to give the thickness and the real shear modulus of the deposited layer. In addition, a QCM experimental methodology was designed to monitor dynamic changes in real shear modulus and thickness of PPy film during electrochemical actuation. The performance of the QCM technique has been confirmed by applying it to standard polymers (polystyrene and poly(styrene-co-isobutylene)) and comparing the results with references and with results obtained from conventional test methods.

The new in situ electrochemical QCM based method was used to study changes in the real shear modulus and the thickness of a PPy layer in two different electrolytes, propylene carbonate and EMI-TFSI ionic liquid. Complex changes in modulus were observed during the electrochemical cycling of PPy. It was shown that the modulus variation can be considered almost reversible with a small hysteresis.

This work also raised a number of issues requiring further work by researchers. At least three processes appear to be involved in the modulus changes including the diffusion of ions and/or solvent producing swelling and a reduction in modulus. In addition, the modulus was found to increase under anodic potentials, which may be due to the stiffening of the polymer chains because of the presence of the positive charges. Further studies are required to fully elucidate the mechanisms for the modulus shift.

Finally, the change in modulus also coincided with changes in the microstructure of polypyrrole as reported in previous work (Warren and Madden, 2006b). Further studies are required to fully elucidate the mechanisms responsible for the modulus shift.

CHAPTER 7: CONCLUSIONS AND RECOMMENDATIONS FOR FUTURE RESEARCH

7.1. Conclusions

The research presented in this thesis has studied the electro-chemo-mechanical modelling of conducting polymer polypyrrole helix tube actuators. The model is able to predict the mechanical response of the actuator based on a given amount of electrical stimulation under external load. The model can be utilised in control engineering and robotics applications to design and set-up advanced model-based control algorithms. The model can also be helpful in optimising and improving actuation performance during the design phase of actuator systems.

In Chapter 1, a brief literature review was presented including the background of conducting polymer materials, actuators, their performance and the summary of the modelling research carried out to date. It was shown that prior models had not fully considered the viscoelastic nature of polypyrrole or the effect of the applied potential on the viscoelastic parameters. The aim of this thesis was to develop a model that included variable viscoelastic elements and to apply this model to the helix tube actuator system.

In Chapter 2, the general experimental set-up has been briefly described. The detailed experimental methodology has been explained in the beginning of each chapter.

Chapter 3 describes the active electrochemical properties of the actuator. Cyclic voltammetry over different ranges of voltage was used to optimise the stimulation voltage range to maximise the actuation strain generated. The strain generated as a function of charge transferred was also studied for different stimulating voltage ranges and scan rates. It was shown that the strain to charge ratio was not constant when a wide voltage range was used. Excess current flows at high positive voltages probably due to secondary, parasitic reactions. These reactions (and the excess charge transferred) cannot be avoided in the electrolyte system chosen if large actuation strains are desired. Consequently, a master curve of strain to charge (density) ratio versus applied voltage was constructed. It has been shown that the voltage ranges and stimulation scan rate have negligible effect on the strain to charge ratio master curve in the practical range of stimulation of PPy helix tube. It has also been shown that applied load has negligible effect on the cyclic

voltametric result of PPy helix tube. Hence the electrical charge transferred is independent of the mechanical loading.

A 'primary model' was proposed based on the 'master curve' for the strain to charge ratio. This model was compared with the constant strain to charge ratio model. These models were investigated by setting up a simulation program to predict the experimental strain results carried out by sinusoidal voltages applied with different frequencies and under different load conditions. The results showed that the 'primary model' better simulated the strain output during wide voltage cycling compared with the constant strain to charge ratio model. However, the 'primary model' still did not accurately predict the magnitude of the strain, indicating that the sinusoidal stimulation produces different strain outputs from triangular waveforms (used to generate the master curve). Also, the 'primary model' was seen to fail when the external load was changed. Hence additional elements need to be included in the model to account for viscoelastic effects and changes in modulus. These modifications were considered in the following chapters.

In Chapter 4, the Viscoelastic Lumped Parameters technique (Della Santa et al., 1997a, Della Santa et al., 1997b, Mazzoldi et al., 2000) was applied to the actuator and utilized to describe the viscoelastic behaviour. The results demonstrate that linear viscoelastic models cannot estimate the mechanical behaviour of PPy fibre, although they are successful on EAP films (Mazzoldi et al., 2000, Della Santa et al., 1997a, Della Santa et al., 1997b, Della Santa et al., 1996, Della Santa et al., 1997c). It was found that at the stresses/strains typically encountered in actuator testing, the PPy helix tube fibres were not fully straight and, hence, showed non-linear stress-strain curves. Wet stress relaxation tests at 0 V were carried out and a mathematical model fitted to the data to give values of stiffness and damping coefficients calculated under different test conditions. It was shown that three viscoelastic branches ($n=3$) plus one main spring in parallel adequately described the mechanical properties of a PPy helix tube fibre in specified isometric strain since the values of R-square, total stiffness and total damping coefficients are not significantly changed by increasing the number of viscoelastic branches. Both stiffness and damping coefficients varied for different applied isometric strains, but the graphs illustrate that the variations were almost linear. This means that the stress-strain diagram is parabolic in the actuation strain area, giving an S-shaped curve over the entire strain range. This behaviour makes the dynamic explanation of the fibre actuators very complicated because the phenomenon of active strain generation of EAP fibres is modelled as a configuration of

many springs and dashpots which do not behave like linear elements. Hence, all elements of the system would be altered during displacement under the effect of electrical stimulation. Thus the system proposed in Chapter 4, moves through different isometric strain conditions during the process of actuation and consequently the characteristic of the system elements varies during the stimulation. However, this variation is predictable linearly and these linear methods can be generalized for PPy fibre actuators.

These observations lead to the development of the 'passive improvement' model. This model was tested by applying the sinusoidal voltage signal with different frequencies under different external loads. A simulation program was designed to predict the output strain and compare it to the experimental strain output. The passive improvement greatly improved the primary model performance by predicting the general creep phenomenon due to an increase in the applied stress. However, the passive improvement did not predict some subtle variations in the experimental data and also under-estimated the peak strains. Further modification to the predictive model is included in Chapter 5 where the effect of applied voltage on the viscoelastic parameters is considered.

In the research presented in Chapter 5, the mechanical properties of the actuator have been determined at different applied voltages. These mechanical properties have then been used to calculate the strain response under load and added to the electrochemical strain to give the 'active and passive improvement' model. A high frequency square wave isotonic stress was employed to compute the total stiffness coefficient, viscosity coefficient and the first viscoelastic time constant values. The accuracy of these results has been confirmed by comparison with the Dynamic Mechanical Analyser instrument.

Results presented in Chapter 5 demonstrate that there is a directly proportional relationship between doping level variation and the total stiffness coefficient, viscosity coefficient and the first viscoelastic time constant of the actuator. The modulus changes in a complex manner with doping level, reflecting the effect of volume changes and inter-chain interaction. Similarly, the viscosity term also changes in a complex manner with doping. The phenomena can be modelled by taking into account that the viscoelastic elements coefficients are decreasing almost linearly during oxidation while the actuator is expanding and are increasing almost linearly during reduction while the actuator is contracting. These techniques were added to the model to produce the 'active and passive improvement' model.

Finally in Chapter 5, experimental data from sinusoidal stimulation have been simulated using the ‘active and passive improvement’ model. A significant improvement of this model was observed compared with the ‘passive improvement’ model. In many cases, the experimental data was closely tracked by the predicted results of the ‘active and passive improvement’ model. It can be concluded that the changes in mechanical properties of the polymer make significant contributions to the strain response when an external load is applied.

Chapter 6 describes results from the electrochemical quartz crystal microbalance which shows that the QCM can be used to develop a better understanding of the real-time dynamic behaviour of polymer actuators. The significance of this method is that it enables the simultaneous measurement of mass transfer and the mechanical parameters variation in the electrochemical environment. A mathematical solver program was developed to calculate both the real shear modulus and the film thickness from the QCM outputs. Software was developed using numerical optimisation methods for solving complicated simultaneous equations to interpret two signals from the QCM system to give the thickness and the real shear modulus of the deposited layer. In addition, a QCM experimental methodology was designed to monitor dynamic changes in real shear modulus and thickness of PPy film during electrochemical actuation. The performance of the QCM technique was confirmed by applying it to standard polymers (polystyrene and poly (styrene-co-isobutylene)) and comparing the results with other published research and with results obtained from conventional test methods. The new in situ electrochemical QCM based method was used to study changes in the real shear modulus and the thickness of a PPy layer in two different electrolytes, propylene carbonate and EMI-TFSI ionic liquid. Complex changes in modulus were observed during the electrochemical cycling of PPy. It was shown that the modulus variation can be considered almost reversible but with a small hysteresis.

7.2. Future work

There is much need for further studies on the electro-chemo-mechanical modelling of conducting polymer actuators. The recommendations in the following list arise from both the findings of the current thesis and possibilities associated with the developed experimental materials and techniques. Recommendations for future studies include:

- Perform the same modelling on more advanced actuators that have been recently developed using PPy doped by Li (TFSI). These are much faster and give larger displacements.
- Research is needed to examine the ability of the formulations studies in the current thesis to operate correctly at higher actuation frequencies.
- Create a practical impedance electrochemical model to combine with the presented electro-mechanical model to predict the mechanical output using just the voltage input.
- Perform the next step toward the control of the actuator and try to predict the electrical input needed to produce a desired mechanical output (i.e. find an inverse dynamic model of the system).
- Perform QCM measurement using more advanced equipment which is able to operate in two resonance frequencies simultaneously. This method will also enable the calculation of the viscosity coefficient of the deposited film as a function of the applied voltage.
- Explore the chemical mechanism behind the ‘modulus shifting’ phenomenon which was introduced and modelled in Chapter 5 and 6.
- Perform the presented calculation method on several conducting polymers such as PANi, PPy and their composites with CNT (carbon nanotube) doped by different ions in various electrolytes.

APPENDIX A: LAPLACE TRANSFORM

The Laplace Transform is a widely used standard technique for analysing linear systems such as electrical circuits, harmonic oscillation and mechanical systems. The Laplace transform provides a method to solve Ordinary Differential Equations (ODE's) of dynamic systems in the time-domain. The Laplace transform is shown in Equation A- 1 and it transforms functions of time to functions of the Laplace parameter “s”. The Laplace transform has many important applications in physics, optics, engineering (electrical, mechanical and control), signal processing and systems analysis in economics and management. The Laplace transform not only greatly reduces the complexity of the mathematical calculations required to solve the differential equations for system analysis but also provides a technique to investigate the behaviour of a system in the frequency-domain.

$$F(s) = L\{f(t)\} = \int_{0^-}^{\infty} e^{-st} f(t) dt \quad \text{Equation A- 1}$$

As shown in Equation A- 2, the Laplace parameter (‘s’) is a complex number.

$$s = \sigma + j\omega \quad \text{Equation A- 2}$$

The inverse Laplace transform is given in Equation A- 3.

$$f(t) = L^{-1}\{F(s)\} = \frac{1}{2\pi j} \int_{\gamma-j\infty}^{\gamma+j\infty} e^{st} F(s) ds \quad \text{Equation A- 3}$$

The Laplace transform has several properties that make it useful and simple for analysing linear dynamic systems. The most significant advantage of Laplace transform is to simplify differentiation and integration by transforming these operations to simple multiplication and division. This changes ODE's to simple polynomial equations in s that are easy to solve. Then the inverse Laplace transform can be used to find a closed form solution of the ODE in the time-domain. Table A- 1 shows the basic Laplace transforms (Refer Equation A- 4)

$$F(s) = L\{f(t)\}$$

$$G(s) = L\{g(t)\}$$

Equation A- 4

Table A- 1 Laplace Transform list.

	Time domain	Laplace domain
1	$a.f(t) + b.g(t)$	$a.F(s) + b.G(s)$
2	$f'(t) = \frac{df(t)}{dt}$	$s.F(s) - f(0)$
3	$f''(t) = \frac{d^2 f(t)}{dt^2}$	$s^2.F(s) - sf(0) - f'(0)$
4	$f^{(n)}(t)$	$s^n.F(s) - s^{n-1}f(0) - \dots - f^{(n-1)}(0)$
5	$\int_0^t f(\tau) d\tau$	$\frac{1}{s}.F(s)$
6	$f(at)$	$\frac{1}{ s }.F\left(\frac{s}{a}\right)$
7	Unit Step: $u(t)$	$\frac{1}{s}$
8	Ramp: $t.u(t)$	$\frac{1}{s^2}$
9	$\sin(\omega t)$	$\frac{\omega}{s^2 + \omega^2}$
10	$\cos(\omega t)$	$\frac{s}{s^2 + \omega^2}$

	Time domain	Laplace domain
11	$e^{at} f(t)$	$F(s-a)$

One of the advantages of Laplace transform is to enable prediction of a system's response when time is approaching zero or infinity without solving the ODE of the system. Equation A- 5 and Equation A- 6 present the 'Final Value' and 'Initial Value' theorems which are standard methods of identifying the system response in time $t=\infty$ and $t=0$, respectively.

Initial Value Theorem:

Equation A- 5

$$f(0) = \lim_{s \rightarrow \infty} (s.F(s))$$

Final Value Theorem:

Equation A- 6

$$f(\infty) = \lim_{s \rightarrow 0} (s.F(s))$$

The Laplace transform defined in Equation A- 1 also can be changed to the continuous Fourier transform by considering only the imaginary part of the Laplace parameter ('s') in Equation A- 2 and replacing $s = j\omega$. Using this replacement enables the easy calculation of system response to steady-state sinusoidal excitation. Further information about Laplace and Fourier transforms can be found in many text books such as (Franklin et al., 1987).

APPENDIX B: STATE-SPACE METHOD

In control engineering, ‘state space’ is a mathematical model of a physical system as a set of inputs and outputs as shown in Figure B- 1. The state space representation provides a convenient and compact way to model and analyse systems with multiple inputs and outputs. This enables a high order Ordinary Differential Equation (ODE) to be considered as a set of first order ODE’s. This process enables the solving of the differential equations in the time-domain using standard simulation programs and methods in numerical analysis such as Runge-Kutta, Adams-Bashforth-Moulton and Gear’s method. These techniques have been standardised in MATLAB software as ODE45 and ODE23 for Runge-Kutta and ODE113 for Adams-Bashforth-Moulton and ODE15s for Gear’s method and been used by researchers in the fields of engineering, economics and many other fields in which the analysis of a process in the time-domain is required.



Figure B- 1 state space model relates ‘p’ inputs to ‘q’ outputs using ‘n’ first order ordinary differential equations.

As shown in Equation B- 1, ‘q’ outputs (y), ‘p’ inputs (u) and ‘n’ states (x) are related by ‘n’ first order equations. The number of state parameters is the same as the number of the first order differential equations. In Equation B- 1 A, B, C and D are matrices that contain the coefficients of the equations.

$$\begin{aligned}\dot{x}_{n \times 1}(t) &= A_{n \times n}(t)x_{n \times 1}(t) + B_{n \times p}(t)u_{p \times 1}(t) \\ y_{q \times 1}(t) &= C_{q \times n}(t)x_{n \times 1}(t) + D_{q \times p}(t)u_{p \times 1}(t)\end{aligned}$$

Equation B- 1

Figure B- 2 shows the location of each matrix in the feed-back model. As shown the model relates the inputs to the outputs with this arrangement. The output of the integrator box ($1/s$) is known as the state vector.

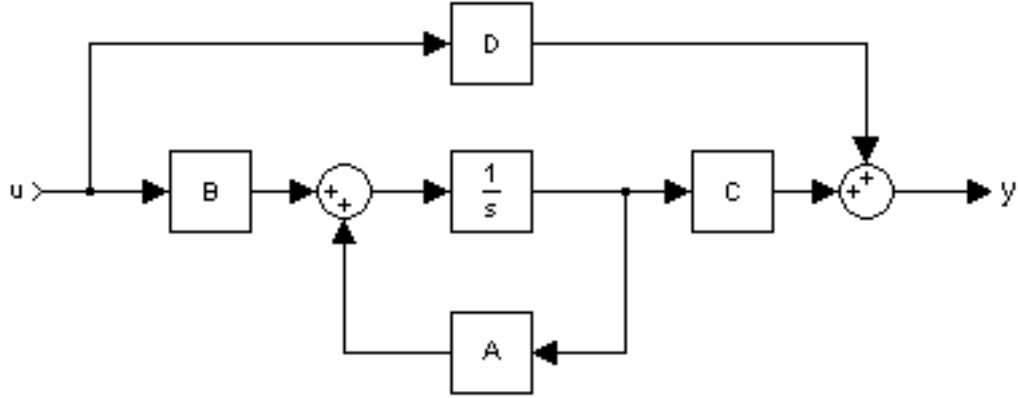


Figure B- 2 the feed-back arrangement of the state-space model matrices and vectors.

As with a single ODE the Laplace transform can be applied to the State Space model in Equation B- 1 as shown in Equation B- 2.

$$\begin{aligned} sX_{n \times 1}(s) &= A_{n \times n}(s)X_{n \times 1}(s) + B_{n \times p}(s)U_{p \times 1}(s) \\ Y_{q \times 1}(s) &= C_{q \times n}(s)X_{n \times 1}(s) + D_{q \times p}(s)U_{p \times 1}(s) \end{aligned} \quad \text{Equation B- 2}$$

The transfer function of this multi-input multi-output system will be a matrix that shows the output to input relation as shown in Equation B- 3

$$\frac{Y_{q \times 1}(s)}{U_{p \times 1}(s)} = G_{q \times p}(s) = C_{q \times n}(sI_{n \times n} - A_{n \times n})^{-1}B_{n \times p} + D_{q \times p} \quad \text{Equation B- 3}$$

Further information about State-Space models can be found in text books such as (Franklin et al., 1987).

BIBLIOGRAPHY

- Andrews, M. K., Jansen, M. L., Spinks, G. M., Zhou, D. Z. and Wallace, G. G. (2004) *Sensors and Actuators a-Physical*, **114**, 65-72.
- Ariza, M. J. and Otero, T. F. (2005) *Colloids and Surfaces A: Physicochemical and Engineering Aspects, Liquids and MesoScience*, **270-271**, 226-231.
- Bandey, H. L., Hillman, A. R., Brown, M. J. and Martin, S. J. (1997) *Faraday Discussions*, **107**, 105-121.
- Bandey, H. L., Martin, S. J., Cernosek, R. W. and Hillman, A. R. (1999) *Analytical Chemistry*, **71**, 2205-2214.
- Bar-Cohen, Y. (2001) *Electroactive polymer (EAP) actuators as artificial muscles : reality, potential, and challenges*, SPIE Press, Bellingham, Wash.
- Bar-Cohen, Y. (2002) In *Paper 4695-02, Proceedings of the SPIE Smart Structures and Materials Symposium, EAPAD Conference* San Diego, CA.
- Baughman, R. H. (1996) *Synthetic Metals*, **78**, 339-353.
- Baughman, R. H., Shacklette, R. L. and Elsenbaumer, R. L. (1991) In *Topics in molecular organization and engineering*, Vol. 7: Molecular electronics : materials and methods (Ed, Lazarev, P. I.) Kluwer Academic Publishers, Dordrecht ; Boston, pp. xi, 337 p.
- Bay, L., Jacobsen, T., Skaarup, S. and West, K. (2001a) *Journal of Physical Chemistry B*, **105**, 8492-8497.
- Bay, L., West, K., Sommer-Larsen, P., Skaarup, S. and Benslimane, M. (2003) *Advanced Materials*, **15**, 310-313.
- Bay, L., West, K., Vlachopoulos, N. and Skaarup, S. (2001b) In *Electroactive Polymer, Actuators and Devices-Smart Structures and Materials 2001- Proceedings of SPIE - The International Society for Optical Engineering*. v 4329 2001., Newport Beach, CA, United States, pp. 54-58.
- Behling, C., Lucklum, R. and Hauptmann, P. (1998) In *Frequency Control Symposium, 1998. Proceedings of the 1998 IEEE International*, pp. 823-830.
- Behling, C., Lucklum, R. and Hauptmann, P. (1999) *Ultrasonics, Ferroelectrics and Frequency Control, IEEE Transactions on*, **46**, 1431-1438.
- Biot, M. A. (1941) *Journal of Applied Physics*, **12**, 155-164.
- Biot, M. A. (1955) *Journal of Applied Physics*, **26**, 182-185.
- Biot, M. A. (1956) *The Journal of The acoustical Society of America*, **28**, 168-178.
- Brandrup, J., Immergut, E. H., Grulke, E. A., Abe, A. and Bloch, D. R. (1989) *Polymers Handbook*, John Wiley and Sons.
- Brown, M. J., Hillman, A. R., Martin, S. J., Cernosek, R. W. and Bandey, H. L. (2000) *Journal of Materials Chemistry*, **10**, 115-126.
- Careem, M. A., Velmurugu, Y., Skaarup, S. and West, K. (2006) *Journal of Power Sources, Special issue including selected papers from the 3rd International Conference on Materials for Advanced Technologies (ICMAT 2005, Singapore, Malaysia) and the Summer School on Synthesis of Nanostructured Materials for Polymer Batteries(Augustow, Poland) together with regular papers*, **159**, 210-214.
- Careem, M. A., Vidanapathirana, K. P., Skaarup, S. and West, K. (2004) In *Fourteenth International Conference on Solid State Ionics* Solid State Ionics Fourteenth International Conference on Solid State Ionics. v 175 n 1-4 Nov 30 2004., Monterey, CA., United States, pp. 725-728.

- Chiarelli, P., Della Santa, A., De Rossi, D. and Mazzoldi, A. (1995) *Journal of Intelligent Material Systems & Structures*, **6**, 32-37.
- Christophersen, M., Shapiro, B. and Smela, E. (2006) *Sensors and Actuators B: Chemical*, **115**, 596-609.
- Cooper, J. M., Cubitt, R., Dalglish, R. M., Gadegaard, N., Glidle, A., Hillman, A. R., Mortimer, R. J., Ryder, K. S. and Smith, E. L. (2004) *Journal of the American Chemical Society*, **126**, 15362-15363.
- De Rossi, D., Della Santa, A. and Mazzoldi, A. (1999) *Materials Science and Engineering: C*, **7**, 31-35.
- Della Santa, A., De Rossi, D. and Mazzoldi, A. (1997a) *Smart Materials & Structures*, **6**, 23-34.
- Della Santa, A., De Rossi, D. and Mazzoldi, A. (1997b) *Synthetic Metals*, **90**, 93-100.
- Della Santa, A., Mazzoldi, A., Tonci, C., Chiarelli, P. and De Rossi, D. (1996) *Proceedings of SPIE - The International Society for Optical Engineering, Bellingham, WA*, **2779**, 371-376.
- Della Santa, A., Mazzoldi, A., Tonci, C. and De Rossi, D. (1997c) *Materials Science and Engineering: C*, **5**, 101-109.
- Ding, J., Liu, L., Spinks, G. M., Zhou, D., Wallace, G. G. and Gillespie, J. (2003a) *Synthetic Metals*, **138**, 391-398.
- Ding, J., Zhou, D., Spinks, G., Wallace, G., Forsyth, S., Forsyth, M. and MacFarlane, D. (2003b) *Chem. Mater.*, **15**, 2392-2398.
- Draper, N. R. and Smith, H. (1998) *Applied Regression Analysis*, John Wiley & Sons, New York.
- Dyreklev, P., Granstrom, M., Ingnas, O., Gunaratne, L. M. W. K., Senadeera, G. K. R., Skaarup, S. and West, K. (1996) *Polymer*, **37**, 2609-2613.
- Ebewele, R. O. (c2000) *Polymer science and technology*, Boca Raton, London.
- Ferloni, P., Mastragostino, M. and Meneghello, L. (1996) *Electrochimica Acta*, **41**, 27-33.
- Franklin, G. F., J. D. Powell and Emami-Naeini, A. (1987) *Feedback Control of Dynamic Systems*, Addison-Wesley.
- Gandhi, M. R., Murray, P., Spinks, G. M. and Wallace, G. G. (1995) *Synthetic Metals*, **73**, 247-256.
- Glidle, A., Hillman, A. R. and Bruckenstein, S. (1991) *Journal of Electroanalytical Chemistry*, **318**, 411-420.
- Grande, H. and Otero, T. F. (1999) *Electrochimica Acta*, **44**, 1893-1900.
- Grande, H., Otero, T. F. and Cantero, I. (1998) *Journal of Non-Crystalline Solids*, **235-237**, 619-622.
- Hara, S., Zama, T., Takashima, W. and Kaneto, K. (2005) *Synthetic Metals*, **149**, 199-201.
- Hara, S., Zama, T., Takashima, W. and Kaneto, K. (2006) *Synthetic Metals*, **156**, 351-355.
- Hillman, A. R. (2003) In *Encyclopedia of Electrochemistry*, Vol. 3 (Eds, Bard, A. J., Stratmann, M. and Unwin, P. R.) Wiley, New York, pp. 230-289.
- Hillman, A. R., Efimov, I. and Skompska, M. (2002) *Faraday Discussions*, **121**, 441-62.
- Hillman, A. R., Efimov, I. and Skompska, M. (2005) *J Am Chem Soc*, **127**, 3817-24.
- Hillman, A. R., Jackson, A. and Martin, S. J. (2001) *Analytical Chemistry*, **73**, 540-549.
- Hollerbach, J. M., Hunter, I. W. and Ballantyne, J. A. (1991) In *The Robotics review 2* (Eds, Lozano-Pérez, T., Khatib, O. and Craig, J. J.) MIT Press, Cambridge, Mass., pp. 301-345.
- Hunter, I. W. and Lafontaine, S. (1992) In *Solid-State Sensor and Actuator Workshop, 1992. 5th Technical Digest., IEEE*, pp. 178-185.
- Hutchison, A. S., Lewis, T. W., Moulton, S. E., Spinks, G. M. and Wallace,

- G. G. (2000) *Synthetic Metals*, **113**, 121-127.
- Jager, E. W. H., Smela, E. and Inganas, O. (1999a) *Sensors and Actuators B: Chemical*, **56**, 73-78.
- Jager, E. W. H., Smela, E., Inganas, O. and Lundstrom, I. (1999b) *Proceedings of Spie - the International Society for Optical Engineering*, **3669**, 377-384.
- Jager, E. W. H., Smela, E., Inganas, O. and Lundstrom, I. (1999c) *Synthetic Metals*, **102**, 1309-1310.
- Kanazawa, K. K. and Gordon, J. (1985) *Analytical Chemistry*, **57**, 1770.
- Kaneto, K., Kaneko, M., Min, Y. and MacDiarmid, A. G. (1995) *Synthetic Metals*, **71**, 2211-2212.
- Kwee, T., Taylor, S. J., Mauritz, K. A. and Storey, R. F. (2005) *Polymer*, **46**, 4480-4491.
- Lagier, C. M., Efimov, I. and Hillman, A. R. (2005) *Anal Chem*, **77**, 335-43.
- Lewis, T. W., Kane-Maguire, L. A. P., Hutchison, A. S., Spinks, G. M. and Wallace, G. G. (1999) *Synthetic Metals*, **102**, 1317-1318.
- Lewis, T. W., Moulton, S. E., Spinks, G. M. and Wallace, G. G. (1997a) *Synthetic Metals*, **85**, 1419-1420.
- Lewis, T. W., Spinks, G. M., Wallace, G. G., DeRossi, D. and Pachetti, M. (1997b) *Abstracts of Papers of the American Chemical Society*, **214**, 284-Poly.
- Lu, W., Fadeev, A. G., Qi, B., Smela, E., Mattes, B. R., Ding, J., Spinks, G. M., Mazurkiewicz, J., Zhou, D. and Wallace et, a. (2002) *Science*, **297**, 983-987.
- Lucklum, R., Behling, C. and Hauptmann, P. (2000) *Ultrasonics, Ferroelectrics and Frequency Control, IEEE Transactions on*, **47**, 1246-1252.
- Lucklum, R. and Hauptmann, P. (1997) *Faraday Discussions*, 123-140.
- Lucklum, R. and Hauptmann, P. (2000a) *Electrochimica Acta*, **45**, 3907-3916.
- Lucklum, R. and Hauptmann, P. (2000b) *Sensors and Actuators B: Chemical*, **70**, 30-36.
- Lucklum, R. and Hauptmann, P. (2001) In *Frequency Control Symposium and PDA Exhibition, 2001. Proceedings of the 2001 IEEE International*, pp. 408-418.
- Lucklum, R., Hauptmann, P. and Cernosek, R. W. (2001) In *Frequency Control Symposium and PDA Exhibition, 2001. Proceedings of the 2001 IEEE International*, pp. 542-550.
- Madden, J. D., Cush, R. A., Kanigan, T. S., Brennan, C. J. and Hunter, I. W. (1999) *Synthetic Metals*, **105**, 61-64.
- Madden, J. D., Cush, R. A., Kanigan, T. S. and Hunter, I. W. (2000) *Synthetic Metals*, **113**, 185-192.
- Madden, J. D., Madden, P. G., Anquetil, P. A. and Hunter, I. W. (2002) *Materials Research Society Symposium - Proceedings*, **698**, 137-144.
- Madden, J. D., Rinderknecht, D., Anquetil, P. A. and Hunter, I. W. (2006) *Sensors and Actuators A: Physical*, **133**, 210-217.
- Madden, J. D. W. (2000) Ph.D. Thesis, Massachusetts Institute of Technology. Dept. of Mechanical Engineering., pp. 2 v. (355 leaves).
- Madden, J. D. W., Madden, P. G. A. and Hunter, I. W. (2001a) In *Electroactive Polymer, Actuators and Devices-Smart Structures and Materials 2001-Proceedings of SPIE - The International Society for Optical Engineering*. v 4329 2001., Newport Beach, CA, United States, pp. 72-83.
- Madden, J. D. W., Schmid, B., Hechinger, M., Lafontaine, S. R., Madden, P. G. A., Hover, F. S., Kimball, R. and Hunter, I. W. (2004a) *Oceanic Engineering, IEEE Journal of*, **29**, 738-749.
- Madden, J. D. W., Schmid, B., Lafontaine, S. R., Madden, P. G. A., Hover, F. S., McLetchie, K. and Hunter, I. W. (2003) In *PROCEEDINGS OF SPIE SPIE - The International Society for Optical Engineering: Smart Structures and Materials 2003*

- Electroactive Polymer Actuators and Devices (EAPAD)* Proceedings of SPIE - The International Society for Optical Engineering, v 5051 2003., San Diego, CA, United States, pp. 437-441.
- Madden, J. D. W., Vandesteeg, N. A., Anquetil, P. A., Madden, P. G. A., Takshi, A., Pytel, R. Z., Lafontaine, S. R., Wieringa, P. A. and Hunter, I. W. (2004b) *Oceanic Engineering, IEEE Journal of*, **29**, 706-728.
- Madden, P. G., Madden, J. D., Anquetil, P. A., Yu, H.-h., Swager, T. M. and Hunter, I. W. (2001b) In *2001 Bio-Robotics Symposium* The University of New Hampshire, USA.
- Madden, P. G. A. (2003) Massachusetts Institute of Technology. Dept. of Mechanical Engineering, pp. 136 p.
- Madden, P. G. A., Madden, J. D. W., Anquetil, P. A., Vandesteeg, N. A. and Hunter, I. W. (2004c) *Oceanic Engineering, IEEE Journal of*, **29**, 696-705.
- Martin, S. J., Bandey, H. L., Cernosek, R. W., Hillman, A. R. and Brown, M. J. (2000) *Analytical Chemistry*, **72**, 141-149.
- Matsumoto, H., Kageyama, H. and Miyazaki, Y. (2003) *Electrochemistry*, **71**, 1058-1060.
- Mazzoldi, A., Degl'Innocenti, C., Michelucci, M. and De Rossi, D. (1998) *Materials Science and Engineering: C*, **6**, 65-72.
- Mazzoldi, A., Della Santa, A. and De Rossi, D. (2000) In *Polymer Sensors and Actuators* (Eds, Osada, Y. and Rossi, D. D.) Springer Verlag, pp. 207-244.
- Meites, L. (Ed.) (1963) *Handbook of analytical chemistry*, McGraw-Hill, New York.
- Moré, J. J. and Sorensen, D. C. (1983) *SLAM Journal on Scientific and Statistical Computing*, **3**, 553-572.
- Murray, P., Spinks, G. M., Wallace, G. G. and Burford, R. P. (1998) *Synthetic Metals*, **97**, 117-121.
- Otero, T. F. and Boyano, I. (2006) *Electrochimica Acta*, **51**, 6238-6242.
- Otero, T. F. and Cantero, I. (1999) *Journal of Power Sources*, **81-82**, 838-841.
- Otero, T. F. and Cortés, M. T. (2003) *Advanced Materials*, **15**, 279-282.
- Otero, T. F. and Grande, H. (1996) *Journal of Electroanalytical Chemistry*, **414**, 171-176.
- Otero, T. F., Grande, H. and Rodriguez, J. (1995) *Journal of Electroanalytical Chemistry*, **394**, 211-216.
- Otero, T. F., Grande, H. and Rodriguez, J. (1996a) *Electrochimica Acta, Electrochemistry of Electroactive Polymer Films*, **41**, 1863-1869.
- Otero, T. F., Grande, H. and Rodriguez, J. (1996b) *Synthetic Metals*, **76**, 285-288.
- Otero, T. F., Grande, H. and Rodriguez, J. (1996c) *Synthetic Metals*, **76**, 293-295.
- Otero, T. F., Lopez Cascales, J. J. and Vazquez Arenas, G. (2006) *Materials Science and Engineering: C*, **27**, 18-22.
- Otero, T. F. and Sansinena, J. M. (1995) *Bioelectrochemistry & Bioenergetics*, **38**, 411-414.
- Otero, T. F. and Sansinena, J. M. (1998) *Advanced Materials*, **10**, 491-494.
- Penner, R. M., Dyke, L. S. V. and Martin, C. R. (1988) *Journal of Physical Chemistry*, **92**, 5274-5282.
- Penner, R. M. and Martin, C. R. (1988) *Journal of Physical Chemistry*, **93**, 984-989.
- Penner, R. M., Van Dyke, L. S. and Martin, C. R. (1989) *Solid State Ionics*, **32-33**, 553-566.
- Randriamahazaka, H., Plesse, C., Teyssie, D. and Chevrot, C. (2005a) *Electrochimica Acta*, **50**, 4222-4229.
- Randriamahazaka, H., Plesse, C., Teyssie, D. and Chevrot, C. (2005b) *Electrochimica Acta*, **50**, 1515-1522.

- Ren, X. and Pickup, P. G. (1995) *Journal of Electroanalytical Chemistry*, **396**, 359-364.
- Reynolds, J. R., Skotheim, T. A. and Elsenbaumer, R. L. (1998) *Handbook of conducting polymers*, M. Dekker, New York.
- Sauerbrey, G. (1959) *Z. Phys*, **155**, 206-222.
- Skaarup, S., Bay, L., Vidanapathirana, K., Thybo, S., Tofte, P. and West, K. (2003) *Solid State Ionics*, **159**, 143-147.
- Skaarup, S., West, K., Gunaratne, L. M. W. K., Vidanapathirana, K. P. and Careem, M. A. (2000) *Solid State Ionics. v 136-137 Nov 2000*, 577-582.
- Smela, E. (2003) *Advanced Materials*, **15**, 481-494.
- Smela, E. and Gadegaard, N. (1999) *Advanced Materials*, **11**, 953-+.
- Smela, E., Inganas, O. and Lundstrom, I. (1993) *Journal of Micromechanics & Microengineering*, **3**, 203-205.
- Smela, E., Kallenbach, M. and Holdenried, J. (1999) *Journal of Microelectromechanical Systems*, **8**, 373-383.
- Spinks, G. M., Campbell, T. E. and Wallace, G. G. (2005) *Smart Materials and Structures*, 406-412.
- Spinks, G. M., Liu, L., Wallace, G. G. and Zhou, D. (2002) *Advanced Functional Materials*, **12**, 437-440.
- Spinks, G. M. and Truong, V.-T. (2005) *Sensors and Actuators A: Physical*, **119**, 455-461.
- Spinks, G. M., Wallace, G. G., Ding, J., Zhou, D., Xi, B. and Gillespie, J. (2003a) In *PROCEEDINGS OF SPIE SPIE - The International Society for Optical Engineering: Smart Structures and Materials 2003 Electroactive Polymer Actuators and Devices (EAPAD)* Proceedings of SPIE - The International Society for Optical Engineering. v 5051 2003., San Diego, CA, United States, pp. 372-380.
- Spinks, G. M., Wallace, G. G., Ding, J., Zhou, D., Xi, B., Scott, T. R. and Truong, V.-T. (2003b) In *PROCEEDINGS OF SPIE SPIE - The International Society for Optical Engineering: Smart Structures and Materials 2003 Electroactive Polymer Actuators and Devices (EAPAD)* Proceedings of SPIE - The International Society for Optical Engineering. v 5051 2003., San Diego, CA, United States, pp. 21-28.
- Spinks, G. M., Wallace, G. G., Liu, L. and Zhou, D. (2003c) *Macromolecular Symposia*, **192**, 161-169.
- Spinks, G. M., Xi, B., Zhou, D., Truong, V.-T. and Wallace, G. G. (2004) *Synthetic Metals*, **140**, 273-280.
- Spinks, G. M., Zhou, D., Liu, L. and Wallace, G. G. (2003d) *Smart Materials & Structures*, **12**, 468-472.
- Tanguy, J. (1991) *Synthetic Metals*, **43**, 2991-2994.
- Tanguy, J., Slama, M., Hoclet, M. and Baudouin, J. L. (1989) *Synthetic Metals*, **28**, 145-150.
- Theisen, L. A., Martin, S. J. and Hillman, A. R. (2004) *Analytical Chemistry*, **76**, 796-804.
- Vidanapathirana, K. P., Careem, M. A., Skaarup, S. and West, K. (2002) *Solid State Ionics*, **154-155**, 331-335.
- Wallace, G. G., Ding, J., Lu, L., Spinks, G. M., Zhou, D., Forsyth, S., Forsyth, M. and MacFarlane, D. (2002) In *Smart Structures and Materials 2002: Electroactive Polymer Actuators and Devices (EAPAD)* Proceedings of SPIE - The International Society for Optical Engineering. v 4695 2002., San Diego, CA, United States, pp. 8-16.
- Wang, X. Z., Shapiro, B. and Smela, E. (2004) *Advanced Materials*, **16**, 1605-+.
- Warren, M. R. and Madden, J. D. (2006a) *Journal of Electroanalytical Chemistry*, **590**, 76-81.

- Warren, M. R. and Madden, J. D. (2006b) *Synthetic Metals*, **156**, 724-730.
- West, K., Careem, M. A. and Skaarup, S. (1993a) *Solid State Ionics*, **60**, 153-159.
- West, K., Jacobsen, T., Zachau-Christiansen, B., Careem, M. A. and Skaarup, S. (1993b) *Synthetic Metals*, **55**, 1412-1417.
- West, K., Zachau-Christiansen, B., Jacobsen, T. and Skaarup, S. (1992) *Materials Science and Engineering B*, **13**, 229-233.
- Xi, B. (2005) Thesis (Ph.D.)--University of Wollongong.
- Yamato, K. and Kaneto, K. (2006) *Analytica Chimica Acta, Molecular Electronics and Analytical Chemistry*, **568**, 133-137.